

UNCLASSIFIED

AD NUMBER
AD905055
NEW LIMITATION CHANGE
TO Approved for public release, distribution unlimited
FROM Distribution authorized to U.S. Gov't. agencies only; Test and Evaluation; MAR 1972. Other requests shall be referred to Air Force Avionics Lab., Wright-Patterson AFB, OH 45433.
AUTHORITY
SAMSO USAF ltr, 11 Apr 1978

THIS PAGE IS UNCLASSIFIED

AFAL-TR-72-307

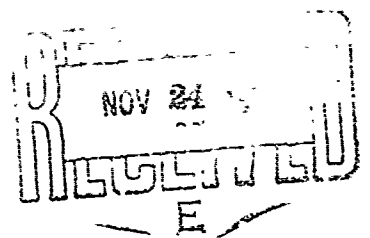
OPTICAL PROPAGATION TESTS STUDY

P. J. Titterton
D. P. Woodman
et al

GTE Sylvania Inc.

TECHNICAL REPORT AFAL-TR-72-307

September 1972



"Distribution is limited to U. S. Government agencies only, by reason of inclusion of test and evaluation data; applied March 1972. Other requests for this document must be referred to AFAL/TEL, Wright-Patterson AFB, Ohio 45433."

Air Force Avionics Laboratory
Air Force Systems Command
Wright-Patterson Air Force Base, Ohio 45433

AD905055

NOTICE

When Government drawings, specifications, or other data are used for any purpose other than in connection with a definitely related Government procurement operation, the United States Government thereby incurs no responsibility nor any obligation whatsoever; and the fact that the Government may have formulated, furnished, or in any way supplied the said drawings, specifications, or other data, is not to be regarded by implication or otherwise as in any manner licensing the holder or any other person or corporation, or conveying any rights or permission to manufacture, use, or sell any patented invention that may in any way be related thereto.

Copies of this report should not be returned unless return is required by security considerations, contractual obligations, or notice on a specific document.

OPTICAL PROPAGATION TESTS STUDY

P. J. Titterton
D. P. Woodman
et al

"Distribution is limited to U. S. Government agencies only, by reason of inclusion of test and evaluation data; applied March 1972. Other requests for this document must be referred to AFAL/TEL, Wright-Patterson AFB, Ohio 45433."

FOREWORD

This report summarizes the four and one half months of work performed on Air Force Contract F33615-72-C-2951 entitled "Optical Propagation Tests Study". The objectives of this work have been to characterize atmospheric turbulence effects on laser beams, to design techniques to minimize these effects on an optical communications link, and to design experiments to verify these effects and design techniques, for atmospheric propagation paths. This report was prepared by the Electro-Optics Organization of GTE Sylvania, Inc., Electronic Systems Group - Western Division, Mountain View, California, and describes work performed in the Program 405B Laser Communications Organization, headed by Mr. Arthur Kraemer. Dr. Paul J. Titterton and Dr. Douglas P. Woodman have been the principal technical investigators on this program. Other major contributors include Mr. Martin Boehme, Mr. John Forkner, Mr. W. Don Huber, Mr. Richard Heinz, Mr. Robert Jones, Mr. Frank Lord, Mr. Scott Overstreet, Mr. William Schick, Mr. Norman Spaulding. Mr. Ted Arken, Mr. Larry Mallery and Mr. Connell Ward also contributed. Professor J. Richard Kerr of the Oregon Graduate Center has been a consultant on this program.

The work performed under this contract was administered by Advanced Development Program/405B at the Air Force Avionics Laboratory (TEL), Air Force Systems Command, Wright Patterson Air Force Base, Ohio. Captain George Matassov has been the technical contract monitor. The project and task designation was 405B-01-56.

This report was submitted in September 1972 and has been reviewed for publication.



ROBERT E. DEAL, ACTING BRANCH CHIEF
Lasers & Electro-Optic Technology Branch
Electronic Technology Division

ABSTRACT

The Optical Propagation Tests Study has analyzed the effects of atmospheric turbulence on atmospheric laser links. Our analyses have found that scintillation (beam breakup), beam spread and beam wander will preclude operation of a high data rate uplink at 1 Gbps with an average F_E of 10^{-6} , unless special techniques are utilized in the ground transmitter design. We have predicted that focusing the beam at or above the tropopause will reduce the scintillation effects sufficiently, and pointing the uplink beam along the instantaneous normal to a downlink wavefront of a beam which originates at the satellite transmitter (reciprocity tracking) will remove most of the wander effects.

We have explored a number of possible experimental techniques, suitable for testing these predictions. Our recommendation is to perform an experiment in May/June 1974 using a variable focus reciprocity tracking ground transceiver and a balloon-borne (altitude 100,000 feet) system that is a modification of that developed in the Balloon Atmospheric Propagation Experiment. This recommendation allows for full utilization of the techniques (and equipment) developed under the 405B Acquisition/Tracking Brassboard programs and will specify the design constraints for the ground station by June 30, 1974.

TABLE OF CONTENTS

<u>Section</u>	<u>Title</u>	<u>Page</u>
I	INTRODUCTION	1
II	SUMMARY	3
	2.1 Introduction	3
	2.2 Turbulence Effects	3
	2.3 Experimental Techniques	6
III	BACKGROUND	11
	3.1 Introduction	11
	3.2 SDR Preliminary Subsystem Design	11
	3.3 Turbulent Analyses and Experiments	13
	3.4 Equipment Availability	14
	3.4.1 Existing Balloon-borne Equipment	14
	3.4.2 Ground Station	14
	3.4.3 Turbulence Sensors	17
	3.5 Summary	17
IV	TURBULENCE THEORY ANALYSES SUMMARY	19
	4.1 Introduction	19
	4.2 Turbulence Effects	19
	4.2.1 Scintillation	19
	4.2.2 Spread	22
	4.2.3 Wander	23
	4.3 Beacon Effects	24
V	EXPERIMENTAL TECHNIQUES	29
	5.1 Introduction	29
	5.2 General Design Considerations	30
	5.2.1 Ground Station	30
	5.2.2 Balloon System	30
	5.3 Basic Experiment Configuration	31
	5.4 Transmitter Mounting Platforms	31
	5.4.1 The NASA Mount (ATLAS)	31
	5.4.2 Separate Mounting Platforms	33
	5.5 Measurement Techniques	34
	5.5.1 Scanning Transmitter - Separate Stable Mount	34
	5.5.1.1 Scanning Transmitter - ATLAS Mount	39

<u>Section</u>	<u>Title</u>	<u>Page</u>
	5.5.2 Dual Scanned Beams - ATLAS Mount	39
	5.5.2.1 Dual Modulated Beams - ATLAS Mount	41
	5.5.3 Complete Intensity Distribution at the Balloon Techniques	42
	5.5.3.1 Image Dissector Approach	42
	5.5.3.2 Diode Array Approach	46
	5.5.4 Reciprocity Tracker Technique	47
	5.5.5 Summary of Experimental Techniques	48
5.6	Basic Balloon Gondola Modifications	48
	5.6.1 Repair, Refurbishment and Minor Modifications	50
	5.6.2 Range Extension	50
	5.6.3 Modifications Suitable for Accurately-Pointed-Laser Aboard	51
5.7	Turbulence Measurements	52
	5.7.1 Introduction	52
	5.7.2 Tropopause Turbulence (~15 km altitude)	53
	5.7.3 Near Ground Turbulence ($h \leq 2$ km)	53
VI	DESIGN OF THE DIODE ARRAY TECHNIQUE	55
6.1	Introduction	55
	6.1.1 Diode Array Experiment Configuration	55
6.2	Laser Transmitter System	57
	6.2.1 Design Considerations	57
	6.2.2 Transmitter Optical System	58
	6.2.3 Mechanical Considerations	58
	6.2.4 Uplink Irradiance	62
6.3	Balloon Receiver System	63
	6.3.1 Mechanical Design of the Diode Array Receiver System	63
	6.3.2 Diode Array Electronics	67
	6.3.2.1 Power Requirements	72
6.4	Weight Budget	73
6.5	Data Analysis and Interpretation	73
	6.5.1 Design Information	74
	6.5.1.1 Diode Size	74
	6.5.1.2 Diode Spacing	74

<u>Section</u>	<u>Title</u>	<u>Page</u>
	6.5.1.3 Array Size/Diode Number	74
	6.5.2 Data Analysis	77
	6.6 Estimated Costs	81
VII	DESCRIPTION OF THE RECIPROCITY TRACKER TECHNIQUE	83
	7.1 Introduction	83
	7.1.1 Reciprocity Tracker Experimental Configuration	83
	7.2 Reciprocity Tracker Transmitter	83
	7.2.1 Accuracy Considerations	85
	7.3 Balloon-borne Receiver	86
	7.4 Star Tracker Analysis	88
	7.5 Data Interpretation and Analysis	91
	7.5.1 Raw Data Manipulation and Analysis	91
	7.5.2 Data Interpretation	92
VIII	EXPERIMENTAL PLAN, PROGRAM SCHEDULE AND ESTIMATED COSTS	95
	8.1 Introduction	95
	8.2 Experimental Plan	95
	8.2.1 Optical Measurements Procedure	96
	8.2.2 Turbulence Measurements Procedure	97
	8.2.3 "Log-Book" Procedure	97
	8.3 Program Schedule	98
	8.3.1 Experiment Planning and Design	98
	8.3.2 Reciprocity Tracker Implementation Design Program	98
	8.3.3 Reciprocity Tracker Equipment Modification Program	101
	8.3.4 System Integration and Tests	101
	8.3.5 Field Experiments	101
	8.3.6 Data Analysis	103
	8.4 Estimated Costs	103
IX	EFFECTS ON A HIGH DATA RATE LASER COMMUNICATION LINK	105
	9.1 Introduction	105
	9.2 High Data Rate Uplink	105
	9.3 Beacon Uplink	107
X	CONCLUSIONS AND RECOMMENDATIONS	109
	10.1 Introduction	109

<u>Section</u>	<u>Title</u>	<u>Page</u>
	10.2 Conclusions	109
	10.3 Recommendations	110
Appendix I	Vacuum Gaussian Beam Propagation	113
Appendix II	Scintillation and Transmitter Aperture Averaging	123
Appendix III	Beam Wander	147
Appendix IV	Probability of Bit Error and Outages for Beam Wander and Scintillation	153
Appendix V	Combined Beam Wander and Scintillation Effects	163
Appendix VI	MTF Parameter ρ_c	177
Appendix VII	Angle of Arrival Fluctuations	187
Appendix VIII	Correlation Length	191
Appendix IX	Transmitter Truncation/Blockage of the Beam	197
Appendix X	Experimental Problems in the Measurements of the Turbulence Effects	207
Appendix XI	Stability of the Atlas Mount	213
Appendix XII	Scanning Transmitter Design	217
Appendix XIII	Balloon Gondola Modifications	225
Appendix XIV	Boresight Monitor and Focussing Equipment	275
Appendix XV	Turbulence Measurements	277
Appendix XVI	Adaptive Threshold Effects	281
REFERENCES		287

ILLUSTRATIONS

Figure	Title	Page
1	Optical Propagation Tests: Program Plan.	8
2	BAPE Receiver System.	15
3	BAPE Experimental Configuration.	16
4	Scintillation Effects on Probability of Error for PGBM.	21
5	Beam Wander Effects on Probability of Error for PGBM.	25
6	Balloon Borne Receiver System.	32
7	Scanning Laser Transmitter Diagram.	36
8	Line Scan Geometry and Data.	37
9	Dual Beam Approach.	40
10	Image Dissector Configuration.	43
11	Image Dissector Signal Waveform.	45
12	Diode Array Experiment Configuration.	56
13	Block Diagram of Transmitter Optical System.	59
14	Physical Layout of the Laser Transmitter.	60
15	Mechanical Layout of the Diode Array.	64
16	Diode Receiver Assembly.	66
17	Photodiode Preamp Block Diagram.	69
18	120 Diode Array Signal Processing.	71
19	Gaussian Irradiance Profile.	75
20	Beam Size at Balloon Receivers.	76
21	Probability of Beam Remaining on the Diode Array: Angular Jitter = 15 μ rad.	78
22	Probability of Beam Remaining on the Diode Array: Angular Jitter = 25 μ rad.	79
23	Data Analysis Flow: Large Diode Array.	80
24	Refractive Reciprocity Ground Transmitter/Receiver	84
25	Diagram of the Receiver Portion of the Reciprocity Tracker.	89
26	OPTS Program Plan.	99

<u>Figure</u>	<u>Title</u>	<u>Page</u>
27	Reciprocity Tracker Implementation Design Program.	102
28	OPTS Program Plan.	111
29	Beam Divergence Versus Beam Waist Radius.	116
30	Beam Size Versus Range; Collimated Beams.	118
31	Radius of Curvature Versus Range; Collimated Beams.	119
32	Beam Size Versus Range for Defocussed, Collimated and Focused Beams.	120
33	Maximum Focusing Range versus Initial Beam Size.	121
34	Ripple versus C_ℓ .	124
35	C_ℓ/C_ℓ^S versus R for Defocussed Conditions: 1	131
36	C_ℓ/C_ℓ^S versus R for Defocussed Conditions: 2	132
37	C_ℓ/C_ℓ^S versus R for Defocussed Conditions: 3	134
38	C_ℓ/C_ℓ^S versus R for Focussed and Satellite Receiver Conditions.	135
39	C_ℓ/C_ℓ^S versus R for Various Initial Beam Size and Focusing.	137
40	C_ℓ/C_ℓ^S versus R for Various Tropopause Altitudes and Focusing.	138
41	C_ℓ/C_ℓ^S versus R for $w = 4.03$ cm and Zenith Angle Effects.	139
42	C_ℓ/C_ℓ^S versus R for $w = 6$ cm and Zenith Angle Effects.	140
43	PGBM Communication Mode.	154
44	Scintillation Effects on P_E for PGBM.	157
45	Beam Wander Effects on P_E for PGBM.	159
46	Beam Wander Parameter Versus Focusing Parameter.	171
47	MTF_{TOTAL} for 7" Aperture	182
48	MTF_{TOTAL} for 10" Aperture.	183
49	Normalized Transmitted Power for a Truncated Aperture.	199

<u>Figure</u>	<u>Title</u>	<u>Page</u>
50	Truncation Effects for $w_0 = 1.5$ cm.	201
51	Truncation Effects for $w_0 = 2.5$ cm.	202
52	Truncation Effects for $w_0 = 3.5$ cm.	203
54	Simultaneous Wander and Scintillation Power Fluctuations.	210
55	Accelerometer Measurements of ATLAS Azimuth Jitter.	214
56	Accelerometer Measurements of ATLAS Elevation Jitter.	215
57	Scanning Transmitter Diagram.	218
58	Scanning Transmitter Detailed Design I.	219
59	Scanning Transmitter Detailed Design, II.	220
60	Scanning Geometry and Data Reduction Procedure.	222
61	Balloon Elevation Axis Semi-Monoque Structure.	226
62	Self-Aligning Elevation Axis Mount.	227
63	Mirror Support Structure.	229
64	Balloon-Borne Laser Subsystem.	231
65	BAPE Servo.	238
66	Bode Plots of Position Loops.	239
67	Bode Plots for New Configuration.	244
68	Block Diagram of New Servo Configuration.	245
69	Tachometer Ripple Sensitivity Determination.	248
70	OPTS Servo's Open Loop Characteristics.	252
71	Tachometer Ripple Sensitivity Determination: Elevation.	254
72	Tachometer Ripple Sensitivity Determination: Azimuth.	256
73	Balloon Package: Argon Receiver.	258
74	Low Noise Op-Amp.	261
75	Photo-Detector Equivalent Circuit	262
76	Logarithmic Angle Sensors I.	265
77	Logarithmic Angle Sensors II.	266
78	AGC Error Functions.	267
79	Block Diagram for AGC Approach.	268

<u>Figure</u>	<u>Title</u>	<u>Page</u>
80	FET Voltage Controlled Resistor Normalized Conductance Versus Normalized Control Voltage.	271
81	AGC Loop Dynamics Block Diagram.	272
82	Open and Closed Loop Response.	273
83	Binary Optical Communication System Performance with Tracking Induced Signal Fading.	282
84	Binary Optical Communication System Performance with Atmospheric Induced Signal Fading.	283
85	Graph of Probability of Error versus Mean Number of Signal Photoelectrons/Bit with $C_g(0)$ as a Parameter for $N_E = 30$ and $n_b G = 0$.	285

TABLES

<u>Table</u>	<u>Title</u>	<u>Page</u>
I	Summary of Turbulence Effects.	5
II	OPTS Experimental Techniques.	7
III	Summary of Turbulence Effects.	26
IV	OPTS Experimental Techniques	49
V	MTF Parameters for Real Turbulence Profiles.	180
VI	Transmitter Optics Tradeoffs.	206

LIST OF ABBREVIATIONS AND SYMBOLS

α	= wander parameter = $\overline{p_c^2}/w^2$, for $\overline{p_c^2}$ = mean square displacement of beam center.
C_ℓ	= variance of the fluctuations of the log amplitude caused by scintillation alone.
$C_N^2(h)$	= index of refraction structure parameter at altitude h.
$C_T^2(h)$	= temperature structure parameter at altitude h.
D_T	= temperature structure function $\equiv \overline{[T(x_1) - T(x_2)]^2}$.
erf	= error function.
k	= wave # = $2\pi/\text{wavelength}$.
ℓ	= log amplitude $\equiv \frac{1}{2} \ln (I/\bar{I})$ for I = instantaneous irradiance and \bar{I} = average irradiance.
P_E	= average probability of bit error.
PGBM	= Pulse Gated Binary Modulation communication mode.
R	= curvature of the wavefront of the gaussian TEM ₀₀ mode amplitude.
ρ_0	= e^{-1} point of the atmospheric MTF.
$\overline{\sigma_p^2}$	= normalized variance of detected power.
θ_{rms}	= root mean square angular beam deflection.
w	= e^{-2} irradiance radius of a gaussian TEM ₀₀ mode beam.
w_0	= e^{-2} irradiance radius of a gaussian TEM ₀₀ mode beam at its waist.

Section I

INTRODUCTION

During the Optical Propagation Tests Study (OPTS), GTE Sylvania has theoretically characterized the atmospheric turbulence effects on optical communication links performance and has developed a preliminary design for experimentally verifying these effects. In particular, the effects of the atmosphere on optical uplinks (ground to synchronous satellite) have been considered.

Atmospheric turbulence will reduce the average power detected at the satellite, and cause it to randomly fluctuate about this average. In the course of this study, the degree and spectra of these link degradations have been quantified in terms of measurable parameters, and techniques to reduce their effects to a minimum have been developed. In addition, an experimental plan to test these techniques has been formulated, after considering a large number of options. Finally, a preliminary design of the equipment modifications needed to perform these experiments has been completed.

The key resulting recommendation is that experiments should be performed in MAY/JUNE 1974. The ground station will include a variable focus/variable aperture/wavefront-tilt-tracking transceiver; the receiver will be mounted on a free-float balloon platform at an altitude of 100,000 feet.

This experiment will directly test the key techniques, and will resolve all the uncertainty regarding the atmospheric turbulence constraints on the performance of a high data rate uplink.

This report is organized as follows: Section II summarizes the work performed under the current contract. Section III discusses the background of the work performed here. Section IV summarizes the Atmospheric Turbulence Analysis (whose details are confined to the Appendices) and

points out the measurements needed to be performed and the techniques that must be tested.

Section V discusses the various experimental options considered in the present program while Sections VI and VII present the recommended experimental techniques, with as much detail as is presently available. Section VIII treats the experimental plan, schedule and costs.

Section IX discusses the impact of our present analytic results on a high data rate laser communication link, and Section X presents our conclusions and recommendations.

Section II

SUMMARY

2.1 Introduction

The high data rate uplink of a laser communication system (ground to Synchronous Satellite) will experience power fluctuations and fades due to the turbulent atmospheric path. The atmospheric turbulence effects are a problem to be overcome if possible (i.e., made absolutely negligible), or to be minimized and accepted.

In other words, for the success of a high data rate uplink, we must determine the following:

- 1) Whether turbulence precludes operating the uplink at 1 Gbp/sec with a $P_E = 10^{-6}$, i.e., whether there are no conditions or designs that will allow testing of the complete satellite system without interfering effects due to turbulence on the uplink.
- 2) What techniques reduce the turbulence effects to a minima.
- 3) The design constraints for a high data rate uplink.

The Optical Propagation Tests Study (OPTS) has quantified these problems in terms of measurable parameters, developed some optimum techniques, outlined an experimental plan, and has begun the design of the equipment needed to do the experiments which test the techniques.

2.2 Turbulence Effects

The range equation for a direct detection uplink in the absence of turbulence is given by

$$P_D = \frac{P_o}{\Omega_o} \frac{A_R}{Z^2} e^{-\beta Z} \quad (2-1)$$

for

- P_o = transmitter power
- Ω_o = transmitter solid angle
- A_R = receiver area
- Z = range to receiver
- γ = optics efficiency
- β = atmospheric extinction coefficient (due to absorption and scattering)
- Z' = range through the atmosphere
- P_D = detected power

P_D is then proportional to the number of signal photoelectrons generated, which then influences the probability of bit error.

Turbulence modifies P_D in two ways:

- 1) P_D is reduced by beam spread (which increases the effective Ω_o), and by beam wander, or motion (which reduces the effective P_o).
- 2) P_D fluctuates due to scintillation, or beam breakup into hot-spots and deep fades, and wander, due to wandering off the peak of the gaussian irradiance distribution ($P_D = P_o e^{-2r^2/w^2}$).

We have analyzed these effects in detail, and our results are summarized in Table I.

Based on this analysis, we have determined that turbulence does not preclude operating an uplink, and that there are optimum techniques available to overcome the bulk of the scintillation and wander effects.

TABLE I

SUMMARY OF TURBULENCE EFFECTS

<u>Turbulence Effect</u>	<u>Characteristic Parameter</u>	<u>Requirement</u>	<u>Technique Proposed to Achieve Same Requirement</u>
Scintillation	$C_\ell = \frac{1}{4} \ln(\sigma_I^2 + 1)$ σ_I^2 = variance of power fluct. Outage Time	$C_\ell \leq 0.01$	Focussing a "large" beam at or above the tropopause.
Wander	$\alpha = \overline{P_C^2} / w^2$ $\overline{P_C^2}$ = mean square beam displacement $w = e^{-2}$ irradiance radius Outage Time	$\alpha \leq .1$	Reciprocity Tracking
Spread	w	Depends on other System Parameters	None

2.3 Experimental Techniques

Scintillation, beam wander, and beam spread have been measured for many years over mostly horizontal paths. However, we must measure all three and/or their effects over a "vertical" path in order to test the proposed techniques. Use of a balloon borne platform (altitude ~100,000 feet) is clearly the optimum selection for the upper end of the link (since it floats well above the tropopause and simulates a satellite receiver, at a small fraction of the cost of an actual satellite link), but that still leaves us the problem of selecting a suitable experimental technique.

A great number of possibilities were considered during the course of OPTS, with the most viable techniques summarized in Table II.

With the understanding that some results were highly desirable by June 30, 1973, we recommended the following:

- 1) Perform all experiments at night, to reduce costs and spurious sun-loading effects.
- 2) Perform the diode array experiment May/June 1973.
- 3) Perform the reciprocity tracker experiment May/June 1974.

At that time (July 17, 1972), the Air Force directed us to plan for a single experiment, the reciprocity tracker, in 1974.

We therefore recommend that the Program Plan outlined in Figure 1 be implemented.

The Reciprocity Tracker Implementation Design Program will enable us to take full advantage of the techniques (and equipment) developed under the 405B Acquisition/Tracking Brassboard Program so that the eventual OPTS experiment can be performed in a cost-effective manner.

The Reciprocity Tracker Equipment Modification Program will ensure that the experimental equipment is modified and tested in time for the May/June 1974 flight dates.

TABLE II. OPTS Experimental Techniques.

Experimental Technique	Ground System Mount	Ground System Pointing & Tracking	Balloon System Data Receivers	Key Technical Problems	Results			Conclusions/Recommendations
					Scintillation	Wander	Spread	
Scanning Single Line (fan)	Separate mount	Stable/fixed during scan	Single (or a few) photodetector(s)	Mount stability; balloon motion	None	Some	Suff.	Done only in conjunction with some scintillation experiment
Dual Beams: Both Scanned or Differently Modulated	NASA mount	$\sim 25 \mu\text{rad}$ rms random pointing fluctuations	Single (or a few) photodetector(s)	Ground Opt. System alignment; balloon motion	None	Some	Suff.	Done only in conjunction with some scintillation experiment
Large Receiver Array on Balloon	NASA mount	$\sim 25 \mu\text{rad}$ rms random pointing fluctuations	Large array of photodiodes	Array implementation; data recording data analysis	Suff.	None	Suff.	A good technique, and the best one doable by next summer
Reciprocity Tracker	To be determined	Fine track on \angle of arrival to within $\lesssim 1 \mu\text{rad}$	A few detectors	Fielding a 1- μrad tracker	Suff.	Suff.	Suff.	<u>Best</u> Simulates actual communication operation and provides data that does not depend on theory for interpretation

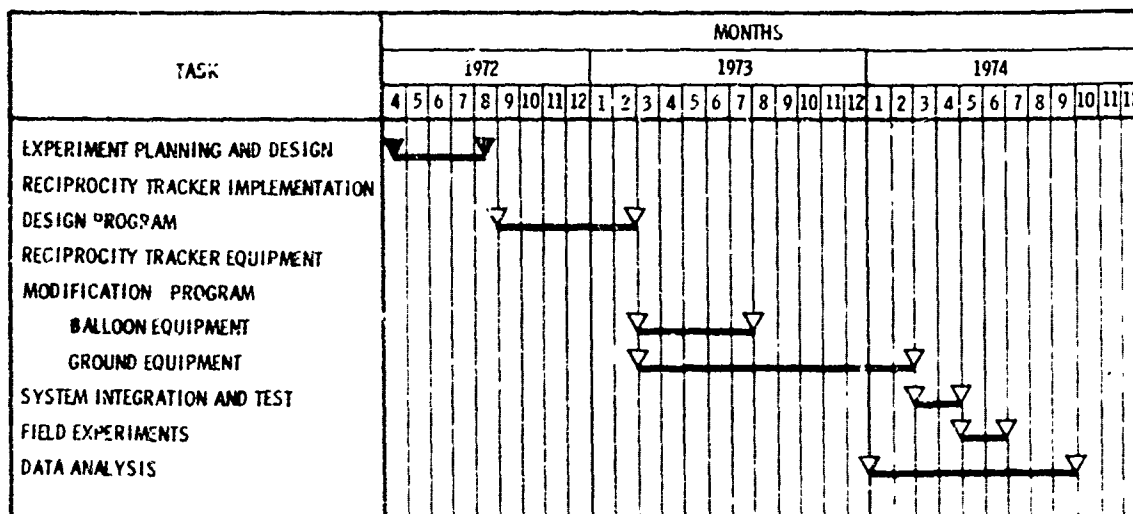


Figure 1. Optical Propagation Tests: Program Plan.

The System Integration and Tests, Field Experiments and Data Analysis will result in definitive tests of the experimental techniques suggested here (focusing to reduce scintillation, reciprocity tracking to reduce beam motion effects). The feasibility and requirements for a high data rate uplink will then be fully determined, and the design constraints for this link will be defined.

Section III

BACKGROUND

3.1 Introduction

The Optical Propagation Tests Study (OPTS) was performed by GTE Sylvania for the Air Force 405B Program Office in the context of three salient facts:

- 1) The recommendations of the Final Report of the SDR Preliminary Subsystem Design⁽¹⁾.
- 2) The state-of-the-art in turbulence effects analysis and experiments.
- 3) The availability of NASA gear, much of which has been developed by GTE Sylvania.

We shall discuss each of these points in some detail :

3.2 SDR Preliminary Subsystem Design

This program primarily dealt with design and analysis of the satellite hardware systems needed for a 1 Gbit/sec data relay link. As a side issue, it became apparent that the full recommended demonstration of the satellite system (using a ground to satellite to ground relay) involves a difficult atmospheric link, that from the ground to the satellite. The high data rate downlink was shown not to be a problem, based on existing theory and experiments⁽²⁾.

A consideration of the problems involved was included in Appendix B, Atmospheric Prediction Analysis⁽²⁾ and Appendix K, Atmospheric Experiment Analyses⁽³⁾. Appendix K recommended that the following experimental measurements be performed:

Optical Propagation

"Transmitter Aperture Averaging - Vertical measurements should be performed to determine the extent of this effect, for transmitter sizes in the regime of 1 foot or less diameter (between e^{-2} points) and beam divergence in the range of 30

micro-radians on down. The measured parameter ought to be the variance of the detailed signal level fluctuations, and their statistics. The interaction of scintillation with fading due to beam wander must be carefully treated.

Beam Size - Both the instantaneous and total beam size should be measured over a vertical path, for small transmitter sizes and beam divergences as cited above.

Reciprocity of Beam Wander and Angle of Arrival Fluctuations -

If transmitter aperture averaging works, this is potentially the most important contributor to system design modifications. This should be measured over a vertical path. Since this is the only one of the three which in principle demands a downlink beam, of course the downlink MTF should also be measured as a direct check on the theory in Appendix B. Beam sizes and divergences should be as cited above."

(Based on the work performed during OPTS, these planned experiments have been refined, as discussed in Section 5.1.)

Atmospheric Turbulence

"The experiment plan is to go to Cloudcroft and perform the following work:

- A. Fly a tethered balloon at ≈ 600 feet with 5 D_T sensors spaced along the tether, and oriented so that they face into the wind. The data would be hard-wired to the ground, and simultaneously recorded, along with the wind profile, temperature profile, cloud conditions, and the state of the atmosphere, i.e., stable, unstable, or neutral. The balloon would be flown continuously until meteorological conditions (high winds, for example) force its descent, so that data can be taken continuously over many days. As an initial

goal, 1 month of data-taking would be attempted. The balloon would be flown as close to the proposed optical transmitter site as possible so that the surface roughness, etc., can be duplicated.

- B. Fly four free-floating special thermosondes with D_T sensors aboard, on standard rawinsonde balloons at Cloudcroft. This involves moving the portable rawinsonde receiver to the launch site. At least one sensor should be flown in each meteorological condition (stable, unstable, and neutral) to ensure that the turbulence beyond the top of the tethered balloon is behaving as expected."

(These planned experiments may also be further refined, based on the results of OPTS. cf, for example, Section 5.7.)

3.3 Turbulent Analyses and Experiments

There have been few non-horizontal and near earth optical propagation experiments⁽²⁾ for a number of reasons:

- A) Theory is most easily developed for a uniform strength of turbulence, as exists over horizontal paths.
- B) Experiments are most easily performed when all parts of the gear are controllable.
- C) The vertical distribution of turbulence is not well known or easy to measure above altitudes greater than a few kilometers.

Therefore, a good deal of the theory for real turbulent paths and optical systems remained to be developed during OPTS, and detailed experiments over a vertical path also had to be designed to yield the necessary answers.

3.4 Equipment Availability

GTE Sylvania and NASA Goddard were involved in one of the few previous vertical laser propagation experiments [Balloon Atmospheric Propagation Experiment (BAPE)]⁽⁴⁾. Although BAPE only did point source up-link measurements, the gear is potentially useful to OPTS.

3.4.1 Existing Balloon-borne Equipment

The balloon-borne receiver system, developed by GTE Sylvania, is shown in Figure 2. The receiver system is basically a recoverable structure that houses a steerable optical receiver system, telemetry and servo electronics, and battery power supplies. The experiment configuration, including the ground station and the balloon-borne receiver system, is shown in Figure 3. The ground station illuminates the optical receiver system and automatically tracks the payload using the retroreflected argon signal. A tracker in the optical receiver package senses the upcoming argon signal and automatically points the detectors towards the ground station. This two-way autotracking system permits continuous data recording and eliminates the effects of balloon motion. The BAPE Receiver System currently has the following characteristics:

Maximum Slant Range:	40 km
Minimum Transmitter Elevation Angle:	25°
Spectral Response of Detectors:	5145Å and 10.6μ (two detectors at each wavelength)
Detector Configuration:	Two movable and two fixed at each wavelength.

3.4.2 Ground Station

The existing ground station (called the ATLAS system) has been used as the ground station for the BAPE experiments of 1970 and 1971. This system consists of a 30-inch (76 centimeters) diameter telescope mounted on an altitude-azimuth tracking mount. It is equipped with a six-mirror Coudé focus, which places the focal plane in a convenient stationary position in a van located adjacent to the telescope. Inside the van, laser receiver equipment is set up in a convenient stable laboratory environment.

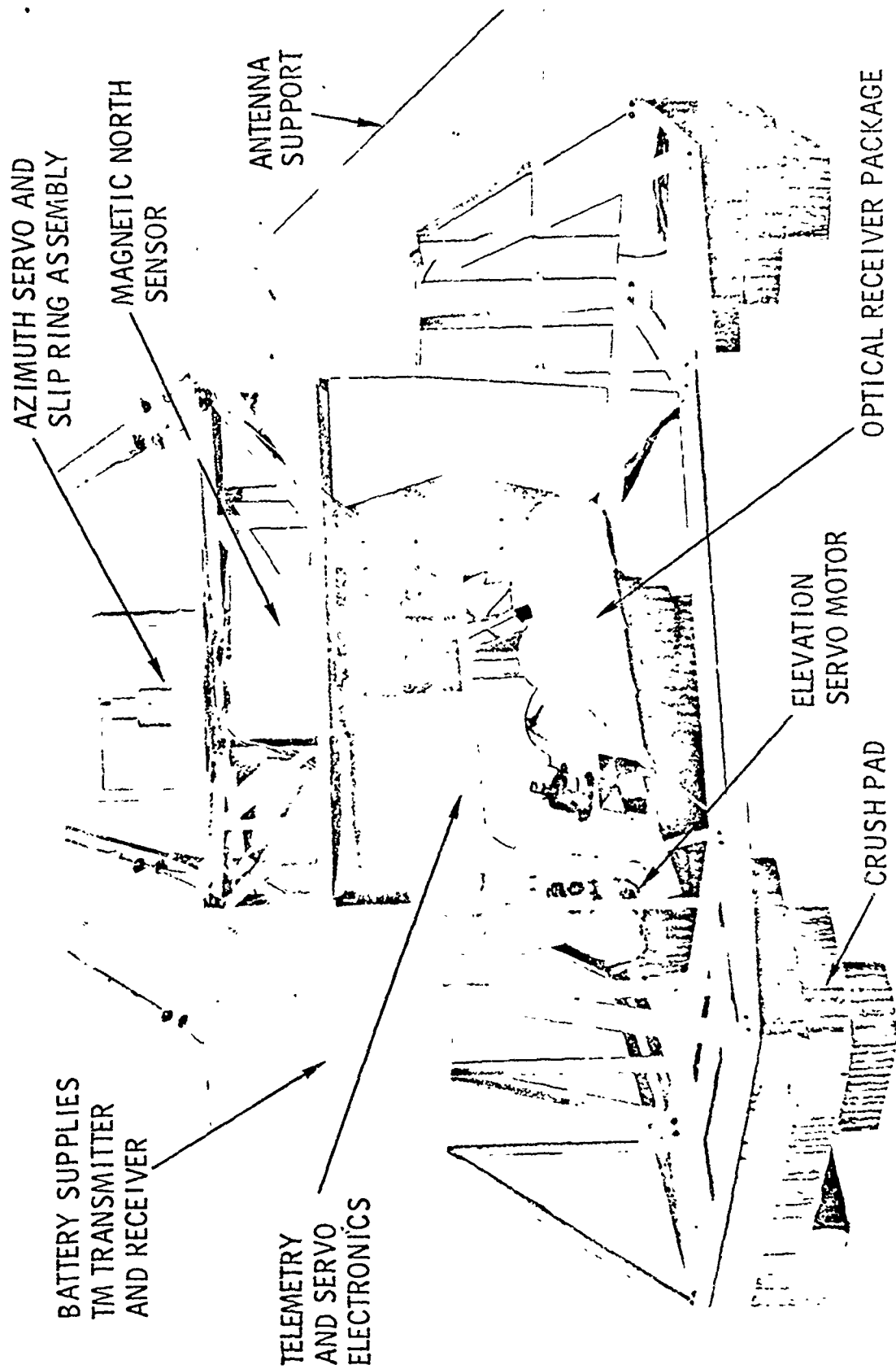


Figure 2. BAPE Receiver System.

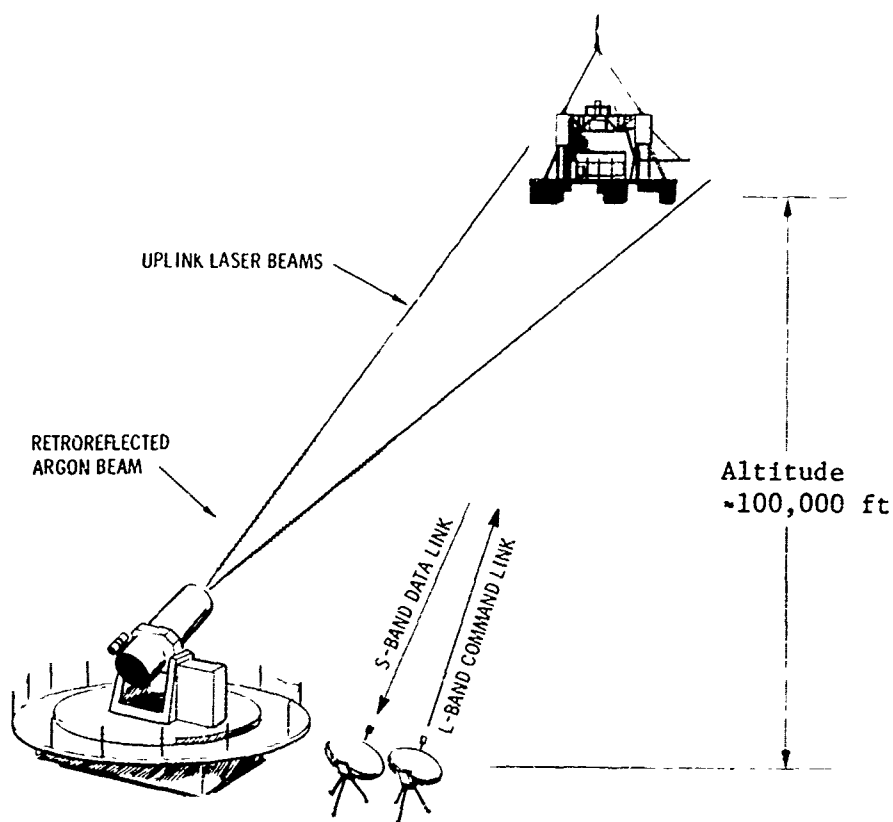


Figure 3. BAPE Experimental Configuration.

At present, both "point source" argon and CO₂ lasers can be simultaneously pointed at the balloon package. The pointing and tracking are accomplished by a star-tracker looking at a retroreflected argon signal. Accuracies as good as 5 μ rad have been observed, with the more usual results being near 25 μ rad rms. In the present system, this includes both tracking and atmospherically induced pointing errors.

Associated equipment includes an L-band command link to control the balloon package's functions, and an S-band receiver to obtain real-time results from the balloon package. Real-time data recording and analysis equipment is also included in the van, so that real-time variances of the intensity fluctuations being measured at the balloon package can be obtained.

3.4.3 Turbulence Sensors

GTE Sylvania developed turbulence sensors for NASA Goddard, suitable for measuring turbulence at altitudes up through the tropopause⁽⁵⁾. These "thermosondes" measure the rms temperature difference between thin wire probes spaced a meter apart, as a function of altitude, and transmit this information to the ground on a real time telemetry link.

3.5 Summary

In summary then, a high data rate laser uplink requires information on turbulence effects. OPTS has sought to extend the turbulence analysis and design experiments with modified existing equipment to obtain this information.

Section IV

TURBULENCE THEORY ANALYSES SUMMARY

4.1 Introduction

Degradation of the uplink beams could result in power fluctuations and fades of sufficient magnitude to prevent successful uplink communication for a high data rate laser system. OPTS seeks to quantify the effects due to atmospheric turbulence and develop techniques to overcome them, if possible.

This section summarizes the analytical work performed towards this end.

4.2 Turbulence Effects

There are three conceptually distinct effects of interest for the uplink :

4.2.1 Scintillation; or beam breakup, is defined here as all amplitude fluctuations that do not result from beam motion. For example, a small detector placed in a very large beam will measure significant fluctuations in received power, although the average detected power remains the same.

As discussed in detail in the Appendices (particularly Appendices II, IV, and V), the received power has a normalized variance

$$\overline{\sigma_p^2} = \exp(4 C_\ell) - 1 \quad (4-1)$$

$$\text{and a ripple} = (\overline{\sigma_p^2})^{1/2} \times 100\% . \quad (4-2)$$

$C_\ell \equiv$ variance of the log amplitude fluctuations, i.e., defining

$$\ell \equiv \frac{1}{2} \ln \left(\frac{I}{\bar{I}} \right) \quad (4-3)$$

for I = instantaneous irradiance

\bar{I} = average irradiance.

$$\text{then } C_\ell = \frac{1}{(\ell - \bar{\ell})^2} \quad (4-4)$$

Moreover, the detected power is described by a log-normal distribution:

$$P(S) = \frac{1}{[2\pi C_\ell]^{1/2}} \frac{1}{2S} \exp \left[-\frac{1}{2C_\ell} \left(\frac{1}{2} \ln(S/S_0) + C_\ell \right)^2 \right] \quad (4-5)$$

while the cumulative probability is given by

$$\text{Prob } (S \leq S_x) = \frac{1}{2} \left\{ 1 + \text{erf} \left(\frac{\frac{1}{2} \ln(S_x/S_0) + C_\ell}{\sqrt{2C_\ell}} \right) \right\} \quad (4-6)$$

for S = instantaneous # of photoelectrons generated (αI)

S_0 = average # of photoelectrons generated ($\alpha \bar{I}$)

For a PGBM system, the average Probability of Bit Error as a function of C_ℓ was calculated in Appendix IV, and is shown here as Figure 4. (A similar curve could be drawn on the basis of outages, as discussed in Appendix V.) The assumptions used in generating this graph are # noise photoelectrons = 1, modulator extinction ratio = 31.6, and a fixed threshold for a long term average S_0 .

Since typically $C_\ell \approx .1$ for uplink point sources⁽⁴⁾, the question in scintillation theory is whether C_ℓ can be reduced to $\leq .01$. (This criterion may be somewhat relaxed for adaptive threshold systems, as discussed in Appendix XVI.)

Appendix II and past theory⁽²⁾ predict that large collimated beams will reduce C_ℓ sufficiently if all the turbulence is concentrated near the ground. However, significant turbulence at the tropopause means that even 30 cm (untruncated) transmitter apertures will not suffice to achieve $C_\ell < .01$.

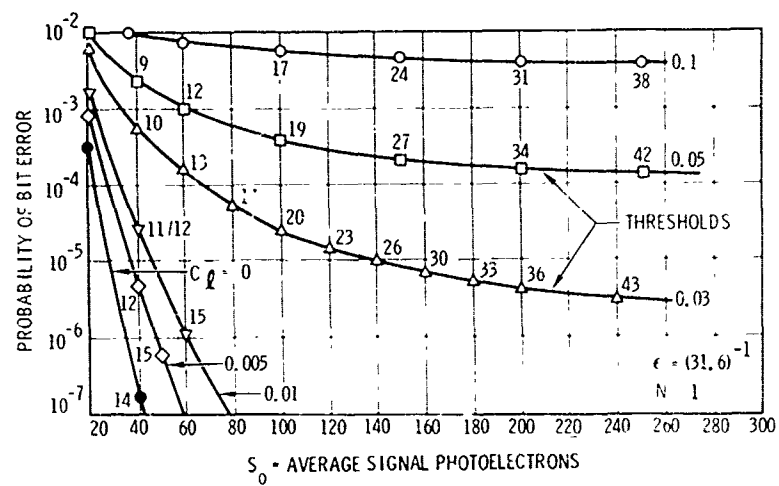


Figure 4. Scintillation Effects on Probability of Error for PGBM.

The work in Appendix II predicts that focussing the beam at or slightly above the tropopause will reduce C_d to $\leq .005$ for that same aperture size. This prediction is key to the success of a high data rate uplink and must be tested by OPTS to fulfill its goal.

4.2.2 Spread: is defined as the enlargement of a beam beyond that size predicted by vacuum propagation theory (as discussed in Appendix I). It results in a decrease of the average power measured by a point receiver which remains at the center of a beam.

We do not discuss this in detail either here or in the Appendices, because we do not know of a viable theory that separates the instantaneous beam size from its average. Since this average includes beam wander effects, and since beam wander effects may be removable by sophisticated tracking procedures while beam spread is not, it is clear that we cannot uniquely specify theoretically the instantaneous size of the beam.

However, we could use the theory of Appendix IV to estimate total average beam size, Δp^2 , and the motion of beam center, p_c^2 . The difference will be the beam spread:

$$\text{SPREAD} = \overline{\Delta p^2} - \overline{p_c^2} \quad (4-7)$$

With the five (5) assumptions made in Appendix V, we find that the SPREAD = 0. (This is related to taking the wave structure function $D(\rho) \propto \rho^2$ instead of $\rho^{5/3}$.) We propose to remove all five assumptions in future work, and then we will have a prediction of SPREAD, consistent with all our analysis.

OPTS must measure SPREAD in order to specify the needed transmitter power on the high data rate uplink.

4.2.3 Wander: or beam motion, is defined here as overall motion of the entire beam. It results in power fluctuations and a reduction in the average power measured by a fixed detector.

As described in detail in the Appendices (particularly Appendices III, IV, and V), the received power has an average,

$$\bar{P} = \frac{P_o}{1+2\alpha} \quad (4-8)$$

a normalized variance, $\frac{\overline{\sigma_p^2}}{\bar{P}^2} = \frac{4\alpha^2}{4\alpha+1}$ (4-9)

and a Ripple = $(\sigma_p^2)^{1/2} \times 100\%$. (4-10)

where $\alpha = \frac{\overline{p_c^2}}{w^2} = 4 \left(\frac{\theta_{rms}}{\theta} \right)^2$ (4-11)

for $\overline{p_c^2}$ = mean square position of beam center

$w = e^{-2}$ irradiance radius at receiver

θ_{rms} = root mean square angular beam displacement

θ = full angular beam size

It is shown in Appendix V that with the five (5) assumptions listed there (which result in totally neglecting beam spread),

$$\alpha = \frac{b^2}{\rho_o^2} \quad (4-12)$$

for $b = e^{-2}$ irradiance radius at the transmitter

$\rho_o = e^{-1}$ point of MTF measured at the transmitter, for a point source at the receiver.

The probability density of detected power is described by a modified beta-distribution

$$P(S) = \frac{1}{2\alpha S_0} \left(\frac{S}{S_0} \right)^{\frac{1}{2\alpha} - 1} \quad (4-13)$$

while the cumulative probability is given by

$$\text{Prob } (S \leq S_x) = \left(\frac{S_x}{S_0} \right)^{\frac{1}{2\alpha}} \quad (4-14)$$

for S = instantaneous number of photoelectrons generated (αP)

S_0 = number of photoelectrons generated at the peak (αP_0).

For a PGBM system (with certain simplifying assumptions), the average Probability of Bit Error was calculated by Paddon⁽²⁾, and is shown in Figure 5. (A similar curve could be drawn on the basis of outages, as discussed in Appendix IV.) The assumptions used in generating this graph are zero background, infinite modulator extinction ratio, and a fixed threshold for a peak level = S_0 . (Appendix XVI shows recent results from Tycz et al⁽⁵⁴⁾ that removes all these assumptions, but comes up with a very similar graph.)

Since typical beam wander (θ_{rms}) is of order 5 μ rad (Appendices V and VII), a 10 μ rad (unspread) beam results in $\alpha = 1$. Therefore, the question in wander theory is whether α can be reduced to < 0.1 , e.g., for a 10 μ rad beam, whether θ_{rms} can be reduced to $< 1.5 \mu$ rad.

Appendices V, VI, and VII and past theory⁽⁶⁾ predict that wander can be substantially reduced by tracking on the normal of a wavefront originating from a source situated at the receiver. This prediction is key to the success of a high data rate uplink, and must be tested for OPTS to fulfill its goal.

A summary of the analytical results is shown in Table III.

4.3 Beacon Effects

All of the above discussion has been directly related to the high data rate uplink, which has the following parameters⁽¹⁾:

$$\lambda = 0.5320 \mu\text{m}$$

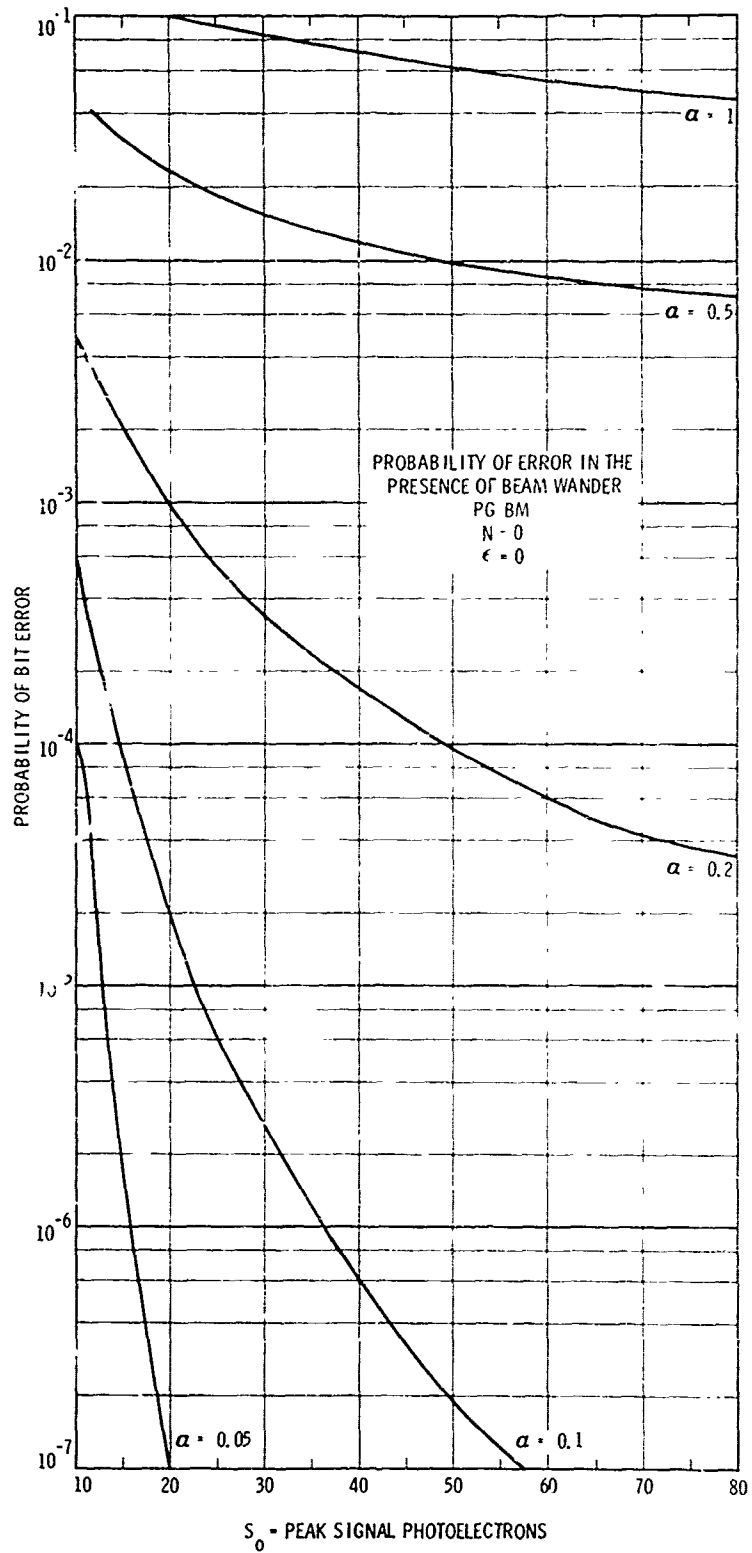


Figure 5. Beam Wander Effects on Probability of Error for PG-BM.

TABLE III

SUMMARY OF TURBULENCE EFFECTS

<u>Turbulence Effect</u>	<u>Characteristic Parameter</u>	<u>Requirement</u>	<u>Technique Proposed to Achieve Same Requirement</u>
Scintillation	$C_\theta = \frac{1}{4} \ln(\sigma_I^2 + 1)$ σ_I^2 = variance of power fluct. Outage Time	$C_\theta \leq 0.01$	Focussing a "large" beam at or above the tropopause.
Wander	$\alpha = \overline{P_C^2} / w^2$ $\overline{P_C^2}$ = mean square beam displacement $w = e^{-2}$ irradiance radius Outage Time	$\alpha \leq .1$	Reciprocity Tracking
Spread	w	Depends on other System Parameters	None

Aperture Size = 30 cm (\approx twice e^{-2} diameter)
 Beam Divergence = 5.4 μ rad
 Zenith Angle = 45°
 Transmitter Power = 250 mwatts

For the beacon uplink, a far different set of parameters apply:

$\lambda = 1.06\mu$
 Beam Divergence = 100 μ rad to 300 μ rad, collimated.
 Aperture Size = 1.35 cm to 0.45 cm (\approx twice e^{-2} diameter)
 Zenith Angle = 45°
 Average Transmitter Power = 100 mwatts

Moreover, the modulation formats are quite different, PGBM for the data link as compared to PIM for the beacon. For scintillation, using the fact ⁽⁴²⁾ that $C_\ell \propto (\lambda)^{-7/6}$, we can estimate a typical value for the beacon of

$$C_\ell = 0.082$$

In order to estimate the added margin needed to keep $P_E \leq 10^{-6}$, we note the equivalence of Eq. 33, p 1-29 of reference (1), (the probability of detection for our PIM link) and equation 5 of Fried and Schmeltzer ⁽⁷⁾ (the probability of miss in a laser radar system). Extrapolating Figure 3 of reference (7), we estimate that an additional margin of 20 dB in signal power is needed for $C_\ell = 0.082$.

We can achieve the needed margin in the following way:

- | | |
|---|---------------|
| (1) Reduce beam divergence during communication | |
| to 40 μ rad | + 8 dB |
| (2) Increase laser power from 100 mwatts to 1.6 | |
| watts | <u>+12 dB</u> |
| | 20 dB |

In order to keep the wander effects minimal ($\alpha \leq .1$) this means that the tracking accuracy must be

$$\theta_{\text{rms}} = \theta(.1)^{1/2} = 6.3 \text{ } \mu\text{rad}.$$

The present baseline design⁽¹⁾ calls out an accuracy of 14 μrad , and so must be improved. It can be done on the ground station.

There is another possibility of relieving this problem, if the large source theory developed in Appendix II is verified, .e., enlarging the beam and focusing it so that the final far-field beam divergence remains unchanged (100 μrad) but C_θ is much reduced.

This change (enlarging and focusing the beam) in the beacon design need not be considered until the theory is verified. In any event, even more laser power could be used to overcome worse effects, since, for example, the GTE Sylvania Model 602 Nd:YAG laser delivers 4 watts of TEM_{00} mode power when Q-switched at 10 kHz.

Section V

EXPERIMENTAL TECHNIQUES

5.1 Introduction

Section IV pointed out that there are a number of key measurements that must be performed in order to specify the design for the high data rate uplink. These measurements are as follows:

- A. Measure the power fluctuations caused by beam breakup (scintillation) to determine if large transmitter beams and/or focusing large beams reduce the power fluctuations as predicted by theory.
- B. Measure the angular-spread of the uplink beam.
- C. Measure enough beam motion parameters (either power fluctuations, or motion of the center of energy itself) to determine if pointing the uplink beam along the normal to a received wavefront will reduce the beam motion effects as predicted by the theory.

This section explores some general design considerations that will enter into any field experiment that requires accuracies in the μ radian regime, and then discusses the basic experimental configuration to be considered. Next, the possible ground based mounting platforms are compared for suitability to OPTS experiments. A number of the possible experimental techniques are then presented, and it is pointed out that only the direct test of the reciprocity tracking technique with a variable beam size/variable focusing/variable aperture ground transmitter will meet all of the experimental requirements listed above.

Section 5.6 summarizes the modifications needed for the present balloon system if any of the techniques are to be implemented. Section 5.7 presents our conclusions regarding the best way to measure the turbulence profile simultaneously with the optical results, so that the OPTS experimental results can be transferrable to any arbitrarily selected optical ground site.

5.2 General Design Considerations

5.2.1 Ground Station

The design of a high data rate uplink transmitter and the control of its mechanical and thermal environment will involve very careful and precise engineering to insure that the system itself can reduce rather than add to the deleterious atmospheric effects. Both the high data rate uplink and the proposed OPTS experiments will require aligning and holding components to fractional arc second tolerances in field-type rather than laboratory-type environments.

In formulating feasible experimental approaches, a careful distinction has been made between long term (greater than several minutes) instabilities of the mechanical or optical components which can be compensated for during an experiment, and short term (0.02 to 5 kHz) instabilities which must be eliminated if they cause undesirable deflections or distortions of the transmitted beams. In analyzing each portion of the systems, factors such as cost and feasibility of stabilization, and complexity of field operation are considered. Telescope focus is an example of a long term instability for which a field adjustment mechanism would be provided. Local turbulence resulting from thermal gradients within the optical system itself is an example of a short term instability. Avoiding the latter effect during daytime operation in a desert type environment would be prohibitively costly and the problem is best avoided by operating the experiments at night when sun loading is not a problem.

5.2.2 Balloon System

With regard to the balloon-borne instrumentation, the key considerations are adequate protection for stresses encountered during passage through the tropopause, parachute opening shock, and landing. The supporting frameworks must not be too rigid or heavy, however, and must be designed for easy field repair of minor damages. The thermal and pressure environment experienced from ground level to 100,000 feet is, of course, considered throughout the design.

5.3 Basic Experiment Configuration

The OPTS experiment will involve the transmission of laser beams from a ground based transmitter system to the balloon-borne gondola, shown in Figure 6. In addition, a He-Ne laser beam will be directed towards the ground station from the gondola. As in the BAPE experiments, experiment control commands will be initiated via an L-band telemetry link and an S-band link will transfer real-time data to the ground. (For the BAPE configuration, cf. Figure 3, Section 3.4.) In the OPTS program, however, additional data may be stored on a balloon-borne tape recorder.

The experiment is conducted in the following manner: After ground checkout of all systems, the balloon is launched and ascends to float altitude. The transmitter is manually steered to illuminate the payload. Using elevation and azimuth pointing readouts which are telemetered from the payload, the payload optical tracker is oriented colinearly with the upcoming beam. Automatic tracking is then initiated on both the ground-based and balloon-borne systems. Having established the uplink, data is acquired as the OPTS ground transmitter parameters are varied. After completion of the experiments, the gondola is recovered, after descent by parachute, and checked out for the next flight.

5.4 Transmitter Mounting Platforms

There are two logical possibilities for the mounting platform to be used on the ground, i.e., the NASA system used in the BAPE experiments or a new mount.

5.4.1 The NASA Mount (ATLAS)

During the BAPE experiments, pointing accuracies in the μ rad regime were not needed. The vibration spectrum of the NASA mount was not of particular interest therefore, since the vibrations were known to be small compared to the 1 mrad transmitted beam divergence. Since the OPTS experiments will use beams of the order of 10 μ rad, the vibration spectrum of the NASA mount needed further investigation.

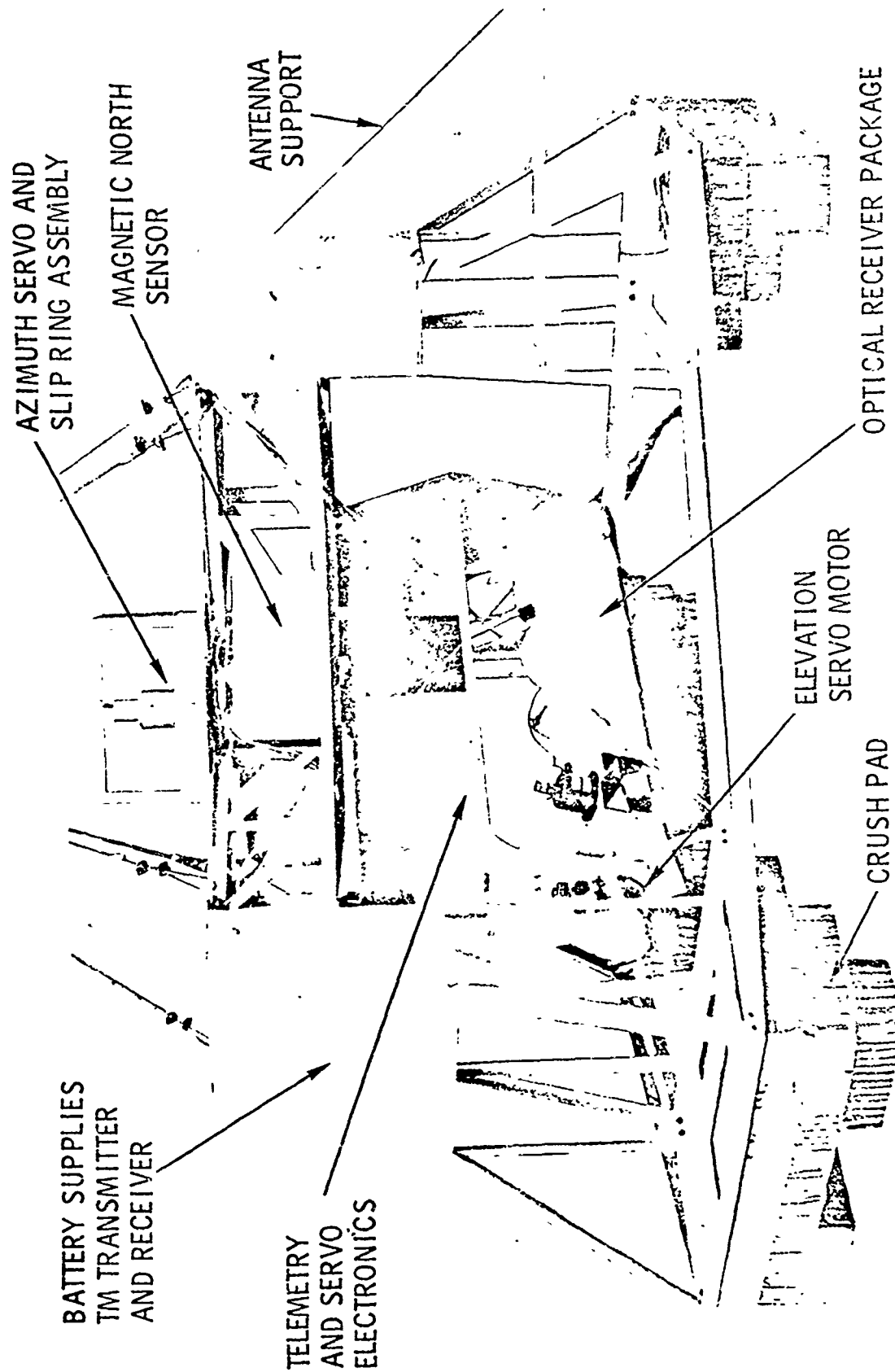


Figure 6. Balloon-Borne Receiver System.

The vibrations of the GSFC Nike/Ajax mount were specified by P. Minott at the start of this program to be of 10.025 mrad amplitude (1 sigma points) and a frequency of about 6 Hz. Since this was inferred from the star tracker error signals, however, the possible motions at frequencies greater than the star tracker bandwidth (probably in the 10 to 50 Hz range) were not known. Cantilever effects, which could occur between the star tracker photosurface and the potential OPTS mounting surface, were not felt to be a problem because of the solid construction of this portion of the telescope system, but accurate vibration information was needed to determine if the mount was suitable for the OPTS application. At the request of GTE Sylvania, NASA Goddard personnel fitted the mount with sensitive accelerometers to measure the vibration environment that a "piggyback" transmitter system would encounter. The results of these measurements are described in Appendix XI.

Aside from a $.04$ arc sec. vibration at 800 Hz, the measurements indicated vibrations of 15 to 20 μ rad rms at low frequencies. We shall see later than even these vibrations present a serious problem to some of the possible experimental techniques.

On the other hand, there are significant advantages to be gained by mounting the OPTS transmitter on the GSFC mount. Assuming that the ATLAS system acquires the balloon payload in the normal fashion, proper pointing of the OPTS transmitter could be assured by very minor and infrequent adjustments of the OPTS transmitter relative to the ATLAS bore-sight axis. This is a significant advantage because planning and controlling balloon trajectories involves a considerable degree of uncertainty.

5.4.2 Separate Mounting Platforms

Since the random pointing errors which are characteristic of the NASA servo system are large compared to the laser beam divergence, two alternative mounting platforms were considered. The first mount was an az-el type, which could be quickly adjusted and then locked and held to a stability of ~ 2 μ rad. Data would then be obtained with a scanning laser

transmitter which would cover a rectangular field through which the gondola was drifting.

The primary advantage of this separate mount is that a better mechanical, thermal, and electrical environment can be provided for the laser transmitter system. Mounts with 2 μ rad stability are available, but they cost in the range of \$40 to \$60K⁽⁸⁾. Separate mounts also suffer from the distinct disadvantage that reacquisition of the target at intervals of approximately 20 seconds is required. Because time is lost during reacquisition, the rate of data acquisition is inherently lower with a non-tracking, separate mount. In addition, separate non-tracking mounts require a scanning laser transmitter which has disadvantages which are discussed in Section 5.5.1.

The second type of separate platform considered was one that duplicated the ATLAS function of active tracking of the balloon system, but did it to an accuracy of approximately 1 μ rad. Since the only reference available with this kind of accuracy is the light beam coming down from the balloon, it became clear that this new mount would have to be part of a Reciprocity Tracking System. This is discussed in detail in later sections, but it should be mentioned now that it overcomes all the disadvantages of the ATLAS and separate stable mount approaches, except costs.

5.5 Measurement Techniques

The feasibility of several measurement techniques has been assessed. For completeness, the following section will include brief descriptions of techniques which were discarded as well as those which appear most promising.

5.5.1 Scanning Transmitter - Separate Stable Mount

A scanning transmitter approach was proposed initially to avoid the problem of tracking the balloon-borne receiver to fractional arc second accuracies. A diagram of the scanning transmitter optical system is shown

in Figure 7. (Detail of the Scanning Transmitter design are presented in Appendix XII.)

The transmitter produces diffraction-limited beams of variable diameter, beam shape, and collimation which can be scanned across a rectangular field covering the position of the balloon-borne detector. A raster scan is generated with beams of spherical cross section, and a one-dimensional scan is used with the fan shaped beams.

Figure 8 shows the scan geometry and the data reduction procedure. Since the beam is "waved" past the balloon-borne detector at a known velocity, a spatial intensity profile of the beam cross section can be reconstructed from the intensity versus time records.

The propagation results would be available as follows:

Spread: from the duration of the signal during each scan, providing the scan was faster than any wander frequency.

Wander: from the relative displacement of the signal from scan to scan (assuming a stable mount and known balloon drift rate).

Scintillation: not available, as discussed below.

In practice, the system would be used as follows: The transmitter would be mounted on an azimuth-elevation mount which was capable of achieving short term stabilities of less than 2 microradians rms pointing error over periods of several minutes (A suitable modified telescope mount is available from Perkin Elmer, Boller and Chivens division⁽⁸⁾.) The mount would be located adjacent to the ATLAS tracking telescope and probably housed in a small portable dome to avoid wind loading problems. Coarse pointing information would be derived from the NASA mount to initially orient the transmitter system. Visual acquisition of the balloon payload would then be accomplished with the boresighted Questar telescope. Having oriented the transmitter properly with respect to the balloon drift direction, a 0.25 mr X 2.0 mrad scan (long axis parallel to drift direction) would be initiated with the mount fixed and stable.

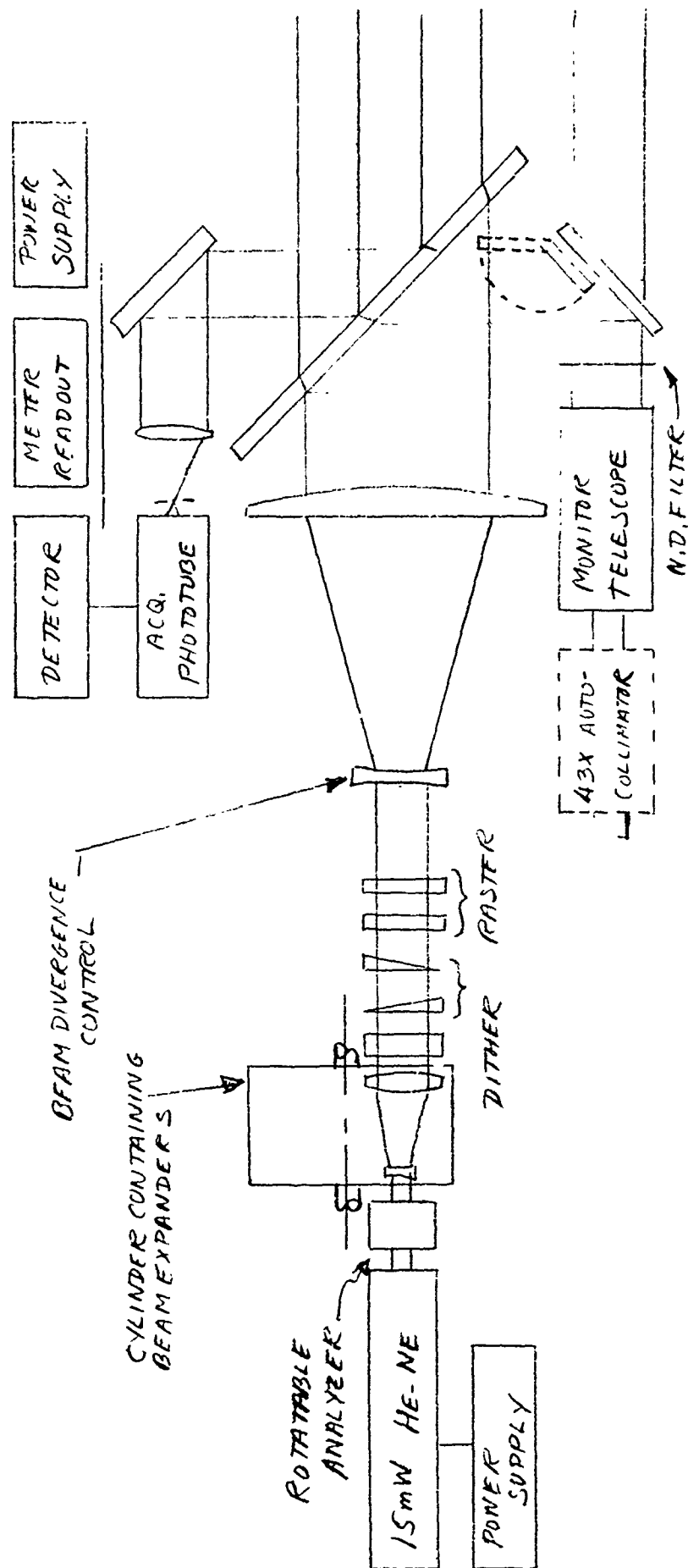


Figure 7. Scanning Laser Transmitter Diagram.

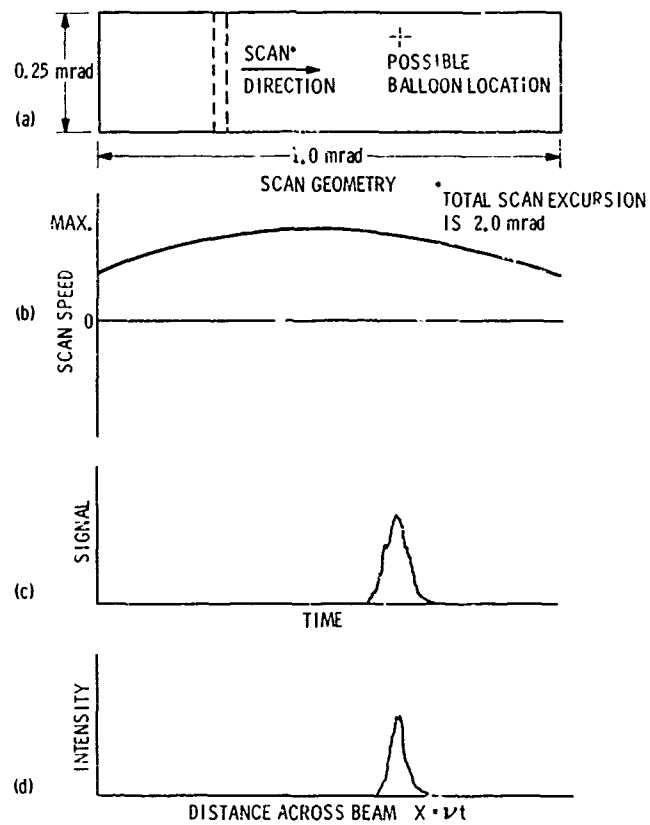


Figure 8. Line Scan Geometry and Data.

Assuming a reasonable balloon drift rate of 50 microradians/sec, this would yield ≥ 20 seconds of data. A data run of this length would permit a determination of beam wander frequencies as low as 0.1 Hz, which includes almost all of the expected beam wander frequencies. After each 20 second data run the transmitter pointing angle would be updated to "lead" the balloon motion.

The scanning Transmitter-Separate Stable Mount approach has the following disadvantages:

1) A separate mount capable of the required stability would cost approximately 40 - 60K and have a 6 month delivery schedule⁽⁸⁾.

2) A small dome would probably be required to protect the mount and transmitter system from wind and acoustic loading⁽⁸⁾.

3) The quality of the acquired data could be degraded because of operator fatigue caused by the tedious and frequent reacquisition of the target. A TV display of the Questar field of view would help alleviate operator fatigue, but the frequent reacquisition problem must still be considered a drawback of this measurement technique.

4) Any accelerations of the balloon payload, if large enough, would cause erroneous beam wander measurements. Pendulous motions of balloon platforms at float altitude of 1° amplitude and 10-18 sec periods have been measured.⁽⁹⁾ There is a potential problem, therefore, in measuring the lower beam wander frequencies, but it is possible that the effects could be removed from the data because of their necessarily narrow frequency spectrum.

5) Because a 0.25 X 2.0 mrad field of view must be scanned and data is acquired only during a small portion of the scan (determined by the angular size of the beam), the rate of data acquisition is slow compared to techniques which do not involve a scanning transmitter.

6) The line scan will yield the required beam spread and wander information at relatively high data acquisition rates compared to the raster scan because the line scan yields one profile for each scan deflection. Since the scintillation is highly dependent upon the degree of collimation of the beam however, diverging the beam to 0.5 mrad (as is required to produce the

fan beam) would not yield valid scintillation data for the desired collimated cases.

We therefore initially considered the use of a spot scan on a two-dimensional raster. However, later discussion and analysis showed that this technique fundamentally distorted the scintillation information because the beam had to be scanned rapidly compared to beam wander frequencies, i.e., this meant that some portions of the atmospheric turbulence along the path would change during a data sample, while other portions would not. Therefore, a modified scintillation magnitude and frequency spectrum would arise from the spot scan measurements, which could not be related to the desired unscanned scintillation results.

Therefore, although the fan scan from a stable mount will provide sufficient spread information, and some wander information (the magnitude of wander, but not whether it can be tracked out), it is not the recommended technique because it can not yield valid scintillation information.

5.5.1.1 Scanning Transmitter - ATLAS Mount

The scanning transmitter described above could be attached to the NASA ATLAS mount. This would solve the reacquisition problem and increase the rate of acquisition of raw data. The mount vibrations would mask the atmospheric-induced beam wander, however, and the results obtained would be limited to beam spread information alone. The experiment, therefore, would measure only the least critical turbulence effect and would not be worth doing.

5.5.2 Dual Scanned Beams - ATLAS Mount

A technique which would permit measurement of the atmospheric beam wander in the presence of mount vibrations would involve a scanning transmitter as described above, but with two exit apertures as shown in Figure 9. The exit apertures of the two beams are one meter apart to

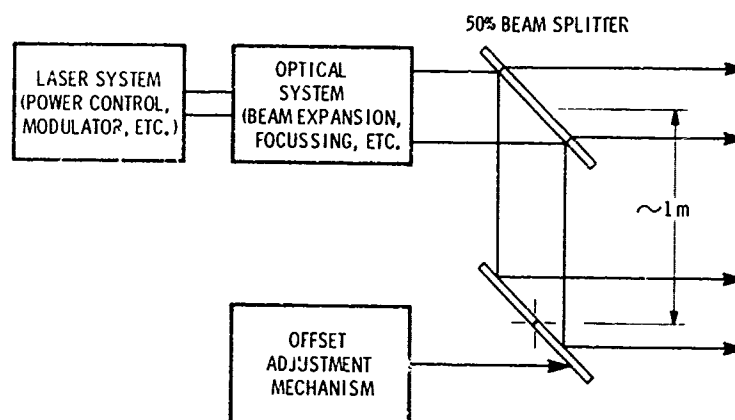


Figure 9. Dual Beam Approach.

insure that the turbulence effects on the beams will be uncorrelated. In addition, one beam is angularly displaced relative to the other so that negligible beam overlap occurs at the receiver. For scan rates much greater than the mount vibration frequencies, mount vibrations will have an identical effect on both beams, whereas atmospheric effects will be uncorrelated. Measuring the relative positions of the beams at the receiver will therefore yield the atmospheric beam wander (but will not test reciprocity tracking, of course). As in the single beam approach, beam spread information, but not scintillation, would be obtained. This approach would permit both beam wander and spread to be measured at relatively high data acquisition rates compared to the Scanning Transmitter - Separate Stable Mount approach. Because the 9" exit apertures must be separated by approximately 1 meter, however, the size of the laser transmitter system would require that two 13" optical flats (1/10 wave accuracy) be mounted with 1 μ rad short-term stability relative to the exit aperture of the expander telescope. Further investigation of this technique was not warranted because of the complexity, cost, more complicated data analysis required, and lack of scintillation data.

5.5.2.1 Dual Modulated Beams - ATLAS Mount

An alternative technique (that should remove most of the balloon motion effects) is to boresight the two beams with the ATLAS tracker, but chop them at different frequencies. (They would also have to be orthogonally polarized to prevent interference at the balloon receiver.) Then the power fluctuations from each beam could be electronically separated. The common power fluctuations would be due to mount vibrations and could, in principle, be separated out leaving the residual atmospheric wander and scintillation effects.

A detailed calculation in Appendix X points out the problems with this technique. First of all, for mount motion of 15 μ rad rms and atmospheric wander of 5 μ rad rms (and an unspread 10 μ rad beam), only 1.4% of the detected variance of the power fluctuations will be due to the atmosphere.

Furthermore, the scintillation effects of interest will only be ~10% of those due to this wander, and so would be impossible to retrieve accurately.

Clearly, this technique does not add anything further to the dual scanned approach, and so is not recommended.

5.5.3 Complete Intensity Distribution at the Balloon Techniques

The approaches discussed thus far have had the serious drawback that they afforded no realistic means of obtaining any scintillation data. To solve this problem, a different tact was taken. Since a "snapshot" of the intensity distribution over the beam cross-section would directly indicate scintillation and beam spread, electro-optical techniques for acquiring this kind of data were investigated.

Two techniques for acquiring this instantaneous intensity profile are covered in the following sections. The image dissector approach requires that the uplink laser illuminate a screen located above the gondola and the diode array approach involves detectors placed directly in the beam cross sections.

5.5.3.1 Image Dissector Approach

Using an image dissector tube to scan a screen illuminated as shown in Figure 10 was considered first. The many disadvantages listed below caused this technique to be discarded.

The image dissector tube would scan the screen in 4 msec to "freeze" scintillation fluctuations of less than 250 Hz. The resulting scan would in effect be an instantaneous intensity contour which would indicate scintillation, beam spread and beam wander due to mount motion plus atmospheric beam wander. If we postulate a correlation length of 20 cm at 100 km range, the "viewed" section of the screen should be approximately 2 cm x 2 cm. The viewed spot will move across the screen at a velocity of 5×10^4 m/sec. It would traverse a typical "hot" spot

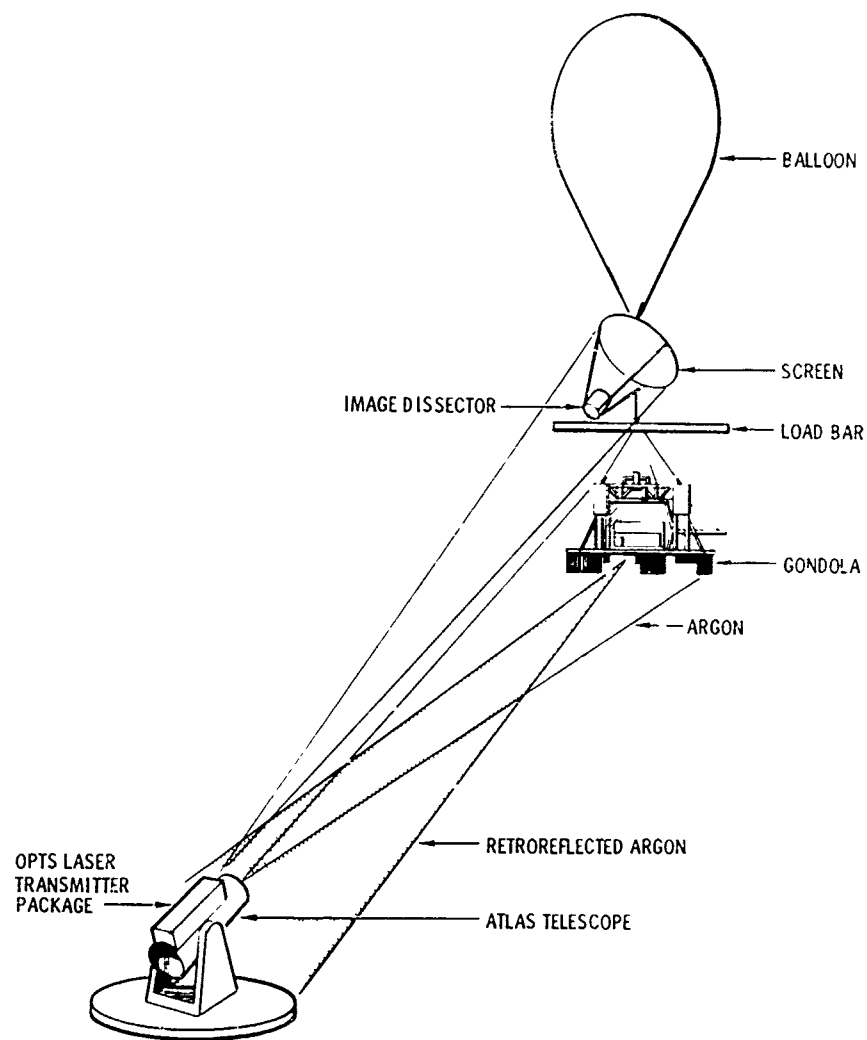


Figure 10. Image Dissector Configuration.

in $0.2\text{m}/5 \times 10^4 \text{ msec}^{-1} = 4 \text{ } \mu\text{sec}$. The frequency response of the data channel, therefore, would have to be at least 500 kHz.

A possible signal waveform is shown in Figure 11. Because of the random structure of the spatial intensity distribution, however, the "hot" and "cold" spots will be closer than 20 cm a portion of the time, resulting in a faster signal risetime and therefore, a higher required bandwidth. For this analysis, a frequency response of 5 times the fundamental will be assumed (2.5 MHz). The geometry would require a 25 kHz deflection scan frequency for the image dissector.

The equations governing the power received at the image dissector and the S/N ratio are

$$P_R \approx \frac{4 P_o A_i A_D}{\pi \theta^2 Z_1^2 Z_2^2} \quad (5-1)$$

$$\left(\frac{S}{N}\right)_p = \frac{\frac{1}{2} \left(\frac{\eta e P_R}{h\nu} \right)^2}{2e \left(\frac{\eta e}{h\nu} [P_R + P_B] \right) \Delta f} \quad (5-2)$$

where

- A_i = area "viewed" on the screen (a diffuse reflector is assumed)
- A_D = area of image dissector lens
- θ = laser beam divergence
- Z_1 = range to screen
- Z_2 = distance from screen to image dissector
- η = quantum efficiency
- e = electronic charge
- $h\nu$ = photon energy
- P_B = background power
- P_o = mean optical power
- Δf = detection bandwidth

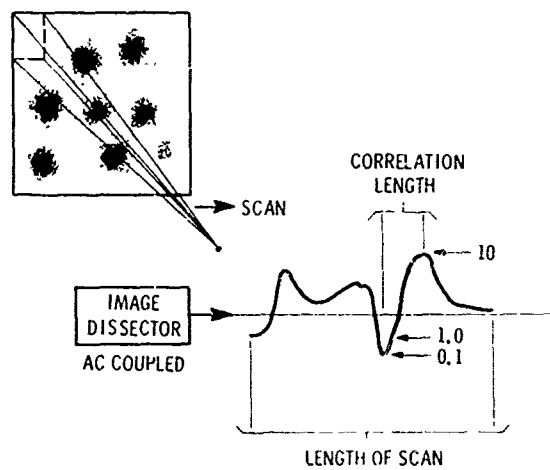


Figure 11. Image Dissector Signal Waveform.

For $P_o = 7.5 \times 10^{-3}$ watts, $A_1 = 4 \text{ cm}^2$, $A_D = 16 \text{ cm}^2$,
 $Z_1 = 100 \text{ km}$, $Z_2 = 3\text{m}$, and $\Delta f = 2.5 \text{ MHz}$, equations (5-1) and (5-2) yield

$$P_R = 1.6 \times 10^{-10} \text{ watts}$$

$$\left(\frac{S}{N}\right)_p = 3$$

The technique, therefore, has inadequate S/N ratio because of the high detection bandwidth and the diffusion of the light on reflection from the target screen. The technique is also fraught with other practical difficulties. A 2m x 2m screen with a 3m tripod structure supporting an image dissector is a rather unwieldy device to point and recover without damage after the parachute descent. Image dissectors used in raster type scans are prohibitively expensive because the effects of compensation must be provided for photocathode non-uniformity and off-axis distortion of the electron focussing. Because of the inadequate signal-to-noise ratio and other implementation difficulties, this technique was discarded.

5.5.3.2 Diode Array Approach

Because the image dissector approach had serious drawbacks, another approach based on the "snapshot" idea was investigated. Higher S/N ratio and lower detection bandwidths were achieved by substituting a matrix of photodiodes for the reflecting screen. Each diode monitors the irradiance fluctuations at one point in the beam with a 500 Hz bandwidth. The irradiance levels at each diode are then sampled and recorded in a short time during which the intensity profile of the beam is "frozen". This technique, which yields scintillation and beam spread, but sees both mount-induced and atmospheric beam wander, is described in detail in Section VI.

5.5.4 Reciprocity Tracker Technique

The reciprocity tracker system solves most of the problems associated with the previously described techniques. The term "reciprocity" refers to the supposition that a downlink beam reflected back on itself will, to an appreciable degree, retrace its original path back to the source. The reciprocity tracker simulates this reflection process by transmitting the uplink beam along the normal of the arriving wavefront. The design required to accomplish this "reciprocity tracking" is discussed further in Section VII.

Any motion of the mount will appear to the optical system like a wavefront tilt of the incident light. The reciprocity tracker will still transmit the uplink beam along the normal to this wavefront, thereby compensating for the mount motion. This eliminates a major drawback of the other approaches, i.e., atmospheric-induced beam wander will not be masked by wander due to mount motion. In addition, the reciprocity tracker will compensate for most of the atmospheric beam wander, and therefore will not measure it directly.

This approach combines the advantages and avoids certain disadvantages of several of the previously described techniques. In particular:

- 1) low frequency (<100 Hz) vibrations of the mount will not degrade the quality of the measurements;
- 2) accurate pointing will yield high data acquisition rates;
- 3) the three important turbulence effects will be measurable (beam spread and scintillation directly, and beam wander insofar as it is not tracked out);
- 4) a large diode array is not required.

The final important point is that the reciprocity tracker will directly test the reciprocity technique in a configuration which will be very similar to that envisioned for a laser high data rate uplink.

5.5.5 Summary of Experimental Techniques

The most promising experimental techniques discussed above are summarized in Table IV. Based on our analysis and the development schedule, we recommended on July 17, 1972 that the diode array approach be implemented for experiments in May/June 1973 and the Reciprocity Tracker be implemented for experiments in May/June 1974.

There were two key reasons for this recommendation:

- (1) We assumed that some results were needed by June 30, 1973.
- (2) The reciprocity tracker implementation had technical, schedule and cost implications that made it impossible to achieve by May/June 1973.

On July 17, 1972, the Air Force directed GTE Sylvania to plan for Reciprocity Tracker experiments in May/June 1974. Therefore, it is the experimental technique adopted and planned for throughout the remainder of the report, except in Section VI, where we summarize the extensive design work we performed on the diode-array approach. Section VII describes the reciprocity tracker technique design approach.

5.6 Basic Balloon Gondola Modifications

As a result of the previous experience of both NASA and GTE Sylvania with the BAPE equipment, several modifications have been recommended to make the equipment suitable for the OPTS application. Those modifications which apply regardless of the specific measurement technique are summarized below. (A fuller discussion is presented in Appendix XIII.) Others are discussed individually in Sections VI and VII.

The basic modifications can be grouped as follows:

- (a) Repair and Refurbishment to fly as is.
- (b) Range Extension, to fly as is, but suitable for data taking at slant ranges up to 100 km.
- (c) Modifications required to place a HeNe laser aboard, and point it accurately back towards the ground station.

We now summarize the needed modifications:

TABLE IV. OPTS Experimental Techniques

Experimental Technique	Ground System Mount	Ground System Pointing & Tracking	Balloon System Data Receivers	Key Technical Problems	Results			Conclusions/Recommendations
					Scintillation	Wander	Spread	
Scanning Single Line (fan)	Separate mount	Stable/fixed during scan	Single (or a few) photodetector(s)	Mount stability; balloon motion	None	Some	Suff	Done only in conjunction with some scintillation experiment
Dual Beams: Both Scanned or Differently Modulated	NASA mount	$\sim 25 \mu\text{rad}$ rms random pointing fluctuations	Single (or a few) photodetector(s)	Ground Opt. System alignment; balloon motion	None	Some	Suff.	Done only in conjunction with some scintillation experiment
Large Receiver Array on Balloon	NASA mount	$\sim 25 \mu\text{rad}$ rms random pointing fluctuations	Large array of photodiodes	Array implementation; data recording data analysis	Suff.	None	Suff.	A good technique, and the best one doable by next summer
Reciprocity Tracker	To be determined	Fine track on \angle of arrival to within $\lesssim 1 \mu\text{rad}$	A few detectors	Fielding a 1- μrad tracker	Suff.	Suff.	Suff.	Best Simulates actual communication operation and provides data that does not depend on theory for interpretation

5.6.1 Repair, Refurbishment and Minor Modifications

The gondola was inspected during the study. Friction, torque and weight measurements and calculations of the moment of inertia were made to aid in the servo analysis. In the course of the inspection and measurements, several areas were noted in which minor mechanical modifications would improve the operation of the system.

As received from NASA, the azimuth drive was misaligned, resulting in rubbing between the stator and rotor of both the drive motor and tachometer. This problem could be alleviated by machining a register to align the motor stator and rotor. This would also provide better shielding of the bearing. A minor modification of the tachometer mounting could reduce its alignment sensitivity.

For convenience, the azimuth mounting flange (which screws onto the bearing shaft) could be redesigned so that play would not develop after repeated landings.

Connectors and bearings should be better shielded from possible contamination by ballast. Although this should not occur if the ballast hoppers are hung properly, the problem has occurred in the past.

5.6.2 Range Extension

The present system will acquire data and telemeter real-time results to the ground station out to slant ranges of 50 km (elevation angle $\sim 37^\circ$). In order to operate out to 100 km (elevation angle $\sim 17^\circ$), the following modifications are needed:

Telemetry - The addition of preamplifiers before both receivers and the replacement of the present 4' ground station receiving antenna with an 8' unit will insure adequate telemetry performance over the increased maximum path length. The signal to noise ratio of the downlink data channels will be better than 30 dB.

Optical Tracker - Since increased pointing accuracy will not be required for the range extension modification, only minor modifications to increase the sensitivity of the optical tracker would be required. These would include the use of lower noise preamplifiers in the detection circuitry, and a larger tracker lens.

Optical Data Receivers - An extended mirror assembly must be added so that the receivers can look out below the crush pads at the lower elevation angles. The mirror assembly will be rotated to a horizontal position during launch and landing. In addition, the gain of the detector circuits must be adjusted for the increased range capability.

5.6.3 Modifications Suitable for Accurately-Pointed-Laser Aboard

The present system has a tracker and servo-system that point the optical receivers to a few milliradians. The accuracy required of the servo system is dependent upon several factors. In general, it is desirable to point a laser with an angular accuracy of approximately 10% of its divergence. This reduces power fluctuations at the receiver which are caused by the reduced irradiance away from the center of the gaussian shaped intensity profile. Because the chosen laser for use in the gondola has a limited power output of 3 mwatts, the required beam divergence (or pointing accuracy) depends on the required irradiance at the ground receiver. NASA indicated that 100 μ rad pointing would be required for their measurements. The OPTS experiments would require considerably less accuracy, depending on the final reciprocity tracker design.

Optical Tracker - This must yield a signal sufficient to drive the servo's to the required accuracy. In Appendix XIII, we have discussed a design suitable to achieve 40 μ rad accuracies (rms) with regard to tracking detector boresight errors signals alone. The actual tracking accuracy of the system will also depend in the servo system (Appendix XIII) as discussed below.

Elevation Axis Structure - This structure must support and protect the basic electronics package (which contains the tracker,

detection and experiment control circuitry), the laser subsystem, and the extended mirror. The resonant frequency and moment of inertia of the package must meet the requirements of the servo design (see Appendix XIII).

Laser Subsystem - The Hughes Model 3079H HeNe laser was chosen for this application because it provided the required environmental specifications with adequate power at a reasonable cost. The techniques used to chop, control beam divergence and align the laser are described in Appendix XIII.

Servo System - As discussed in Appendix XIII, the degree to which the present servo system can be improved depends on moments of inertia, tracker noise levels, mechanical resonant frequencies, etc. Our present best estimate is that a ~ 1 mrad rms azimuth error and a ~ 0.5 mrad rms elevation pointing error should be achievable by modifications of the existing equipment. For better accuracies (in the 100 μ rad regime particularly), fundamentally different techniques must be investigated and implemented. Possible design approaches are discussed in Appendix XIII, but we will not consider them for OPTS until a further specification of the Reciprocity Tracker determines whether they are needed.

Power System - It is not anticipated that servo modifications will result in additional power drain. The laser, however, will require 35 watts, and an additional 10 watts could be required for control circuitry. Assuming a 3 hour experiment period, 150 watt-hours would be required. For a 24 volt battery, this would be 6.3 amp hours. The size battery closest to this requirement which allows adequate safety margin is the Sonotone CA-24A. This battery weighs 26 lbs. and has a 26 amp hour rating.

5.7 Turbulence Measurements

5.7.1 Introduction

Because the knowledge gained with the optical experiments must be transferrable to other sites, the turbulence profile must be

measured and correlated with the optical effects. Both near earth and high altitude turbulence is important, as discussed in Appendix XV.

During the course of this program, we have studied a number of possible techniques to measure the turbulence.

5.7.2 Tropopause Turbulence (~ 15 km altitude)

The optimum technique is to launch free-floating Thermosondes, developed by GTE Sylvania under a NASA contract. These devices directly measure $C_T^2(h)$ and transmit it to a rawinsonde ground station over a standard rawinsonde link.

However, they require ~ 50 minutes to reach the tropopause and another 35 to 40 minutes to descend. Therefore, point source scintillation measurements should be taken quasi-continuously to monitor the shorter term tropopause strength variations. (As pointed out in Appendix II, Section II-2 and exemplified in equation (II-9), the point source results are crucially dependent on the strength of the high altitude turbulence, and will directly indicate its strength.)

5.7.3 Near Ground Turbulence ($h \leq 2$ km)

Although the high altitude free-float thermosondes discussed above will also give information on the near-ground profile and strengths, they will not be launched frequently enough to give sufficient knowledge of the near ground effects. We have therefore considered other techniques:

(1) Acoustic Radars - These do not have the necessary sensitivity and/or range at present, but may perhaps develop sufficiently by 1974.⁽¹⁴⁾

(2) Tethered Thermosondes - Stringing a host of thermosondes along the tether of a low-lying tethered balloon would work, but would be extremely expensive and cumbersome since approximately 15 thermosondes would be needed, with power and data lines to and from each one.

(3) Single Tethered Thermosonde - Raising and lowering a single tethered thermosonde would be sufficient, if it could be done rapidly enough and to a high enough altitude. At present, neither of these appears achievable.⁽¹⁵⁾

(4) Low Altitude Free-Float Thermosondes: This involves flying free float thermosondes to ≤ 2 km and having them immediately descend. Total flight time would be ~ 10 minutes, assuring a complete low-level profile once every 5 minutes. Moreover, the packages should descend ~ 1 mile away from launch site, and therefore, all be recoverable for re-use. This, therefore, is the recommended technique unless acoustic radars are sufficiently improved in the near future.

Section VI

DESIGN OF THE DIODE ARRAY TECHNIQUE

6.1 Introduction

As discussed in Section V, a large array of diodes on the balloon platform will yield spread and scintillation information even in the presence of mount motions which would be experienced if the ground transmitter were mounted on the ATLAS telescope. This section discusses the design of such a system, since a significant portion of the OPTS program was committed to this design before we were directed to concentrate solely on the Reciprocity Tracker Technique.

Section 6.1 presents the basic experiment configuration. Section 6.2 discusses the ground laser transmitter system and Section 6.3 presents our design of the balloon receiver system.

The interpretation and analysis of the resulting data is outlined in Section 6.4 while Section 6.5 lists the estimated costs of implementing this design. These costs, in conjunction with the fact that no atmospheric wander results were derivable from the diode array technique, were a key to the selection of the Reciprocity Tracker as the preferred technique.

6.1.1 Diode Array Experiment Configuration

The experiment configuration is shown in Figure 12. The ATLAS system tracks the gondola with its argon beam, and a dual auto-track link is established between the ATLAS and the gondola experiment package. The OPTS laser transmitter package is attached to the ATLAS telescope and directs laser beams of variable diameter and divergence towards the diode array which is located above the gondola. The diode array frame is driven in azimuth by a motor which responds to the same error signals which drive the experiment package in the gondola. This control of the azimuth orientation of the diode array keeps the uplink laser within the field of view

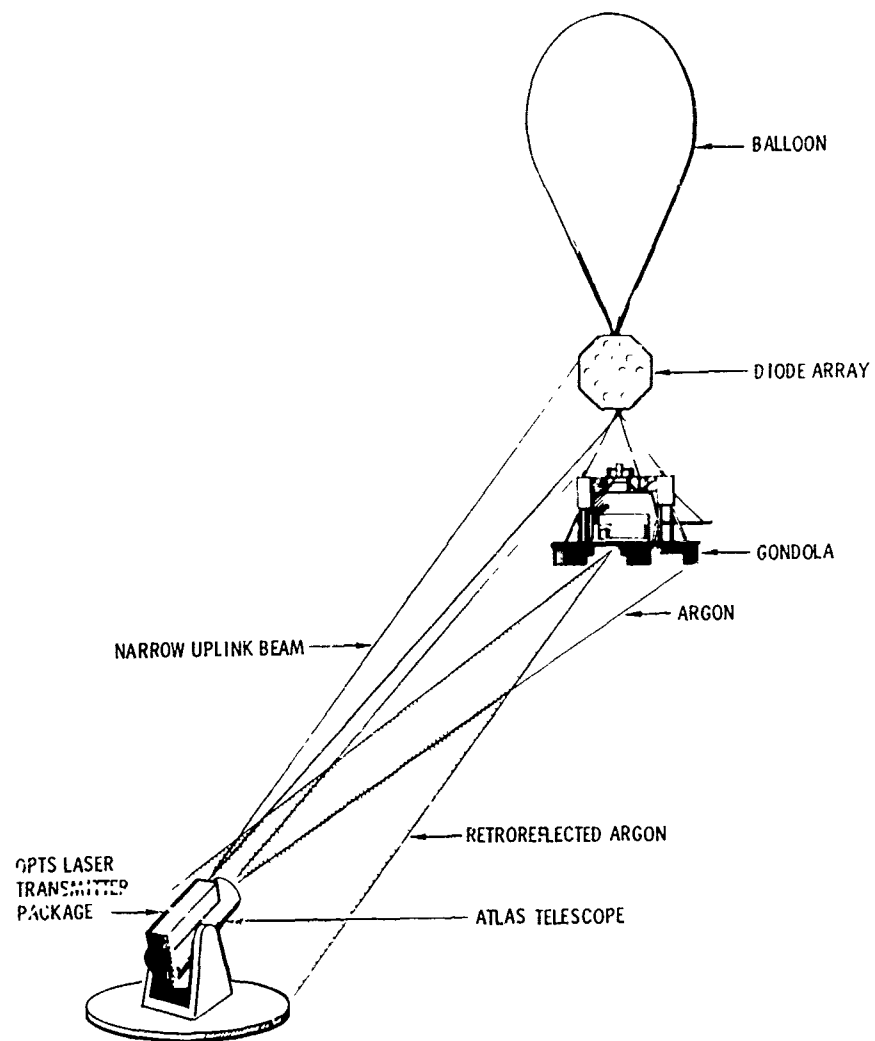


Figure 12. Diode Array Experiment Configuration.

of the detectors. By orienting the diode receivers at 35° with respect to horizontal and using a fan-shaped field of view, the need for elevation control of the array is eliminated.

The signal levels at each diode are sampled sequentially, amplified, and recorded on the balloon-borne tape recorder. All of the diodes are sampled in a time which is short compared with the highest scintillation frequencies. The signal levels at four of the diodes are transmitted, real-time, to the ground station to aid in alignment of the uplink beam. The laser transmitter and balloon receiver systems are discussed further in the following sections.

6.2 Laser Transmitter System

6.2.1 Design Considerations

The design of the ground transmitter optical system depends upon several factors. First, the equipment must provide uplink beams with a range of variable characteristics. The range of beam parameters must be chosen to encompass regions over which an unambiguous test of the theory can be achieved. In addition, the range of data points should "bracket", if possible, the optimum range as predicted by theory. This extra margin will insure that sufficient data points are available to establish trends in the event that results depart significantly from the theoretical predictions.

The analysis described in Appendix II indicates the character of the beams which must be provided by the transmitter system. The optimum collimated beam sizes for comparison with theory are 6.0 cm, 4.03 cm, and 1.61 cm (e^{-2} radius) and the optical system must provide for both focusing and defocussing of the beams.

The necessity of having an accurate monitor of the output beam divergence is shown by Figures 36 and 37 of Appendix II. The parameter $C_L(o)/C_L^S(o)$ changes from 0.64 for the collimated 10 μ rad beam to 0.81 when the beam is diverged to 11 μ rad. The beam divergence of the laser must be known, therefore, to 0.5 μ rad when data is being taken for nearly

collimated beams. This capability is provided by the special Questar telescope and 43X auto-collimator (see Appendix XIV).

Appendix IX shows that truncation of the transmitted beam at less than twice the c^{-2} diameters, and center blockage should be avoided, if practical. Avoiding truncation is practical, but to hold the cost of the transmitter optics within reasonable limits, the small center blockage of a Cassegranian system will probably have to be tolerated. This will result in a small increase in the complexity of the data analysis, but can be treated as discussed in Appendix V.

6.2.2 Transmitter Optical System

A block diagram of the system is shown in Figure 13. The laser, which is linearly polarized, passes through an analyzer, an electro-optic modulator, and two sets of Risley prisms before entering the variable power telescope. By rotating the analyzer, the power output of the laser is adjusted to keep the irradiance at the gondola constant as the transmitter beam divergence and the range to the gondola are changed. The Risley prisms are used to maintain the correct alignment of the laser transmitter system with respect to the ATLAS system. The monitor telescope and 43X auto-collimator are used for system alignment and adjustment of the transmitter optical system as described in Appendix XIV.

6.2.3 Mechanical Considerations

Figure 14 shows the basic transmitter housing layout. The major weight (and deflection producing) components are all concentrated in an area directly adjacent to the mounting location. This fact, along with the single plane of gravity deflection associated with an elevation over azimuth pedestal allows a structure approximately 2 feet high of monocoque construction to have less than a microradian deflection between components over the 90 degrees of elevation travel.

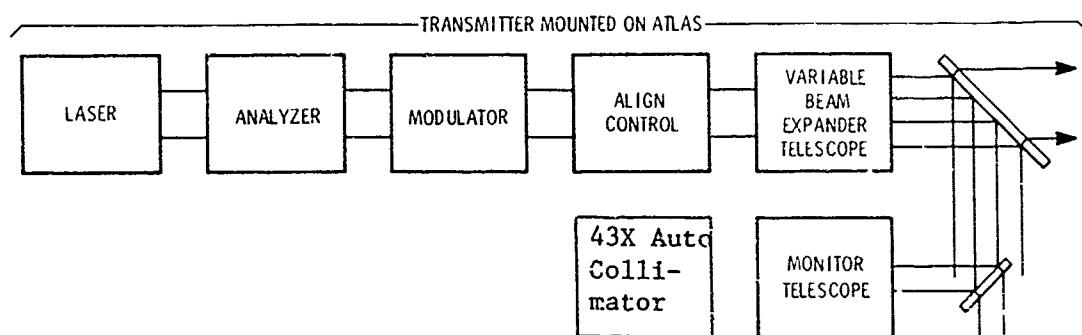


Figure 13. Block Diagram of Transmitter Optical System.

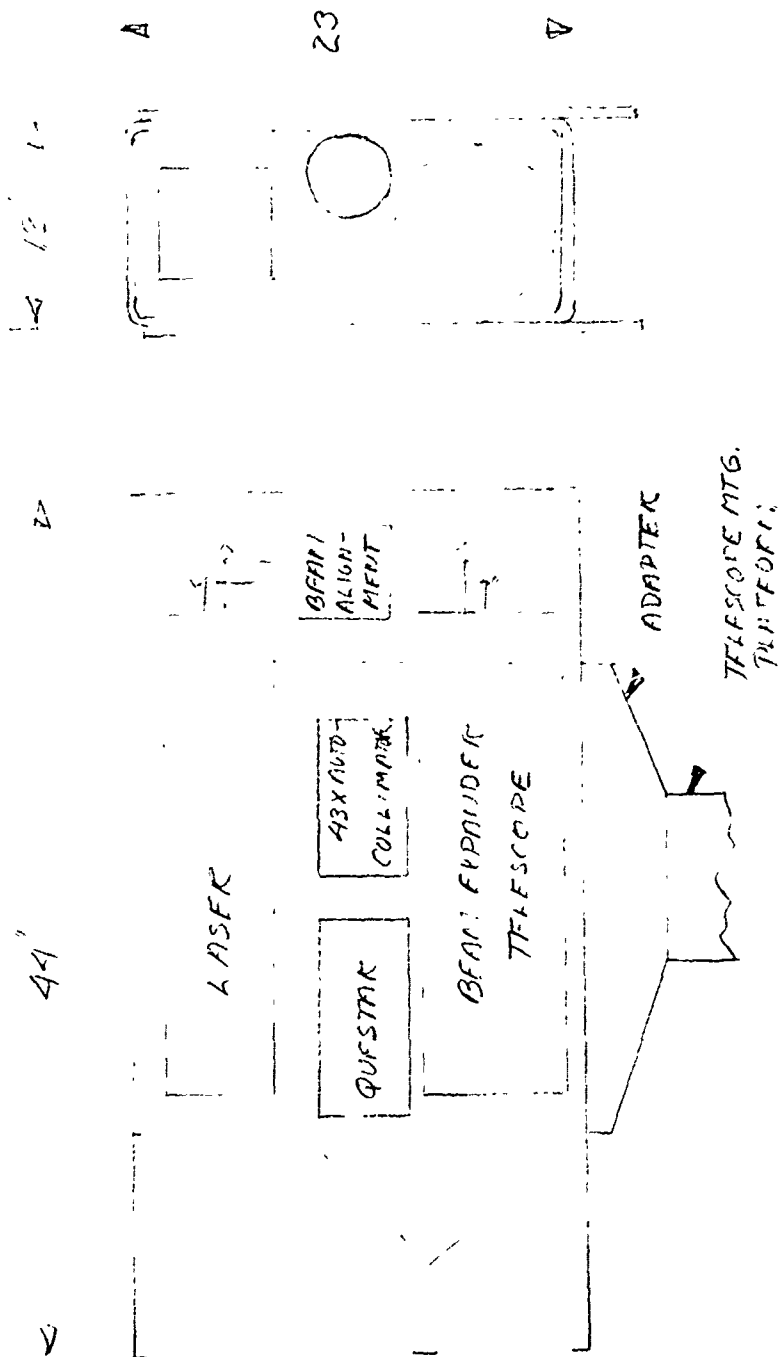


Figure 14. Physical Layout of the Laser Transmitter.

Deflections of the order of microradians caused by sagging of the housing during a change of elevation angle, for instance, are not a problem because the laser beam can be realigned with the Risley prisms. Such adjustments would be required, in fact, even if the housing were perfectly rigid, because the angle between uplink laser and the ATLAS telescope axis changes slightly as the elevation angle varies. The extreme case of a one microradian deflection was analyzed, however, because the stiffness required of the housing and component mountings is also dependent upon the vibrations transmitted to the optical elements from the ATLAS pedestal, or acoustic sources.

The final design will require additional consideration of these effects, but this initial analysis, which has considered representative sizes and weights for the transmitter system components, indicates that adequate rigidity of the housing should be readily achievable.

The separate optical components shown in the block diagram of Figure 13 are subject to different alignment and mounting requirements depending upon their position in the optical path. Elements which follow the variable beam expander telescope must be held to 1/10 wave surface figures, and be mounted in such a way as to avoid beam deflections of greater than a microradian. The telescope must be basically of standard astronomical quality (assuming a reflective system is used) having a good stable secondary mounting and provision for fine mechanical adjustment for focus changes caused by temperature cycling. To facilitate field adjustments of the system and maximize the data acquisition duty cycle during the relative short flight time, alignment mechanisms should be accessible, accurate and easy to use. Component mountings should be rigid enough to avoid coupling of mechanical or acoustical "noise" into the beam pointing optical components.

Components proceeding the beam expander telescope will have less stringent angular tolerances (of order 10 arc sec) because of the angular demagnification of the telescope.

6.2.4 Uplink Irradiance

The function of each detector in the array is to measure the irradiance fluctuations in the uplink beam cross section with a detection bandwidth of 500 Hz. For an uplink wavelength of either 4417Å or 5300Å, the detectors could be either photomultipliers or photodiodes. Photodiodes would be the obvious choice, if the irradiance at the balloon is high enough, because the cost and complexity of a photomultiplier array would be more than an order of magnitude larger than a photodiode array. The added cost results from the fact that rugged photomultipliers cost at least twenty times as much as the diodes. In addition, the detection electronics circuitry is more expensive because well regulated and filtered high voltage power supplies are required, and potting must be used to avoid low pressure arcing.

The irradiance at the gondola is given by

$$H = \frac{4 P \tau_o e^{-\beta Z}}{\pi \theta^2 Z} \quad (6-1)$$

and, since $A_D = \pi d^2/4$, the required power is

$$P_R = \frac{P \tau_o d^2 e^{-\beta Z}}{\theta^2 Z^2} \quad (6-2)$$

where

P = mean optical power

τ_o = optics transmission factor

$e^{-\beta Z}$ = atmospheric transmission factor

β = attenuation coefficient

Z = range

θ = beam divergence (full angle e^{-2})

d = receiver aperture diameter

For the case at hand, $P \approx 7.5$ mW, $\tau_o = 0.5$, $e^{-\beta Z} = 0.5$, $Z = 100$ km, $d = 2$ cm, and $\theta = 20$ μ rad. Allowing for beam spreading, the worst case beam divergence will be of order 28 μ rad. The power reaching the detector,

under worst case conditions, will then be 10^{-7} watts. Since the responsivity of a photodiode is 0.4 amperes/watt, this power will produce a current of 4×10^{-8} amperes at the photodiode. This is a more than adequate signal level for the photodiodes, and the photomultiplier detectors will not be required. The uplink S/N ratio is discussed further in Section 6.3.2.

6.3 Balloon Receiver System

The balloon system modifications discussed in Section V would not all have to be implemented in order to perform the diode array experiment, because the downlink He-Ne laser is not needed. Therefore, the repair, refurbishment and minor modifications of Section 5.6.1 and the Range Extension modifications of Section 5.6.2 are all that are required.

This section discusses the rest of the balloon system, i.e., the large array of diodes that would be positioned above the present gondola.

6.3.1 Mechanical Design of the Diode Array Receiver System

The array consists of a framework to which individual diode receiver units are attached. The diodes are positioned in a uniformly distributed manner as shown in Figure 15. The resultant pattern is best suited to a hexagonal main frame with parallel bars added to support the elements. Two support members, added to span the hexagon, divide the structure into six equilateral triangles; the most weight effective shape possible. The support members are tubular of a high strength aluminum aircraft alloy such as 7075 T-6 with bonded joints. All corners have shielding members which protrude beyond the diodes for landing protection.

The bearings support the diode/frame/recorder module on the main shaft. The bearing design is self-aligning and floating to minimize machining and distortion due to thermal and landing loads. A spare array framework would need to be available in the event that an unusual landing situation results in catastrophic damage to the array. Under normal conditions, however, only minor realignment of the frame and diode units would be required.

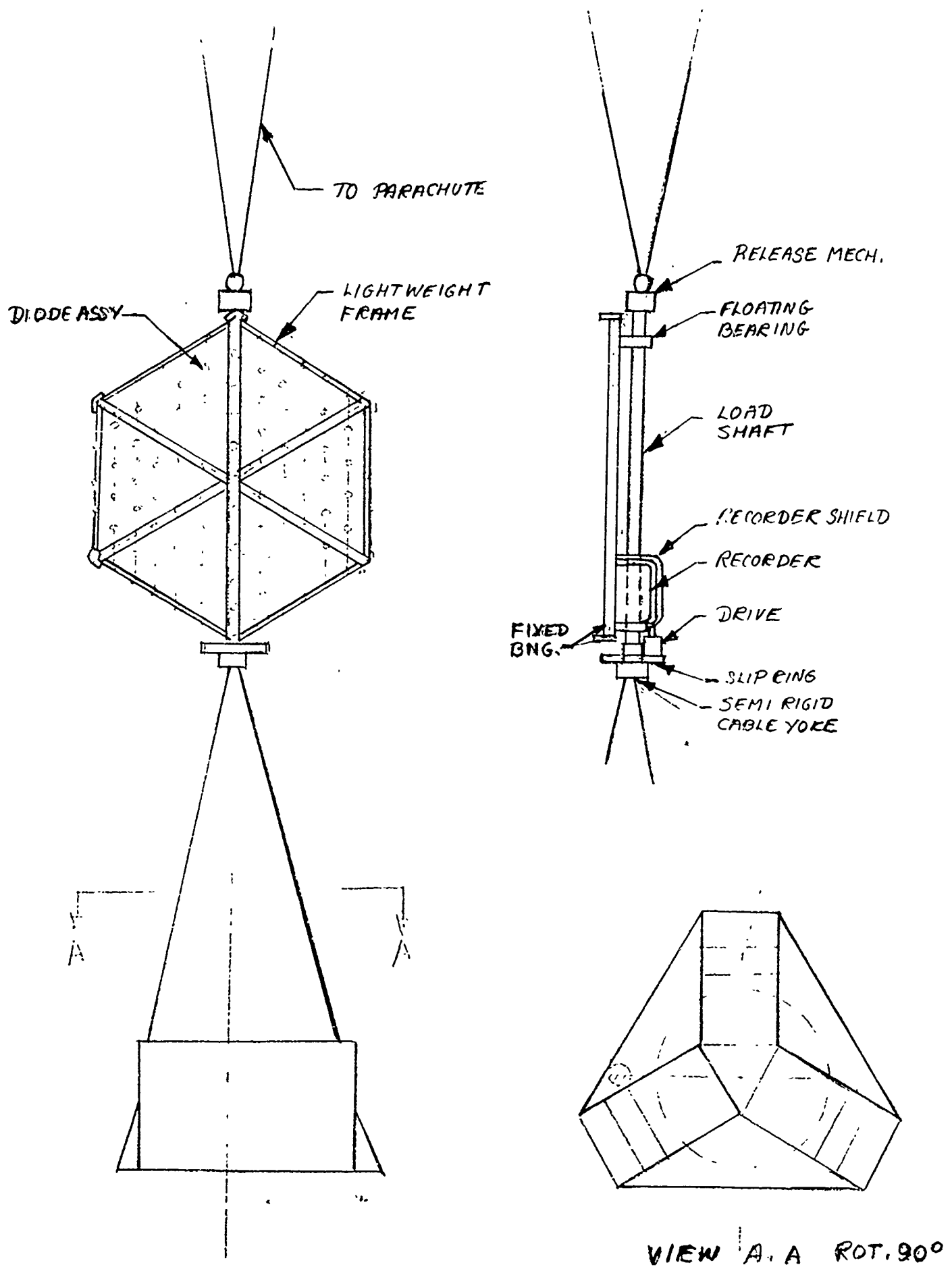


Figure 15. Mechanical Layout of the Diode Array.

Two alternatives exist for the positioning of the diode array.

1) The array could be placed between the load bar and the gondola support cables. In this case, the load bar should be three feet above the array to avoid obstruction of the uplink beam by the balloon control instrumentation which hangs from the load bar. Particular care would have to be taken in shielding all of the equipment because the ballast is released from the load bar position. In addition, the load bar and associated equipment could damage the array during landing.

2) The array could replace the load bar. In this case, the balloon control equipment, normally hung from the load bar, would be distributed on the gondola. This would be the best alternative from the user standpoint, but might not be acceptable to the Holloman AFB personnel because their flight termination equipment would have to be activated through slip rings in the array mechanism. Since normal procedure is for the user and balloon control instrumentation to be independent, this subject would require further discussion with Balloon Branch personnel.

Each diode detector consists of a simple cast housing with internal insulation and a mounting bracket as shown in Figure 16. The sealed housing would enclose the diode, filter, and P.C. card with suitable insulation to keep the operating temperature in an acceptable range.

Angular orientation of the array is accomplished with a simple open loop drive capable of positioning the array in azimuth to within a few degrees of the elevation package orientation within the gondola. This accuracy is adequate because of the wide field of view of the diodes.

The tape recorder mounts directly to the array and rotates with it in azimuth. A small diameter slip ring assembly allows power for the recorder, and real time readouts from four of the diodes to be transmitted by the gondola T/M system.

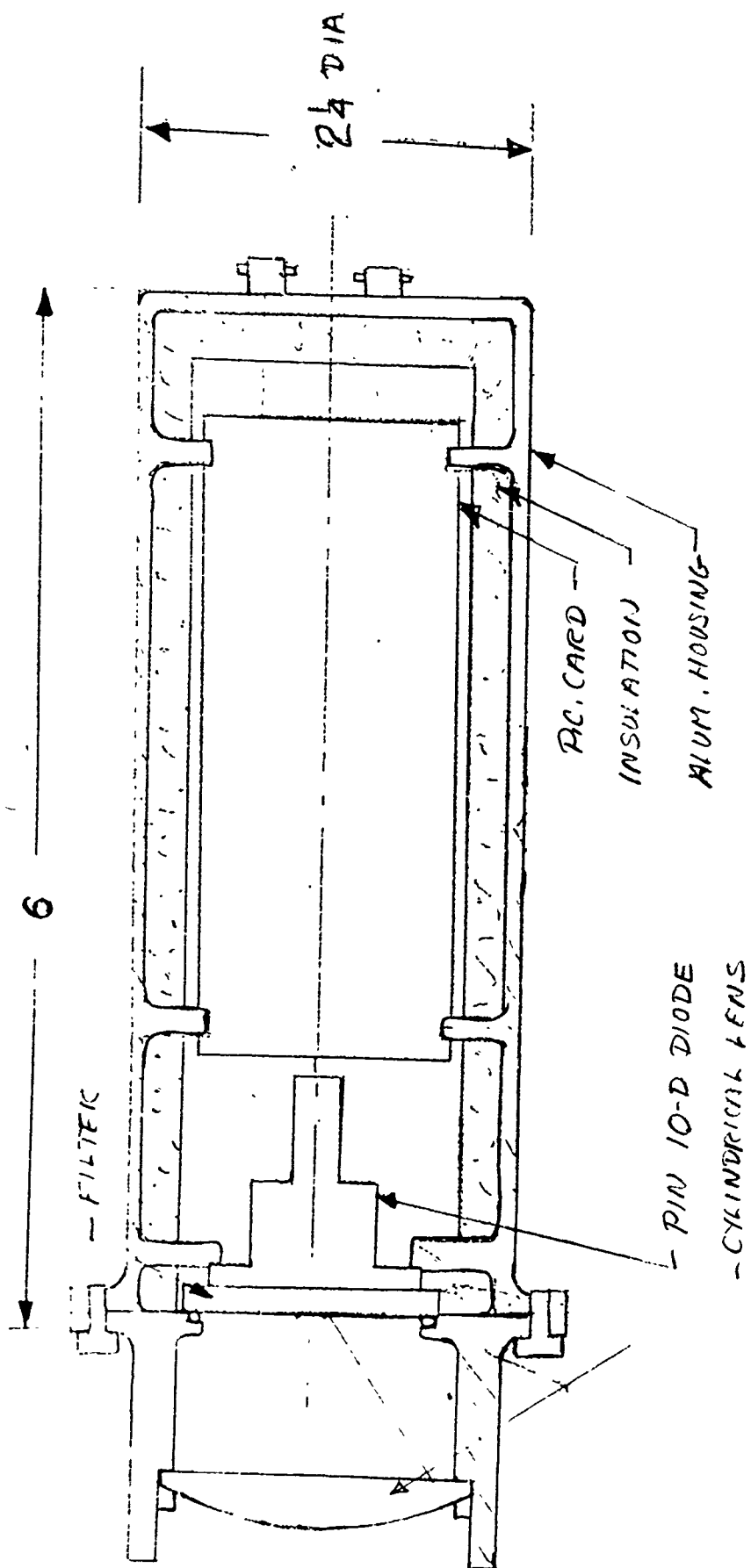


Figure 16. Diode Receiver Assembly.

6.3.2 Diode Array Electronics

The diode array is intended to analyze the laser beam intensity variations across the array surface by recording the laser power seen by each photodetector. The baseline design for the array contains 120 detectors. Each photodetector assembly contains the electronics (i.e., preamps, filters and detectors) necessary to generate a high level analog signal suitable for recording. The 120 outputs are split up into 12 channels of 10 photodiodes each. Each channel is assigned to one track of a 14 track magnetic tape recorder. The power level from each of the ten photodetectors assigned to a channel are then sequentially switched to a log amplifier and the result recorded. The other two tracks on the recorder are used for timing and test identification information.

The laser transmitter on the ground is intensity modulated at a 3 kHz rate by an electro-optical modulator. A mechanical light chopper (such as a Bulova L2C) is not used because of truncation effects. Chopping facilitates detection of the laser beam in the presence of background light.

The photodetector array is mechanically steered by a coarse servo in azimuth to follow the BAPE azimuth yoke so the array will point at the laser transmitter on the ground.

Each photodetector assembly contains a photodiode, a low noise transconductance amplifier, a 3 kHz bandpass filter, a full-wave rectifier and appropriate output filtering. This results in an output dc level proportional to the amount of light incident on the diode. Background illumination is rejected by the 3 kHz bandpass filter.

The photodiode is a United Detector Technology PIN-10D operated in the photoconductive mode. It has a 1 cm^2 active area which, as shown in Section 6.2.4, intercepts a nominal 10^{-7} watts of laser power. Assuming a 500 Hz detector bandwidth and no noise contribution by ambient light, the signal to noise ratio at the photodiode preamp output will be

about +69 dB or 2800/1. Even if the signal fades by a factor of 10 in power, the S/N ratio is still +49 dB or 280/1. This means preamp noise results in less than 0.4% measurement error.

Under worst case (daylight) background conditions, the S/N ratio would be 48.7 dB for the nominal signal power. For the recommended nighttime experiments, the effect of background light is negligible.

The preamp output goes to a 500 Hz wide bandpass filter centered at the 3 kHz modulation frequency, where most of the background signals are removed. The filtered signal is full-wave rectified and low pass filtered to a 250 Hz bandwidth. The signal is also sent through a 6 kHz notch filter to remove any remaining ripple at the second harmonic of the carrier frequency. The result is buffered and sent out of the photodetector module. A block diagram of this photodetector preamp is shown in Figure 17.

All of the photodetector electronics will be packaged along with the photodiode itself in a package about 1.5" diameter and 5" long. Each module will require about 1/2 watt of power.

Unfortunately, the responsivity of the photodetectors will change up to 5% as the ambient temperature changes. To prevent any errors due to temperature changes, a light emitting diode and diffuser is mounted in front of the array for calibration purposes. It is switched on and off at a 3 kHz rate to provide a pseudo-uniform illumination on the array so the relative responsivities of the photodiodes may be measured. The calibration signal does not remain constant with temperature, but since we are only interested in the relative responsivities of the diodes, it gives a valid calibration signal as long as the different distances of the detectors to the light source are taken into account.

Since each channel of the magnetic tape recorder is assigned to record 10 photodetector signals, an analog multiplexer is used to sequentially switch each of the 10 signals to a single logarithmic amplifier. This log amp then drives one of the tape recorder channel inputs. Thus, twelve 10 channel analog multiplexers and twelve log amps are required to record the 120 photodetector outputs on 12 recorder channels.

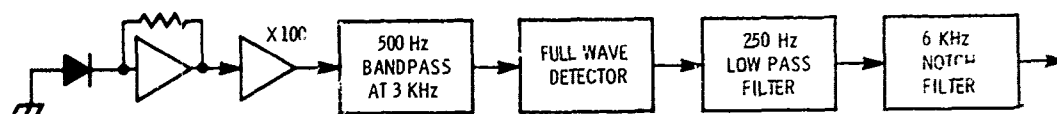


Figure 17. Photodiode Preamp Block Diagram.

The multiplexers are controlled by a divide-by-ten counter which continuously commutates each log amp input between its associated ten photodetector outputs. The commutation rate is set at 5 kHz by an oscillator. The 5 kHz rate is set by the sampling theorem which requires a sample rate of twice the signal bandwidth. Thus, for a 250 Hz signal bandwidth, each photodetector output must be sampled at a minimum rate of 500 Hz. To sample 10 outputs, each at a 500 Hz rate, requires a 5 kHz clock frequency.

The counter output is also sent to a 4 bit digital to analog (D/A) converter which puts a voltage level on channel 13 of the tape, proportional to the counter position. This makes it possible to identify which photodiode signal level is on the tape at any one time.

Channel 14 will be driven by the telemetry inputs to identify each test, time of day, or whatever may be required.

A block diagram of this on board signal processing is shown in Figure 18.

The 5 kHz clock frequency requires a recorder bandwidth of about 10 kHz in order to fully reconstruct the resultant waveform. This imposes certain requirements on the tape recorder since a minimum of 2 hours of recording time is required. Fortunately, it is possible to get recorders which can achieve a dc to 10 kHz bandwidth at 15 inches/seconds such as the Ampex AR1700. With a 14 inch reel of tape, this results in two hours of recording time. However, the signal to noise ratio on the tape is only 46 dB for the peak input signal.

The worst case range of signal amplitude variation is 40 dB, or 100 to 1. In order to get this dynamic range on the tape with a reasonable signal to noise ratio, a log amplifier is used at each channel input to compress the input signal range and thus increases the signal to noise ratio. Without using a log amp, the S/N ratio will be from 6 to 46 dB

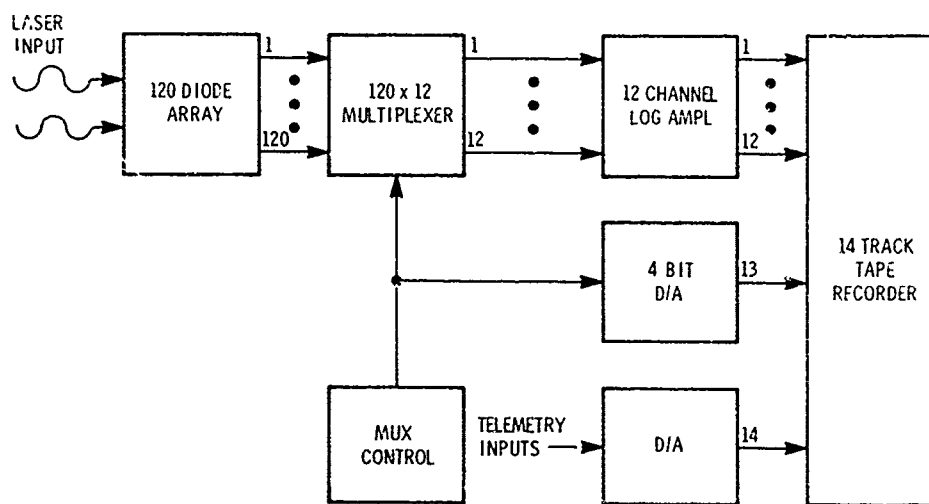


Figure 18. 120 Diode Array Signal Processing.

depending on signal strength. With the log amp, the S/N for the low level signal could be increased to 32 dB with little trouble while the high level S/N would remain at 46 dB.

The noise bandwidth at the recorder output is 10 kHz. Since the information bandwidth is only 250 Hz, it is possible to increase the S/N by up to $\frac{10 \text{ kHz}}{250 \text{ Hz}} = 40/1$, or 32 dB by computer filtering of the data points of the individual photodiode outputs to a 250 Hz bandwidth.

6.3.2.1 Power Requirements

The electronics only needs to be on for two hours during a flight since that is all the recording time there is. However, the tape recorder must be kept warm until its tape is used up, in order to prevent damage to the tape. At worst, the recorder must be kept warm for 12 hours.

In order to determine battery requirements, the electronics will be assumed on for 2 hours and the recorder heater on for 12 hours. The recorder has a 250W heater but with proper insulation of the recorder, only 100W of average heater power will be required.

Power Budget

Electronics (2 hours)

120 photodetectors @ 0.5W	60W
120 x 12 multiplexer	7W
12 log amps @ 1.5W	18W
tape recorder (Ampex AR1700)	300W
Array position control servo	<u>15W</u>
	400W
tape recorder heater (12 hours)	100W avg.
total battery power required:	
electronics 400W for 2 hours	800 watt hours
heater 100W for 12 hours	<u>1200</u> watt hours
Total	2000 watt hours

for a 24V battery:

$$\frac{2000 \text{ watt hours}}{24V} = 83 \text{ amp hours}$$

So, at least two Sonotone CA-5 batteries at 40 amp hours each are required.

Weight Budget

Estimated Electronics Weight

Photodetector ass'y. 120 @ 1 lb.	120 lbs.
Multiplexer and log amps	10
Recorder	100
Batteries 2 @ 100 lbs.	<u>200</u>
	430 lbs.

6.4 Weight Budget

Worst case weight estimates are listed below:

Diode Assemblies 120 @ 1 lb.	120 lbs.
Multiplexer and log amps	10
Recorder	100
Batteries 2 @ 100 lbs.	200
Array Mechanism and Cabling	<u>200</u>
	630 lbs.

Since the basic gondola weighs approximately 900 lbs, the total payload weight would be 1530 lbs.

6.5 Data Analysis and Interpretation

This section derives preliminary estimates of the diode array design constraints, so that its data would yield valid scintillation and spread information. Then the data analysis procedure (with the array generated data) is outlined.

6.5.1 Design Information

6.5.1.1 Diode Size

The receiving aperture for each diode is 2 cm x 2 cm. This is far smaller than any of the amplitude correlation distances (as discussed in Appendix VIII) and so each diode will act as a point detector, yielding valid scintillation results.

6.5.1.2 Diode Spacing

Because the diodes are not infinitely dense, and we always need one at the "center" of the beam, their spacing depends on the beam size. Figure 19 shows a gaussian irradiance profile as a function of r/w , for r the transverse dimension and w the e^{-2} irradiance radius. Choosing $r/w \leq .225$ insures that we are within 10% of the peak irradiance. Therefore, a spacing between diodes of $2r = .45w$ will insure that one diode is within ten percent of the peak. (Since we seek to see a minimum $C_\ell = .01$, and this corresponds to a ripple $\approx 16\%$, this spacing is adequate.)

For the $6.7 \mu\text{rad}$ ($w_0 = 6 \text{ cm}$) 6328\AA collimated beam, $w \approx 12 \text{ cm}$ at a range of 30 km, neglecting beam spread as seen in Figure 20. Taking this as our minimum spot size on the array, diode spacing $2r = 5.4 \text{ cm}$. We therefore set the center-to-center diode spacing at 5 cm.

6.5.1.3 Array Size/Diode Number

There are two criteria for determining the necessary size of the array:

- (a) The extent of the random motion of the spot.
- (b) The length of time needed to obtain a valid scintillation statistic.

We can calculate the cumulative probability that the center of the beam will remain on a given size array by utilizing the formulation of Appendix III. The result is

$$\text{Prob } (\rho \leq \rho_0) = 1 - \exp \left\{ \frac{-\rho_0^2}{\theta_{\text{rms}}^2 Z^2} \right\} \quad (6-3)$$

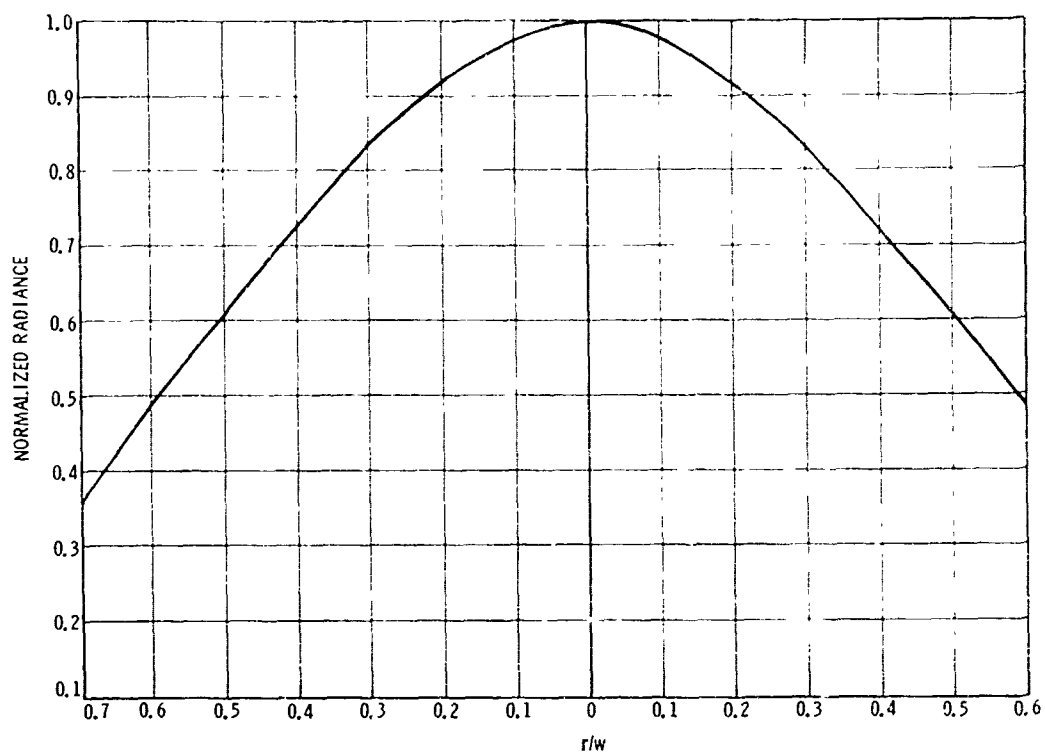


Figure 19. Gaussian Irradiance Profile.

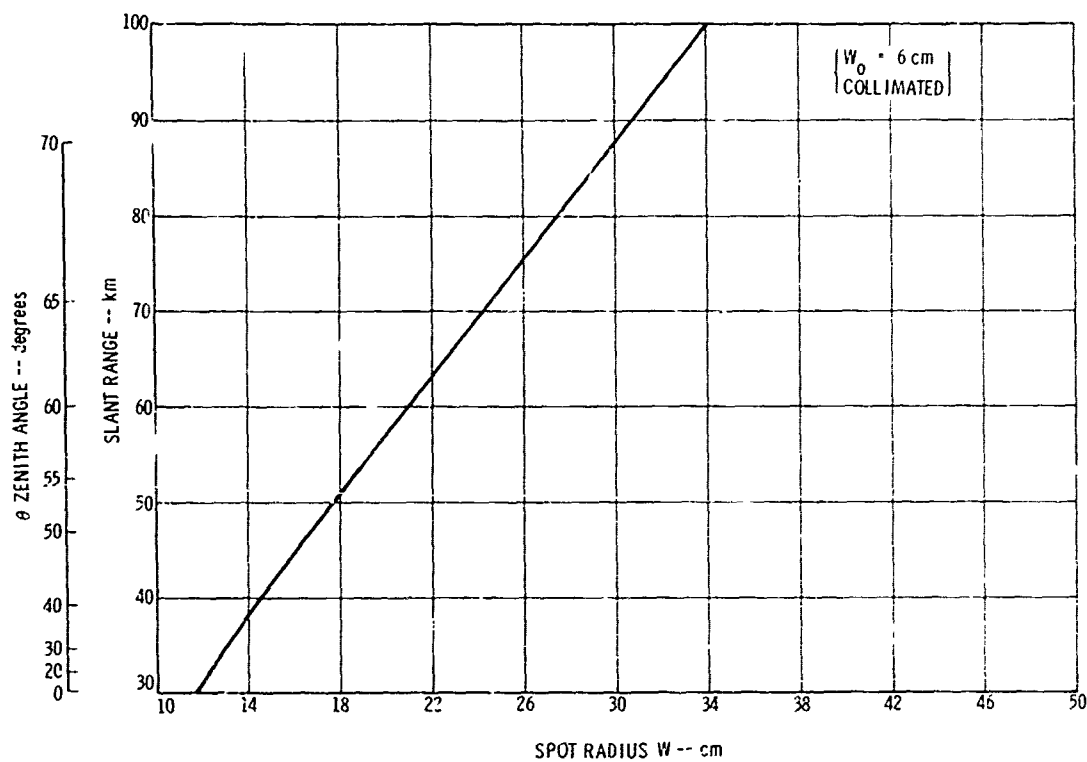


Figure 20. Beam Size at Balloon Receivers.

for ρ = distance from array center to beam center
 ρ_o = radius of (assumed circular) array
 Z = range from transmitter to array
 θ_{rms} = rms angular beam motion due to all effects.

This probability is plotted versus range (and zenith angle for a receiver altitude of 30 km) with ρ_o as a parameter in the next two figures. Figure 21 has $\theta_{rms} = 15 \mu\text{rad}$ and Figure 22 has $\theta_{rms} = 25 \mu\text{rad}$.

Based on these figures, it appears that a circular array with radius $\rho_o = 50$ cm will be sufficient over most ranges for the 15 μrad case, i.e., a prob $\geq 25\%$ is present out to a zenith angle of $\sim 62^\circ$.

For 30 seconds of data, therefore, a 2 minute data gathering period would be sufficient.

It takes approximately 240 diodes to fill this array, for 5 cm spacing. The baseline design discussed previously is easily extended to this regime, still using a single tape recorder, and post-detection processing will insure that the average SNR of 40 dB is maintained over the two hour recording period. Alternatively, we could use a smaller array (120 diodes) and take a longer time to collect the data. (The tradeoffs between these two approaches were still being formulated when we were directed to abandon this technique in favor of the Reciprocity Tracking approach of Section VII.)

6.5.2 Data Analysis

Given the data collected by the array, Figure 23 shows the data analysis flow, resulting in all the spread and scintillation parameters needed for SDR high data rate uplink design.

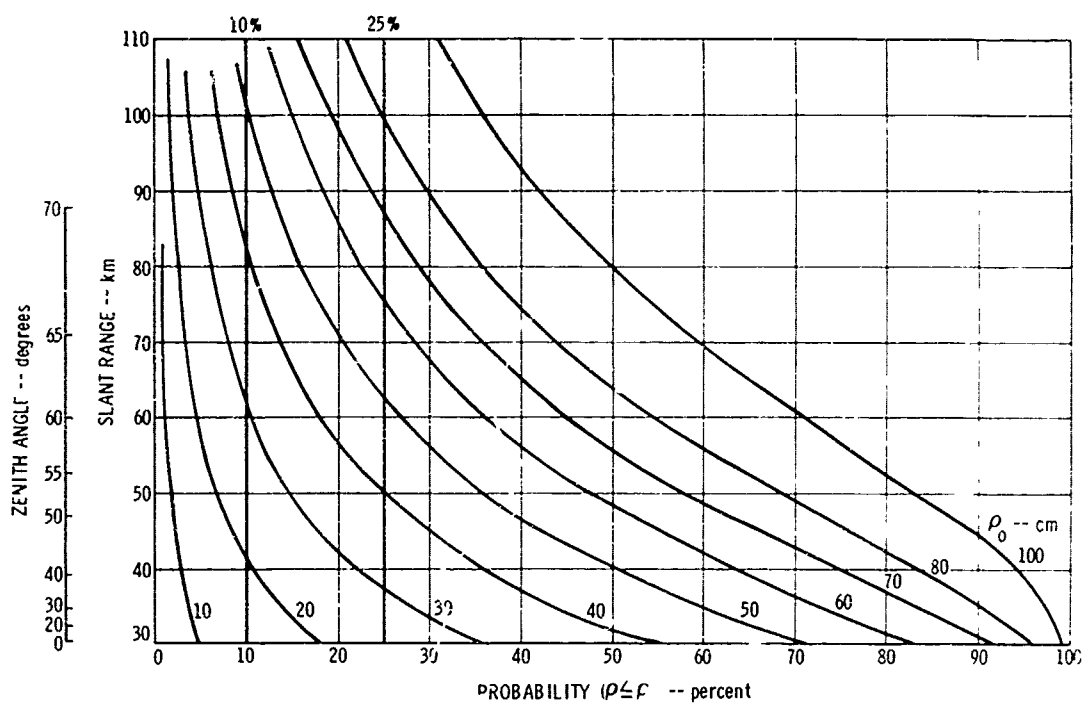


Figure 21. Probability of Beam Remaining on the Diode
Array: Angular Jitter = 15 μ rad.

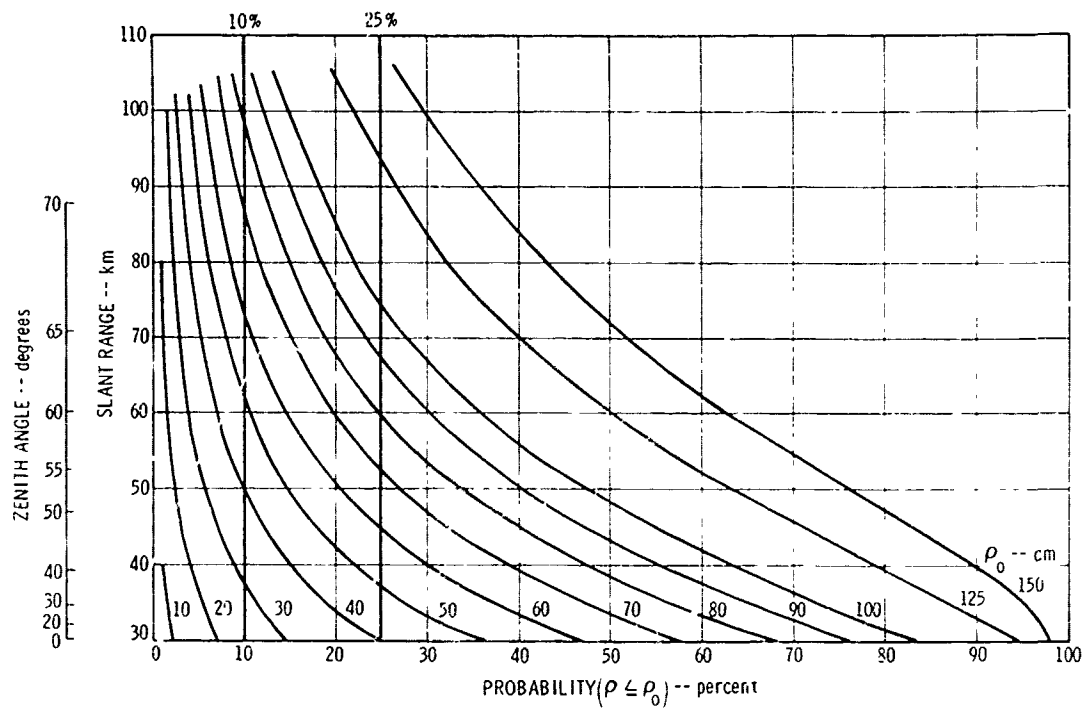


Figure 22. Probability of Beam Remaining on the Diode Array: Angular Jitter = 25 μ rad.

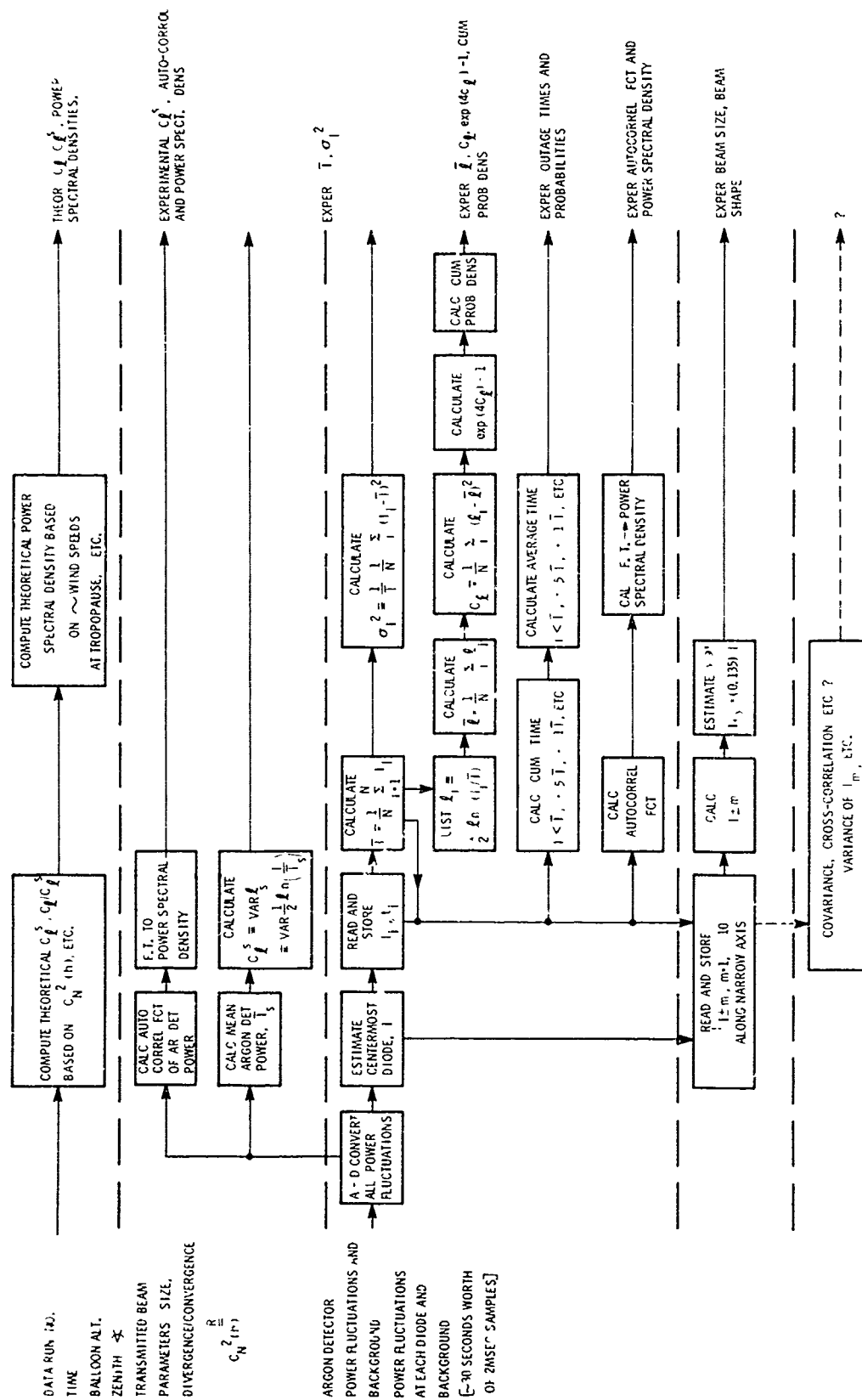


Figure 23. Data Analysis Flow: Large Diode Array.

6.6 Estimated Costs

The diode array involves large costs that arise in none of the other techniques considered for two principal reasons:

- (a) The large number of optical receivers required.
- (b) The on-board tape recorder, such as the Ampex AR1700.

We provided the following budgetary estimates to the Air Force on July 17, 1972, for the equipment modification and systems integration and test phases.

Balloon System

Repair and Refurbishment	}	\$ 40K
Range Extension		
Diode Array (120 diodes)		\$165K
Ground System, including Integration and		\$175K
Test, and Turbulence Sensors		
	Total	<hr/> \$380K

Balloon System

Placing Finely Pointed Laser Aboard (to	\$ 60K
the limit of the present servo equipment)	

The diode array costs include \$75K of materials. Additional diodes could be added at a price of ~\$200 each, in batches of 120.

Section VII

DESCRIPTION OF THE RECIPROCITY TRACKER TECHNIQUE

7.1 Introduction

The reciprocity tracker technique, although not feasible in the MAY/JUNE 1973 time scale because of technical, schedule and cost problems, is now described as we conceive it for MAY/JUNE '74 experiments.

Because of the short duration of this study, the bulk of the system analysis was devoted to the diode array approach (Section VII), which was feasible from a technical and schedule viewpoint for limited experiments next summer.

Therefore, the following sections present a brief description of the reciprocity tracker approach.

7.1.1 Reciprocity Tracker Experimental Configuration

The experiment will look very much like the BAPE configuration of Figure 3 (Section 3.4) except for two changes:

- 1) The ground station mount may not be the ATLAS.
- 2) The balloon system will include a finely pointed HeNe laser, and a small array of receivers mounted on the elevation axis.

These points are discussed in the following sections.

7.2 Reciprocity Tracker Transmitter

Figure 24 shows a schematic of a possible refractive reciprocity tracker system. (The final design, however, may use a Cassegrain telescope.) The primary feature of the system is the common path of the received and transmitted beams. The secondary controlled beam steering mirror derives error signals from the star tracker when the received light from the balloon borne HeNe laser deviates from the optical axis of the telescope. Since the mirror is driven to produce a null error signal at the

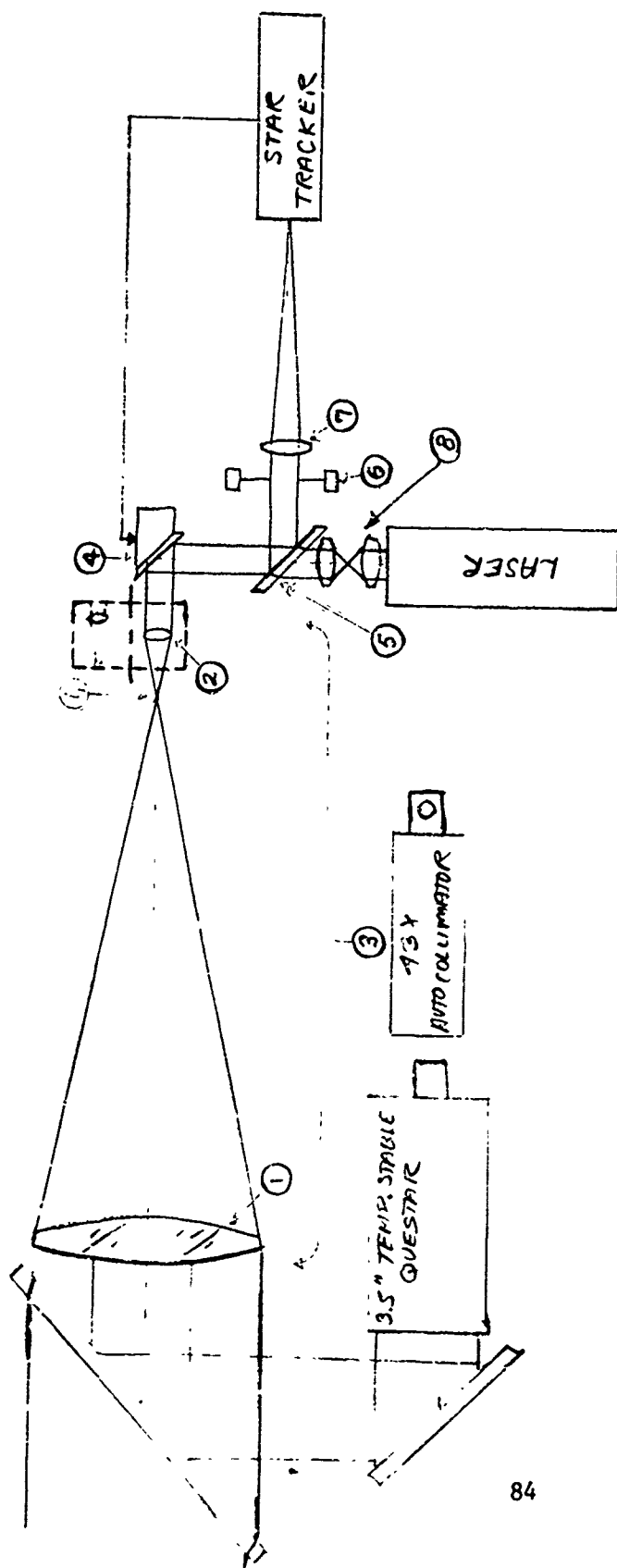


Figure 24. Refractive Reciprocity
Ground Transmitter/Receiver.

1. Objective Lens Group
2. Eyepiece Turret
3. Telescope
4. Beam Steering Mirror
5. Dichroic Beamsplitter
6. Aperture Stop
7. Tracker Lens
8. Focussing Optics

star tracker, an off-axis downlink beam will cause the uplink beam to be directed back along the path of the downlink beam. This will occur independently of whether the off-axis condition was caused by atmospheric image dancing or random motions of the mount. By changing the magnifications of the telescope, the transmitted beam waist can be varied while still retaining the tracking action. Uplink focussing or defocussing is accomplished before the dichroic beamsplitter so that the receiver optical path is not affected.

The iris can be set larger or smaller than the e^{-2} diameter of the laser beam and insures that the effective aperture of the received beam "matches" the exit aperture of the transmitted beam. A two-axis piezoelectrically driven mirror called the IMC (Image Motion Compensator)⁽¹⁶⁾ has been considered because it appears suited to the OPTS application and may be available at no cost. The device has an angular throw of $\pm 2.5^\circ$ and a resonant frequency (mirror plus mounting) of 100 Hz. An angular deviation of 2.5° (43.5 mrad) at the beam steerer would correspond to 362 μ rad at the exit aperture of a 120 power telescope.⁽¹⁷⁾ Since, for any reasonably accurate mount the mount motions will not exceed 100 μ rad, the angular throw of the IMC will be adequate. Since the ATLAS mount exhibited no significant vibrations with frequencies of greater than 20 Hz (as seen in Appendix XI), the resonant frequency is also adequate.

Isolation of the uplink and downlink beams could be achieved by using different wavelengths, but the uplink laser has not been selected. He-Cd, doubled YAG and Argon are being considered. The fieldable Argon lasers are too bulky, and the doubled YAG lasers have less amplitude stability than would be desirable for the scintillation measurements. A likely solution would be modification of RCA's He-Cd lab laser⁽¹⁸⁾ for field use.

7.2.1 Accuracy Considerations

Because the turbulence theory is not tractable for beams of arbitrary characteristics, this experiment will use TEM₀₀ beams, diffraction limited optics, and as little truncation or blockage as is practical.

The critical accuracy considerations from a mechanical standpoint are the telescope construction, the alignment mechanisms, and the mounting techniques as discussed in Section VI. With the reciprocity tracker system, however, there is the added constraint that the receiver and transmitter optical paths must be collinear to within 10% of their beamwidths.

7.3 Balloon-borne Receiver

The receiver equipment needed for the reciprocity system is slightly more complex than the existing BAPE equipment and significantly less complex and costly than the array of receivers needed for the diode array system. The BAPE equipment only used one detector for the scintillation variance measurements (although two separable detectors were used for the covariance measurements), because the mount tracking inaccuracies were insignificant relative to the 1 mrad uplink beam divergence. In contrast, the diode array approach required a matrix of 120 diodes because beams of approximately 10 μ rad divergence were to be transmitted with no compensation for mount or beam wander motions. Because the reciprocity system tracks out all mount motion and a significant part of the atmospheric beam wander, only a small matrix of diodes, which can be conveniently located in the elevation axis package, is needed.

The number of these detectors needed has not been firmly established, but will be ≈ 10 . If 10 are needed, the data could be telemetered (real time) to the ground station with only minor modifications of the existing telemetry equipment. If, for example, 20 diodes are used, five 5 kHz data channels would be required and more extensive telemetry modifications could be required. In this case, it may be more practical to just transmit four symmetrically placed diode power levels to assist the operator in tracking the balloon and use a magnetic tape recorder to record the power levels from the rest of the diode array. Since there is so much less data to record compared to the large diode array system (Section 6.3), the recorder required would be smaller, lighter and less power consuming than that

used with the 120 diode array. A typical recorder which meets these reduced requirements is the Leach MTR-3200. Comparing specifications with the Ampex AR1700:

	<u>AR1700</u>	<u>MTR-3200</u>
# tracks	14	14
# feet of tape	9600	2400
size	1.85 ft ³	0.95 ft ³
weight	100 lb.	54 lb.
power consumption	300W	70W
avg. heater pwr. req'd	100W	25W
bandwidth	10 kHz @ 15 ips	2.5 kHz @ 3-3/4 ips
record time	2 hr.	2 hr.
S/N	46 dB	38 dB

(38 lb corresponds to a voltage SNR of 80/1, which insures far better than the 5% accuracy required.)

No servo is required to make the array track the ground transmitter since it is mounted directly to the balloon laser transmitter and so will always be pointed towards the ground transmitter.

Now, instead of ten photodetector outputs being assigned to one recorder channel, only two are required. This reduces the multiplexer clock frequency to 1 kHz and thus the recorder bandwidth required is reduced to 2 kHz.

The new power requirements are:

20 diode array @ 1/2W	10W
20 x 10 multiplexer	5W
10 log amps @ 1.5W	15W
tape recorder	<u>70W</u>
	100W
recorder heater	25W
Battery power required:	
electronics 2 hr x 100W	200
recorder heater 12 hr x 25W	<u>300</u>
	500 watt-hours

One Sonotone CA-20 battery is good for 600 watt hours and would satisfy our requirements nicely.

Electronics Weight

Photodetector array 20 x 1 lb	20 lb
multiplexer and log amps	10
recorder	60
battery	<u>50</u>
	140 lb

Because of the complexity and cost of the recorder system, real time telemetry transmission of the data would be desirable. The final selection between the two approaches will depend upon the required number of diodes.

7.4 Star Tracker Analysis

Because of the tight schedule and the requirement for a field-able reciprocity tracker transmitter, proven and environmentally qualified components have been used whenever possible. Since the star tracker is a particularly critical component of the reciprocity tracker, discussions were held with ITT, San Fernando to determine if they had an existing and proven design which could be easily adapted to the OPTS application. Although specific details were not available from ITT, they felt that the irradiance level at the star tracker, error signal bandwidth and accuracy requirements for the OPTS application were compatible with their ODC star tracker system.

To gain additional assurance that the required tracking accuracy could be achieved, an estimate of the noise-free tracking accuracy was made. The receiver portion of the reciprocity tracker is shown schematically in Figure 25.

The displacement of the image in the focal plane of lens A is given by

$$\Delta x \approx \frac{f_1}{f_2} f_3 \Delta \theta = M f_3 \Delta \theta \quad (7-1)$$

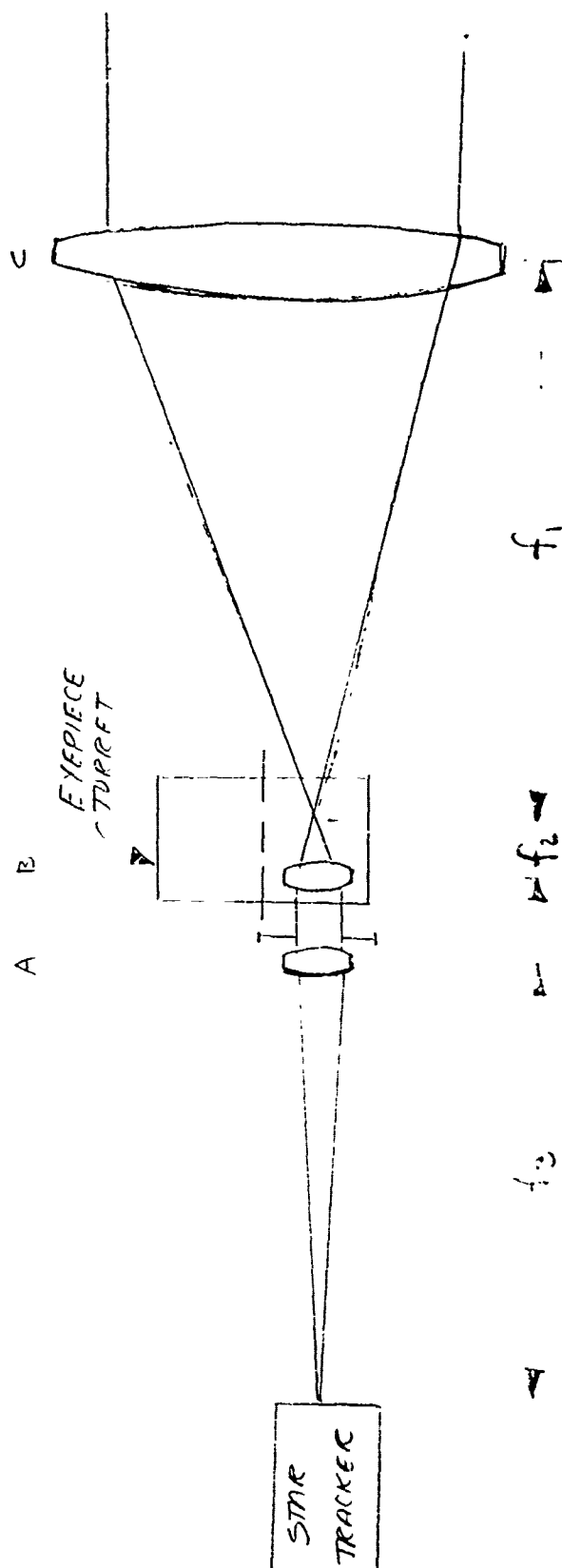


Figure 25. Diagram of the Receiver Portion of the Reciprocity Tracker.

where $\Delta\theta$ = angular deflection at lens C
 M = magnification

In typical star tracker applications, the instantaneous aperture should be three times the image size and a motion of 1% of the aperture can be sensed. The minimum detectable wave front tilt is then given by

$$\Delta\theta = \frac{(.01) 3d}{M f_3} \quad (7-2)$$

where $d = \frac{2.4\lambda}{D_3} f_3$ = diffraction spot size

and D_3 = stop size at lens A \approx 1 mm.

The following expression, in which $\Delta\theta$ is independent of f_3 , holds for the case under consideration

$$\Delta\theta = \frac{(.01) (3) (2.4) (.63 \times 10^{-4})}{M \times 10^{-1}} = \frac{4.5 \times 10^{-5}}{M}$$

Thus, for $M = 120^*$, $\Delta\theta = 0.38 \text{ } \mu\text{rad}$

and for $M = 16$, $\Delta\theta = 2.8 \text{ } \mu\text{rad}$

This analysis indicates, therefore, that adequate pointing accuracies should be achievable with the proposed star tracker and optical system.

* 120 power corresponds to a 6.7 μrad collimated beam width and 16 power corresponds to a 25 μrad collimated beam width.

7.5 Data Interpretation and Analysis

As discussed in Section 7.3, one balloon receiver will be collinear with the He-Ne balloon transmitter. Other receivers (their number is still to be determined) will be offset, so that information on the average beam profile will also be gathered.

The center or collinear receiver will be detecting power fluctuations identical in character to those that would be present at a satellite receiver. This, therefore, suggests two worthwhile approaches to the data analysis: First, using the raw data to construct the statistical quantities of interest. and, second, testing our theories with the data.

7.5.1 Raw Data Manipulation and Analysis

Approximately 30 seconds of raw data (power fluctuation) are needed to construct valid signal statistics⁽¹⁹⁾. Once the transmitter parameters are fixed (wavefront curvature and beam radius), it should take only 30 seconds to gather the data because the transmitted beam is always pointed at the balloon receiver.

Therefore, approximately 40 separate transmitter settings should be performed over an hours time.

Consider one 30 second run for the centermost receiver.

Using the instantaneous intensity, I_i , from each 2 millisecond piece of that 30 seconds (15,000 samples) we construct the mean,

$$\bar{I} = \frac{1}{N} \sum_{i=1}^N I_i \quad (7-3)$$

the second moment,
$$\overline{I^2} = \frac{1}{N} \sum_{i=1}^N I_i^2 \quad (7-4)$$

the variance,
$$\sigma_I^2 = \overline{I^2} - \bar{I}^2 \quad (7-5)$$

the normalized variance, $\frac{\sigma_I^2}{\bar{I}^2} = \frac{\sigma_I^2}{\bar{I}^2}$ (7-6)

the third moment, $\bar{I}^3 = \frac{1}{N} \sum_i I_i^3$ (7-7)

and the cumulative probability, $\text{Prob} (I < I_a)$

Using the analog data (intensity as a function of time), we construct:

the autocorrelation function, $A(\tau) = \frac{1}{T} \int_0^T I(t) I(t-\tau) dt$ (7-8)

for $T = 30$ seconds,

the power spectral density, $P(\omega) = \text{fourier transform of } A(\tau)$,

the probability of outage, i.e., average times between $I < I_a$
for $I_a = .1 \bar{I}, .3 \bar{I}, \text{ etc.}$

Using the data from the other receivers we construct:

Average irradiance Profile

Average e^{-2} Point

Using the data gathered from the thermosondes, we construct the turbulence profile, $C_N^2(h)$, corresponding to each of the optical measurement times.

Given all the analyzed data, we shall have an excellent prediction of the uplink results to the satellite if the satellite experiment were performed at the same site, with the same turbulence conditions and with the same transmitter configuration. In order to predict the uplink behavior for other conditions, we must interpret the experimental results in terms of a theory.

7.5.2 Data Interpretation

Based on the theory presented in the appendices, we can predict: the mean, variance, cumulative probability, etc for power fluctuations caused by scintillation at beam center; the mean, variance, cumulative probability, etc for power fluctuations caused by beam wander; the mean and variance of the power fluctuations caused by the combination of wander and scintillation for a very large, untruncated and unobstructed transmitted beam, with no beam spread.

However, the OPTS experiment involves a detector that senses power fluctuations caused by scintillation and wander simultaneously, i.e., whatever wander remains after reciprocity tracking is used. It also involves an $\sim 10''$ transmitter, which is not "very large" in turbulence terms, and which does slightly truncate the beam. In addition, the transmitter may have a center blockage. Of course, the beam is also going to spread.

Therefore, in order to interpret the data we must extend the theory in two areas:

- (1) Remove all the assumptions of Appendix V, so that we can predict the mean and variance of the detected power fluctuations for arbitrary apertures and with beam spreading included.
- (2) Extend the analysis of Appendix IV, so that we can predict the probability distribution for the detected power fluctuations.

Given these results we will be able to interpret the raw data and predict the important results (Probability of Bit Error and/or Outage) for any conditions on the uplink.

Of course, this statement assumes that the extended theory will be correct, and that reciprocity tracking and the degree of alleviation of beam wander will fit within this theory. We believe that both of these assumptions are sound because of previous experimental checks of the present theory, and the fact that we can separately treat the scintillation alone, and combined wander and scintillation, as presented in Appendices II and V.

As a further aid to our data interpretation, we will use the following additional facts:

- (a) Scintillation power fluctuations extend to much higher frequencies than those caused by beam wander⁽¹⁹⁾.
- (b) The moments of the power fluctuations caused by the two effects behave far differently, i.e., using the probability distributions listed in Appendix IV, we find the results listed below:

	<u>Wander Alone</u>	<u>Scintillation Alone</u>
\bar{I}	$\frac{I_o}{1+2\alpha}$	I_o
$\frac{\bar{I}^2}{I^2}$	$\frac{I_o^2}{1+4\alpha}$	$I_o^2 e^{4C_\ell}$
$\frac{\bar{I}^3}{I^3}$	$\frac{I_o^3}{1+6\alpha}$	$I_o^3 e^{12C_\ell}$
\vdots	\vdots	\vdots
$\frac{\bar{I}^n}{I^n}$	$\frac{I_o^n}{1+2n\alpha}$	$I_o^n e^{2n(n-1)C_\ell}$

for I_o = intensity at the center of the beam

for α = wander parameter = $\frac{\bar{p}^2}{w^2}$

\bar{p}^2 = mean square displacement of beam center

w = e^{-2} irradiance radius

and C_ℓ = variance of the log of the amplitude fluctuations caused by scintillation.

The higher moments of a combined distribution will be dominated by scintillation, since $\exp [2 n(n-1)C_\ell] / (1+2n\alpha)^{-1}$ is much greater than unity for realistic values of C_ℓ and α .

(c) We will also derive various combined wander and scintillation probability densities, based on the approach summarized in Appendix IV, and compare them to the experimental data to obtain best fits.

It therefore is possible to derive techniques that will separate and identify the effects of scintillation and wander, and enable us to predict the uplink effects at any site (given its $C_N^2(h)$ distribution) from the OPTS results.

Section VIII

EXPERIMENTAL PLAN, PROGRAM SCHEDULE AND ESTIMATED COSTS

8.1 Introduction

This section first discusses how the MAY/JUNE 1974 experiments would be performed, using the reciprocity tracker system discussed in Section VII. Then a program schedule is presented, which will take us from the completion of this study through data analysis of the experimental results. Finally, the estimated costs of the remainder of the program are given in Section 8.4, except for the modifications to the ground transceiver, which still have to be defined.

8.2 Experimental Plan

This plan assumes that the program schedule described in the next section has been implemented, i.e., there has been a period of system integration and test which includes both the balloon and ground packages, and that a data analysis program will have begun at least four months before the flight experiments.

Based on the analyses summarized in Section IV, and the system parameters cited in Section VII, Appendix II, Section II.4 and Appendix V, Section V.4, the following parameters will be varied during the experiments, in order to test our predictions:

A) e^{-2} radius w will be varied from 1.61 cm to 4.03 cm to 6 cm, corresponding to 25 μ rad, 10 μ rad and 6.7 μ rad collimated beam sizes;

B) Focusing parameter R , for each of the beam sizes above, will be varied as follows:

$$10^4 \text{ m} \leq |R| \leq 10^5 \text{ m, for } R < 0, \text{ focusing}$$

$$R = \infty \text{ collimated}$$

$$R = 5 \times 10^4 \text{ m, for } R > 0, \text{ defocussing.}$$

- C) Receiver aperture size, from ~10" (25.4 cm) diameter down to a value still to be determined.

The experimental procedure involves simultaneous measurements of optical and meteorological results, so that it can be considered as two parallel efforts.

8.2.1 Optical Measurements Procedure

A) Balloon system, ground system and all subsidiary gear is thoroughly checked out.

B) Balloon System Launched, and achieves float altitude.

C) Acquisition and Lock-up performed ground-to-balloon-to-ground.

D) SYSTEM CALIBRATION, including telemetry.

E) INITIATE DATA TAKING

SELECT SIZE, 2w

SELECT FOCAL PARAMETER, R.

CHANGE FOCAL PARAMETER, R.

CHANGE FOCAL PARAMETER, R.

F) Vary aperture size until minimum power fluctuations are achieved.

.	.	.	.
.	.	.	.
.	.	.	.

G) Repeat E, F

H) Repeat E, F

.	.
.	.
.	.

K) Repeat E, F

.	.	.
.	.	.
.	.	.

- N) TURN OFF BALLOON SYSTEM, AFTER 1 HR DATA TAKING.
- O) PERFORM "REAL TIME" DATA ANALYSIS, TO DETERMINE VARIANCE OF DETECTED POWER FLUCTUATIONS.
- P) RE-INITIATE DATA TAKING, REPEATING STEPS E, F, etc.
- . . .
- . . .
- . . .
- X) RETURN BALLOON SYSTEM TO EARTH.
- Y) RECOVER AND REPAIR FOR NEXT FLIGHT.
- Z) TRANSMIT DATA TO GTE SYLVANIA FOR DETAILED DATA ANALYSIS, PRECEEDING NEXT FLIGHT.
- REPEAT FOR FIVE (5) FLIGHTS.

8.2.2 Turbulence Measurements Procedure

- A) Thermosonde System, receiver systems are checked out and calibrated.
- B) As acquisition and lock-up is performed on the optical system, launch high altitude thermosonde.
- C) Launch low altitude thermosonde every 10 minutes until optical data taking is complete.
- D) Repeat B, C for each 1 hr segment of optical data.
- E) Recover and repair all low altitude thermosondes for next flight (also high altitude thermosonde if feasible).
- F) Transmit data to GTE Sylvania for detailed data analysis, preceeding next flight.

8.2.3 "Log-Book" Procedure

During each data run, the following parameters will be recorded:

- Beam Radius, w
- Beam Curvature, R
- Time of Day
- Zenith Angle
- Range to Balloon

Turbulence Distribution
Downlink Angle of Arrival Spectra
Power Fluctuations at the Balloon Receiver(s)
Estimated Real Time Variance
Synoptic Conditions
Relative Transmit/Receive Aperture Size.

It is to be expected that for the first flight, all the parameters will be varied, while during succeeding flights, the experiments will narrow down to the most interesting areas, i.e.

- (a) Determining the exact R (for a given w) at which the power fluctuations are minimized.
- (b) Determining the best relative transmit/receive aperture sizes so that most of the wander effects are tracked out.
- (c) Determining the parameter dependence of beam spread.

8.3 Program Schedule

The overall program schedule, enabling the field experiments described above to be performed in May/June 1974, is shown in Figure 26.

8.3.1 Experiment Planning and Design

This is the Final Report of the Experimental Planning and Design portion of OPTS.

8.3.2 Reciprocity Tracker Implementation Design Program

The Reciprocity Tracker Implementation Design Program proceeds from the present status to a point enabling us to build the hardware. It involves the following tasks:

- I. Evaluate compatibility of OPTS requirements with the Acq/Trk Brassboard System, and design the reciprocity transmitter system.

Sub-Tasks include:

- A. Investigate suitability of Cloudcroft facility for ground station. Present advantages and disadvantages of using Cloudcroft ground station as compared to NASA ground station. Cost, technical, and logistical factors will be considered.

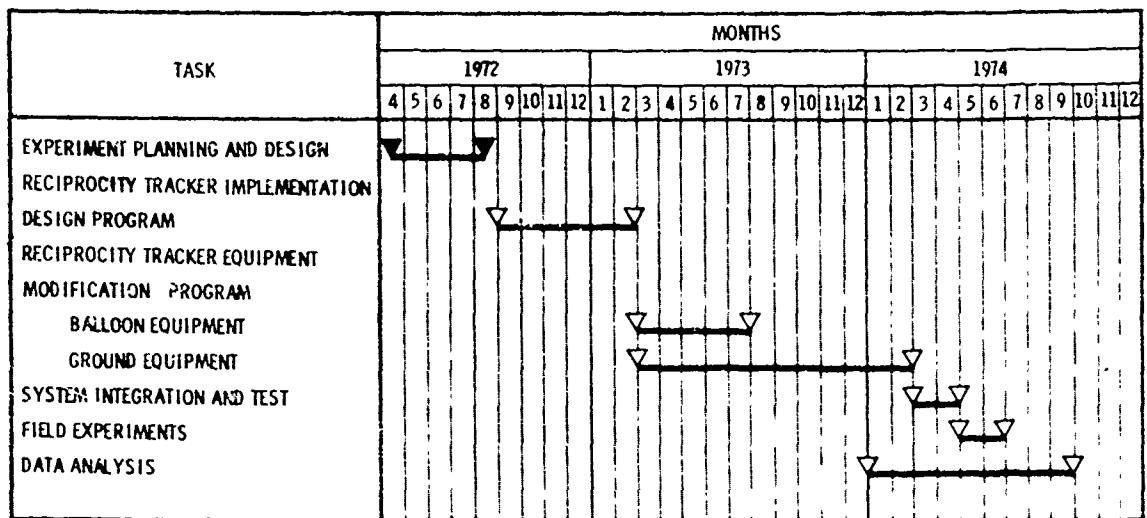


Figure 26. OPTS Program Plan.

B. Estimate the Power Fluctuations caused by combined Wander and Scintillation for Arbitrary Transmitter Size and Aperture Character: This task will determine the predicted effects of truncation, center blockage, etc. in addition to the combined wander and scintillation effects. It will determine whether refractive or reflective optics should be used, the size optics needed, and how to interpret the resultant data for other optical systems.

C. Perform the Design of the Transmitter System, including design techniques to implement the unique OPTS aspects of modifications to the Acq/Trk brassboard, including variable apertures, variable focussing, λ changes and mounting on a suitable ground station.

II. Design modifications to balloon package which are required for the reciprocity system, but were not covered in the diode array approach, (i.e., laser selection, small receiver array on elevation axis, wavelength changes).

III. Program and Experimental Planning, including:

A. Identification of Experimental Systems and Support Needed: This task will identify the equipment and personnel needed to do the job. For example, if the Cloudcroft site is selected, we would still require the NASA T/M system to command, control and receive data from the balloon system. Other items which may be required include tape recorders, a stable optical table, extra power, etc.

B. This task will present the program plan for the Reciprocity Tracker experiment, and specify the costs of the rest of the program.

IV. Calculations of the Probability of Bit Error and Outages for Combined Wander and Scintillation.

This task will evaluate the formulation presented in the OPTS report, and enable us to set the design limits on the link. We presently know, for example, that for scintillation alone, $C_{\ell} \leq 0.01$ is required for a fixed threshold, while for wander alone $\alpha \leq .1$. This task will specify the trade-offs between C_{ℓ} and α , with a minimum outage and/or probability of bit error as the criterion, and using adaptive thresholds.

V. Final Report

A final report will be written, summarizing the results of all the tasks.

A detailed program schedule for this program is shown in Figure 27.

8.3.3 Reciprocity Tracker Equipment Modification Program

The Reciprocity Tracker Equipment Modification Program has two aspects: the balloon platform work and the ground station work. The balloon platform portion can be performed in a shorter period, and at any appropriate time between 3/73 and 3/74. The ground station portion will receive further definition during the Reciprocity Tracker Implementation Design Program with regard to both schedule and cost.

8.3.4 System Integration and Tests

The system Integration and Test Program involves the ground station and balloon platform in overall system tests.

8.3.5 Field Experiments

Assuming that Holloman Air Force Base is the launch site, the balloon flights should run from mid-May through June, 1974. Five flights should be adequate to obtain the data needed.

Real-time data analysis of the variance of the intensity fluctuations recorded at the balloon should ensure that all the experimental gear is operating correctly during the flights.

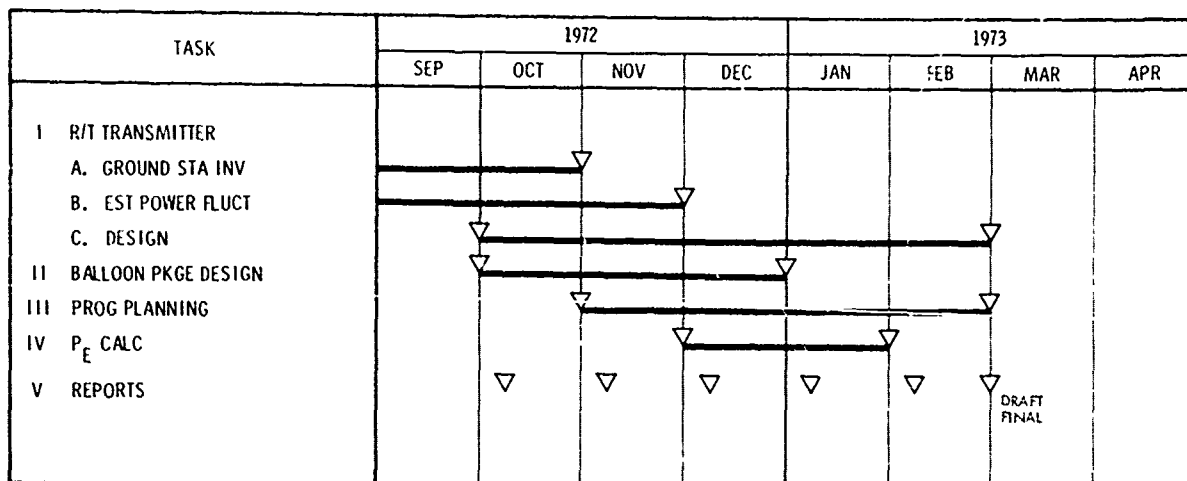


Figure 27. Reciprocity Tracker Implementation Design Program.

8.3.6 Data Analysis

Development of the detailed data analysis techniques should start during the equipment modification, so that by the time the experiments are run, the data tapes can be immediately analyzed. This will ensure that all the experiments are optimally performed, and all propagation effects well understood.

This phase ends the overall program with a definitive report, stating whether transmitter aperture averaging works, the effects of focusing/defocusing, the magnitude of the beam spread, the magnitude and character of beam wander, whether reciprocity holds, and the frequency spectrum and magnitude of the angle of arrival fluctuations. The feasibility and requirements for a high data rate uplink will then be determined.

8.4 Estimated Costs

The following are future program costs, to the extent that they are identified now. All but those for the Reciprocity/Tracker Implementation Design Program should be considered as budgetary.

R/T Implementation Design Program	\$ 60,000
R/T Equipment Modification	
Balloon System Portion	\$125,000*
Ground System Portion	Not Available
System Integration and Test	\$ 20,000
Field Experiments	
AFCRL Balloon Launch Costs	\$ 56,000
GTE Sylvania Field Support	\$ 40,000
Data Analysis	\$ 50,000

The balloon system portion has an * following it to indicate that this estimate will take the present balloon system and improve it to the limit of its present servo design, as discussed in Appendix XIII.

If NASA funds improvements or relevant modifications, this cost would be less than the number given. If the R/T Implementation Design Program finds that a more accurate servo system is needed, these costs could be greater than the number given.

The ground system portion costs are not available because they are a key output of the R/T Implementation Design Program, and depend on the mount used and the results of the Acq/Trk Brassboard program to a large degree.

Section IX

EFFECTS ON A HIGH DATA RATE LASER COMMUNICATION LINK

9.1 Introduction

The purpose of the total OPTS program is to determine the system design best suited to make the effects of the turbulent atmosphere negligible on a high data rate communication link. Based on the analysis performed during this study portion of OPTS, we can indicate some changes that ought to occur in a baseline design as previously completed.⁽¹⁾ Definitive statements about the final design must await the OPTS experiments and data analysis.

Our analysis indicates no changes are needed in the High Data Rate or Beacon downlink designs. However, it does suggest some significant changes be implemented in the High Data Rate and Beacon uplink designs. These changes involve both the schedule, and the design constraints.

The chief impact on the schedule is that results from the experimental OPTS work will not be available until June, 1974. Therefore, a final design cannot be initiated prior to then.

We will consider the design changes on the high data rate and beacon transmitters separately.

9.2 High Data Rate Uplink

As presented in Reference 1 (Volume III, p A-34), the high data rate ground based transmitter (Package A) had the following characteristics:

Modulation Format = PGBM

$\lambda = 5320\text{\AA}$

$P_o = 250$ mwatts

Beam Divergence = 5.4 μ rad

Average Received Photoelectrons/Bit = 156

Margin = 5.76 dB

Because the tropopause was neglected, it was erroneously predicted that $C_\ell \approx 0.001$ for the uplink beam.

Common receive/transmit optics were assumed, and reciprocity tracking to within 1 μ rad, so that $\alpha = 0.137$ for a 5.4 μ rad collimated beam.

However, since a 30 cm diameter receiver was utilized, and the e^{-2} diameter of the collimated 5.4 μ rad beam is only 12.54 cm, it was assumed that the beam will be defocussed to fill the aperture.

For negligible truncation (beam diameter ≈ 15 cm), we extend the analysis of Appendix V⁽²⁰⁾ and find the wander parameter is reduced to $\alpha \approx 0.002$, which means the wander is negligible.

This design must be changed because such a defocused beam will have a scintillation parameter $C_\ell > 0.1$, as seen in Appendix II.

Therefore, the common optics and reciprocity tracking must be used, but the tropopause effects demand that the beam be focused on or above it, i.e., that the beam waist of 12.54 cm be at a range of ≈ 22 km from the transmitter, neglecting the fact that the transmitter may be on a mountaintop.

Using the formulation of Appendix I, we find the beam at the transmitter must be described by

$$U = U_0 e^{-\left(\frac{2r^2}{w^2} + \frac{ikr^2}{2R}\right)} \quad (9-1)$$

for $w = 8.64$ cm
and $R = 4.65 \times 10^4$ m.

This results in a $C_\ell < 0.01$ for the expected turbulence distribution.

The beam is now truncated at 1.736 its e^{-2} diameter, which results in negligible loss of energy to the sidelobes. The wander parameter, as discussed in Appendix V, is reduced to ~ 0.5 of its former value, since $R \propto kw^2/2$. Therefore, $\alpha = (.5) (.137) = .07$ which is sufficiently small.

Therefore (based on the present theory), we recommend no change in power or far field beam divergence. However, the beam should be focused at or above the tropopause, instead of defocused. The effect of beam spread has yet to be seen, of course.

9.3 Beacon Uplink

As discussed in detail in Section 4.3, we recommend a change in the beacon beam divergence (100 μ rad to 40 μ rad), average power (100 mwatts to 1.6 watts) and tracking accuracy (14 μ rad to 6.3 μ rad).

This is the brute-force approach to overcoming scintillation, i.e., C_ℓ will be $\sim .082$ but these changes will add 20 db of scintillation margin and keep $\alpha \leq .1$ so that a $P_E \leq 10^{-6}$ is retained. Enlarging and focusing the beam might be considered if the theory is verified in the OPTS experiments, and if the system design is easier that way.

Section X

CONCLUSIONS AND RECOMMENDATIONS

10.1 Introduction

This section summarizes the conclusions to be derived from the OPTS study, and the recommendations we are making to enable a high data rate laser link to be successfully designed. Details are found in earlier sections, and the Appendices.

10.2 Conclusions

OPTS has considered the effects of atmospheric turbulence on optical communication links, with the following conclusions:

- 1) The high data rate downlink, synchronous satellite to ground, is not seriously degraded by turbulence as discussed in Reference 2.
- 2) The beacon downlink is also not seriously degraded by turbulence.
- 3) Turbulence effects on the beacon uplink can be overcome by adding enough additional margin to make them negligible.
- 4) The high data rate uplink is tremendously degraded by turbulence effects. However, the key prediction of the OPTS program is that this link can be successfully completed with the available laser power (so long as beam spread is not a problem), if the following ground station design is implemented:
 - A) Common optics between the beacon receiver and high data rate transmitter.
 - B) Equivalent beam sizes of received and transmitted beams.
 - C) Pointing the transmit beam along the normal to the received wavefront. (A, B and C encompass what is usually called Reciprocity Tracking).
 - D) Focussing the transmitted beam at or above the tropopause.

Based on the theory developed during OPTS, these four constraints should reduce the power fluctuations to a minima at the satellite. We have not been able to consistently characterize beam spread as yet, and so the average power at the satellite has still to be estimated.

10.3 Recommendations

A) Experiments should be run to determine the correctness of the prediction cited above.

B) Theory should be extended to:

Consistently estimate beam spread;

Estimate the simultaneous power fluctuations due to all turbulence effects for arbitrary transfer optics;

Estimate the average probability of bit error/outages for the simultaneous power reduction and power fluctuations caused by all the turbulence effects.

These three theoretical tasks are formulated in the Appendices, and require a relatively minor effort to complete them. The experiment is a major effort. In order to complete it in a timely and effective manner, we recommend the program plan discussed in detail in Section 8.3 and summarized in Figure 28.

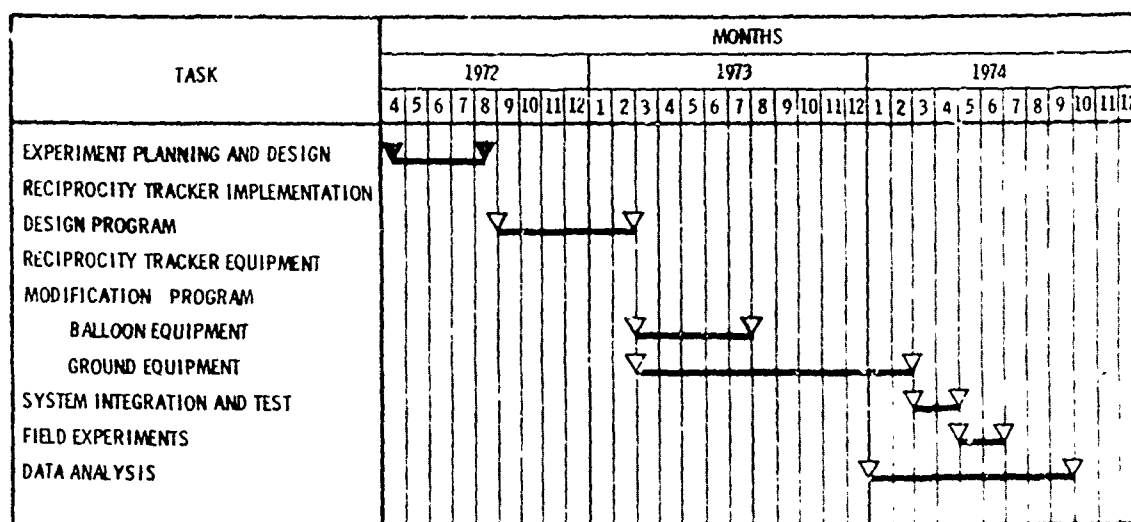


Figure 28. OPTS Program Plan.

Appendix I

Vacuum Gaussian Beam Propagation

I.1 Introduction

The purpose of this appendix is to review the theory of Gaussian beam propagation in the absence of turbulence, truncation, and center blockages. We rely heavily on the work of Kogelnik and Li⁽²¹⁾ and some straightforward manipulation of their results.

I.2 Theory

Kogelnik and Li found that a TEM₀₀ mode from a cylindrically symmetric resonator could be described at any point by the amplitude

$$U = U_0 e^{-\left(\frac{r^2}{w^2} + \frac{ikr^2}{2R}\right)} \quad (\text{I-1})$$

for

- $w = e^{-2}$ irradiance radius
- $R =$ radius of curvature of the wavefront
- $r =$ transverse dimension in the beam, i.e., perpendicular to the direction of propagation
- $k =$ wave number $(2\pi/\lambda)$

Furthermore, w and R can be written as functions of two other parameters,

$w_0 = e^{-2}$ irradiance radius at the beam waist

$Z =$ distance measured from the waist.

$$w^2 = w_0^2 \left[1 + \left(\frac{\lambda Z}{\pi w_0^2} \right)^2 \right] \quad (\text{I-2})$$

$$R = Z \left[1 + \left(\frac{\pi w_0^2}{\lambda Z} \right)^2 \right] \quad (\text{I-3})$$

One can manipulate these equations to yield three other useful ones:

$$\frac{\lambda Z}{\pi w_0^2} = \frac{\pi w^2}{\lambda R} \quad (\text{I-4})$$

$$w_0^2 = \frac{w^2}{\left[1 + \left(\frac{\pi w^2}{\lambda R}\right)^2\right]} \quad (\text{I-5})$$

$$Z = \frac{R}{\left[1 + \left(\frac{\lambda R}{\pi w^2}\right)^2\right]} \quad (\text{I-6})$$

Consider the first two equations again:

We see that w_0 is the minimum size that the beam can be, and $w = w_0$ at $Z = 0$. As Z increases, w monotonically increases so that for large Z ,

$$w^2 = \left(\frac{\lambda Z}{\pi w_0}\right)^2 \quad (\text{I-7})$$

We can then define a far-field (Z large enough to make this approximation, or, $Z > \pi w_0^2 / \lambda$) full angle beam divergence by

$$\Theta = \frac{2w}{Z} = \frac{4\lambda}{\pi(2w_0)} \quad (\text{I-8})$$

The radius of curvature of the wavefront behaves far differently. We see from I-3 that

$$R \rightarrow \infty \text{ as } Z \rightarrow 0$$

$$\text{and } R \rightarrow \infty \text{ as } Z \rightarrow \infty$$

In between, R reaches a minima at

$$Z = \frac{\pi w_0^2}{\lambda} \quad (\text{I-9})$$

and that minimum is $R_{\min} = \frac{2\pi w_0^2}{\lambda}$. (I-10)

We now consider some further implications of these equations for the three possible types of beams: collimated, defocused, and focused.

I.2.1 Collimated Beams, $R = \infty$ at the Aperture

We here consider the simplest case, the collimated or diffraction-limited divergence case. The beam waist is at the transmitter aperture, so that the far-field beam divergence is given by (I-8),

$$\theta = \frac{4\lambda}{\pi(2w_0)}$$

We have plotted this result for $\lambda = 5320\text{\AA}$ and 6328\AA in Figure 29.

I.2.2 Defocused Beams, $R > 0$ at the Aperture

This refers to the case of the beam waist being virtually present behind the transmitter aperture. Given the beam size, w , and radius of curvature, R , at the aperture, one uses equations (I-5) and (I-6) to establish the equivalent beam waists and the distance behind the transmitter at which it occurs. The far-field beam divergence is then obtained from (I-8) again.

I.2.3 Focused Beams, $R < 0$ at the Aperture

This refers to the case for the beam being reduced in size for a certain distance (focused), before it spreads. Again the beam at the aperture is characterized by a size, w , and radius of curvature, R . We then use (I-5) and (I-6) to calculate the real focal spot size, w_0 , and range to that spot, Z . Thereafter, (I-2) and (I-3) are used to trace out the beam size and curvature.

The far-field beam divergence is again given by (I-8).

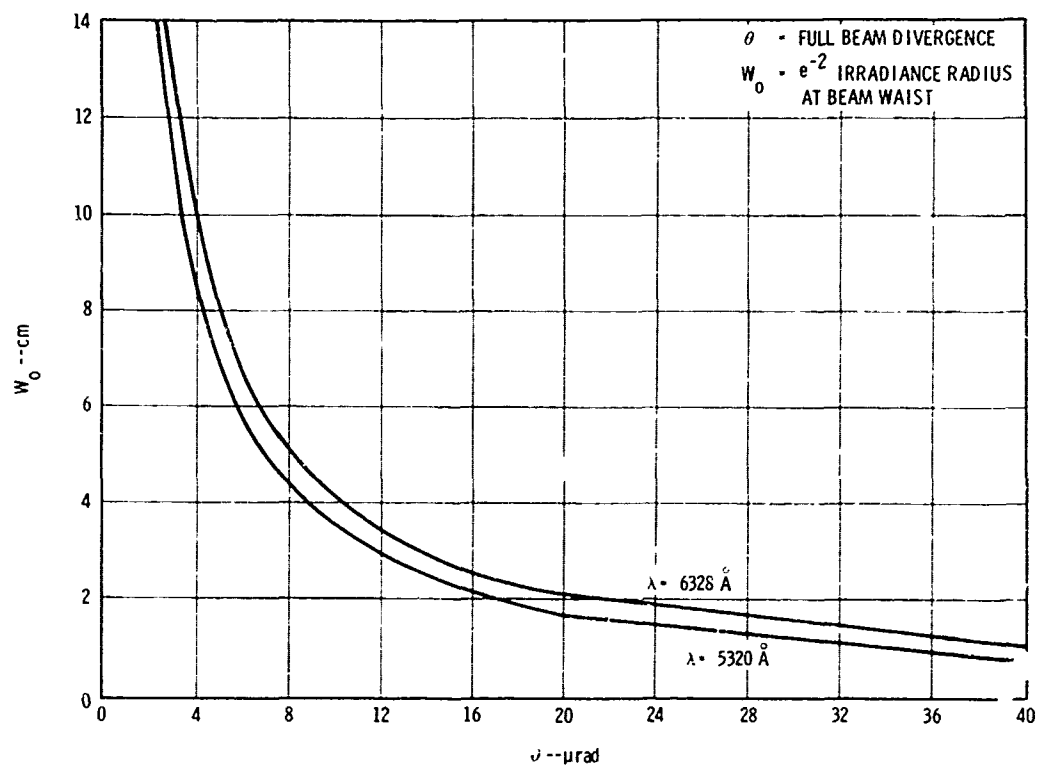


Figure 29. Beam Divergence Versus Beam Waist Radius.

The focal spot cannot occur at an arbitrary range, for a given sized transmitter aperture, due to diffraction. It is straightforward to show that for a given aperture size, w , the maximum distance at which the beam can be focused is given by

$$Z = \frac{\pi w^2}{2\lambda} \quad (\text{I-11})$$

The size of this focal spot is $w_o^2 = \frac{w^2}{2}$ (I-12)

and the curvature at the aperture is given by

$$R = \frac{2\pi w_o^2}{\lambda} = \frac{\pi w^2}{\lambda} = R_{\min} . \quad (\text{I-13})$$

To further exemplify these points, we have plotted beam size as a function of range Z in Figure 30 for a collimated beam; radius of curvature as a function of range Z in Figure 31 for a collimated beam; and beam size as a function of range Z for defocused, collimated, and focused beams with $w = 6$ cm and $\lambda = 6328\text{\AA}$ in Figure 32.

Finally, in Figure 33 we have plotted the maximum focusing range for a given w , as a function of w , for $\lambda = 6328\text{\AA}$.

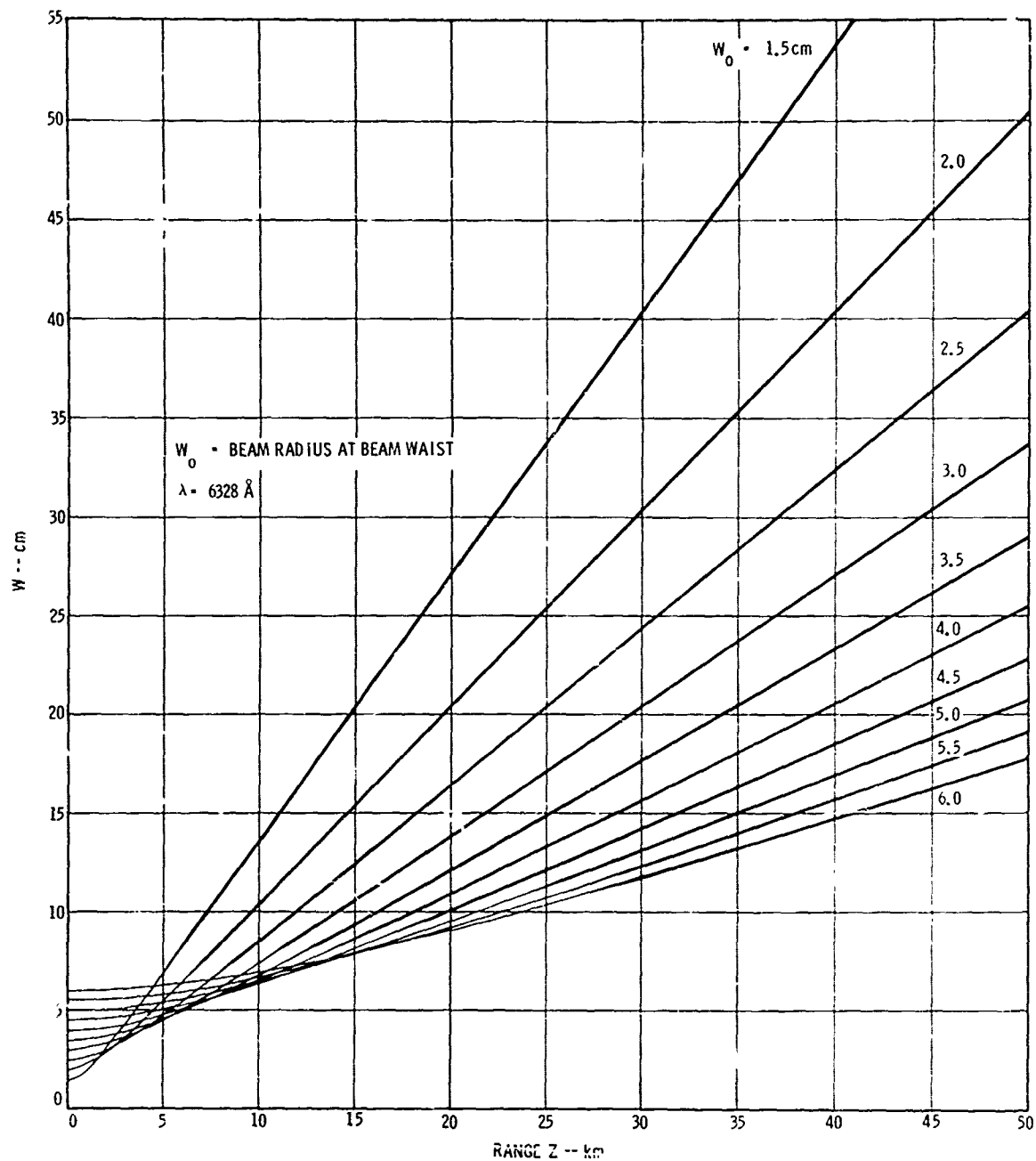


Figure 30. Beam Size Versus Range; Collimated Beams.

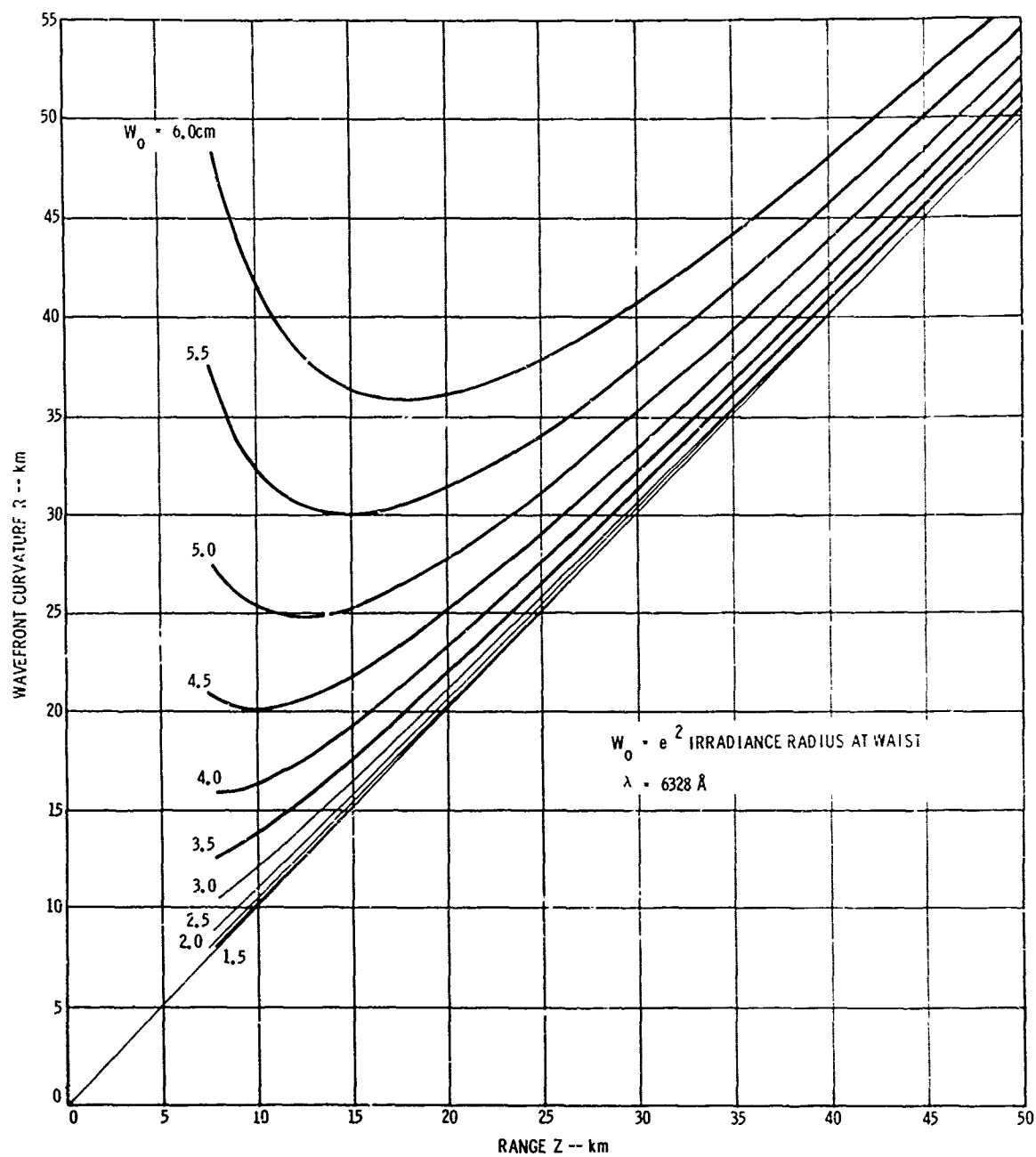


Figure 31. Radius of Curvature Versus Range;
Collimated Beams.

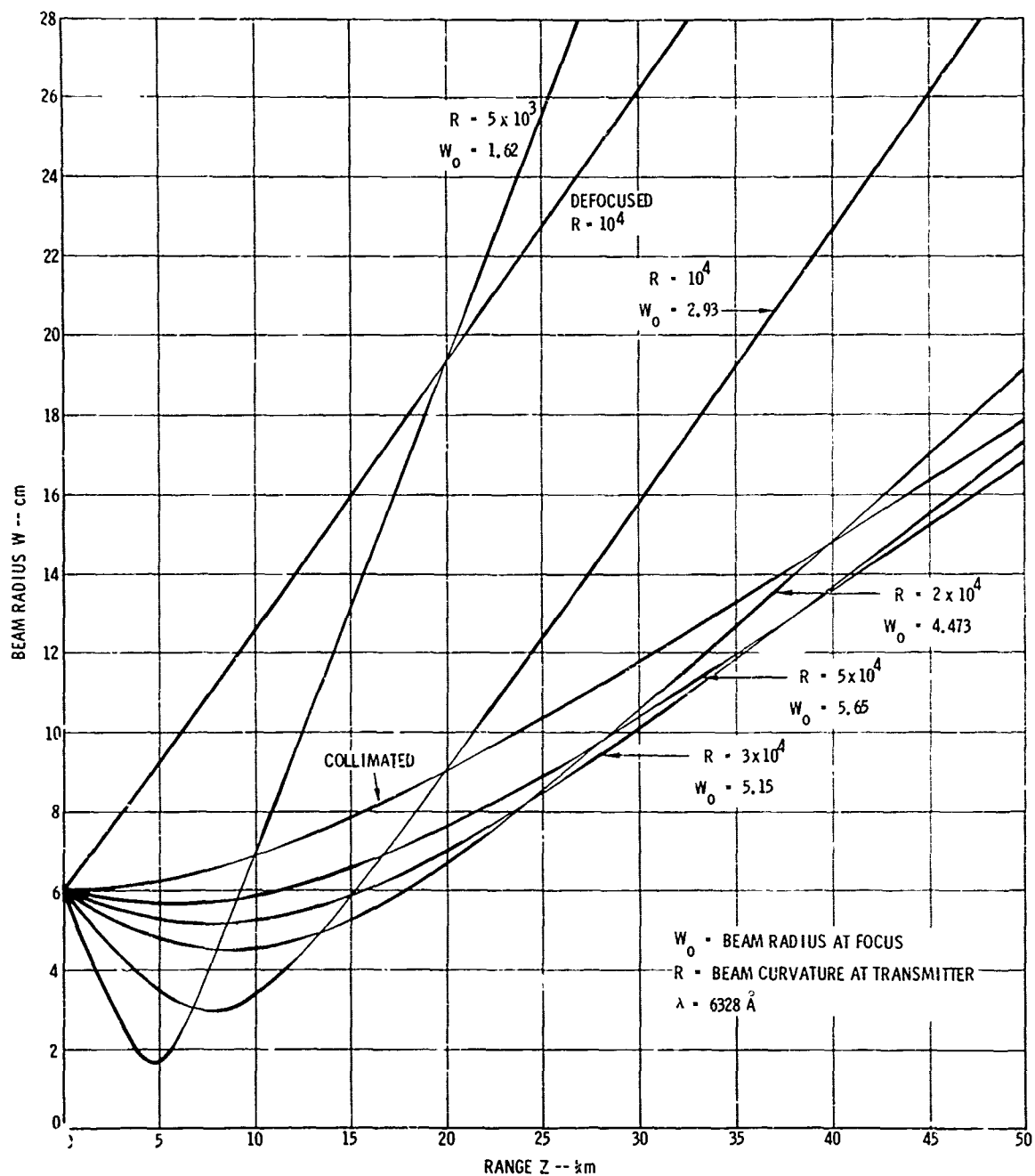


Figure 32. Beam Size Versus Range for Defocussed, Collimated and Focused Beams.

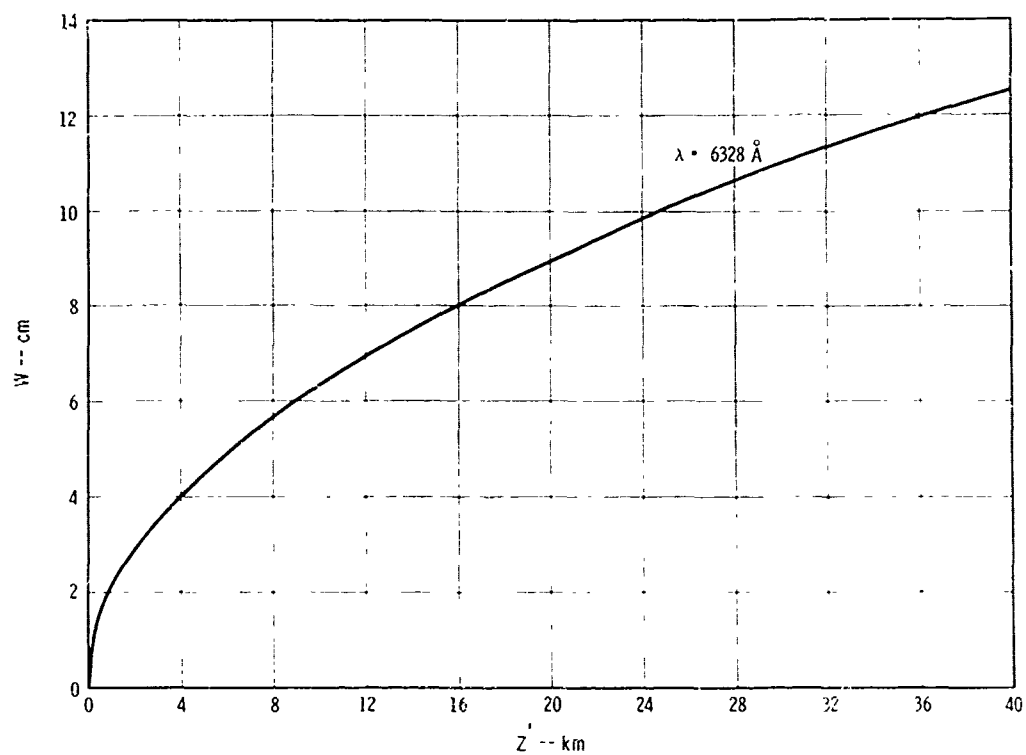


Figure 33. Maximum Focusing Range versus Initial Beam Size.

Appendix II

SCINTILLATION AND TRANSMITTER APERTURE AVERAGING

II.1 Introduction

Atmospheric turbulence causes an optical beam to break-up into hot spots and deep fades, so that a small detector placed in such a beam would measure large power fluctuations. These power fluctuations, caused only by beam breakup, are called scintillation. (Other power fluctuations, caused by beam wander of a beam with a "tapered" irradiance profile, will be considered in Appendix III.)

Scintillation is usually characterized by the variance of the log of the amplitude fluctuations, C_ℓ , where⁽²²⁾

$$C_\ell \equiv \overline{(\ell - \bar{\ell})^2} \quad (\text{II-1})$$

$$\text{for } \ell \equiv \frac{1}{2} \ln (I/\bar{I}) \quad (\text{II-2})$$

I = instantaneous irradiance

\bar{I} = average irradiance

C_ℓ is related to the normalized variance of the irradiance fluctuations by⁽²²⁾ (using the log-normal scintillation property),

$$\sigma_I^2 = e^{4C_\ell} - 1 \quad (\text{II-3})$$

$$\text{and the Ripple} = (\sigma_I^2)^{1/2} \times 100\%. \quad (\text{II-4})$$

In Figure 34 we plot the ripple as a function of C_ℓ .

The rest of this Appendix is devoted to estimating appropriate values of C_ℓ for "real" turbulence distributions and for large transmitter apertures and beams.

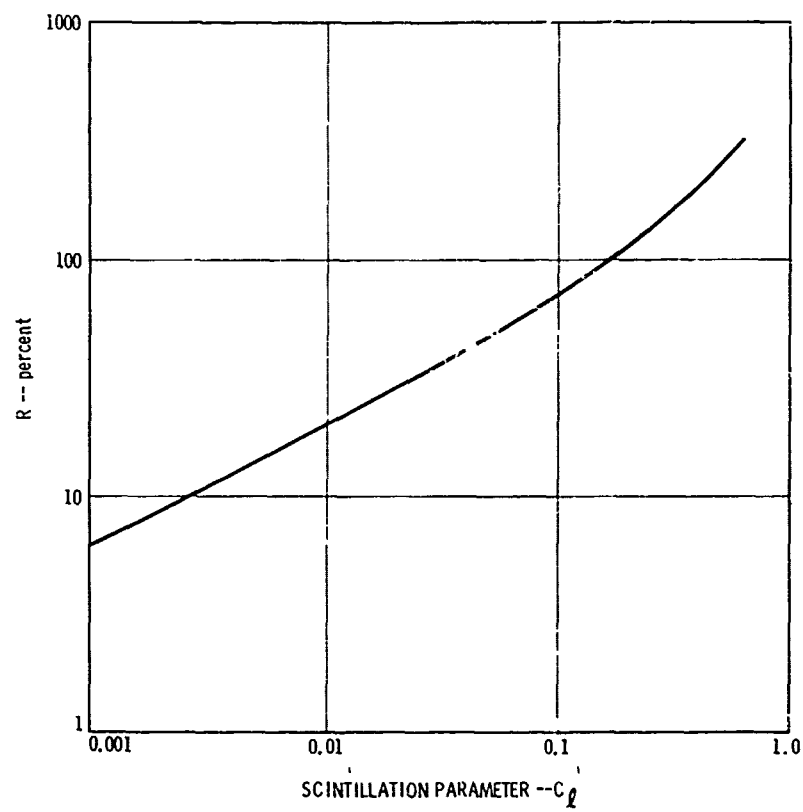


Figure 34. Ripple versus C_l .

II.2 Theory

There have been three equivalent theoretical treatments of the scintillation of beam waves, although many treatments of plane and spherical wave sources are extant. These three treatments, by Schmeltzer⁽²³⁾, Ishimaru⁽²⁴⁾, and Lee and Harp⁽²⁵⁾, have been shown to be equivalent by Lee and Harp. All three only consider power fluctuations near the beam axis, and assume the beam axis remains fixed on or near a fixed direction in space.

When a beam randomly wanders this last assumption breaks down. However, we shall assume that their theories hold along the instantaneous beam axis even if the beam wanders far from its average direction. In any event, if beam wander is compensated for by a reciprocity tracker (as discussed in Appendices V and VI), then their assumptions hold and the beam will scintillate as they predict.

Although their theories have been formulated in general, few particular predictions have been made. It has been predicted:

- (1) For uniform turbulence (C_N^2 constant along path):
 - (a) A beam focused on the receiver will have greatly reduced scintillation compared to a point source at longer ranges⁽²⁶⁾.
 - (b) A beam focused on infinity (collimated beam) will scintillate about the same as a point source or plane wave⁽²⁶⁾.
 - (c) A beam slightly defocussed around the receiver plane will scintillate worse than a point source⁽²⁴⁾.
- (2) For turbulence that monotonically decreases with path length as $h^{-1/3} \exp - (h/3200)$, for
h = altitude in meters:
 - (d) A beam focused at infinity (collimated beam) will have greatly reduced scintillation compared to a point source at longer ranges⁽²⁷⁾.

Of these four predictions, only (a) and (c) have been qualitatively tested by Kerr⁽²³⁾. The high data rate uplink depends on a prediction not formulated in the literature, viz., the scintillation on a beam when it propagates through a realistic turbulence distribution, which includes the tropopause.

In order to make this prediction we proceed as follows:

Our analysis begins with the Schemltzer⁽²³⁾ expression for the variance of the log of the amplitude fluctuations (which has used the Rytov approximation):

$$C_{\ell}(0) = \frac{8.16}{8\pi} k^2 \operatorname{Re} \left\{ \int_0^S dz C_N^2(z) \int_0^\infty d\sigma \sigma^{-11/6} \right. \\ \left. \left\{ \exp \left[\frac{\sigma}{2} \operatorname{Re} \gamma(S, Z) \right] - \exp \left[\frac{\sigma}{2} \gamma(S, Z) \right] \right\} \right\} \quad (\text{II-5})$$

for $k = \text{wave \# } (2\pi/\lambda)$

$\sigma = \text{spectral variable, (and we've assumed the Kolmogorov spectrum holds over the entire range of integration) in the 2-dimensional spatial Fourier transform of the amplitude correlation function, units of } m^{-2}.$

$S = \text{range from transmitter to receiver.}$

$C_N^2(z) = \text{index of refraction structure parameter at the point } z$
and the integration is from the transmitter to the receiver.

$$\gamma(S, Z) = 2 \frac{S-Z}{ik} \left[\frac{Z - ik\alpha^2}{S - ik\alpha^2} \right] \quad (\text{II-6})$$

$$\text{for } \frac{1}{\alpha^2} = \frac{1}{\alpha_0^2} - \frac{ik}{R} \quad (\text{II-7})$$

and the field at the transmitter is given by

$$U = A \exp - \left\{ \frac{r^2}{2\alpha_0^2} - \frac{ikr^2}{2R} \right\} \quad (\text{II-8})$$

$$= A \exp - \left\{ \frac{r^2}{w^2} - \frac{ikr^2}{2R} \right\} \quad (\text{II-8'})$$

for $w = e^{-2}$ irradiance radius
 R = radius of the spherical wavefront curvature.

With the field as written,

$R > 0 \rightarrow$ defocussed beam

$R < 0 \rightarrow$ focused beam

$R = \infty \rightarrow$ collimated beam.

We retain this expression in its full generality, making no further assumptions.

We can write:

$$\alpha^2 = \frac{\alpha_o^2 (1 + i k \alpha_o^2 / R)}{1 + (k \alpha_o^2 / R)^2}$$

Substituting this in the integral expression and bringing the R inside the integral, we find (for $w \rightarrow 0$),

$$C_\ell^s(o) = 5.6086 (10^{-14}) K_o k^{7/6} (\sec\theta)^{11/6} \int_0^H f(h) \left(1 - \frac{h}{H}\right)^{5.6} h^{5/6} dh \quad (\text{II-9})$$

for $C_\ell^s(o)$ = point source log amplitude variance ($w \rightarrow 0$)

H = altitude of receiver

θ = zenith angle, so that $S = H/\cos\theta$

and $Z = h/\cos\theta$

$$\text{and } C_N^2(h) = 10^{-13} K_o f(h) \quad (\text{II-10})$$

K_o = normalized turbulence strength at $h = 1$ meter.

Note that the kernel of the integral is weighted towards the middle of its range. Therefore if $f(h)$ should have a contribution there, its effect will be magnified. When $H = 30$ km, as for a balloon receiver, $f(h)$ has a contribution at almost exactly $H/2$ due to the tropopause⁽¹³⁾ and so a large value of C_ℓ^S will result.

For satellite altitudes, $H \gg$ any h at which $f(h) > 0$, and so $(1 - h/H)^{5/6} \rightarrow 1$. This means the turbulence at the tropopause is even more heavily weighted, and $C_\ell^S(o)$ measured at the satellite will be larger than that measured at the balloon.

For the beam wave ($w \neq 0$),

$$\frac{C_\ell(o)}{C_\ell^S(o)} = 3.8637 \left[\int_0^H f(h) \left(1 - \frac{h}{H}\right)^{5/6} h^{5/6} dh \right]^{-1} \times$$

$$\left[\int_0^H f(h) (H-h)^{5/6} \left\{ \left(\frac{M^2 + N^2}{P^2} \right)^{5/12} \right. \right. \quad (II-11)$$

$$\left. \left. \cos^{\frac{5}{6}} \left(\tan^{-1} \left(\frac{N}{M} \right) \right) - \left(\frac{M}{P} \right)^{5/6} \right\} dh \right]$$

for $C_\ell(o)/C_\ell^S(o)$ = ratio of large beam to point source log-amplitude variance.

$$M = \left(\frac{H-h}{\cos \theta} \right) A \left(1 + \left(\frac{A}{R} \right)^2 \right) \quad (II-12)$$

$$N = \left\{ \frac{h}{\cos \theta} \left(1 + \left(\frac{A}{R} \right)^2 \right) + \frac{A^2}{R} \right\} \left\{ \frac{H}{\cos \theta} \left(1 + \left(\frac{A}{R} \right)^2 \right) + \frac{A^2}{R} \right\}^{1/2} \quad (II-13)$$

$$P = \left\{ \frac{H}{\cos \theta} \left(1 + \left(\frac{A}{R} \right)^2 \right) + \frac{A^2}{R} \right\}^2 + A^2 \quad (II-14)$$

$$\text{and } A = \frac{\pi w^2}{\lambda} \quad (II-15)$$

Note:

(1) As $w \rightarrow 0$, $M \rightarrow 0$ and $(N/P)^{5/6} \rightarrow (h/H)^{5/6}$.

Of course $C_\ell/C_\ell^s \rightarrow 1$.

(2) In order for C_ℓ/C_ℓ^s to become less than 1, which would represent the sought for reduction in scintillation, $N/M \ll 1$, or the entire parenthesis term must be small.

We shall explore these points in detail later.

In order to estimate realistic values of the turbulence effects we need a realistic estimate of the turbulence distribution. Measurements⁽¹³⁾ with the GTE Sylvania Thermosonde have found a great deal of structure present at all times of the day and night but with two repeatable features:

- (1) A general decrease with altitude, except for:
- (2) A contribution due to the tropopause at around 15 km.

Consequently, we have evaluated our integral expressions for the following profiles:

$f(h) = h^{-1/3} e^{-h/1000}$, so that we can compare our results with those generated for collimated beams by Fried⁽²⁷⁾;

$f(h) = h^{-4/3}$, since there is a substantial body of evidence indicating this dependence near the ground⁽³⁾;

$$f(h) = h^{-4/3} + 0.001 \exp - \left(\frac{h - 1.5 \times 10^4}{10^3} \right)^2, \text{ as a rough}$$

estimate of a suitable contribution due to the tropopause⁽¹⁹⁾;

$$f(h) = h^{-4/3} + \begin{Bmatrix} 0.0035 \\ 0.00243 \\ 0.00168 \end{Bmatrix} \exp - \left\{ \frac{h - 1.5 \times 10^4}{10^3} \right\}^2, \text{ as}$$

a fit of the Hufnagel⁽²⁹⁾/Brookner⁽³⁰⁾ model (the upper and lower values representing standard deviations from the mean strength);

$$f(h) = h^{-4/3} + 0.00243 \exp - \left\{ \frac{h - h_p}{10^3} \right\}^2$$

for $h_p = 12 \text{ km}, 15 \text{ km and } 18 \text{ km}.$

II.2.1 Defocussed Results, $R > 0$ at the Aperture

Figure 35 shows the result of evaluating (II-11) as a function of R for

$$f(h) = h^{-1/3} e^{-h/1000}$$

$$\lambda = 6328 \text{ \AA}$$

$$K_o = 1$$

$$\theta = 45^\circ$$

$w = 4.03 \text{ cm}, 1.61 \text{ cm and } 0.537 \text{ cm},$ corresponding to collimated beams with full angle beam divergence of $10 \text{ } \mu\text{rad}, 25 \text{ } \mu\text{rad and } 75 \text{ } \mu\text{rad}$ respectively.

The other beam divergences entered in the figure are generated as discussed in Appendix I, Section I.2.2. We may conclude that

- (a) Defocussing always increases the scintillation;
- (b) For collimated beams and this turbulence profile, scintillation is decreased as the beam size at the transmitter increases in agreement with Fried's result⁽²⁷⁾.

Figure 36 shows the ratio of C_ℓ/C_ℓ^s as a function of R for

$$f(h) = h^{-4/3}$$

and with the rest of the parameters as before.

The shape of the curves is substantially unchanged so our previous conclusions hold. The only major distinction is that C_ℓ^s itself is far less for this profile, and so therefore is C_ℓ itself even though C_ℓ/C_ℓ^s is somewhat greater.

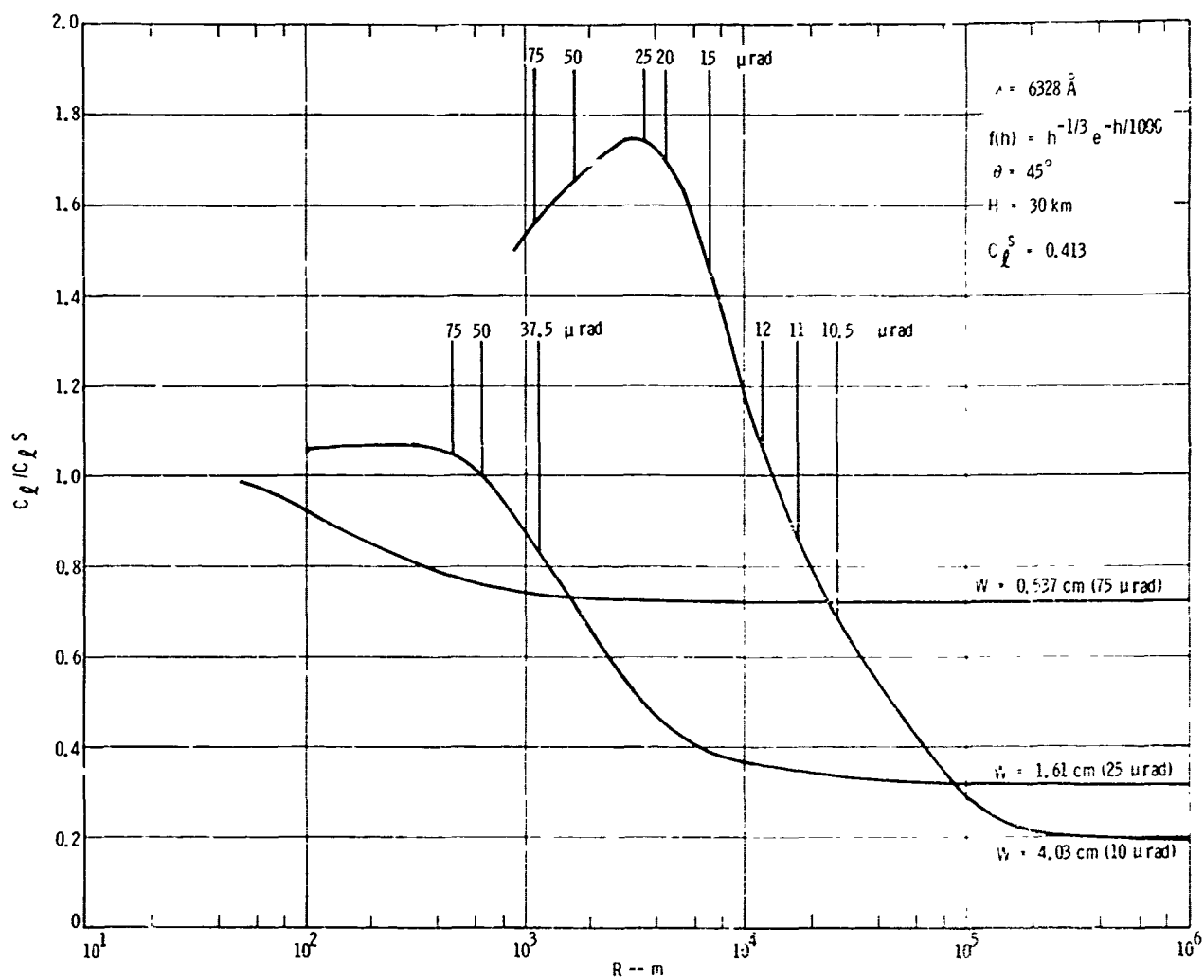


Figure 35. C_l/C_l^s versus R for Defocused Conditions: 1.

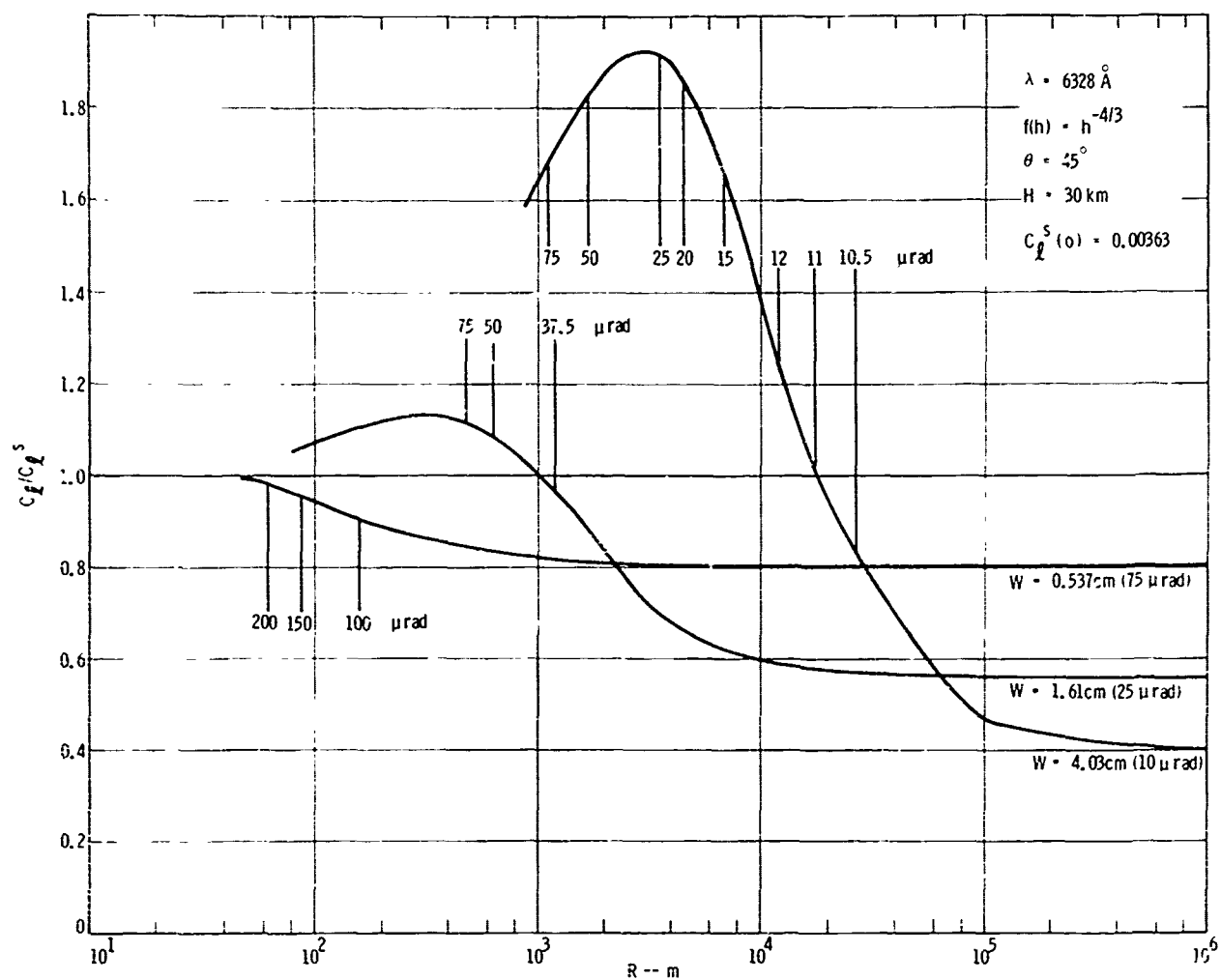


Figure 36. C_l/C_l^S versus R for Defocussed Conditions: 2.

Figure 37 shows the result as a function of R for

$$f(h) = h^{-4/3} + 0.001 \exp - \left\{ \frac{h - 1.5 \times 10^4}{10^3} \right\}^2$$

and with the rest of the parameters as before.

Clearly turbulence at the tropopause dominates the defocussed beam wave case. C_ℓ^S is 13.7 times as large as for the pure $h^{-4/3}$ profile. Moreover, the decrease of scintillation with large beam collimation has been reduced. However, the fact that defocusing always increases scintillation has remained invariant.

As we shall see in Appendix IV, a value of $C_\ell < 0.01$ is necessary if an average Probability of Bit Error $< 10^{-6}$ is to be achieved. None of these collimated or defocussed cases achieve that value (for the realistic parameters chosen) so we must investigate the results of focusing.

II.2.3 Focused Results, $R < 0$ at the Transmitter

In Figure 38 we have plotted the ratio C_ℓ/C_ℓ^S as a function of $|R|$ for

$$f(h) = h^{-4/3} + 0.00243 \exp - \left\{ \frac{h - 1.5 \times 10^4}{10^3} \right\}^2$$

$$K_o = 1$$

$$\lambda = 5320 \text{ \AA}$$

$$\theta = 45^\circ$$

$$H > 3000 \text{ km}$$

$$w = 8.48 \text{ cm}$$

The first thing to note is that there are a whole range of R's such that $C_\ell < 0.01$, even though $C_\ell^S = 0.25$. This case most realistically represents the SDR uplink and predicts that scintillation can be reduced sufficiently to complete the link as planned.

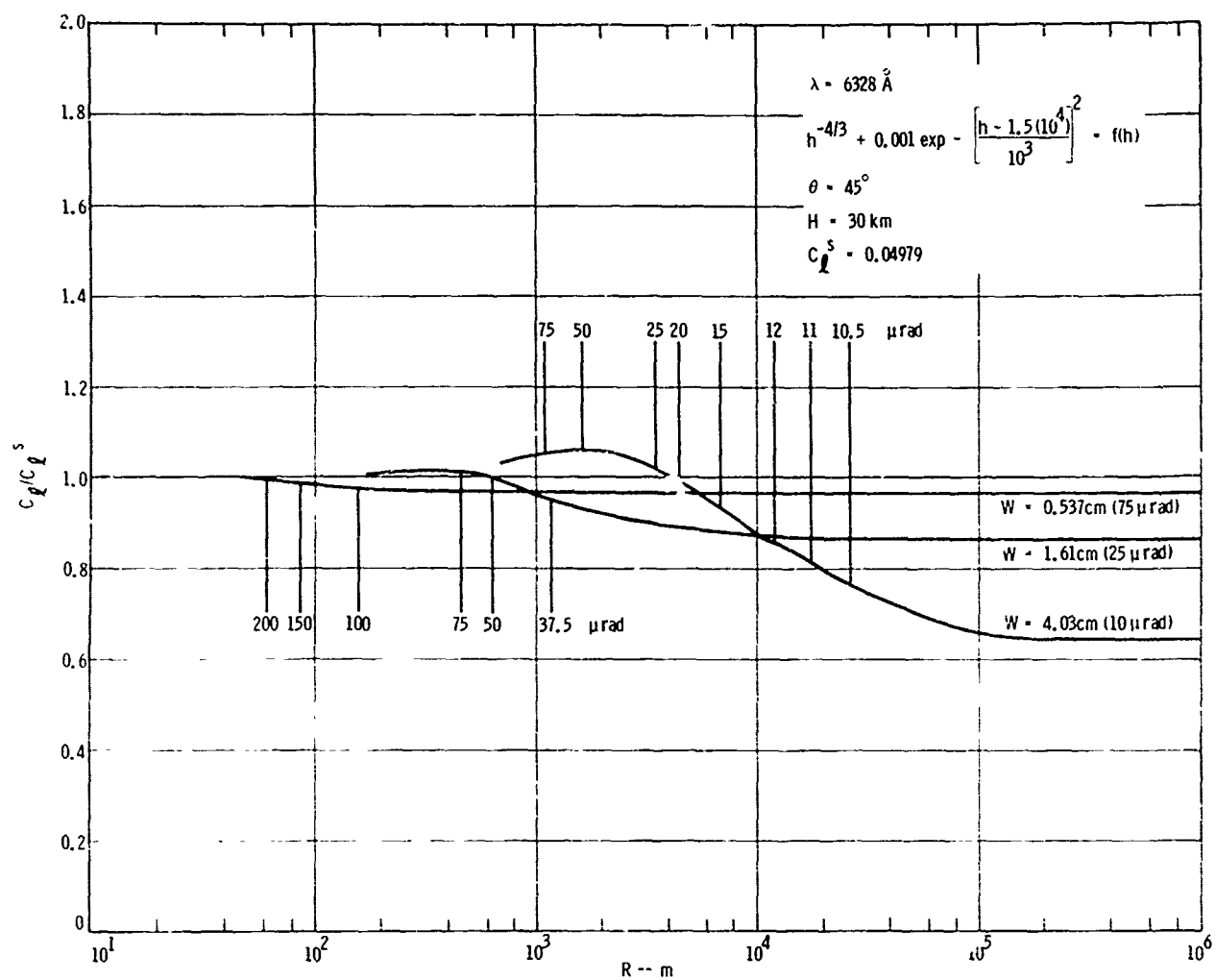


Figure 37. C_{ℓ}/C_{ℓ}^S versus R for Defocused Conditions: 3.

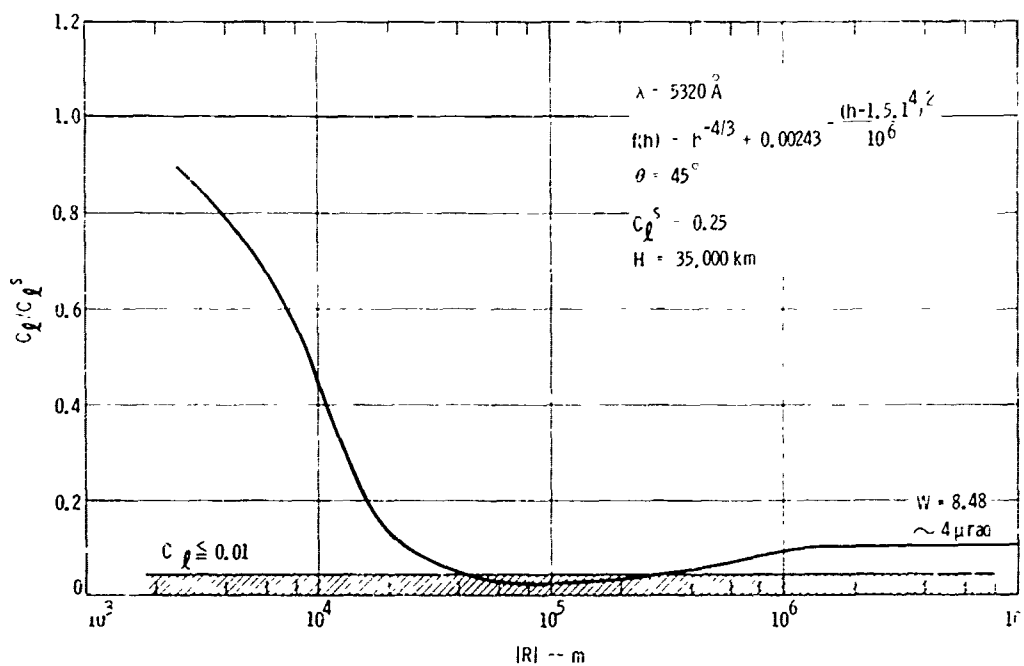


Figure 38. C_l/C_l^S versus R for Focussed and Satellite Receiver Conditions.

In order to determine whether this prediction can be tested at balloon altitudes, we have also computed the results of focusing when the receiver is at balloon altitudes.

Figure 39 shows the ratio C_ℓ / C_ℓ^s as a function of $|R|$ for that same profile $[f(h) \text{ and } K_0]$ but for

$$\begin{aligned}\lambda &= 6328\text{\AA} \\ \theta &= 45^\circ \\ H &= 30 \text{ km} \\ w &= 4.03 \text{ cm, } 4.5 \text{ cm, } 5.0 \text{ cm, } 5.5 \text{ cm, } 6.0 \text{ cm, } 6.5 \text{ cm} \\ &\text{and } 8.06 \text{ cm.}\end{aligned}$$

From this figure, we conclude:

- (1) The existence of the dip is critically dependent on w and R .
- (2) A $w = 6 \text{ cm}$ should be sufficient to show the effect, since a (typical) measurement accuracy should be achievable.
- (3) The minima point (as a function of R) shifts towards larger R as w increases.
- (4) Balloon altitudes are sufficient to test the prediction.

In Figure 40 we have tested the effect of the altitude of the tropopause on the result for

$$w = 6 \text{ cm}$$

$$\text{and tropopause altitude } h_p = 12 \text{ km, } 15 \text{ km, } 18 \text{ km.}$$

Clearly, the value of the minima decreases as h_p decreases.

We have also considered varying the strength (coefficient) of the tropopause term. from 0.0035 to 0.00243 to 0.00168. The ratio curves remains unchanged, although the value of C_ℓ^s follows almost linearly.

Finally, in Figures 41 and 42 we consider the zenith angle effects, for

$$\begin{aligned}w &= 4.03 \text{ cm and } 6 \text{ cm} \\ \theta &= 10^\circ, 45^\circ \text{ and } 75^\circ\end{aligned}$$

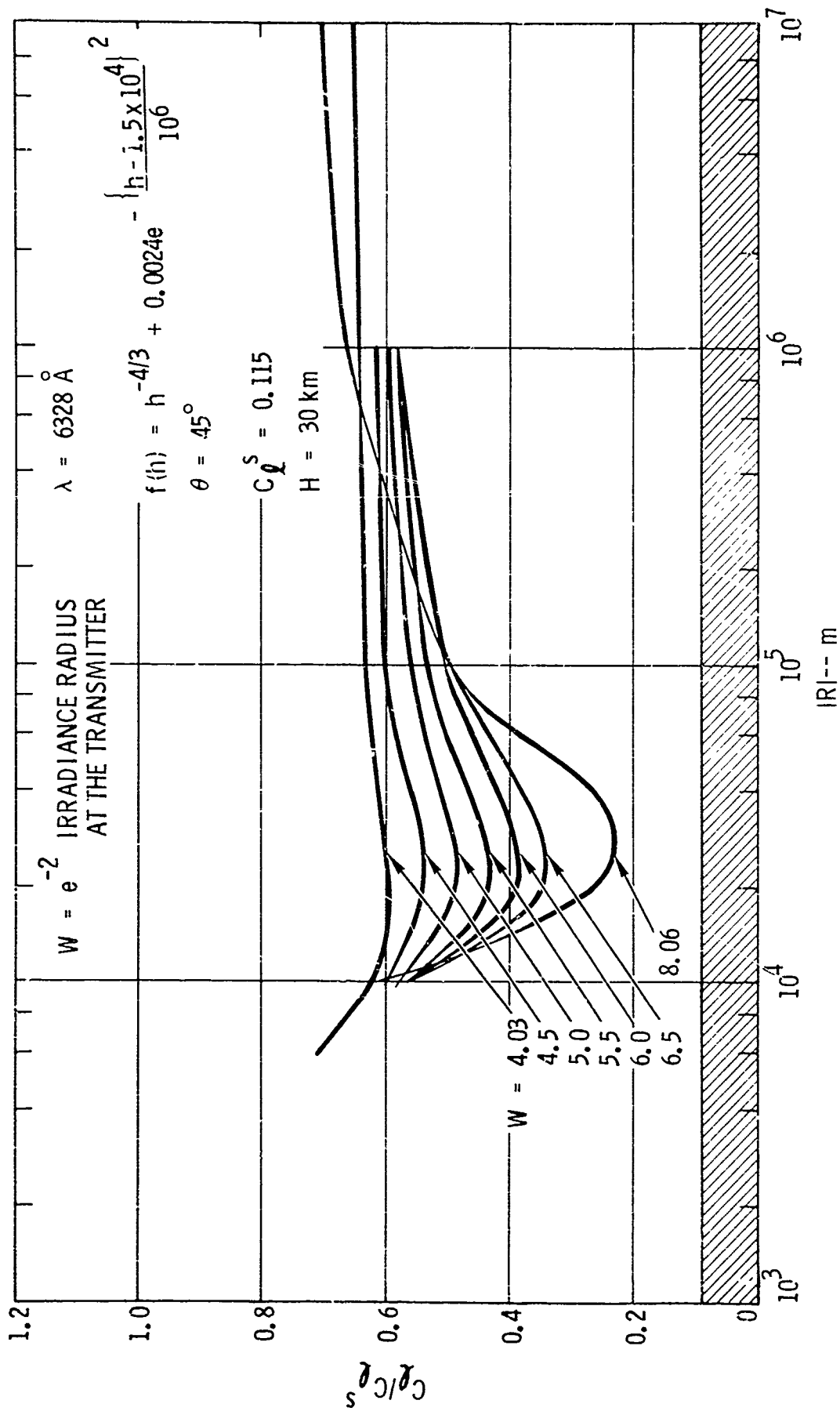


Figure 39. C_ρ/C_ρ^S versus R for Various Initial Beam Size and Focusing.

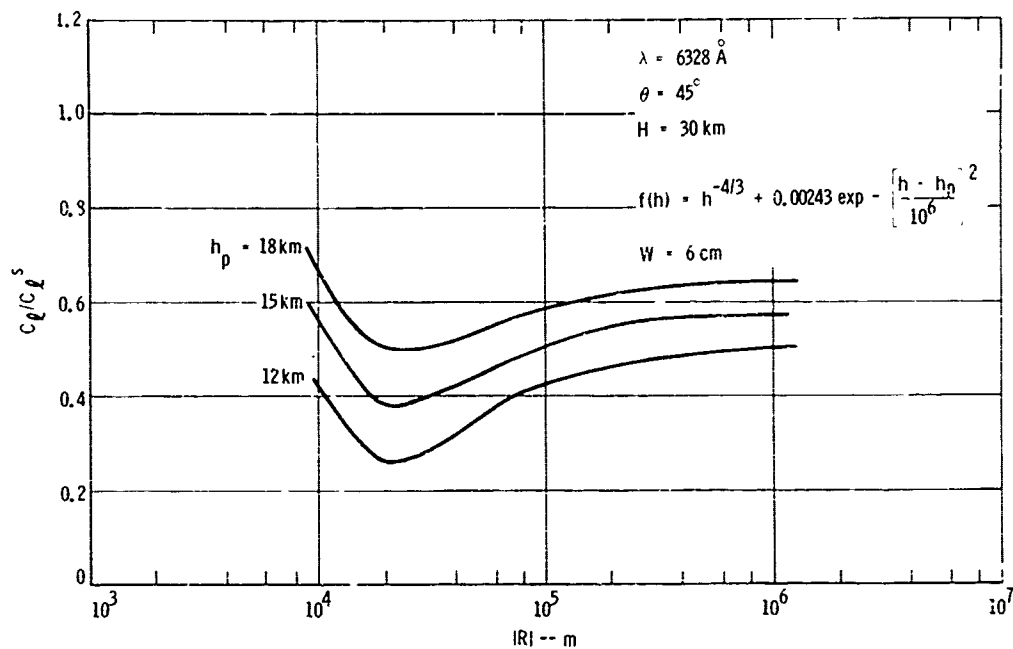


Figure 40. C_l/C_l^s versus R for Various Tropopause Altitudes and Focusing.

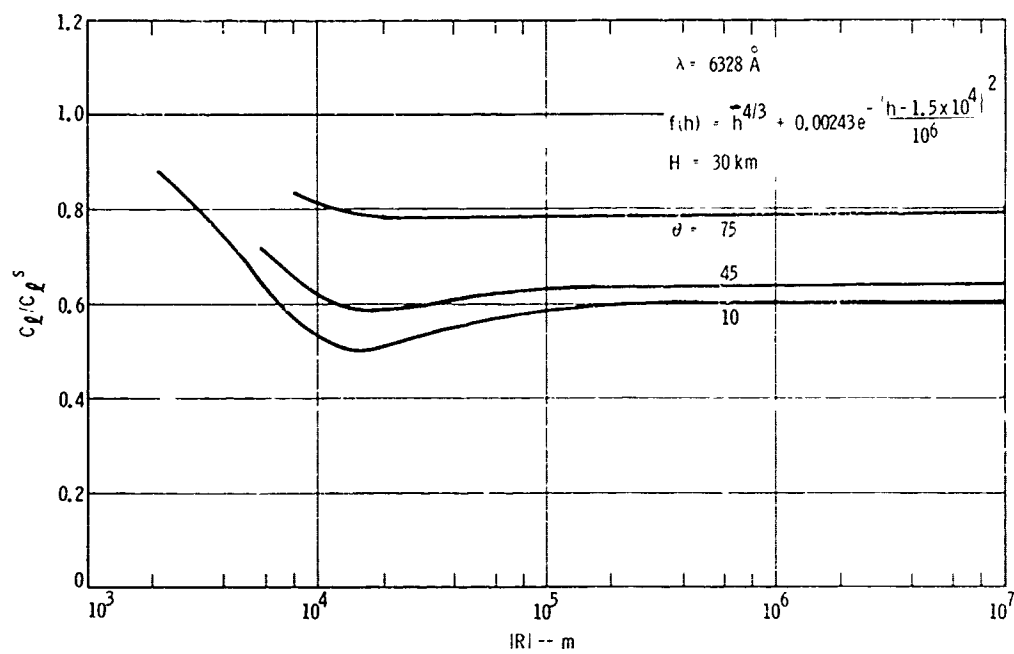


Figure 41. C_l/C_l^s versus R for $w = 4.03 \text{ cm}$ and
Zenith Angle Effects

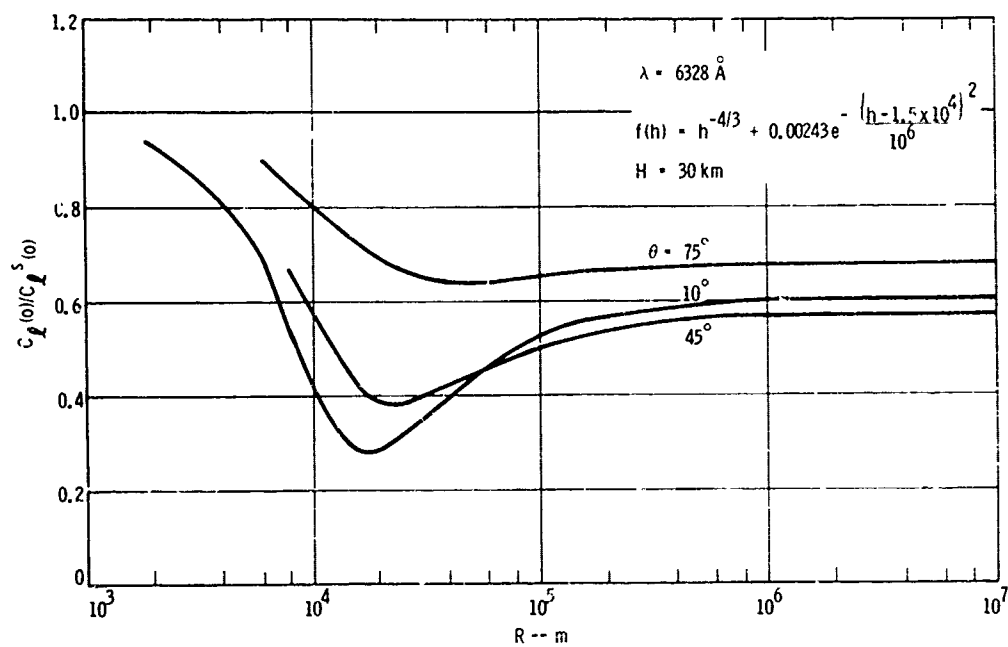


Figure 42. C_l^S/C_l^S versus R for $w = 6 \text{ cm}$ and Zenith Angle Effects.

The nearer zenith the beam is pointed, the more effective a given size optics is in producing the dip, and the deeper the dip is.

Summarizing, then, a receiver at balloon altitudes (30 km) will be able to verify the focused transmitter aperture averaging theory in detail, although the magnitude of C_ℓ may never reach the value to be obtained at satellite altitudes.

II.3 Physical Interpretation

The existence of the dip shown in the figures for the large focused beams is crucial to the success of a high data rate uplink. Therefore, we shall explore its physical basis in more detail.

Recall the integrand of the ratio C_ℓ/C_ℓ^S :

$$J \equiv (H-h)^{5/6} f(h) \left\{ \left\{ \frac{M^2 + N^2}{P^2} \right\}^{5/12} \cos \left(\frac{5}{6} \tan^{-1} \frac{N}{M} \right) - \left(\frac{M}{P} \right)^{5/6} \right\} \quad (\text{II-16})$$

In general, one would consider varying J as a function of all its parameters to determine the combination that yields a minimal integral of J . We, however, do not consider that procedure here, but rather try to minimize the parts of J that were contributing most heavily at the tropopause.

Now, $J \rightarrow 0$ if $N/M \ll 1$ at the tropopause, and

$$\begin{aligned} \frac{N}{M} = \frac{Z S}{(S-Z)A} \left(1 + \frac{A^2}{R^2} \right) - \left(\frac{S+Z}{S-Z} \right) \frac{A}{R} + \frac{A^3}{(S-Z)R^2(1+A^2/R^2)} \\ + \frac{A}{(S-Z)(1+A^2/R^2)} \end{aligned} \quad (\text{II-17})$$

$$\text{for } Z = \frac{h}{\cos \theta} \text{ and } S = \frac{H}{\cos \theta}$$

11.3.1 Satellite Case

For this condition, $S \gg Z$ for all Z at which $f(h) > 0$ and II-17 becomes

$$\frac{N}{M} = \frac{Z}{A} \left(1 + \frac{A^2}{R^2} \right) - \frac{A}{R} + \frac{A}{S} \quad (\text{II-18})$$

For $S = 10^7 \text{ m}$, $w = 8.48 \text{ cm}$ and $\lambda = 5320 \text{ \AA}$, (as in Figure 38), the last term is of order 10^{-3} , and therefore negligible. Retaining the first two terms, we look for the relation among Z , R and A such that N/M will be a minimum at the turbulence distribution peak, i.e., $Z = \text{tropopause range}$.

$$\frac{d}{dR} \left(\frac{N}{M} \right) = 0 = \frac{-2ZA}{R^3} + \frac{A}{R^2} \quad (\text{II-19})$$

Therefore, $R = 2Z$ will insure N/M is a minima, independent of A (and w , the beam size at the transmitter).

Substituting $R = 2Z$ into the equation, we find that the minimum N/M reaches is given by

$$\frac{N}{M} = \frac{Z}{A} - \frac{A}{4Z} \quad (\text{II-20})$$

For the case plotted in Figure 38, the range to the tropopause was $Z = 21.21 \text{ km}$, and $A = 43.5 \text{ km}$, so that

$$N/M \approx 0.025 \text{ at } Z = 21.21 \text{ km.}$$

Note, in general, that for $Z = A/2$, $N/M \approx 0$.

We therefore have the following conditions which the theory demands for its minima:

$$R = 2Z \quad (\text{II-21})$$

$$A = 2Z; \quad Z = \frac{\pi w^2}{2\lambda} \quad (\text{II-22})$$

In a system such as the SDR, Z is fixed by the zenith angle and range to the tropopause. Then R and A (w) are fixed by these two conditions if the minimum scintillation is needed.

From Appendix I, we see that these two conditions correspond to

- (1) Focusing the beam exactly on the tropopause.
- (2) Having the minimum wavefront curvature (minimum $|R|$) at the transmitter aperture.

We may note from the breadth of the dip in Figure 38 that these conditions need not be exactly fulfilled, and that for a whole range of values of " R " the value of C_θ will be sufficiently small.

Note that when these two conditions are fulfilled, the satellite receiver (in the far field of the beam waist) will receive energy from every portion of that waist. This, clearly, results in the optimum averaging of the turbulence present at that waist.

II.3.2 Balloon Case

Because the balloon may not be in the far field of the beam waist, and the optics sizes considered may not be sufficient to focus the beam at the tropopause, we should not be surprised if different conditions arise for the balloon case.

Because we have consistently chosen the altitude of the tropopause = 15 km and that of the balloon = 30 km (except in Figure 38), we may take $S = 2Z$, and II-17 becomes:

$$\frac{N}{M} = \frac{2Z}{A} \left(1 + \frac{A^2}{R^2} \right) - \frac{3A}{R} + \frac{A}{Z} \quad (\text{II-23})$$

Proceeding as before, we find that N/M will be minimized for $R = 4Z/3$, and selecting $Z = A/4$ will assure that $N/M \approx 0$.

We are not able to achieve these conditions for $w = 6$ cm and $Z = 21.21$ km, and in fact, for these parameters, $N/M \approx 2.27$.

Evidently the dip in the scintillation curves for $w = 6$ cm is due to a complicated combination of parameters, for two reasons:

- (a) $w = 6$ cm \rightarrow we cannot focus on the tropopause
- (b) The balloon receiver is not in the far field of the transmitter (or focal spot).

We can explore this one step further, by considering the case of maximum focal range for a given size beam at the transmitter, i.e., as discussed in Appendix I, for that case

$$|R| = 2 \frac{\pi w^2}{2\lambda} = \frac{\pi w^2}{\lambda} = A.$$

(We see from Figure 39 that this is not the minimum point of the dip, but it is in the dip at least.)

Putting $R = -A$ in (II-16) and setting $Z = \alpha A$, we find

$$\left(\frac{M^2 + N^2}{P^2} \right)^{5/12} = \left(\frac{4\alpha^2 - 2\alpha + 1}{8\alpha^2 - 4\alpha + 1} \right)^{5/6}$$

$$\frac{N}{M} = \frac{4\alpha^2 - 3\alpha + 1}{\alpha}$$

$$\text{and } \left(\frac{M}{P} \right)^{5/6} = \left(\frac{\alpha}{8\alpha^2 - 4\alpha + 1} \right)^{5/6}$$

We have evaluated $J/f(h) (H-h)^{5/6}$ for those values of α corresponding to values of Z near the tropopause in the following table:

$$\alpha = \frac{\left[\left(\frac{M^2 + N^2}{P^2} \right)^{5/12} \cos \frac{5}{6} \tan^{-1} \left(\frac{N}{M} \right) - \left(\frac{M}{P} \right)^{5/6} \right]}{1}$$

1	.1328
1.5	.1122
2.0	.09806
2.5	.1035
10	.1305

From these results, we see that there is no weighting function at the tropopause when the beam is focused as specified.

Therefore, at balloon altitudes, although the mathematics is more complex, the physical result is the same, and scintillation is reduced. Thus, the theory of focusing for a satellite-borne receiver can be tested using a balloon-borne receiver, e.g., a $w_0 = 6$ cm should see a 100% change in the value of C_ℓ (at balloon altitudes) caused by focussing.

II.4 OPTS Tests of the Theory

Based on the analysis given above, OPTS will sufficiently test this theory if the following transmitter beam parameters are used with the balloon receiver; for $\lambda = 6328\text{\AA}$:

<u>w, e^{-2} irradiance radius</u>	<u>$R, \text{ wavefront curvature}$</u>
6 cm	$+10^4$
	∞
	$-10^4 \rightarrow -10^5$
4.03 cm	$+10^4$
	∞
	$-10^4 \rightarrow -10^5$

APPENDIX III

BEAM WANDER

III.1 Introduction

We now consider the case of pure-beam wander, i.e., the wavefront preserves its vacuum form but the entire beam is moving randomly about some fixed direction. All power fluctuations caused by scintillation are neglected here, but significant power fluctuations will still be seen by a fixed receiver since the power density across the wavefront is described by a Gaussian profile.

III.2 Theory

Esposito⁽³¹⁾ first formulated the problem as follows. The irradiance at a receiver of radius r , due to a randomly moving beam of e^{-2} irradiance radius w , is given by

$$I(x, y, \xi, \eta) \propto \exp -2 \left\{ \frac{(x-\xi)^2 + (y-\eta)^2}{w^2} \right\} \quad (\text{III-1})$$

for $\xi(\eta)$ the random orthogonal displacement of the center of the beam in the $x(y)$ direction from its ideal direction.

If we write $\rho = \sqrt{\xi^2 + \eta^2}$, Esposito showed that the instantaneous power detected is given by

$$\begin{aligned} P(r, w, \rho) &= \iint_{x^2 + y^2 < r^2} I(x, y, \rho) dx dy \\ &= 1 - Q(\rho/w; r/w) \end{aligned} \quad (\text{III-2})$$

for $Q(a,b) = \text{Marcum's Q Function}^{(32)}$

$$= \int_b^\infty t \exp \left(-\frac{t^2 + a^2}{2} \right) I_0(at) dt$$

for I_0 the modified Bessel function⁽³³⁾.

Assuming that beam center is undergoing a random walk, i.e., that ξ and η are zero-mean Gaussian variables with equal variances, implies the probability density of ρ is Rayleigh, so that

$$f(\rho) = \frac{2\rho}{\overline{\rho^2}} \exp \left(-\rho^2 / \frac{\overline{\rho^2}}{2} \right) \quad (\text{III-3})$$

for $\overline{\rho^2}$ = mean square displacement of beam center.

Esposito further showed that this implied that the probability density of the detected power is given by

$$f(P) = \frac{2w^2}{\overline{\rho^2} r} \exp \left(-\frac{r^2}{w^2} \right) \left\{ \frac{\rho \exp \left[-\left(\frac{1}{\overline{\rho^2}} - \frac{1}{2w^2} \right) \rho^2 \right]}{I_1(\rho r/w^2)} \right\} \quad (\text{III-4})$$

ρ cannot be eliminated from this expression in general so $f(P)$ cannot be written directly in terms of P . However, in general one could obtain any moment of the detected power by performing the integral :

$$\overline{P^n} = \int P^n f(P) dP$$

III.3 Application to Detectors in the Far Field

For the case of interest ($r \ll w$) these expressions simplify and become analytically manageable. It is straightforward to show that

$$f(P) = \frac{1}{2\alpha P_0} \left(\frac{P}{P_0} \right)^{\frac{1}{2\alpha} - 1} \quad (\text{III-5})$$

for P_0 = power at beam center

$$\alpha = \overline{\rho^2} / w^2. \quad (\text{III-6})$$

Therefore, the cumulative probability is given by:

$$P_r (P < P_x) = \left(\frac{P_x}{P_0} \right)^{\frac{1}{2\alpha}} \quad (\text{III-7})$$

The mean power is given by

$$\overline{P} = \frac{P_c}{1 + 2\alpha} \quad (\text{III-8})$$

and the normalized variance of the detected power is given by

$$\frac{\overline{P^2}}{\overline{P}^2} - 1 = \frac{4\alpha^2}{4\alpha + 1} \quad (\text{III-9})$$

and therefore the ripple is given by

$$\text{RIPPLE} = \frac{2\alpha}{\sqrt{4\alpha + 1}} \times 100\% \quad (\text{III-10})$$

α is the key parameter, of course, and can be expressed in many ways. For example, if the full angular beam width is given by θ , and θ_{rms} is the root mean square angular motion of the center of the beam, then

$$\alpha = \frac{\overline{\rho^2}}{w^2} = 4 \left(\frac{\theta_{\text{rms}}}{\theta} \right)^2 \quad (\text{III-6'})$$

We shall see in Appendix V one estimate of $\overline{\rho^2}$ which, neglecting atmospheric spread, leads to the additional expression:

$$\alpha = \frac{b^2}{\rho_o^2} \quad (\text{III-6''})$$

where $b = e^{-2}$ irradiance radius of the beam at the transmitter

$\rho_o = e^{-1}$ point of the MTF measured at the transmitter for a spherical wave propagating in the opposite direction.

We shall not graph $P_r (P < P_x)$, \overline{P} and $\overline{c_p^2}$ since they are simple expressions in terms of α , which in turn is a simple ratio expression of the physical parameters.

Paddon⁽²⁾ extended our theory to treat the case of static pointing errors. Dynamic pointing errors due to other than atmospheric turbulence are treated as above, with ρ^2 (or θ_{rms}) now derivable from the error source, such as mount jitter, servo stiction, etc.

III.4 Application to High Data Rate Uplink Specifications

We shall see in Appendix IV that $\alpha < .1$ is a necessary condition for the average probability of bit error, P_E , to be $\lesssim 10^{-6}$. This means that the rms pointing fluctuations due to all causes must be as given in

the following table:

θ , Full Angle Beam Divergence, μRAD	θ_{rms} , Pointing Error, (for $\alpha_N .1$) μRAD
5	.79
5.4	.85
6.7	1.06
10	1.58
25	3.95
40	6.32
50	7.91
100	15.81

Appendix IV

Probability of Bit Error and Outages for Beam Wander and Scintillation

IV.1 Introduction

Appendices II and III have discussed power fluctuations caused by pure scintillation and pure wander. In this appendix we derive the probability of bit error (and outage) for a communication system using a pulse-gated-binary-mode modulation format, in the presence of these independent power fluctuations.

IV.2 Theory

The basic PGBM system is shown in Figure 43. The expression for the probability of error is given by⁽³⁴⁾

$$P_E = P(N) P_{FA} + P(S) (1 - P_D) \quad (IV-1)$$

where

- $P(N)$ = Probability of transmitting a "0", i.e., no signal
- $P(S)$ = Probability of transmitting a "1", i.e., signal
- P_{FA} = Probability of receiving a "1" given a "0" is transmitted, i.e., "false alarm"
- P_D = Probability of receiving a "1" given a "1" is transmitted, i.e., "detection," so that $1 - P_D$ is the probability of non-detection.

For the low numbers of photons involved here, the detection process is correctly describable by Poisson Statistics. Therefore

$$P_{FA} = \sum_{j=k}^{\infty} e^{-(N+\epsilon S)} \frac{(N+\epsilon S)^j}{j!} \quad (IV-2)$$

$$P_D = \sum_{j=0}^{\infty} e^{-(S+N)} \frac{(S+N)^j}{j!} \quad (IV-3)$$

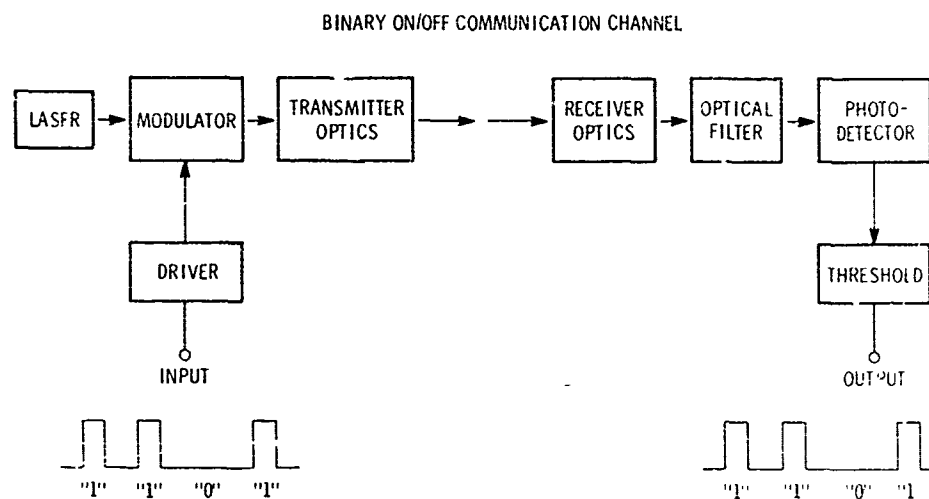


Figure 43. PGBM Communication Mode.

for S = number of signal photoelectrons/pulse
 N = number of background noise photoelectrons/pulse
 k = threshold photoelectron level
 ϵ = (extinction ratio)⁻¹

The extinction ratio takes into account the leakage of the modulator, i.e., when a "0" is being transmitted, some photons still are being transmitted due to incomplete blockage.

There is an optimum threshold, determined by the equality

$$\frac{P(k_{\text{opt}}/S+N)}{P(k_{\text{opt}}/N+\epsilon S)} = \frac{P(N)}{P(S)} \quad (\text{IV-4})$$

which is $k_{\text{opt}} = \frac{S(1-\epsilon) + \ln[P(N)/P(S)]}{\ln\left(\frac{N+S}{N+\epsilon S}\right)} \quad (\text{IV-5})$

In the usual situation, as many "0"s as "1"s are sent so that

$$P(N) = P(S) = 1/2$$

and $k_{\text{opt}} = \frac{S(1-\epsilon)}{\ln\left(\frac{N+S}{N+\epsilon S}\right)} \quad (\text{IV-5'})$

In order to account for the further statistical effects not included in the Poisson detection process, we must characterize them by a probability density, $f(S)$, and integrate the detection probabilities over all values of S , i.e., we find

$$P_D = \int_{-\infty}^{\infty} ds f(S) \left\{ \sum_{j=k}^{\infty} e^{-(S+N)} \frac{(S+N)^j}{j!} \right\} \quad (IV-6)$$

$$\text{and } P_{FA} = \int_{-\infty}^{\infty} ds f(S) \left\{ \sum_{j=k}^{\infty} e^{-(N+\epsilon S)} \frac{(N+\epsilon S)^j}{j!} \right\} \quad (IV-7)$$

$$\text{and } P_E = \frac{1}{2} P_{FA} + \frac{1}{2} (1 - P_D) \quad (IV-8)$$

Of course, this also changes the optimum threshold, in general, to an entirely new expression.

Atmospheric turbulence is responsible for generating the $f(S)$ to be used.

IV.3 Scintillation Alone

The probability density of detected signal photoelectrons is given by ⁽⁷⁾

$$f(S) = \frac{1}{[2\pi C_\ell]^{1/2}} \frac{1}{2S} \exp \left[-\frac{1}{2C_\ell} \left(\frac{1}{2} \ln (S/S_0) + C_\ell \right)^2 \right] \quad (IV-9)$$

For $0 \leq S \leq \infty$

$= 0$, for $S < 0$.

where $C_\ell = \text{variance of the distribution of } \ell = 1/2 \ln (S/S_0)$

$S_0 = \text{mean number of signal photoelectrons.}$

We have evaluated P_E as a function of S_0 in Figure 44 for

$\epsilon = (31.6)^{-1}$, i.e., an extinction ratio of 15 db

$N = 1$

and with C_ℓ as a parameter. Each curve is also labeled with the value of threshold k for which the P_E is minimized, said threshold always being less than k_{opt} as previously derived.

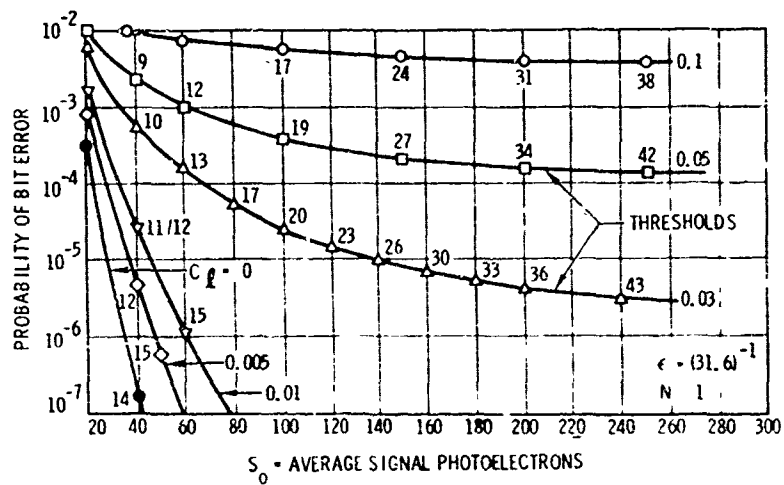


Figure 44. Scintillation Effects on P_E for PGEM.

These curves imply that $C_0 \leq 0.01$ is a necessary condition for the average P_E to be $< 10^{-6}$, with realizable laser powers. cf Appendix XVI for the results for an adaptive threshold.

IV.4 Wander Alone

Paddon⁽²⁾ has treated the case of the probability of bit error for pure wander and zero pointing error, i.e.,

$$f(S) = \frac{1}{2\alpha S_0} \left(\frac{S}{S_0} \right)^{\frac{1}{2\alpha} - 1} \quad (\text{IV-10})$$

where $\alpha = \overline{\rho^2} / w^2$ (IV-11)

for $\overline{\rho^2}$ = means square displacement of beam center

$w = e^{-2}$ irradiance radius of the beam.

Assuming (1) $P_{FA} \ll (1 - P_D)$

(2) $N \rightarrow 0$

(3) $\epsilon \rightarrow 0$

he was able to solve the equation for P_E in closed form, i.e.,

$$P_E = \frac{1}{2} e^{-S_0} M \left(1, \frac{1}{2\alpha} + 1, S_0 \right) \quad (\text{IV-12})$$

for S_0 = number of photoelectrons generated at beam center

M = confluent hypergeometric function.

The result is plotted in Figure 45, for

$\epsilon = 0$ (infinite extinction ratio)

$N = 0$, no background

and with α as a parameter.

The curves show that $\alpha \leq .1$ is necessary if the average P_E is to be $< 10^{-6}$ for realizable laser powers. Section III.4 of Appendix III relates this requirement to various beam divergences.

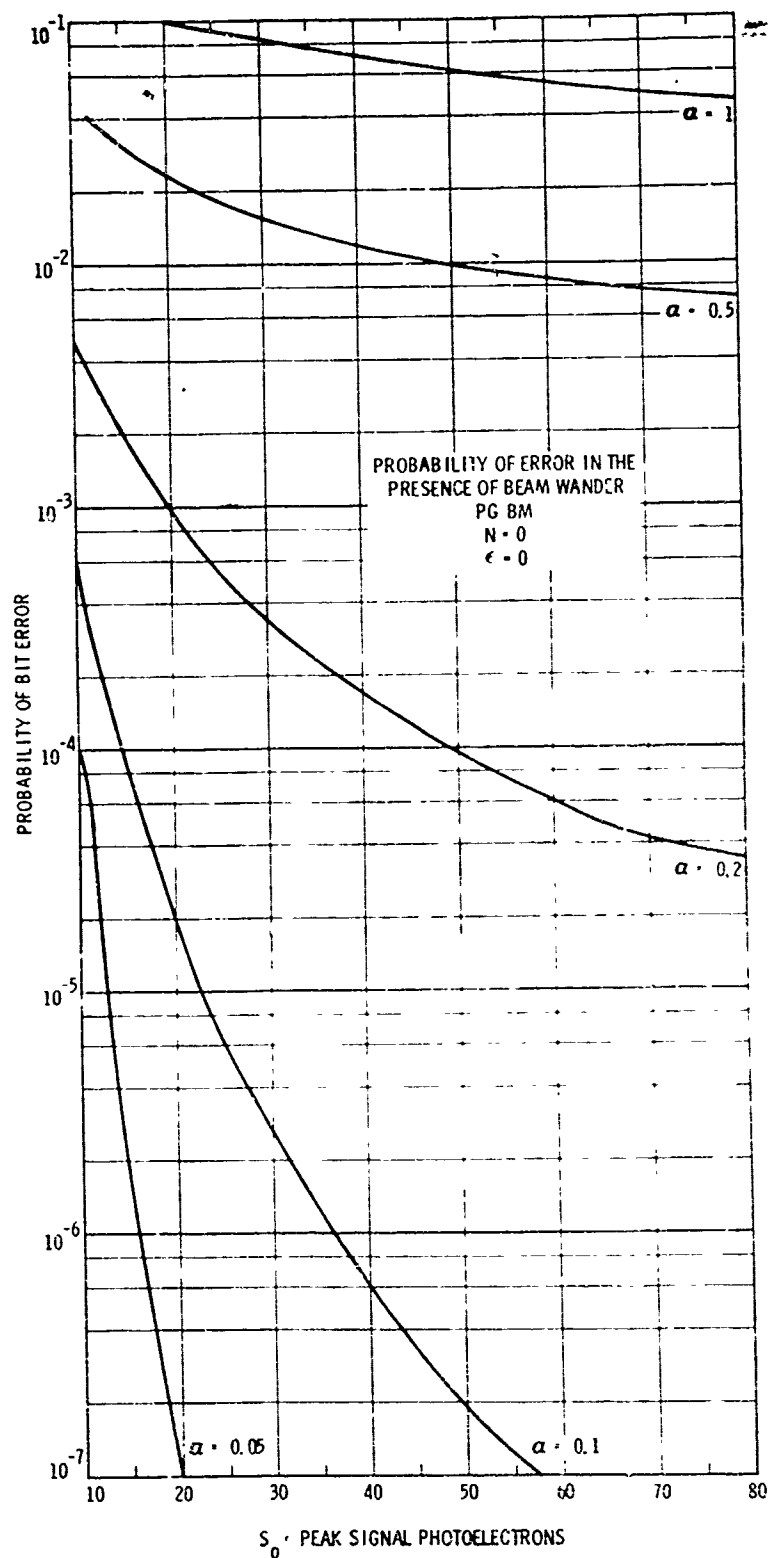


Figure 45. Beam Wander Effects on P_E for PG-BM.

IV.5 Combined Wander and Scintillation

The formulation for combined scintillation and wander depends on their assumed independence. Physically there appears to be very sound grounds for this assumption over an uplink path, since the scintillation is dominated by tropopause effects while wander has a large contribution from near-earth effects.⁽¹⁹⁾ From a frequency spectra point-of-view, this is also evident, since scintillation extends to much higher frequencies than does wander.^(19,35) Therefore we may consider a beam slowly wandering randomly while a detector sees rapid scintillations at every point on the irradiance profile.

We formulate the probability density as follows:

$$\text{Wander: } f_2(y) = \frac{1}{2\alpha S_0} \left(\frac{y}{S_0} \right)^{\frac{1}{2\alpha} - 1} ; 0 \leq y \leq S_0 \quad (\text{IV-10'})$$

where, as before, S_0 is the number of photoelectrons generated at beam center. Scintillation can then be expressed as a conditional density:

$$\begin{aligned} \text{Scintillation: } f_1(S|y) &= \frac{1}{[2\pi C_\ell]}^{1/2} \frac{1}{2S} \exp \left[-\frac{1}{2C_\ell} \left(\frac{1}{2} \ln(S/y) + C_\ell \right)^2 \right] \\ &0 \leq S \leq \infty \\ &0 \leq y \leq S_0 \end{aligned} \quad (\text{IV-9'})$$

Therefore the probability that the power at the detector is proportional to S and that the mean value of S is y is given by

$$f(S, y) = f_1(S|y) f_2(y) \quad (\text{IV-13})$$

Then the probability density is given by

$$\begin{aligned} f(S) &= \int_{-\infty}^{\infty} f(S, y) dy = \int_0^{S_0} f_1(s|y) f_2(y) dy \\ &= \frac{1}{4\alpha S_0} \frac{1}{[2\pi C_\ell]}^{1/2} \int_0^{S_0} dy \left(\frac{y}{S_0} \right)^{\frac{1}{2\alpha} - 1} \exp \left[-\frac{1}{2C_\ell} \left(\frac{1}{2} \ln \left(\frac{S}{y} \right) + C_\ell \right)^2 \right] \end{aligned} \quad (\text{IV-14})$$

Putting this expression into (IV-6) and (IV-7) we could calculate P_E as a function of S_0 with ϵ , N , α and C_ℓ as parameters. (We have not done it in the present program because it was not necessary in order to derive the best experimental techniques for testing the uplink theory.)

There is one assumption made in this development which must be tested, namely that C_ℓ is independent of y . Ho⁽³⁶⁾ has estimated that C_ℓ at beam center is much less than what it is near beam edge (e^{-2} irradiance point).

Therefore, we propose to obtain P_E both for constant and variable C_ℓ . The way in which C_ℓ varies with y will be determined by theoretical estimates based on work discussed in the next Appendix.

IV.6 Outage

An average bit error rate is only one of a number of possible ways to characterize a communication link. One alternative is to consider the cumulative probability, set it equal to some value, and assume that below that value the link is "out". This can be formulated as follows:

$$\text{CUM PROB } (S < S_x) = \int_{-\infty}^{S_x} f(S) dS \quad (\text{IV-15})$$

Then Cum Prob $(S < S_x) = 10^{-6}$ results in a relation among the parameters which implies the margin needed to maintain this outage level.

Outage is appropriate in characterizing a link when the duration of errors is \gg duration of a bit interval. This is the case for the high data rate uplink, since deep fades caused by scintillation (or wander) last for $<10^{-3}$ seconds, while the bit decision interval is $\sim 10^{-9}$ seconds. For the beacon command links the choice between appropriate characterizations is far less clearcut, since the decision interval is $\sim 10^{-4}$ seconds.

IV.6.1 Scintillation Alone

Using the appropriate probability density we find:

$$\begin{aligned} \text{Prob } (S < S_x) &= \frac{1}{2} \left\{ 1 + \text{erf} \left(\frac{\frac{1}{2} \ln (S_x/S_o) + C_\ell}{\sqrt{2C_\ell}} \right) \right\} \\ &= P \left\{ \frac{\frac{1}{2} \ln (S_x/S_o) + C_\ell}{\sqrt{C_\ell}} \right\} \end{aligned} \quad (\text{IV-16})$$

Prob ($S < S_x$) = 10^{-6} implies

$$\left[\frac{1}{2} \ln (S_x/S_o) + C_\ell \right] / \sqrt{C_\ell} = -4.7$$

$$\text{i.e., } S_x/S_o = \exp 2 \left\{ -4.7 \sqrt{C_\ell} - C_\ell \right\} \quad (\text{IV-17})$$

for S_o = average number of photoelectrons generated.

Thus, for a given C_ℓ , there is a fixed ratio of S_x/S_o such that the detected signal falls below S_x only 10^{-6} of the time. Alternatively, one could consider this as the equation determining the necessary increase in S_o such that the signal level falls below a given S_x only 10^{-6} of the time.

IV.6.2 Wander Alone

As derived in Appendix III,

$$\text{Prob } (S < S_x) = \left(\frac{S_x}{S_o} \right)^{\frac{1}{2\alpha}} \quad (\text{IV-18})$$

so that an outage of 10^{-6} implies

$$\frac{S_x}{S_o} = 10^{-12\alpha} \quad (\text{IV-19})$$

This is then interpreted as above.

IV.6.3 Combined Wander and Scintillation

We propose to treat the combined case with a computer analysis in the next phase of the OPTS Program.

Appendix V

COMBINED BEAM WANDER AND SCINTILLATION EFFECTS

V.1 Introduction

As has been mentioned in the earlier appendices, scintillation, wander, and spread occur simultaneously. Appendix II treated scintillation alone because it was restricted to considering only those power fluctuations that occur on or near beam axis, said beam axis remaining co-linear with a fixed direction in space. Appendix III treated wander alone because it was restricted to considering an undeformed wavefront. In this Appendix we formulate the equations that treat all the effects simultaneously.

V.2 Theory

The best starting point is that of Lutomirski and Yura⁽³⁷⁾. They modified the Huygens-Fresnel principle to yield the instantaneous irradiance at a point p:

$$I(p) = U(p) U^*(p) = \left(\frac{1 + \cos X_0}{2 \lambda S_0} \right)^2 \iint d^2 r_1 d^2 r_2 \exp \left[ik (S_1 - S_2) \right] \\ \times \exp \left[\psi(r_1) + \psi^*(r_2) \right] U(r_1) U^*(r_2) \quad (V-1)$$

where the integration is over the transmitter aperture;

$S_{1,2}$ is the distance from p to $r_{1,2}$

λ = wavelength = $2\pi/k$

S_0 = average distance from p to the transmitter

$\psi(r_1)$ = complex phase for a beam originating at p.

$U(r_1)$ = field at r_1 as transmitted

The turbulence effects/information are all contained in the complex phase term. Because the instantaneous distribution of turbulence is unknown, we can only predict average values of the irradiance, etc.

In principle one can calculate all the moments of the irradiance for arbitrary ranges, turbulence conditions and initial beam shapes. In practice, the calculations become quite difficult for the higher moments.

V.3.1 First Moment: Average Irradiance

Lutomirski and Yura showed that for a receiver in the far field of the transmitter, the average irradiance is given by

$$\overline{I}(\rho) = \left(\frac{k}{2\pi Z}\right)^2 \int d^2\rho \, e^{-\frac{1}{2} D(\rho)} e^{-\frac{ik}{Z} (\vec{\rho} \cdot \vec{\rho})} \times \int d^2r \, U(r+\rho/2) U^*(r-\rho/2) e^{\frac{ik}{Z} (\vec{\rho} \cdot \vec{r})} \quad (V-2)$$

for Z = range, receiver to transmitter

$D(\rho)$ = wave structure function⁽³⁵⁾ for a spherical wave propagating from the receiver to the transmitter, and the limits on the integrals are obtained from the transformation equations

$$\vec{\rho} = \vec{r}_1 - \vec{r}_2$$

$$\vec{r} = \frac{1}{2} (\vec{r}_1 + \vec{r}_2)$$

If we assume

- | |
|--|
| (1) No transmitter truncation, so that the upper limit of the integration $\rightarrow \infty$ |
| (2) No center blockage, so that the lower limit of the integration $\rightarrow 0$ |
| (3) A collimated gaussian beam, so that |

$$U(r_1) = A_0 e^{-r_1^2/a^2} \quad (V-3)$$

for $a = e^{-2}$ irradiance diameter at the transmitter

We find

$$\overline{I(p)} = \left(\frac{k}{2\pi Z}\right)^2 \frac{\pi a^2}{2} |A_o|^2 2\pi \int_0^\infty d\rho \rho e^{-\frac{1}{2} D(\rho)} e^{-\rho^2/2b^2} J_o\left(\frac{k\rho\rho}{Z}\right) \quad (V-4)$$

$$\text{for} \quad \frac{1}{2b^2} = \frac{1}{2a^2} + \frac{k^2 a^2}{2(4Z^2)} \quad (V-5)$$

Further assuming ⁽³⁸⁾ (4)

$$e^{-\frac{1}{2} D(\rho)} \equiv \text{MTF} = e^{-(\rho/\rho_o)^{5/3}} \approx e^{-(\rho/\rho_o)^2} \quad (V-6)$$

and using the formula ⁽³³⁾

$$\int_0^\infty e^{-\gamma y} J_o(n\sqrt{y}) dy = \frac{1}{\gamma} e^{-n^2/4\gamma} \quad (V-7)$$

we find:

$$\overline{I(p)} = \frac{\pi^2 a^2 d^2}{2} \left(\frac{k}{2\pi Z}\right)^2 |A_o|^2 e^{-\frac{k^2 d^2 p^2}{4Z^2}} \quad (V-8)$$

$$\text{for} \quad \frac{1}{d^2} = \frac{1}{2b^2} + \frac{1}{\rho_o^2} \quad (V-9)$$

Therefore, with these approximations the average beam is broadened as determined by the factor ρ_o . Note, however, that because this is an average, both beam spread and beam wander are included in this expression.

If instead of a collimated beam we consider the general case with a radius of wavefront curvature $\neq \infty$ at the transmitter, then

$$U(r_1) = A_0 \exp - \left\{ \frac{r_1^2}{a^2} + \frac{ik r_1^2}{2R} \right\} \quad (V-10)$$

for R = radius of wavefront curvature (for this formulation $R > 0 \rightarrow$ focusing and $R < 0 \rightarrow$ defocusing).

We find

$$\overline{I(p)} = \frac{\pi^2 a^2 g^2}{2} \left(\frac{k}{2\pi Z} \right)^2 |A_0|^2 e^{-\frac{k^2 g^2 p^2}{4Z^2}} \quad (V-11)$$

$$\text{for} \quad \frac{1}{g^2} = \frac{1}{2f^2} + \frac{1}{\rho_o^2} \quad (V-12)$$

$$\text{and} \quad \frac{1}{2f^2} = \frac{1}{2a^2} + \frac{k^2 a^2}{2 \cdot 4} \left(\frac{1}{z} - \frac{1}{R} \right)^2 \quad (V-13)$$

We propose, in future work, to remove assumptions (1), (2) and (4) so that the general case may be treated.

V.2.2 Second Moment: Variance of the Irradiance Fluctuations

The expression for the instantaneous product of the irradiance at points p_1 and p_2 is given by

$$I(p_1) I(p_2) = \left(\frac{1 + \cos X_0}{2\lambda S_0} \right)^4 \iiint \exp \left[ik (S_1 - S_2 + S_3 - S_4) \right] \exp \left[\psi(r_1) + \psi^*(r_2) + \psi(r_2) + \psi^*(r_4) \right] \\ \times U(r_1) U^*(r_2) U(r_3) U^*(r_4) d^2 r_1 d^2 r_2 d^2 r_3 d^2 r_4 \quad (V-14)$$

Now $\overline{I(p_1) I(p_2)}$ involves $\langle \exp [\psi(r_1) + \psi^*(r_2) + \psi(r_3) + \psi^*(r_4)] \rangle$

Fried⁽³⁹⁾ has shown that this expression is exactly given by:

$$\begin{aligned} \langle \rangle = \exp \left[-\frac{1}{2} \left\{ D(|r_1-r_2|) - D(|r_1-r_3|) + D(|r_1-r_4|) \right. \right. \\ \left. \left. + D(|x_2-x_3|) - D(|x_2-x_4|) + D(|x_3-x_4|) \right\} \right. \\ \left. + 2 \left[C_\ell(|x_1-x_3|) + C_\ell(|x_2-x_4|) \right] \right] \end{aligned} \quad (V-15)$$

We now make the assumption (which is somewhat inaccurate for $D(\rho) \propto \rho^{5/3}$)

that (5)

$$\begin{aligned} \langle \exp [\psi(r_1) + \psi^*(r_2) + \psi(r_3) + \psi^*(r_4)] \rangle = \\ \exp \left[-\frac{1}{2} D(|x_1-x_2+x_3-x_4|) \right. \\ \left. + 2 \left[C_\ell(|x_1-x_3|) + C_\ell(|x_2-x_4|) \right] \right] \end{aligned} \quad (V-16)$$

and (6) as with assumption (1), that the transmitter aperture is so large that $\exp 2 \left[C_\ell(|x_1-x_3|) + C_\ell(|x_2-x_4|) \right]$ can be taken outside the integral in the form $\exp 4\beta C_\ell$ for $\beta \ll 1$, i.e., significant aperture averaging is occurring⁽³⁹⁾.

Then

$$\begin{aligned} \overline{I(p_1) I(p_2)} = \left(\frac{1 + \cos X_0}{2\lambda s_0} \right)^4 e^{4\beta C_\ell} \iiint \exp \left\{ ik (S_1 - S_2 + S_3 - S_4) \right\} \\ \times \exp -\frac{1}{2} \left\{ D(|r_1-r_2+r_3-r_4|) \right\} U(r_1)U^*(r_2) U(r_3)U^*(r_4) d^2r_1 d^2r_2 d^2r_3 d^2r_4 \end{aligned} \quad (V-17)$$

Making the change of variables:

$$\begin{aligned}\vec{\rho} &= \vec{r}_1 - \vec{r}_2 & \vec{\beta} &= \vec{r}_4 - \vec{r}_3 \\ \vec{\delta} &= \frac{1}{2} (\vec{r}_1 + \vec{r}_2) & \vec{\gamma} &= \frac{1}{2} (\vec{r}_4 + \vec{r}_3)\end{aligned}$$

and using assumptions (1), (2) and (3) again we find

$$\overline{I(p_1) I(p_2)} = \left(\frac{\pi a^2}{2} \right)^2 \pi b^2 |A_0|^4 \left(\frac{k}{2\pi Z} \right)^4 e^{4\beta C_\ell} \frac{k^2 b^2 (\overline{p_1 - p_2})^2}{4Z^2} \times \int_0^\infty dx x e^{-x^2/4b^2} e^{-\frac{1}{2} D(x)} J_0 \left(\frac{kx |p_1 + p_2|}{2Z} \right) \quad (V-18)$$

where we have again used equation (V-7).

Again making assumption (4),

$$\overline{I(p_1) I(p_2)} = \left(\frac{\pi a^2}{2} \right)^2 \pi^2 b^2 c^2 |A_0|^4 \left(\frac{k}{2\pi Z} \right)^4 e^{4\beta C_\ell} e^{-\frac{k^2 b^2 (p_1 - p_2)^2}{4Z^2}} e^{-\frac{k^2 c^2 (p_1 + p_2)^2}{16Z^2}} \quad (V-19)$$

$$\text{where } \frac{1}{c^2} = \frac{1}{4b^2} + \frac{1}{\rho_o^2} \quad (V-20)$$

Using this and our earlier result for $\overline{I(p)}$ we find for the collimated case that the variance of the detected signal is given by

$$\sigma_I^2 = \frac{\overline{I^2(p)} - \overline{I(p)}^2}{\overline{I(p)}^2} = \frac{b^2 c^2}{d^4} e^{4\beta C_\ell} e^{-\frac{k^2 p^2}{4Z^2} (c^2 + 2d^2)} - 1 \quad (V-21)$$

(This expression should give us some indication how the scintillation increases away from beam center ($p \neq 0$)).

At the (average) beam center ($p = 0$),

$$\sigma_I^2 = \frac{b^2 c^2 e^{4\beta C_\ell}}{d^4} - 1 \quad (V-22)$$

$$= \frac{4\alpha^2 e^{4\beta C_\ell} + (4\alpha+1)(e^{4\beta C_\ell} - 1)}{4\alpha+1} \quad (V-22')$$

$$\text{where } \alpha = \frac{b^2}{\rho_o^2} \approx a^2/\rho_o^2 \quad \text{in the far field.} \quad (V-23)$$

For a very large transmitter, $\beta \rightarrow 0$ and

$$\overline{\sigma_I^2} \rightarrow \frac{4\alpha^2}{4\alpha+1}, \quad \text{the pure wander expression of Appendix III} \quad (V-24)$$

(which shows this expression asymptotically approaches the correct expression for larger apertures), if $\alpha = \frac{b^2}{\rho_o^2}$ is set equal to $\frac{\rho^2}{w^2}$, where

$$\begin{aligned} \overline{\rho^2} &= \text{mean square displacement of beam center} \\ w &= e^{-2} \text{ irradiance diameter.} \end{aligned}$$

Since for a collimated Gaussian beam (neglecting atmospherically induced beam spread)

$$w = \frac{\lambda Z}{\pi a}$$

$$\text{this implies that } \overline{\rho^2} = \left(\lambda Z / \pi \rho_o \right)^2 \quad (V-25)$$

We shall calculate the beam wander, $\overline{\rho^2}$, in the next section, and show that V-25 is indeed the case for all these assumptions. The significance of this equality will be discussed in Section V-4.

Again removing assumption (3) we find the same expression for $\overline{I(p_1)I(p_2)}$, but with

$$\frac{1}{2b^2} \rightarrow \frac{1}{2f^2}$$

Defining $\eta = \frac{f^2}{\rho_o}$, equation V-22' remains the same with $\alpha \rightarrow \eta$, and $\overline{\sigma_I^2} \rightarrow \frac{4\eta^2}{4\eta+1}$

for very large transmitters. Therefore the relative power fluctuations due to wander for focussed/defocussed beams and collimated beams depends on the ratio

$$\frac{\eta}{\alpha} = \frac{f^2}{b^2} \quad (V-26)$$

For identical beam sizes at the transmitter⁽⁴⁰⁾

$$\frac{\eta}{\alpha} = \frac{4 R^2 Z^2 + R^2 k^2 a^4}{4 R^2 Z^2 + k^2 a^4 (R-Z)^2} \quad (V-27)$$

Defocussed beams ($R < 0$) mean $\eta/\alpha < 1$ for all Z , as is intuitively reasonable, i.e., for a bigger beam one does not fall off the center peak as readily. Focused beams ($R > 0$) vary in their effects:

$$R > 3 Z/2 \quad \text{means} \quad \eta/\alpha < 1$$

$$\frac{Z}{2} < R < 3Z/2 \quad \text{means} \quad \eta/\alpha > 1$$

$$R < Z/2 \quad \text{means} \quad \eta/\alpha < 1$$

Since this last is the case desired, it seems the beam wander may be reduced by focusing, at least under our assumptions.

η/α is plotted as a function of $|R|/Z$ for focused beams in Figure 46 to demonstrate this point.

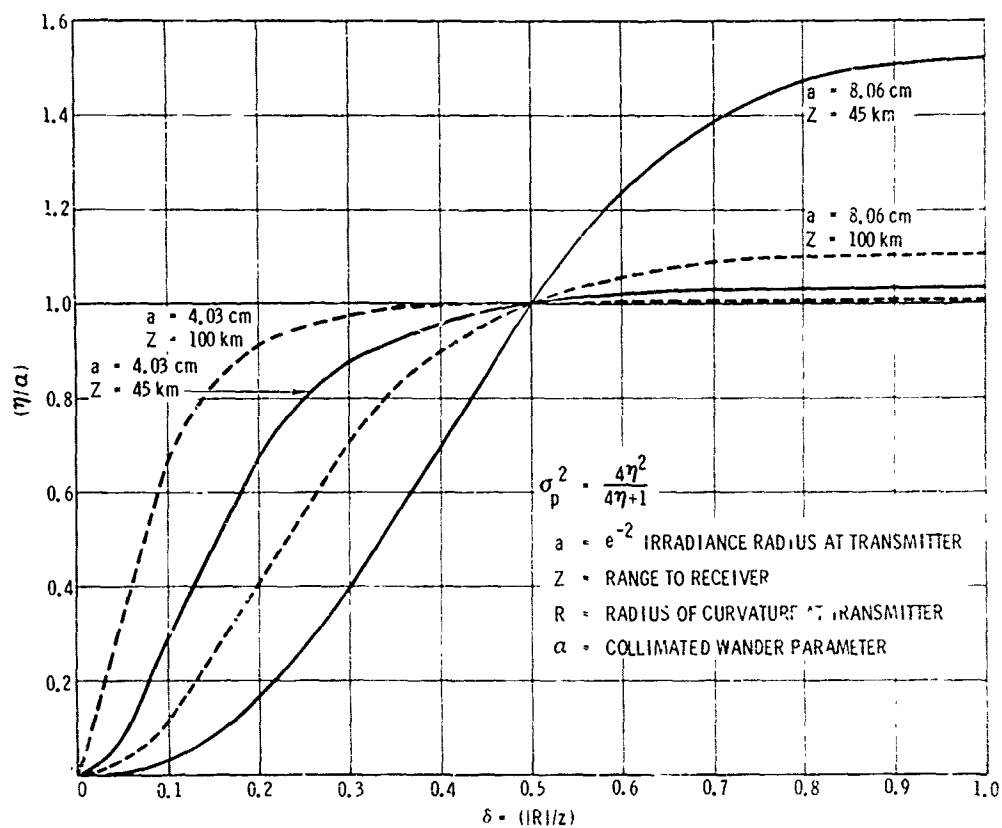


Figure 46. Beam Wander Parameter versus Focusing Parameter.

We propose to remove assumptions (1), (2), (4), (5) and (6) in future work. This is necessary if we are to realistically predict up-link system behavior for realistic optical systems, optics sizes and turbulence.

As an example of the results expected, we have formulated the expression for $\overline{I^2}$ for the Gaussian beam case and no other assumptions except for no center blockage, (2):

$$\begin{aligned} \overline{I^2} = & \left(\frac{k}{2\pi Z} \right)^4 |A_0|^4 \int_0^d \int_0^{2\pi} \delta d \delta d\theta_1 \int_0^{d/2} \int_0^{2\pi} \gamma d \gamma d\theta_2 \int_0^d \int_0^{2\pi} \alpha d \alpha d\theta_3 \int_0^{d/2} \int_0^{2\pi} \beta d \beta d\theta_4 \\ & \times \exp i \left[\frac{k}{2} \left(\frac{1}{Z} - \frac{1}{R} \right) \left\{ 2\gamma^2 + \frac{\delta^2}{2} - (2\beta^2 + \frac{\alpha^2}{2}) \right\} \right] \\ & \times \exp \left\{ C_\ell \left[4 - \frac{2}{\rho_a^{5/3}} \left(\delta^{5/3} + \alpha^{5/3} \right) \right] \right\} \\ & \times \exp - \left\{ \frac{1}{a^2} \left[\gamma^2 + \frac{\delta^2}{2} + 2\beta^2 + \frac{\alpha^2}{2} \right] \right\} \\ & \times \exp - \left[\frac{1}{\rho_o^{5/3}} \left\{ \left| \gamma - \beta + \frac{\delta - \alpha}{2} \right|^{5/3} - |\delta|^{5/3} + \left| \gamma - \beta + \frac{\delta + \alpha}{2} \right|^{5/3} + \left| \beta - \gamma + \frac{\delta + \alpha}{2} \right|^{5/3} \right. \right. \\ & \quad \left. \left. - |\alpha|^{5/3} + \left| \gamma - \beta + \frac{\alpha - \delta}{2} \right|^{5/3} \right\} \right] \end{aligned} \quad (V-28)$$

for $d < \rho_a$, where

ρ_a = amplitude correlation length at the transmitter

d = transmitter diameter

For $d > \rho_a$, two regimes arise: as above for $|\delta|, |\alpha| \leq \rho_a$;
and $\exp C_\ell [] \rightarrow 1$ For $|\delta|, |\alpha| > \rho_a$.

A computer analysis of this result will be performed.

V.3 Beam Wander

Feizulin and Kratsov⁽⁴¹⁾ have shown that the mean square position of beam center is given by

$$\overline{\rho^2} = \frac{\iint \vec{p}_1 \cdot \vec{p}_2 \overline{I(p_1)} \overline{I(p_2)} d^2 p_1 d^2 p_2}{\left[\int \overline{I(p)} d^2 p \right]^2} \quad (V-29)$$

where the integration is over the receiver plane.

Inserting our expression for the collimated beam case and using the change of variables

$$\vec{x} = \vec{p}_1 - \vec{p}_2 ; \quad \vec{y} = \frac{1}{2} (\vec{p}_1 + \vec{p}_2)$$

we find immediately

$$\overline{\rho^2} = \frac{\lambda^2 Z^2}{\pi^2 \rho_o^2} e^{4\beta C_\ell} \quad (V-30)$$

For a very large transmitter $\beta \rightarrow 0$ and

$$\overline{\rho^2} = \left(\frac{\lambda Z}{\pi \rho_o} \right)^2 \quad (V-25)$$

as predicted earlier. Therefore our pure wander analysis and the present analysis are consistent, even with (or perhaps because of) the vast number of assumptions used.

For the defocussed/focussed case it is easy to show that this result remains unchanged, i.e., with these assumptions the motion of the center of the beam (for large transmitted beams) is independent of beam size and/or wavefront curvature at the transmitter.

We propose to recalculate these results after removing all the assumptions used in obtaining $\overline{I(p)}$ and $\overline{I(p_1) I(p_2)}$.

V.4 Reciprocity

Expressing the beam motion in terms of an angle suggests a further extension of the theory :

$$\theta_{\text{rms}}^2 = \frac{\overline{\rho^2}}{z^2} = \frac{\lambda^2}{\pi^2 \rho_o^2} = \frac{4}{k^2 \rho_o^2} \quad (\text{V-31})$$

As will be discussed in Appendix VII, the mean square angle-of-arrival fluctuations of a beam (along one dimension) are given by⁽⁴²⁾

$$(\Delta\phi)_x^2 = \frac{1}{k^2 \rho_o^2} D_\phi(\rho) \quad (\text{V-32})$$

for $D_\phi(\rho)$ = phase structure function.

For the turbulence in the near-field of the receiver⁽³⁵⁾,

$$D_\phi(\rho) \sim D(\rho) \quad (\text{V-33})$$

Using assumption (4) again,

$$(\Delta\phi)_x^2 = \frac{1}{k^2 \rho_o^2} \left(\rho'_{o_o} \right)^2 = \frac{2}{k^2 \rho_o^2} \quad (\text{V-34})$$

For the general case then

$$(\Delta\phi)^2 = (\Delta\phi)^2_x + (\Delta\phi)^2_y = \frac{4}{k^2 \rho_o^2} \quad (V-35)$$

and $(\Delta\phi)^2 = \theta_{rms}^2 \quad (V-36)$

One can therefore predict⁶ that tracking on the angle-of-arrival fluctuations, $\Delta\phi$, will reduce θ_{rms} . Of course, it will have no effect on the scintillation (at beam center) or the beam spread.

We propose to theoretically check this key result without any of the assumptions involved here in the next phase.

V.5 Beam Spread

Using our results and the Feizulin and Kratsov⁽⁴¹⁾ formulation to calculate the mean square instantaneous size of the beam is straightforward. However, it results in the unlikely expression

$$SPREAD = 0 \quad (V-37)$$

Fried⁽⁴³⁾ has shown that assumption (4), viz

$$D(\rho) = \left(\frac{\rho}{\rho_o}\right)^2 \quad (V-38)$$

means that only wavefront tilt is retained in the turbulence effects, i.e., the beam will wander but not spread with this formulation.

Therefore, when we remove assumption (4) from our formulation we should obtain a consistent estimate of beam spread, beam wander and scintillation. This we propose to do in the next phase.

V.6 OPTS Tests of the Theory

Based on the analyses given above, OPTS will sufficiently test the theory if, in addition to the transmitter beam parameters listed in Section II.4 of Appendix II, the following is performed:

(a) Use an irradiance radius = 1.61 cm (25 μ rad collimated) to see the effects of an aperture $\sim \rho_o$ in size (see Appendix VI).

(b) Point the transmitter beams along the normal to a wavefront that originated at the balloon receiver. Measure the power fluctuations with a receiver at the point of origin of this downlink beam.

(c) Vary the receiver aperture independently of the transmitter beam size, to determine the meaning of "common optics" when a uniform irradiance distribution is received and a gaussian irradiance distribution is transmitted.

(d) Measure the size of the beam at the balloon receiver.

(e) Measure the effects of truncation and center blockage on the power fluctuations and beam size.

(f) Monitor the angle of arrival fluctuations at the ground receiver.

Appendix VI

MTF PARAMETER ρ_o

VI.1 Introduction

The MTF of an optical system is defined as the absolute magnitude of the two-dimensional spatial Fourier transform of the image spread function, i.e., it is a measure of the reduction in contrast suffered by each Fourier component of the object after transmission through the entire imaging system. Of course, the atmosphere (considered a part of the imaging system) degrades this MTF.

As seen in Appendix V, the spatial separation, ρ_o , at which the atmospheric MTF reaches its e^{-1} point plays a fundamental part in the theory of combined scintillation and wander effects. This Appendix, therefore, will estimate the atmospheric MTF parameter ρ_o , and discuss its measurability.

VI.2 Theory

Many different analytic techniques^{(12), (37), (38)} have found that the MTF of the atmosphere is given by

$$\text{MTF} = e^{-1/2 D(a,Z)} \quad (\text{VI-1})$$

for $D(a,Z)$ the wave structure function,⁽³⁵⁾

a = transverse dimension in the beam.

The general expression for the wave structure function from a point source is⁽³⁷⁾:

$$D(a,Z) = \frac{k^2}{2\pi} \int_0^Z dS \int_0^\infty d\sigma \, \Phi(\sigma^{1/2}; S) \left\{ 1 - J_0 \left(\sigma^{1/2} \frac{aS}{Z} \right) \right\} \quad (\text{VI-2})$$

for the propagation path from $S = 0$ to $S = Z$.

k = wave # ($2\pi/\lambda$)

J_0 = Bessel Function of zero-order.

The Kolmogorov spectrum of turbulence fluctuations implies⁽³⁵⁾

$$\Phi(\sigma^{1/2}, S) = 8.16 C_N^2(S) \sigma^{-11/3} \quad (\text{VI-3})$$

and the expression for a point source or spherical wave becomes

$$D^{SW}(a) = 2.91 k^2 a^{5/3} \int_0^Z dS C_N^2(S) (S/Z)^{5/3} \quad (\text{VI-4})$$

while for a plane wave source

$$D^{PW}(a) = 2.91 k^2 a^{5/3} \int_0^Z dS C_N^2(S) \quad (\text{VI-5})$$

for $C_N^2(S)$ = index of refraction structure parameter at S .

Taking the e^{-1} point of the MTF as the definition of ρ_o , we find

$$\rho_o^{SW} = 5.04 (10^7) \left[\frac{K_o k^2}{\cos \theta} \int_0^H dh \left(1 - \frac{h}{H}\right)^{5/3} f(h) \right]^{-3/5} \quad (\text{VI-6})$$

$$\rho_o^{PW} = 5.04 (10^7) \left[\frac{K_o k^2}{\cos \theta} \int_0^H dh f(h) \right]^{-3/5} \quad (\text{VI-7})$$

where we have used

$$C_N^2(h) = 10^{-13} K_o f(h) \quad (\text{VI-8})$$

θ = zenith angle so that $Z = H/\cos$ and $S = h/\cos$, and we are treating the case(s) of a point source (plane-wave source) at the altitude H .

For the transmitter at satellite altitudes, $H \gg$ all altitudes at which $f(h)$ is > 0 , and

$$\rho_o^{SW} = \rho_o^{PW} \quad (\text{VI-9})$$

For balloon altitudes, this is not the case. We have computer analyzed these expressions for many different forms of $f(h)$, $\lambda = 6328\text{\AA}$,

$H = 30$ km, $\theta = 45^\circ$. The results are summarized in Table V. Other values of K_0 can be included by noting $\rho_0 \propto K_0^{-3/5}$, and $10^{-3/5} \approx 0.25$.

From the table, we see that significant turbulence at the tropopause can greatly increase the ratio of point source to plane wave e^{-1} point, as seen by the five profiles listed which include a tropopause contribution centered at 15 km, i.e., the 2nd through 5th $f(h)$, and the last one.

As an example of the Table's use, consider the turbulence profile

$$C_N^2(h) = 10^{-13} \left\{ h^{-4/3} + 0.001 \exp - \left(\frac{h - 1.5 \times 10^4}{10^3} \right)^2 \right\} \quad (\text{VI-10})$$

For a satellite transmitter, we find

$$\rho_0 = (.25) (27.55) = 6.89 \text{ cm.}$$

If we consider a 10 μ rad collimated beam (at $\lambda = 6328\text{\AA}$), then its e^{-2} radius is $b = 4.03$ cm.

Using the results of Appendices III and V,

$$\alpha = \left(\frac{4.03}{6.89} \right)^2 = (.585)^2 = 0.342$$

We therefore find a predicted signal variance (at the satellite) due to wander alone given by

$$\overline{\sigma_p^2} = \frac{4\alpha^2}{4\alpha+1} = 0.198$$

and a ripple = $(.198)^{1/2} = 44.5\%$.

From Appendix IV, we see that this α leads to an average

$P_E \approx 10^{-3}$ at a peak signal level of 60 photoelectrons/bit interval (for fixed threshold detection).

This dramatically indicates the need to reduce these wander effects.

Table V

MTF Parameters for Real Turbulence Profiles

$K_o f(h)$	$\rho_o^{sw}(cm)$	$\rho_o^{pw}(cm)$	ρ_o^{sw}/ρ_o^{pw}
$h^{-1/3} e^{-h/1000}$	0.7414	0.7242	1.023
$.1 \left[h^{-4/3} + (0.1)e^{-\left(\frac{h-1.5 \times 10^4}{5 \times 10^2}\right)^2} \right]$	7.04	3.578	1.968
$.1 \left[\text{" } + (0.61) \text{ " } \right]$	23.34	13.29	1.756
$.1 \left[\text{" } + (0.001) \text{ " } \right]$	42.89	34.01	1.26
$.1 \left[\text{" } + (1) \text{ " } \right]$	1.807	0.905	1.996
$h^{-4/3}$	12.27	11.86	1.035
$h^{-5/6} e^{-h/100}$	6.696	6.683	1.002
$h^{-5/6} e^{-h/1000}$	3.689	3.648	1.01
$h^{-2/3} e^{-h/100}$	4.569	4.559	1.002
$h^{-2/3} e^{-h/1000}$	2.229	2.196	1.015
$.1 \left[h^{-4/3} + (0.001)e^{-\left(\frac{h-1.5 \times 10^4}{10^3}\right)^2} \right]$	38.53	27.55	1.4

VI.3 Measurement of the MTF

One way to test the theory utilized above would be to measure the MTF on the ground while measuring the wander at the balloon (or satellite).

Neglecting practical considerations for the moment, we could measure the MTF due to the atmosphere and optical receiver, for the point source on the balloon at an altitude ≈ 30 km.

The governing equation⁽¹⁹⁾ is:

$$MTF_{total} = MTF_{optics} \times MTF_{atmosphere} \quad (VI-11)$$

We may take the MTF_{optics} for an unobstructed circular aperture (neglecting aberrations, astigmatism, defocussing, etc.) as⁽⁴⁴⁾

$$MTF_{optics} = \frac{2}{\pi} \left\{ \cos^{-1} \left(\frac{a}{D} \right) - \frac{a}{D} \left[1 - \left(\frac{a}{D} \right)^2 \right]^{1/2} \right\} \quad (VI-12)$$

for D = the aperture diameter.

We have plotted the MTF_{total} in Figures 47 and 48 for $D = 7$ " (17.78 cm) and 10 " (25.4 cm) for a range of ρ_o values.

From the figures, it is clear that by measuring the system MTF at a range of spatial frequencies, we could obtain ρ_o , so long as $\rho_o < 15$ cm.

However, there are complex problems with the optical receiver system MTF. We must know it very well in the field in order to recover the effects of the atmosphere alone. Very small defocussing, aberration and astigmatism have large effects⁽⁴⁴⁾ and have caused us to consider this straightforward technique to be impractical.

There are two basic alternatives. The first is to test the theory indirectly as follows:

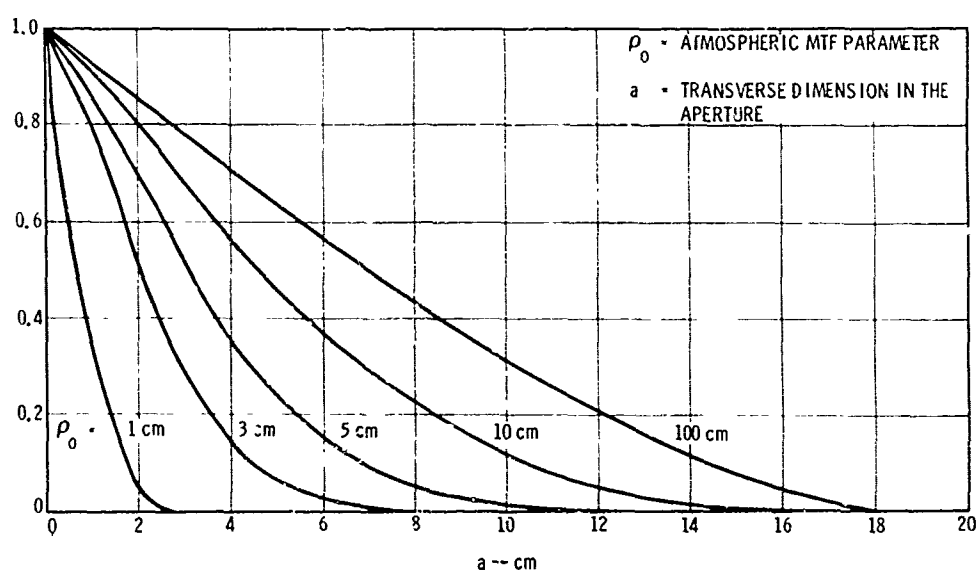


Figure 47. MTF_{TOTAL} for 7" Aperture.

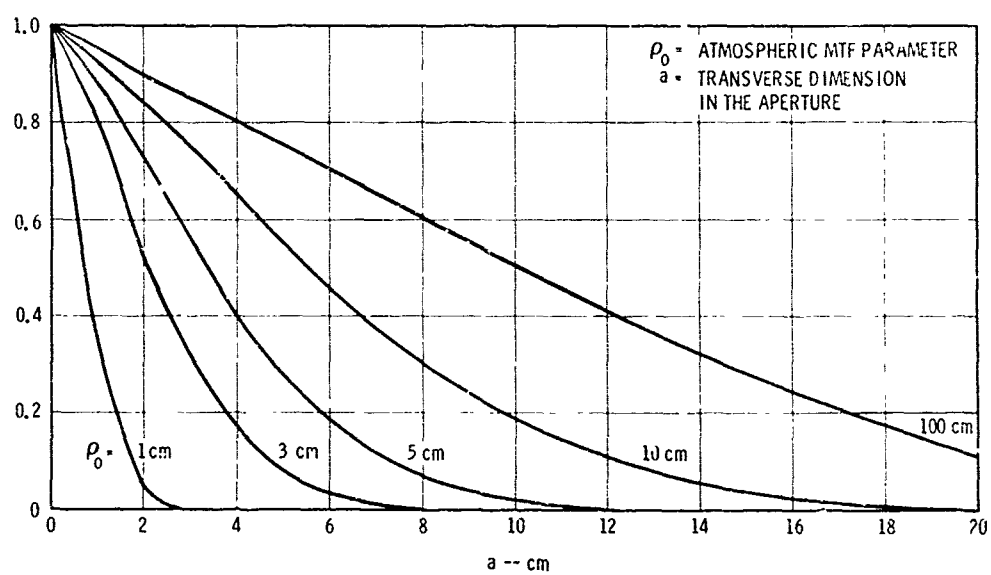


Figure 48. MTF_{TOTAL} for 10" Aperture.

Recall

$$MTF_{atmos} = \exp^{-1/2 D(\rho)}$$

This is a result of all optical turbulence theories, where

$$D(\rho) = \text{wave structure function} = 2(\rho/\rho_o)^{5/3} \quad (VI-13)$$

From fundamental statistical wave theory⁽³⁵⁾,

$$D(\rho) = D_\ell(\rho) + D_\phi(\rho) \quad (VI-14)$$

for $D_\ell(\rho)$ = log-amplitude structure function

$D_\phi(\rho)$ = phase structure function.

Moreover⁽²³⁾, $D_\ell(\rho) = 2(C_\ell(o) - C_\ell(\rho))$ (VI-15)

for $C_\ell(o)$ = variance of the log-amplitude fluctuations

and $C_\ell(\rho)$ = covariance of the log-amplitude fluctuations.

In addition⁽⁴²⁾

$$\sigma_\phi^2 = \frac{1}{k^2 \rho^2} D_\phi(\rho) \quad (VI-16)$$

for σ_ϕ^2 = variance of angle of arrival fluctuations measured by
a receiver of aperture diameter ρ

k = wave # $(2\pi/\lambda)$

Therefore, if we measure downlink variance, covariance and angle of arrival fluctuations, the MTF and/or ρ_o can be obtained from the equation

$$2 \left(\rho/\rho_o \right)^{5/3} = 2 \left\{ C_\ell(o) - C_\ell(\rho) \right\} + k^2 \rho^2 \sigma_\phi^2(\rho) \quad (VI-17)$$

This involves a covariance receiver on the ground, but avoids the difficult field measurement of the MTF.

The second alternative is to test the implications of the theory developed in Appendix V by tracking on the angle of arrival fluctuations, i.e., returning the uplink beam along the instantaneous normal to

the downlink wavefront. Since this is a direct test of the system proposed for use in the ground station of a high data rate uplink, it is a superior choice, and is our recommendation.

Appendix VII

ANGLE OF ARRIVAL FLUCTUATIONS

VII.1 Introduction

As seen in Appendices V and VI, theory predicts that a transmitter which tracks on received angle-of-arrival fluctuations will substantially reduce the beam wander effects. Moreover, it is clear from Appendix IV that the beam wander effects must be substantially reduced if the uplink is to operate.

For example, a 10 μ rad collimated beam that has an rms wander of 5 μ rad results in the wander parameter

$$\alpha = 4 \left(\frac{5 \times 10^{-6}}{10 \times 10^{-6}} \right)^2 = 1$$

a signal variance at the satellite of

$$\frac{\sigma_p^2}{2} = \frac{4\alpha^2}{4\alpha+1} = 0.8$$

a ripple = $(0.8)^{1/2} = 89\%$

and an average probability of bit error of

$$P_E = 5 \times 10^{-2} \text{ at a peak signal level of 60 photoelectrons/bit interval for fixed threshold detection.}$$

Therefore, we must consider the amplitude and frequency dependence of these angle-of-arrival fluctuations in order to determine the system design needed to track on them.

VII.2 Theory

The variance of the angle-of-arrival fluctuations is related to the power-spectral-density of those fluctuations by the equation^{(35), (42), (45)}

$$\sigma_{\theta}^2 = \int_f W(f) df \quad (\text{VII-1})$$

$$\text{so that } \int_f \frac{W(f) df}{\sigma_{\theta}^2} = 1 \quad (\text{VII-2})$$

Experimentally and theoretically^{(35), (42), (45)}, it has been found for large apertures that

$$\frac{W(f)}{\sigma_{\theta}^2} = 0.045 \sin^2 \left(\frac{\pi b f}{v_{\perp}} \right) \left(\frac{b}{v_{\perp}} \right)^{-5/3} f^{-8/3} \quad (\text{VII-3})$$

for f = frequency of fluctuations

b = receiver aperture diameter

v_{\perp} = transverse wind velocity.

We determine the normalized (or percentage) contribution of the high-frequency components by evaluating the integral

$$\int_F^{\infty} \frac{W(f) df}{\sigma_{\theta}^2}$$

$$\text{Defining } \delta = v_{\perp}/b \quad (\text{VII-4})$$

and integrating by parts, we find

$$\begin{aligned} \int_F^{\infty} \frac{W(f)}{\sigma_{\theta}^2} df = 0.045 \left\{ 0.3 (\delta/F)^{5/3} \right. \\ + (\delta/F)^{8/3} \frac{1}{4\pi} \sin \left(\frac{2\pi F}{\delta} \right) \\ - (\delta/F)^{11/3} \frac{1}{3\pi^2} \cos \left(\frac{2\pi F}{\delta} \right) \\ - \left(\frac{\delta}{F} \right)^{14/3} \frac{11}{18\pi^3} \sin \frac{2\pi F}{\delta} \\ \left. + \dots \dots \dots \right\} \end{aligned}$$

This expression is useful for $(\delta/F) \leq 1$. We have evaluated it for four values of this ratio in the following table.

δ/F	$\int_F \frac{W(f)}{\sigma_\theta^2} df$
1	0.012
0.67	0.00727
0.5	0.0041
0.33	0.0021

In other words, for $F = v_\perp/b$, only 1.2% of the variance of angle of arrival fluctuations is contributed by all frequencies $\geq F$, etc.

For a crosswind of 10 mph ($v_\perp = 440$ cm/sec), we find

δ	b
86.6 Hz	5.08 cm (2")
43.3 Hz	10.16 cm (4")
28.87 Hz	15.24 cm (6")
21.65 Hz	20.32 cm (8")
17.32 Hz	25.4 cm (10")

Theory and experiment also find that ⁽⁴⁵⁾ for large apertures,

$$\sigma_\theta^2 = Ab^{-1/3} \sec\theta \int_0^\infty C_N^2(h) dh \quad (\text{VII-5})$$

for starlight, where

θ = zenith angle

and $C_N^2(h)$ = index of refraction structure parameter. Daytime measurements ⁽⁴⁵⁾ have found $\sigma_\theta^2 \leq 4.9 \cdot 10^{-11} \text{ rad}^2$ for $b = 5$ cm at zenith. We might take these as typical daytime (and therefore worst-case) results, and estimate:

$\sigma_\theta^2 \text{ [rad}^2\text{]}$	b
$(7 \times 10^{-6})^2$	5.08 cm (2")
$(5.6 \times 10^{-6})^2$	15.24 cm (6")

Therefore, due to atmospheric turbulence effects alone, a ground station receiver must be able to track over $\leq 10 \mu\text{rad}$ rms with a bandwidth $\geq 25 \text{ Hz}$ if past theory and experiments are applicable.

VII.3 Measurement of the Angle of Arrival Fluctuations

As in the case of the MTF parameter ρ_0 , there are two practical alternatives to ascertaining the worth of the theory.

The first is to measure the angle of arrival fluctuations on the ground at the same time as measuring wander at the balloon (or satellite) receiver. For parallel turbulence paths and equivalent transmitter/receiver apertures the average angular deflections and frequency spectra should be equal. This, however, only tests the reciprocity theory on the average. To verify the prediction that instantaneously tracking on the angle-of-arrival fluctuations removes beam wander effects requires not parallel but common atmospheric paths, and the removal of instrumental effects.

Therefore, the second alternative, which is to do the reciprocity tracking directly, is the best choice. It not only directly tests the theory but also simulates the system to be used in high data rate uplink laser system.

Appendix VIII

CORRELATION LENGTH

VIII.1 Introduction

Scintillation results in beam break-up. The size (diameter) of the break-up areas is given by the correlation length. Therefore, the correlation length has two implications:

- A. The energy within a correlation area fluctuates coherently.
- B. For receiver aperture averaging to occur, the receiver diameter must be much larger than the correlation length^{(35), (42), (47)}.

Based on the theory developed in Appendix V, it appears that transmitter aperture averaging will also depend on the relative size of transmitter and correlation length, but verification of this awaits further computer analysis and experiments.

This Appendix, therefore, estimates the correlation lengths appropriate to the various links.

VIII.2 Theory

The correlation length theory tries to estimate the parameter ρ_a , which is the separation at which two receivers are uncorrelated in amplitude. For example, if $C_\ell(\rho)$ is the log amplitude correlation function⁽³⁵⁾ defined by

$$C_\ell(\rho) = \langle (\ell(x_1) - \bar{\ell}) (\ell(x_2) - \bar{\ell}) \rangle \quad (\text{VIII-1})$$

$$\text{for } |x_1 - x_2| = \rho$$

$$\text{and } \ell = \frac{1}{2} \ln (I / \bar{I})$$

for I = beam irradiance

\bar{I} = average irradiance,

Then ρ_a is defined by

$$C_\ell(\rho_a) = 0 \quad (\text{VIII-2})$$

where ρ_a is the first zero. In order to be consistent with the wave structure function formulation,

$$C_\ell(\rho) \approx C_\ell(0) \left(1 - (\rho/\rho_a)^{5/3}\right) \quad (\text{VIII-3})$$

In order to estimate ρ_a , we again start with the general expression derived by Schmelzer⁽²³⁾:

$$C_\ell(\rho) = \frac{-k^2}{8\pi} \operatorname{Re} \left\{ \int_0^Z ds \int_0^\infty \Phi(\sigma^{1/2}, S) J_0 \left(\frac{\sigma^{1/2} \rho S}{Z} \right) \exp \left[\frac{\sigma \gamma(Z, S)}{4} \right] \right. \\ \left. \times \left\{ \exp \left[\frac{\sigma \gamma(Z, S)}{4} \right] - \exp \left[\frac{\sigma \gamma^*(Z, S)}{4} \right] \right\} \right\} \quad (\text{VIII-4})$$

for k = wave #

Z = range

ρ = transverse dimension in the beam

Φ = spectrum of turbulence

J_0 = zero-order Bessel function.

and

$$\gamma(Z, S) = 2 \left(\frac{Z-S}{ik} \right) \left(\frac{S-ik\alpha^2}{Z-ik\alpha^2} \right) \quad (\text{VIII-5})$$

for

$$\frac{1}{\alpha^2} = \frac{1}{\alpha_0^2} - \frac{ik}{R} \quad (\text{VIII-6})$$

and the field at the transmitter given by

$$U = A \exp - \left\{ \frac{r^2}{2\alpha_0^2} - \frac{ikr^2}{2R} \right\} \quad (\text{VIII-7})$$

so that $2\alpha_o^2 = w^2$ in our usual formulation.

The integration over S is from transmitter to receiver.

Fried⁽⁴⁶⁾ specialized this result to a point source ($\alpha_o = 0$) and for a Kolmogorov spectrum of turbulence to find:

$$C_{\ell}^S(\rho) = \frac{8.16}{4\pi} k^2 \Gamma(-5/6) \operatorname{Re} \left\{ \int_0^Z ds C_N^2(S) \left\{ \left(\frac{S\rho}{Z} \right)^{5/3} \left[2^{8/3} \Gamma(11/6) \right]^{-1} \right. \right. \\ \left. \left. - \frac{1}{2} \left[\frac{1S(Z-S)}{kZ} \right]^{5/6} {}_1F_1 \left[-5/6; 1; \frac{1k\rho^2 S}{4(Z-S)Z} \right] \right\} \right\} \quad (\text{VIII-8})$$

We have performed a like analysis, making no assumptions with regard to source size, wavefront curvature or range, and have found

$$C_{\ell}(\rho) = \frac{8.16}{4\pi} k^2 \Gamma(-5/6) \left\{ \int_0^Z ds C_N^2(S) \frac{\cos(5\pi/6)}{2} \left(\frac{Z-S}{k} \right)^{5/6} X^{5/6} {}_1F_1 \left(-5/6; 1; \frac{-(\rho S/Z)^2}{\frac{4(Z-S)}{k} X} \right) \right. \\ \left. - \operatorname{Re} \int_0^Z ds C_N^2(S) \frac{1}{2} \left(\frac{Z-S}{k} \right)^{5/6} \left[X^2 + Y^2 \right]^{5/12} e^{i(5\phi/6)} {}_1F_1 \left(-5/6; 1; \frac{-(\rho S/Z)^2 (X-iY)}{\frac{4(Z-S)}{k} (X^2 + Y^2)} \right) \right\} \quad (\text{VIII-9})$$

where ${}_1F_1$ is a hypergeometric function

$$X = \frac{k \alpha_o^2 (C-B)}{C^2 + (k \alpha_o^2)^2} \quad (\text{VIII-10})$$

$$Y = \frac{k \alpha_o^2 + CB}{C^2 + (k \alpha_o^2)^2} \quad (\text{VIII-11})$$

$$\phi = \tan^{-1} \left[\frac{Y}{X} \right] + \pi \quad (\text{VIII-12})$$

$$B = S(1+A^2) + k \alpha_o^2 A \quad (\text{VIII-13})$$

$$C = Z (1+A^2) + k \alpha_o^2 A \quad (\text{VIII-14})$$

$$A = k \alpha_o^2 / R \quad (\text{VIII-15})$$

Assuming a thin-layer of turbulence is responsible for the amplitude fluctuations, we proceed as Minott did for the point source⁽⁴⁾. He manipulated the point source result to obtain

$$\frac{C_{\lambda}^S(\rho)}{C_{\lambda}^S(o)} = G(x) = 3.86 \operatorname{Re} \left[{}_1F_1^{5/6}(-5/6; 1; ix) \right] - 4.09x^{5/6} \quad (\text{VIII-16})$$

$$\text{for } x = \left(\frac{\rho}{\sqrt{\frac{4(Z-S)Z}{kS}}} \right) \quad (\text{VIII-17})$$

and $G(x) \rightarrow 0$ for $x \rightarrow 1$.

S is the range to the thin turbulent layer from the transmitter.

The equation $x = 1$ determines what we shall call the correlation length for a point source. As seen below for a receiver at balloon altitudes, (for $\lambda = 6328\text{\AA}$), the altitude of the turbulent layer is crucial.

Z	S	Correlation Length, ρ_a
30 km	15 km	11 cm
50 km	25 km	14 cm
100 km	50 km	20 cm
30 km	3 km	33 cm

We have considered the effect of a thin layer of turbulence located at a range S on the general source equation. For a test case, we considered a collimated beam, so that $R \rightarrow \infty$, $A \rightarrow 0$, $C \rightarrow Z$, and $B \rightarrow S$. Our estimate indicates that for the collimated beam the correlation length is larger than that for the point source, for the same turbulence profile.

We therefore shall use the point source estimate of ρ_a for an estimate of the correlation length for the paths of interest, i.e.,

$$\rho_a = \sqrt{\frac{4 (Z-S) Z}{kS}} \quad (\text{VIII-18})$$

VIII.3.1 Uplink to Balloon Receiver

For this case $\rho_a \geq$ the values given in the Table. With regard to an array of receivers, this means diodes spaced ≤ 10 cm apart would always see correlated power fluctuations, relative to their position on the Gaussian irradiance profile. Moreover, a receiver of 1 cm diameter will measure the variance of scintillation accurately, since no aperture averaging will occur over the receiver aperture.

VIII.3.2 Uplink to a Satellite Receiver

Using the equation, for $Z = 35,000$ km and $S = 15$ km, $\rho_a = 181$ meters. No aperture averaging will occur over the 160 cm diameter receiver aperture.

VIII.3.3 Downlink from a Balloon Transmitter

For this case, the first three entries in the table in Section VIII.2 also apply. However, the near earth turbulence will now have an opposite effect, as seen below;

Table

<u>Z(km)</u>	<u>S(km)</u>	<u>ρ_a (cm)</u>
30	27	3.66
50	45	4.73
100	90	6.69

and so a receiver with 10" (25.4 cm) diameter will result in significant receiver aperture averaging.

VIII.3.4 Downlink from a Satellite Transmitter

For a transmitter at satellite altitudes, the expression becomes

$$\rho_a \approx 2 \sqrt{\frac{Z-S}{k}} \quad (\text{VIII-19})$$

<u>Z-S (km)</u>	<u>ρ_a (cm)</u>
5	4.5
25	10

These values are for $\lambda = 6328\text{\AA}$ and a zenith angle $\sim 45^\circ$. Clearly, this approximate theory predicts that very large receiver apertures ($48'' = 122\text{ cm}$) will result in significant aperture averaging for this link.

Appendix IX

TRANSMITTER TRUNCATION/BLOCKAGE OF THE BEAM

IX.1 Introduction

In Appendices I, II, III, and IV, we have considered beams whose amplitude and phase at the transmitter were described by

$$U = A \exp - \left(\frac{r^2}{w^2} + \frac{ikr^2}{2R} \right) \quad (\text{IX-1})$$

for r = transverse dimension in the beam
 k = wave # ($2\pi/\lambda$)
 $w = e^{-2}$ irradiance radius
 R = radius of curvature of the wavefront.

As discussed in detail in Appendix I, this expression is the TEM₀₀ mode solution of the wave equation. Kogelnik and Li⁽²¹⁾ showed that the field at any distance Z from the waist of the beam (the point where w is a minimum ($\equiv w_0$) and $R = \infty$) is given by IX-1,

$$\text{for } w^2 = w_0^2 \left[1 + \left(\frac{\lambda Z}{\pi w_0^2} \right)^2 \right] \quad (\text{IX-2})$$

$$\text{and } R = Z \left[1 + \left(\frac{\pi w_0^2}{\lambda Z} \right)^2 \right] \quad (\text{IX-3})$$

Real optical systems modify these expressions and, in general, make them non-analytic. This is due to truncation, center blockage and aberrations that may be present.

In this Appendix we consider the effects of truncation and blockage, in order to estimate the potential additional effects of turbulence on these beams, over and above those calculated in Appendices II, III, and IV.

IX.2 Truncation

Two effects are treated:

- 1) The power transmitted/lost due to truncation.
- 2) The irradiance distribution as a function of path length.

Consider the power:

The irradiance pattern at any point in the beam is given by

$$I(Z) = I_0 e^{-\frac{2r^2}{w^2}} \quad (\text{IX-4})$$

To obtain the relative transmitted power for a beam truncated at radius = a, we calculate

$$\bar{P} = \frac{\int_0^a r e^{-2r^2/w^2} dr}{\int_0^\infty r e^{-2r^2/w^2} dr} = 1 - e^{-2a^2/w^2} \quad (\text{IX-5})$$

We have plotted this answer in Figure 49. It is clear that choosing $a/w \geq 2$ ensures > 99% of the power is transmitted.

The irradiance distribution as a function of path length cannot be obtained analytically except on axis. Extending some previous analyses (48), (49), (50) we can write the amplitude on axis for a collimated beam ($R = \infty$)

$$U(0, Z) = \frac{A}{Z} \int_0^a r e^{-r^2/w_0^2} dr \quad (\text{IX-6})$$

$$\text{for } \frac{1}{\alpha^2} = \frac{1}{w_0^2} - \frac{ik}{2Z} \quad (\text{IX-7})$$

Then

$$\begin{aligned} \overline{I}(0, Z) &= |U(0, Z)|^2 \\ &= \frac{k^2 w_0^4}{4Z^2 + k^2 w_0^4} \left\{ 1 + e^{-\frac{2a^2}{w_0^2}} - 2e^{-\frac{a^2}{w_0^2}} \cos\left(\frac{ka^2}{2Z}\right) \right\} \quad (\text{IX-8}) \end{aligned}$$

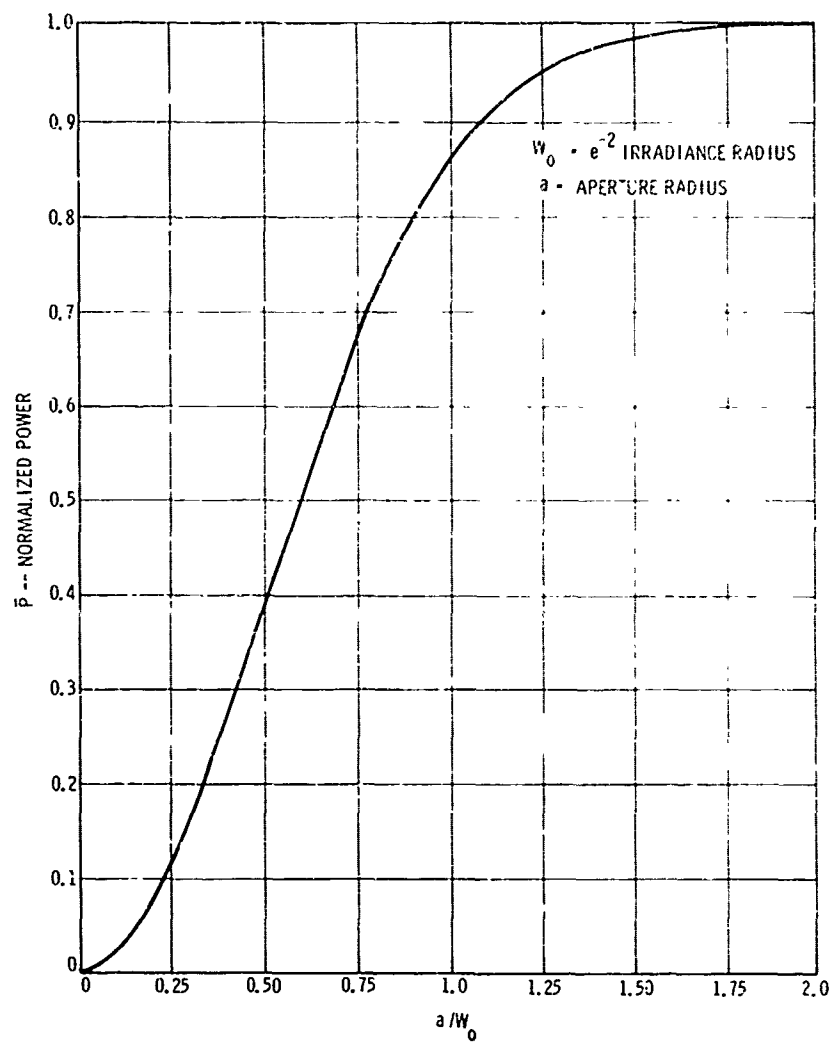


Figure 49. Normalized Transmitted Power for a Truncated Aperture.

and we have normalized the result so that $\overline{I(0,0)} = 1$. Considering the part in parenthesis, the result is oscillatory, with mean value $= 1 + e^{-2a^2/w_o^2}$ at a given Z , and oscillation amplitude $= 2 e^{-a^2/w_o^2}$. For $a > w_o$, this oscillation amplitude is less than the mean.

The zeroes of the oscillation bunch up near $Z = 0$, and the final minimum of the oscillation is at $Z = \infty$, i.e.,

$$\frac{ka^2}{2Z} \rightarrow 0 \quad (\text{IX-9})$$

The last maxima of the oscillation is at

$$\frac{ka^2}{2Z} = \pi, \text{ OR, } Z = \frac{ka^2}{2\pi} = \frac{a^2}{\lambda} \quad (\text{IX-10})$$

For $\lambda = 6328\text{\AA}$ and $a = 11.43 \text{ cm}$ (appropriate dimensions for a 9" refractive system), the last maxima is at $\sim 20.7 \text{ km}$ and there will be no oscillations at balloon altitudes.

We have plotted the effects of truncation on the on-axis irradiance for $w = 1.5 \text{ cm}$, 2.5 cm and 3.5 cm and $\lambda = 6328\text{\AA}$ in Figures 50, 51, and 52. It appears that $a/w \geq 2$ will ensure negligible effects again.

IX.3 Blockage and Truncation

Two effects are again treated:

- (1) The power transmitted/lost due to blockage.
- (2) The irradiance distribution as a function of path length.

To calculate the relative transmitted power for a beam with a center blockage of radius $= b$ and truncated at radius $= a$, we calculate

$$\overline{P} = \frac{\int_b^a r e^{-2r^2/w^2} dr}{\int_0^\infty r e^{-2r^2/w^2} dr}$$

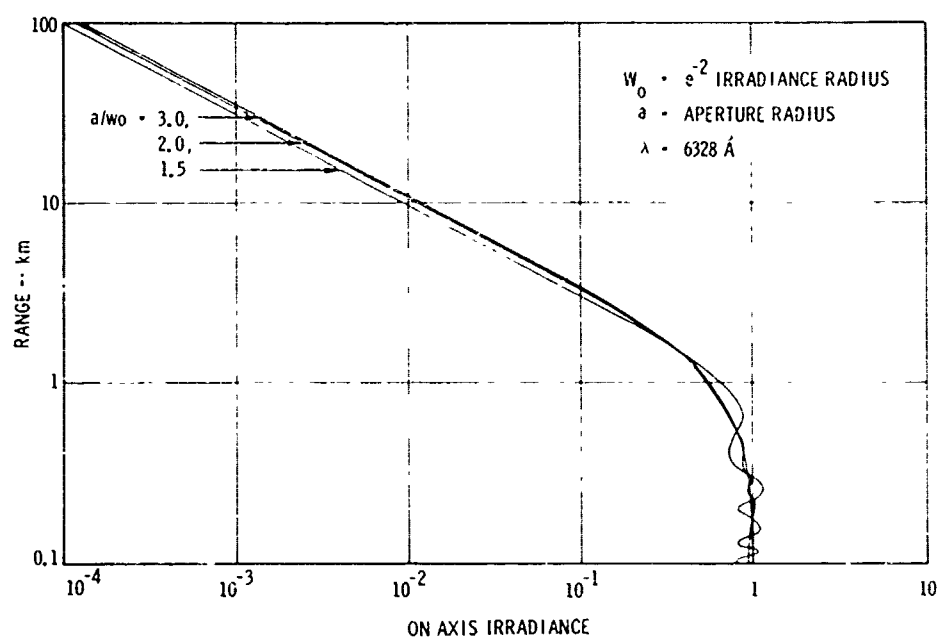


Figure 50. Truncation Effects for $w_0 = 1.5 \text{ cm}$

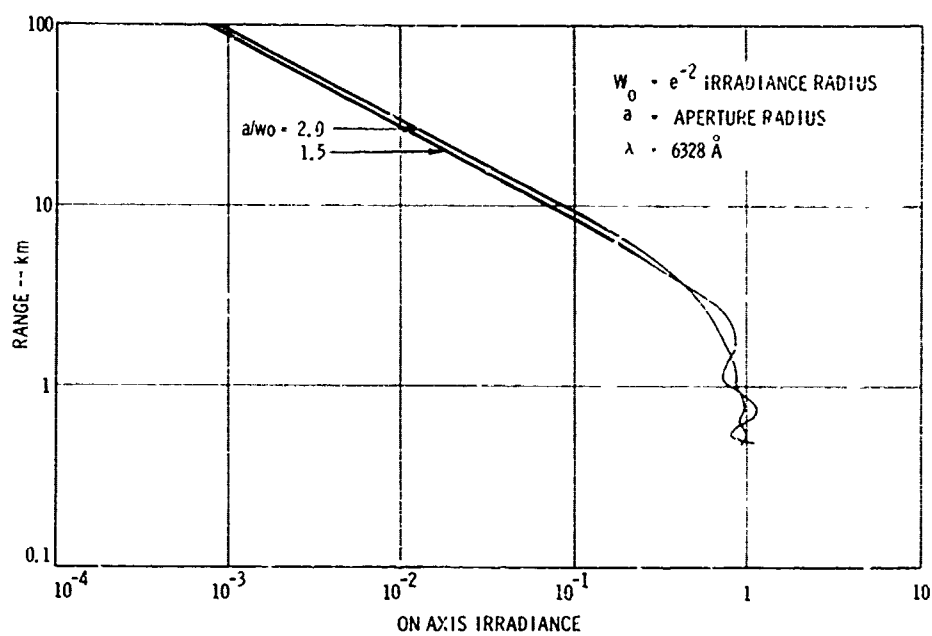


Figure 51. Truncation Effects for $w_0 = 2.5 \text{ cm}$.

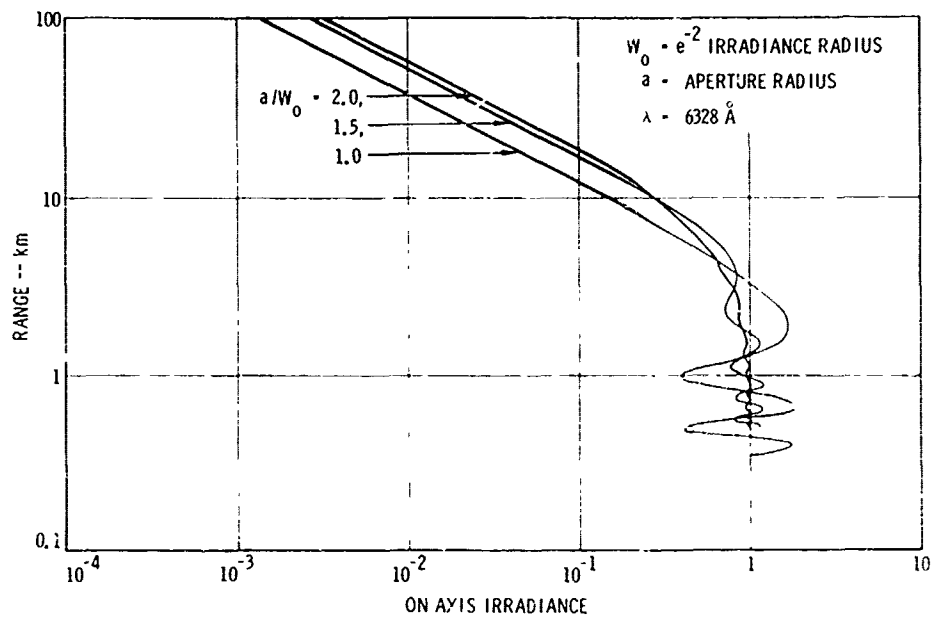


Figure 52. Truncation Effects for $w_0 = 3.5$ cm.

$$\bar{P} = e^{-\frac{2b^2}{w^2}} - e^{-\frac{2a^2}{w^2}} \quad (\text{IX-11})$$

The form of this answer shows that even for $a \gg w$, the transmitted power is reduced by the factor e^{-2b^2/w^2} .

To calculate the irradiance distribution we proceed as before and find for an initially collimated beam:

$$I(0, Z) = \frac{k^2 w_o^2}{4Z^2 + k^2 w_o^2} \left\{ e^{-\frac{2b^2}{w_o^2}} + e^{-\frac{2a^2}{w_o^2}} - 2e^{-\frac{a^2+b^2}{w_o^2}} \cos\left(\frac{k}{2Z}(a^2-b^2)\right) \right\} \quad (\text{IX-12})$$

Again, the result is oscillatory, with mean value $e^{-\frac{2b^2}{w_o^2}} + e^{-\frac{2a^2}{w_o^2}}$ at a given Z , and oscillation amplitude $= 2e^{-\frac{a^2+b^2}{w_o^2}}$.

The zeroes of the distribution again bunch up towards $Z = 0$, and the final minima is again at $Z = \infty$, i.e.,

$$\frac{k(a^2-b^2)}{2Z} \rightarrow 0 \quad (\text{IX-13})$$

The last maxima of the oscillation is at

$$\frac{k(a^2-b^2)}{2Z} = \pi, \text{ or, } Z = \frac{a^2-b^2}{\lambda} \quad (\text{IX-14})$$

which is nearer to the transmitter by the factor b^2/λ , i.e., for $\lambda = 6328\text{\AA}$, $a = 12.7\text{ cm}$ and $b = 3.175\text{ cm}$ (appropriate dimensions for

the 10" Celestron), the last maxima is at $25.5 - 1.6 = 23.9$ km.

Except for the fact that the mean value is less and the zeroes end sooner, this form is very like the case of zero-blockage, and so $a/w \geq 2$ should again insure negligible effects.

IX.4 Focussed and De-Focussed Beams

Avizonis et al⁽⁵¹⁾ and Webb⁽⁵²⁾ considered the case of focussed truncated beams and found

$$\overline{I}(0,Z) = \frac{k^2 w^4 R^2}{4Z^2 R^2 + k^2 w^4 (Z-R)^2} \left\{ 1 + e^{\frac{-2a^2}{w^2}} - 2e^{\frac{-a^2}{w^2}} \cos\left(\frac{ka^2}{2Z} \left(\frac{Z-R}{R}\right)\right) \right\} \quad (\text{IX-15})$$

They have extensive plots of this result in their papers. From the form of this result it behaves differently near the region $Z = R$ than the other results, and we must be careful to check this effect for our proposed focused system.

IX.5 Application to the Proposed Experiment

We can use the above equations to help determine the optimum optical configuration for our ground transmitter. The two basic candidates are compared in Table VI for collimated beams.

However, we cannot proceed to a final design without determining the turbulence effects. We must do this (for focussed beams, too) in future work by using the theory in Appendix V. This will check the effects of the fluctuations in irradiance off the optical axis also.

Table VI
Transmitter Optics Trade-offs

Candidate Systems	Radius	Radius of Blockage	HeNe Laser Beam Radius	N.F. On Axis Irrad Fluct.	F.F. Irrad. at Beam Center	F.F. Beam Divergence Effects, etc.
Refractive	4.5" 11.43 cm	-	6 cm	±5%	1	6.7 μ rad (coll)
	4.5" 11.43 cm	-	4.03 cm	±0.00974%	1	(10 μ rad) (coll)
Celestron Cassegrain	5" 12.7 cm	1.25" 3.175 cm	6 cm	±3%	57%	Same as refractive: Neg. Broad & side lobes
	5" 12.7 cm	1.25" 3.175 cm	4.03 cm	±0.018%	28.4%	Slight broadening and side lobes

Appendix X

EXPERIMENTAL PROBLEMS IN THE MEASUREMENTS OF THE TURBULENCE EFFECTS

X.1 Introduction

Any experiment designed to test the theories of scintillation and reciprocity tracking developed in Appendices II and V will have problems of interpretation unless it is very carefully designed. This is because all three turbulence effects (scintillation, wander and spread) result in simultaneous effects (power reduction and power fluctuations) for the narrow beams of interest.

Previous experimental efforts have measured the scintillation of very large beams⁽⁴²⁾ (negligible wander and spread), or the motion of focused beams at the focal spot⁽⁵³⁾ (which is indirectly related to its power fluctuations) but no power fluctuations on axis there.

In considering the possible experimental options, we have come up against two particular problems that will be discussed in detail here. Our conclusions concerning the best experimental technique are given in Sections V, VI, and VII of this report.

X.2 Mount Motion

Because we are interested in beams that are ≤ 10 μ radians in full angle beam divergence, we must measure beam motions of a small part of this, say ~ 1 μ rad. However, if the transmitter is randomly pointing the beam (due to mechanical, acoustical, thermal or electrical "noise"), then the effects of atmospheric wander will be masked, i.e., a receiver in the beam will be unable to distinguish between the two possible causes.

To obtain the relative amount of the power fluctuations caused by each, we utilize the beam wander analysis of Appendix III.

We take

β = rms angular pointing inaccuracies due to mount motion

Z = range to receiver

$w = e^{-2}$ irradiance radius at balloon

θ = full angle beam divergence

ϕ = rms pointing inaccuracies due to the atmosphere.

$$\text{Defining } \gamma = 4 (\beta/\theta)^2 \quad (X-1)$$

$$\text{and } \alpha = 4 (\phi/\theta)^2 \quad (X-2)$$

the normalized variance of the power fluctuations caused by the mount is

$$\overline{\sigma_M^2} = \frac{4\gamma^2}{4\gamma+1} \quad (X-3)$$

while that caused by the atmosphere is

$$\overline{\sigma_A^2} = \frac{4\alpha^2}{4\alpha+1} \quad (X-4)$$

To find the total effect, we add the unnormalized variances

$$\sigma_T^2 = \left(\frac{4\gamma^2}{4\gamma+1} \right) (2\gamma+1)^2 + \left(\frac{4\alpha^2}{4\alpha+1} \right) (2\alpha+1)^2 \quad (X-5)$$

which becomes

$$\sigma_T^2 = A(\beta, \theta) \left\{ 1 + B(\beta, \phi, \theta) \right\} \quad (X-6)$$

$$\text{for } B(\beta, \phi, \theta) = \left(\frac{\phi}{\beta} \right)^4 \left\{ \frac{(8\phi^2 + \theta^2)(16\beta^2 + \theta^2)}{(16\phi^2 + \theta^2)(8\beta^2 + \theta^2)} \right\} \quad (X-7)$$

$B(\beta, \phi, \theta)$ is the fractional part of the total variance contributed by the atmospheric wander. For it to be distinguished from mount motion, $B \geq 1$ is a reasonable condition.

For $\theta = 10 \mu\text{rad}$, $\phi = 5 \mu\text{rad}$ and $\beta = 15 \mu\text{rad}$, the value of $B = 0.014$ is obtained, i.e., only 1.4% of the total power fluctuations caused by beam motion are caused by atmospheric beam motion for these realistic parameters.

Clearly mount motion is a tremendous problem, and this is reflected in the further discussions in Section V.

X.3 Simultaneous Power Fluctuations Caused by Wander and Scintillation

Suppose now that some dual beam technique has removed all the mount motion effects, as described in Section V. A single detector will see power fluctuations caused by both scintillation and wander. If the atmospheric wander is not tracked out, then the power fluctuations it causes will swamp the scintillation effects of interest. This is shown by the following analysis:

Based on the analysis in Appendix II, we must measure values of the log amplitude variance, C_θ , in the realm of .01 to .05, or scintillation induced variances of power fluctuations in the realm of .04 to .022.

However, a randomly moving beam will result in a variance of power fluctuations that is far greater, as described by (X-2) and (X-4).

The relative magnitude of the power fluctuations can be seen from Figure 54, where we have plotted the normalized variance of power fluctuations due to each effect.

For example, $\theta = 10 \mu\text{rad}$ and $\phi = 5 \mu\text{rad}$ result in a variance of 0.8, which is 20X larger than for a scintillation of $C_\theta = .01$.

Now, in order to see the focusing induced reduction of scintillation at balloon altitude, we chose an (equivalent collimated) beam with $\theta = 6.7 \mu\text{rad}$ ($w = 6 \text{ cm}$, $\lambda = 6328 \text{ \AA}$) in Appendix II. $\phi = 5 \mu\text{rad}$ means this beam

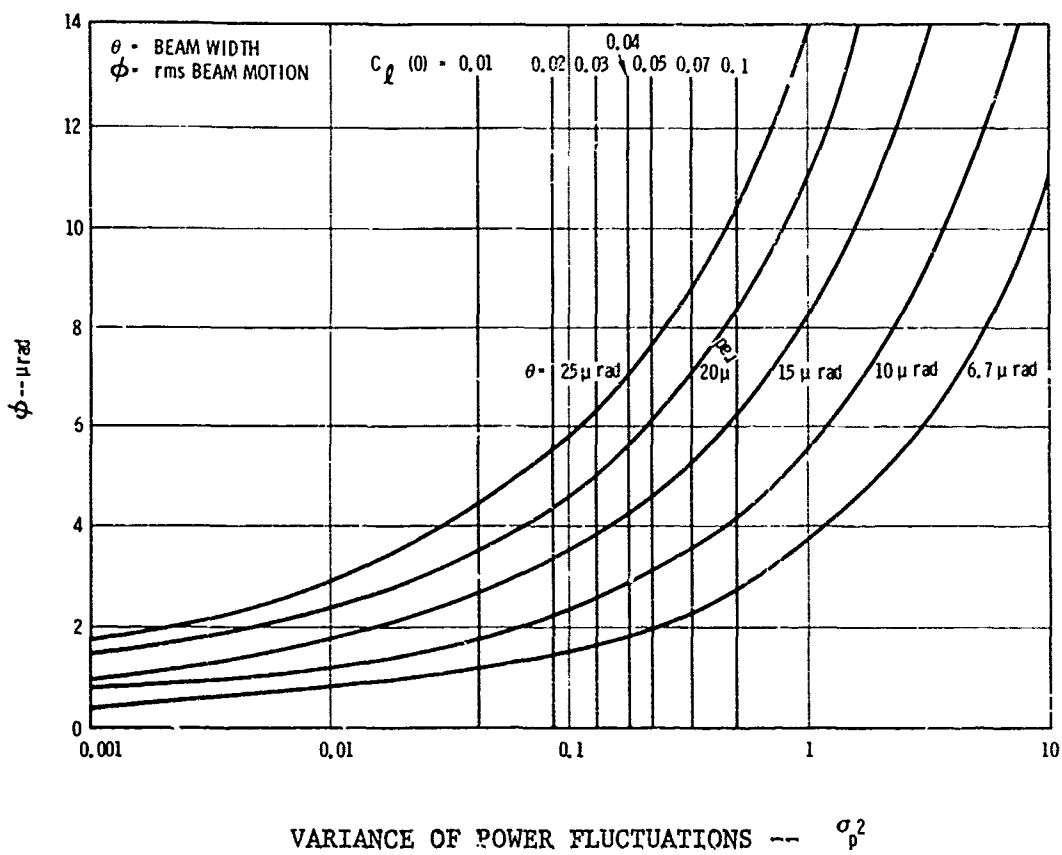


Figure 54. Simultaneous Wander and Scintillation Power Fluctuations.

has a wander induced power fluctuation of $\sigma_p^2 = 2$, ~ 10 times greater than the .19 value caused by scintillation alone ($C_\ell \sim .048$), as seen in Figure 39.

Clearly the values of the variance do not become commensurate until $\phi \sim 1 \mu\text{rad}$, and this is the likely specification of a reciprocity tracker.

In summary, unless the wander effects are reduced to $\sim 1 \mu\text{rad}$, the power fluctuations from a single detector will not be able to test the scintillation theory of Appendix II.

Appendix XI

STABILITY OF THE ATLAS MOUNT

XI.1 Introduction

During the course of the CPTS program, it became clear that the magnitude and frequency spectra of the ATLAS mount motions would be fundamentally important in selecting an experimental technique. Therefore, in late June, 1972, GTE Sylvania requested Mr. P. O. Minott of NASA-CSFC to measure them, and provide us with his results. This Appendix summarizes the results of his measurements, which were sent to us in mid-July.

XI.2 Frequency Spectra

Accelerometers were attached to the portion of the ATLAS' mount that would be appropriate for mounting OPTS equipment. Because of the attendant circuitry used, the measured results are meaningless below 5 Hz.

Figure 55 shows the results for the azimuth axis. We see that by 25 Hz, the magnitude of the fluctuation is $\leq 1 \mu\text{rad}$.

Figure 56 shows the results for the elevation axis. Again the magnitude of the fluctuations is $\leq 1 \mu\text{rad}$ for frequencies $\geq 25 \text{ Hz}$.

XI.3 Magnitude

The only results that go to $\leq 5 \text{ Hz}$ and yield reliable magnitudes are error signals from the star tracker on the ATLAS. Both balloon retroreflection tracking results, and starlight tracking results imply an rms jitter $\leq 15 \mu\text{rad}$.

July 14, 1972

1000

($\frac{\text{SEC}}{\text{HZ}}$)

5.4

214

2.7

POWER SPECTRAL DENSITY

AZIMUTH AXIS POSITION

ERROR FREQUENCY SPECTRUM

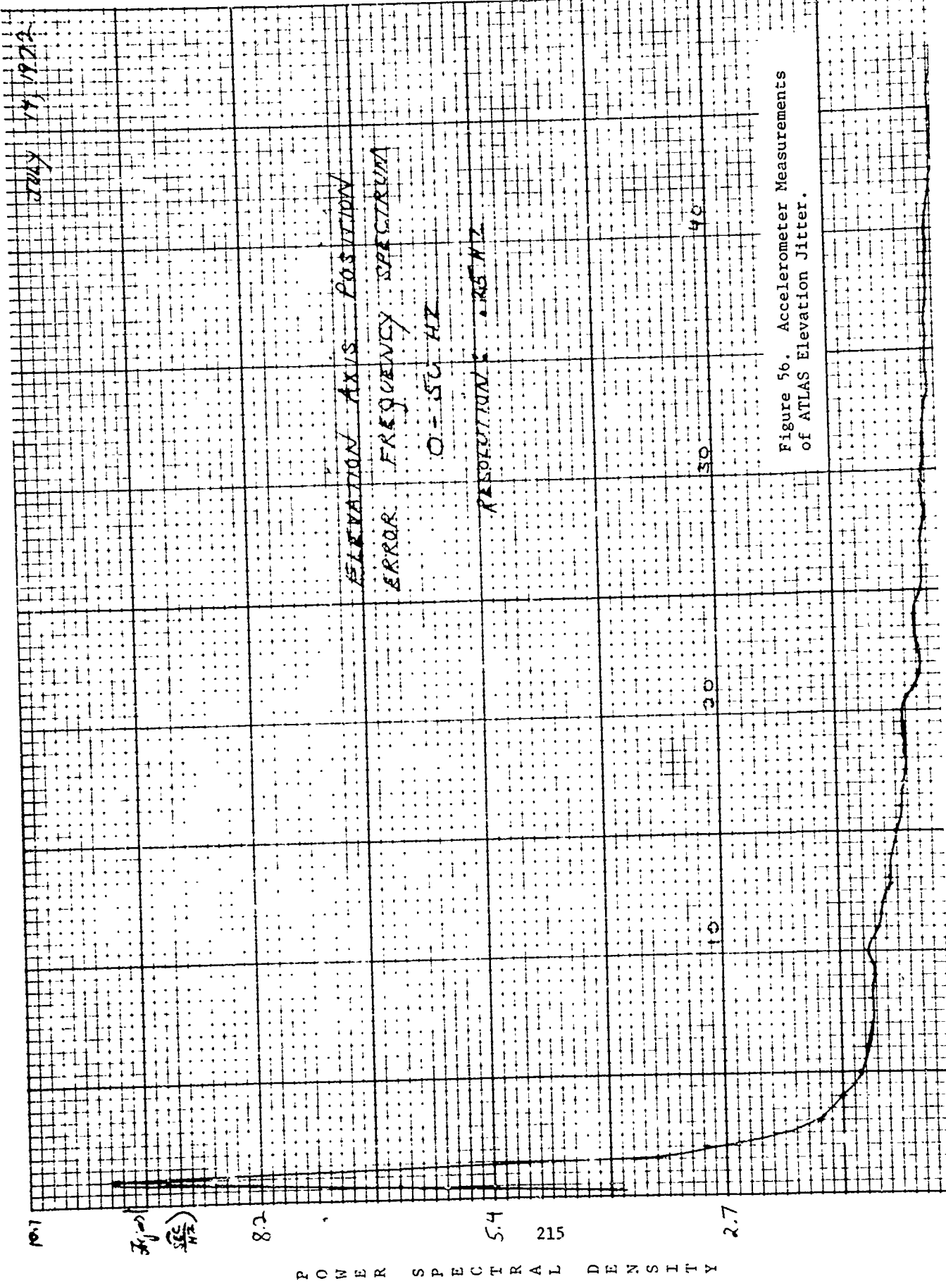
0 - 50 HZ

RESOLUTION = 25 HZ

10 30 40

Frequency (Hz)

Figure 55. Accelerometer Measurements of ATLAS Azimuth Jitter.



Appendix XII

SCANNING TRANSMITTER DESIGN

XII.1 Introduction

As discussed in Section V, a scanning transmitter approach was initially considered, because it was apparent that it had two basic advantages:

- 1) By scanning faster than any beam motion frequencies, we could in principle separate the spread and motion effects.
- 2) By scanning over a "region of uncertainty" of balloon position, we would be able to avoid the problem of tracking the balloon-borne receiver to fractional arc-second accuracies.

Based on these advantages, and because of the compressed schedule of the OPTS study, an optical design of a transmitter suitable for this approach was begun.

Later in the program it became apparent that scintillation could not be obtained from this technique, and so it was abandoned. However, the optical design had reached a stage in which it was worthy of inclusion in this final report, and so this Appendix outlines it.

XII.2 Optical Transmitter Design

A diagram of the scanning transmitter optical system is shown in Figure 57, and design details are presented in Figures 58 and 59.

A Spectra Physics 15 mW He-Ne laser was chosen because of its reliability for field use and adequate power output. The polarized laser beam passes through a rotatable analyzer, which controls the power output, and then through a turret which contains three beam expanders. The beam

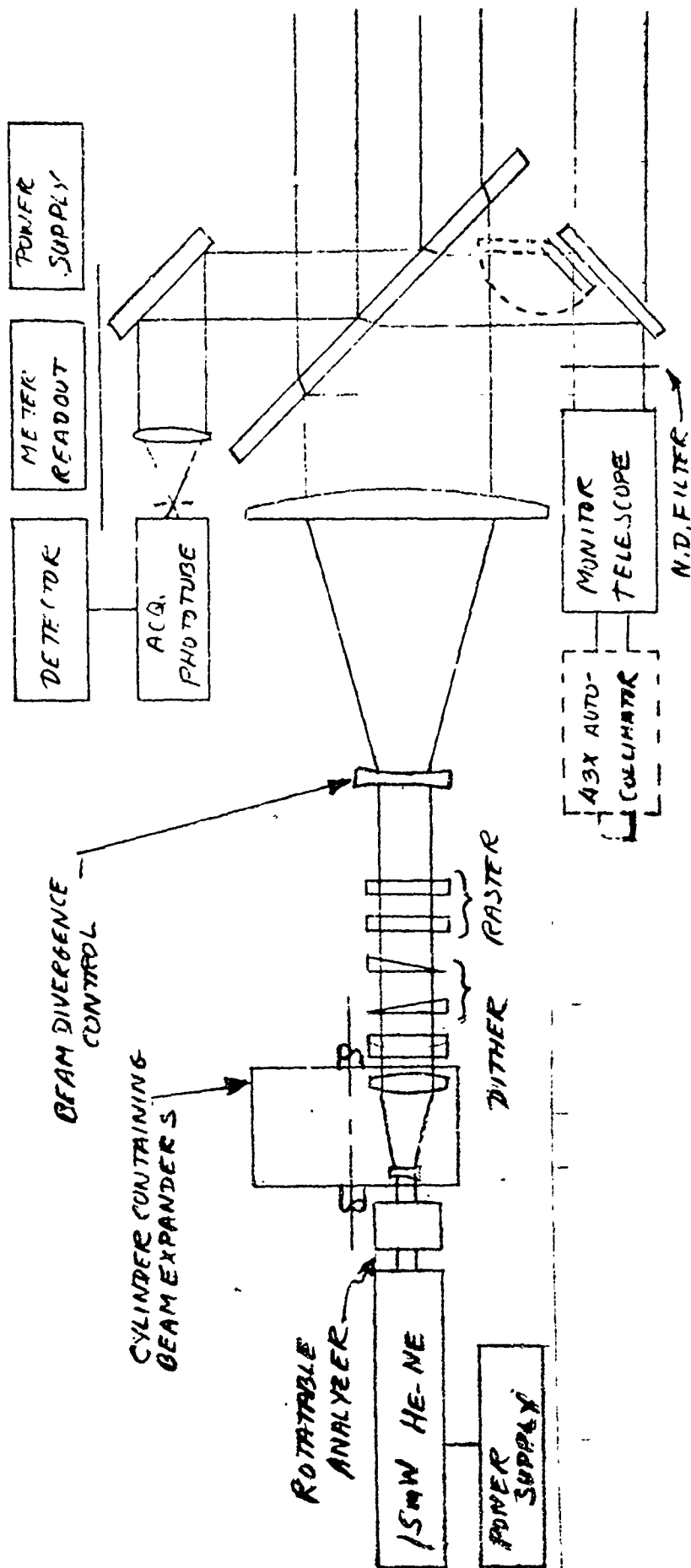


Figure 57. Scanning Transmitter Diagram

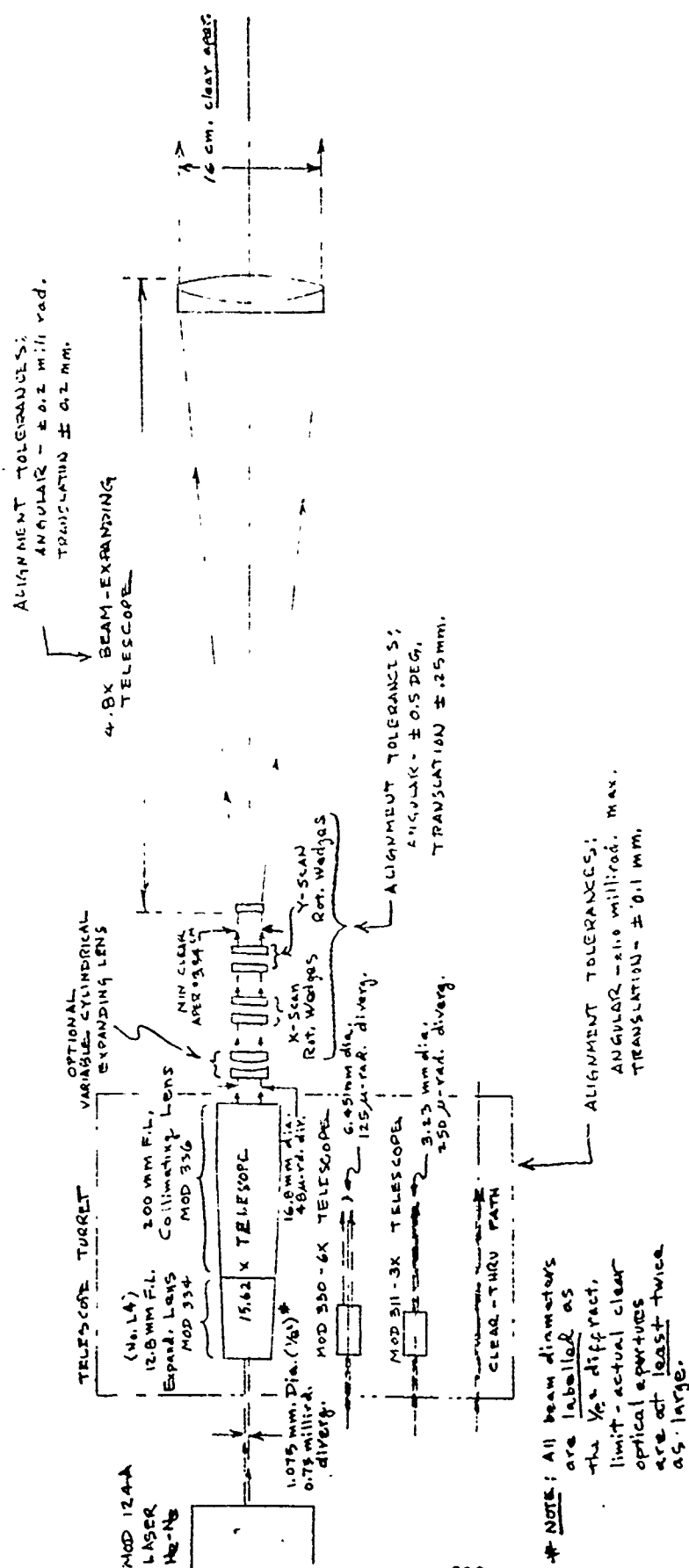


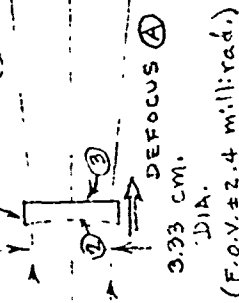
Figure 58. Scanning Transmitter Detailed Design 1.

LENS DIMENSIONS				
ITEM	SURF	SAD	THK.	MEDIUM
APR. STOP	1	FLAT	10.000000	AIR
SPREADER LENS	2	-10.100000	0.371000	B.L.
	3	99.200000	64.376900	AIR
COLLIMATOR LENS (DOUBLET)	4	774.508292	1.000000	B.L.
	5	25.155470	0.070557	AIR
	6	24.838515	3.000000	B.L.
	7	-35.459801	1.000000	AIR

(ALL DIMEN. IN CM.)

APR. STOP - 10 CM.

TILT & DECENTER TOLER. (E)



NOTES:

A - MOVEMENT OF SPREADER LENS TOWARD FRONT COLLIM. LENS WILL DEFOCUS THE BEAM TO AN ANGLE GIVEN BY:

$$\delta_{(TOT)} = \frac{\Delta F}{F \cdot f} \quad \text{WHERE: } \Delta F = \text{FOCUS SHIFT}$$

$$F = \text{COLL. LENS FOC. LENGTH, } f = \text{COLL. f - NO. (20 1/2" APER.)}$$

$$= \frac{\Delta F (CM.)}{84 \times 10.5}$$

B - DECENTERING SPREADER LENS REL. TO FRONT COLLIM. BY 0.010 CM. INCREASES WAVE FRONT DISTORT. TO $\lambda/10$. TILTING THIS LENS REL. TO COLLIM. BY 0.175 MILLIRAD. (0.6 MIN. OF ARC) ALSO CAUSES $\lambda/10$ WAVEFRONT DISTORTION. CALCULATED PERFORMANCES: WAVEFRONT DISTORTION - ON-AXIS - $< \lambda/50$

OFF-AXIS - $\lambda/20$ over 90% of area.

NOTE - SURFACE 7 IS ASPHERIC WITH SURF. GIVEN BY:

$$Z = \frac{r^2}{R + \sqrt{R^2 - p^2}} + Dp^4 + Ep^6 + Fp^8 + Gp^{10}$$

$$D = -7.0842 \times 10^{-7}$$

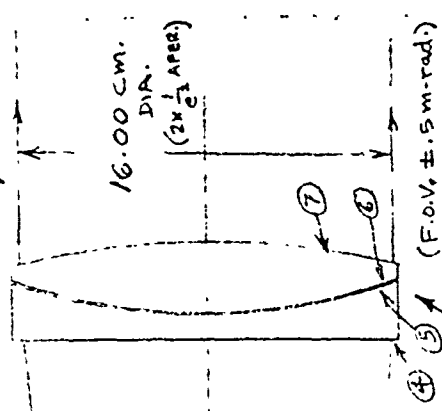
$$E = -7.3603 \times 10^{-10}$$

$$F = -7.3268 \times 10^{-12}$$

$$G = 1.3212 \times 10^{-13}$$

$$R = -35.4598$$

DECENTER TOL. (E) CAUSES 120μ-R. BM SHIFT
TILT TOL. (E) CAUSES 135μ-R. BEAM-SHIFT



84 CM. F.L.
f/10.5 OBJ. LENS

4.8 X BEAM-EXPANDING TELESCOPE

5 CM.

Figure 59. Scanning Transmitter Detailed Design II.

expanders are diffraction limited units which can be purchased off-the-shelf from Spectra Physics, with the exception of the largest expander which could require a stainless steel barrel for thermal stability. A raster-type scan is produced as the beam passes through two sets of counter-rotating wedges (Risley Prisms), i.e., a spot beam is scanned over a rectangular area.

A fan beam scan can be produced by disabling one set of wedges and inserting the cylindrical lens system. Divergence control is accomplished by moving the negative lens in the final beam expander. Variable motor speeds provide scan velocity control and the angular excursion of the scan is determined by the wedge angle of the prisms. The wedge position readout signals are recorded simultaneously with the data telemetered from the balloon payload so that each beam profile measurement can be corrected for the sinusoidal scan velocity produced by the Risley Prisms.

Figure 60 shows the scan geometry and the data reduction procedure. Since the beam is "waved" past the balloon-borne detector at a known velocity, a spatial intensity profile of the beam cross section can be reconstructed from the intensity versus time records.

A temperature stable Questar telescope (Cervit mirror, Invar barrel, and quartz corrector) serves to visually acquire the downlink He-Ne beam and to check the quality of the transmitted beams. When observing the transmitted beams, adequate attenuation is achieved by employing a high optical quality N.D. filter in addition to the attenuation effect produced by the low reflectance beam splitters.

With a particular beam expander in position, collimation of the beam is assured by adjusting the negative lens for minimum spot size as viewed through the monitor telescope and 43X autocollimator. Accurately diverged or focussed beams are produced in a similar manner with the Questar eyepiece displaced a fixed amount. Use of the stable reference

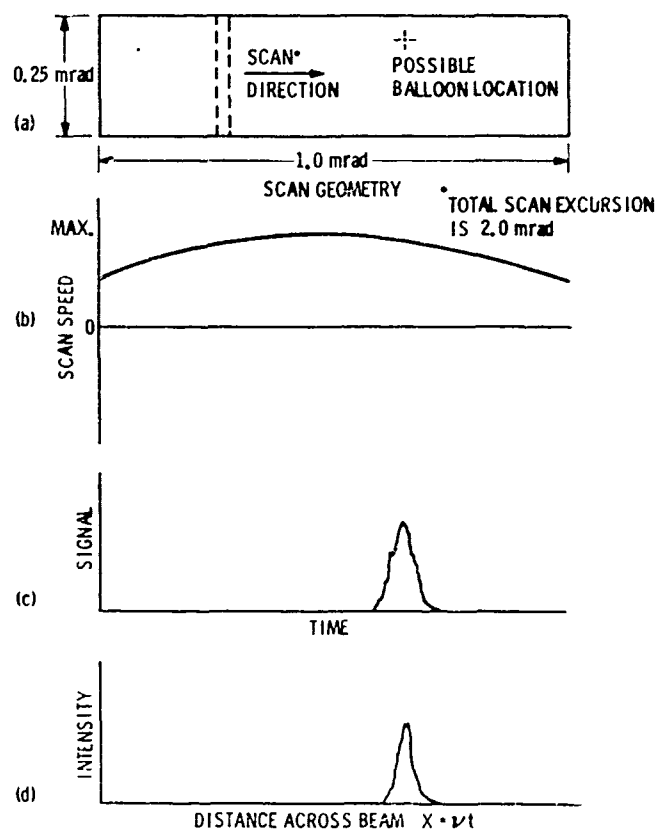


Figure 60. Scanning Geometry and Data Reduction Procedure.

telescope greatly relaxes the thermal and mechanical requirements on the optical elements of the transmitter and permits fast field adjustment of the transmitter beam characteristics.

In practice, the system would be used as follows: The transmitter would be mounted on an azimuth-elevation mount which was capable of achieving short term stabilities of less than 2 microradians rms pointing error over periods of several minutes. (A suitable modified telescope mount is available from Perkin Elmer, Boller and Chivens division.) The mount would be located adjacent to the ATLAS tracking telescope and housed in a small portable dome to avoid wind loading problems. Coarse pointing information would be derived from the ATLAS mount to initially orient the transmitter system. Visual acquisition of the balloon payload would then be accomplished with the boresighted Questar telescope. Having oriented the transmitter properly with respect to the balloon drift direction, a $0.25 \text{ mr} \times 2.0 \text{ mrad}$ scan (long axis parallel to drift direction) would be initiated with the mount fixed and stable. Assuming a reasonable balloon drift rate of 50 microradians/sec, this would yield 20 seconds of data. A data run of this length would permit a determination of beam wander frequencies as low as 0.1 Hz. This would include almost all of the expected beam wander frequencies. After each 20 second data run the transmitter pointing angle would be updated to "lead" the balloon motion.

Appendix XIII

BALLOON GONDOLA MODIFICATIONS

XIII.1 Introduction

This appendix discusses the modifications to the elevation axis housing and components, the telemetry system, the servo system, and the tracker system. The results of this appendix are summarized in Section 5.6.

XIII.2 OPTO-Mechanical Aspects for the Elevation Axis Package

XIII.2.1 Elevation Structure

The elevation structure has been redesigned in order to improve its torsional stiffness to be compatible with a more accurate servo system and to provide improved access to all components. The basic elevation axis structure is of semi-monocoque design. Torsional stiffness is maintained by developing shear forces in the two main side plates (top and bottom are non-structural covers). In order to properly handle the shear end condition without excessive weight, the end plates are reinforced top and bottom. The basic structure is shown in Figure 61.

All metal flexible disks are used between the elevation structure and the end support flanges. The disk provides the axial and angular misalignment capabilities to compensate for component static and dynamic errors. It also provides adequate torsional rigidity to keep the mechanical natural frequency above the range of the servo loop. A design for this disk is shown in Figure 62.

XIII.2.2 Extended Mirror

The present BAPE receivers are obstructed by the crush pads at elevation angles of less than 25°. For the OPTS application, an extended mirror has been designed in order to allow a clear field of view for the various laser beams between 10 degrees from horizontal through 5 degrees from vertical. The mirror must be light weight in order to minimize the

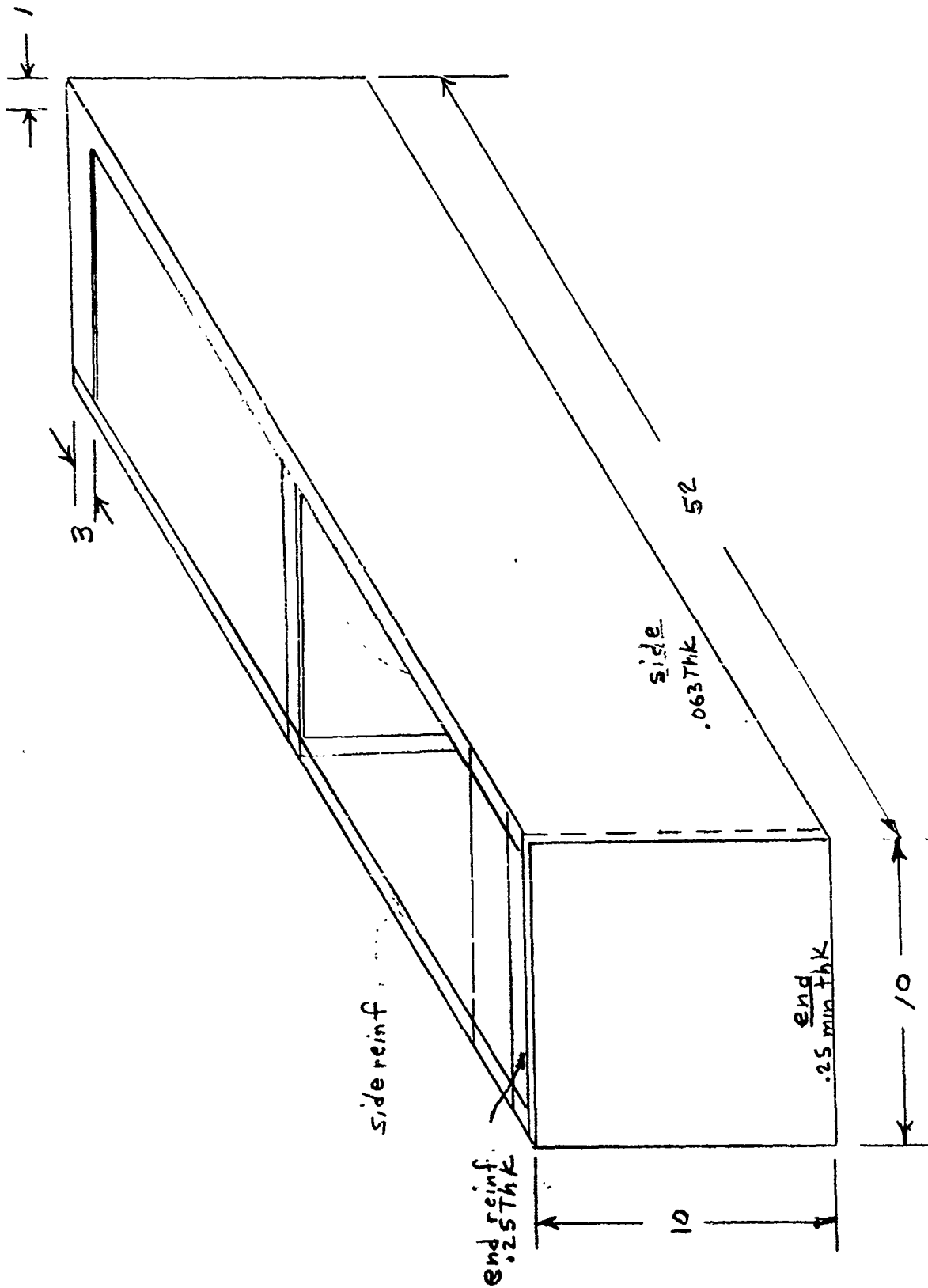


Figure 61. Balloon Elevation Axis Semi-Monoque Structure.

SECTION
A-A

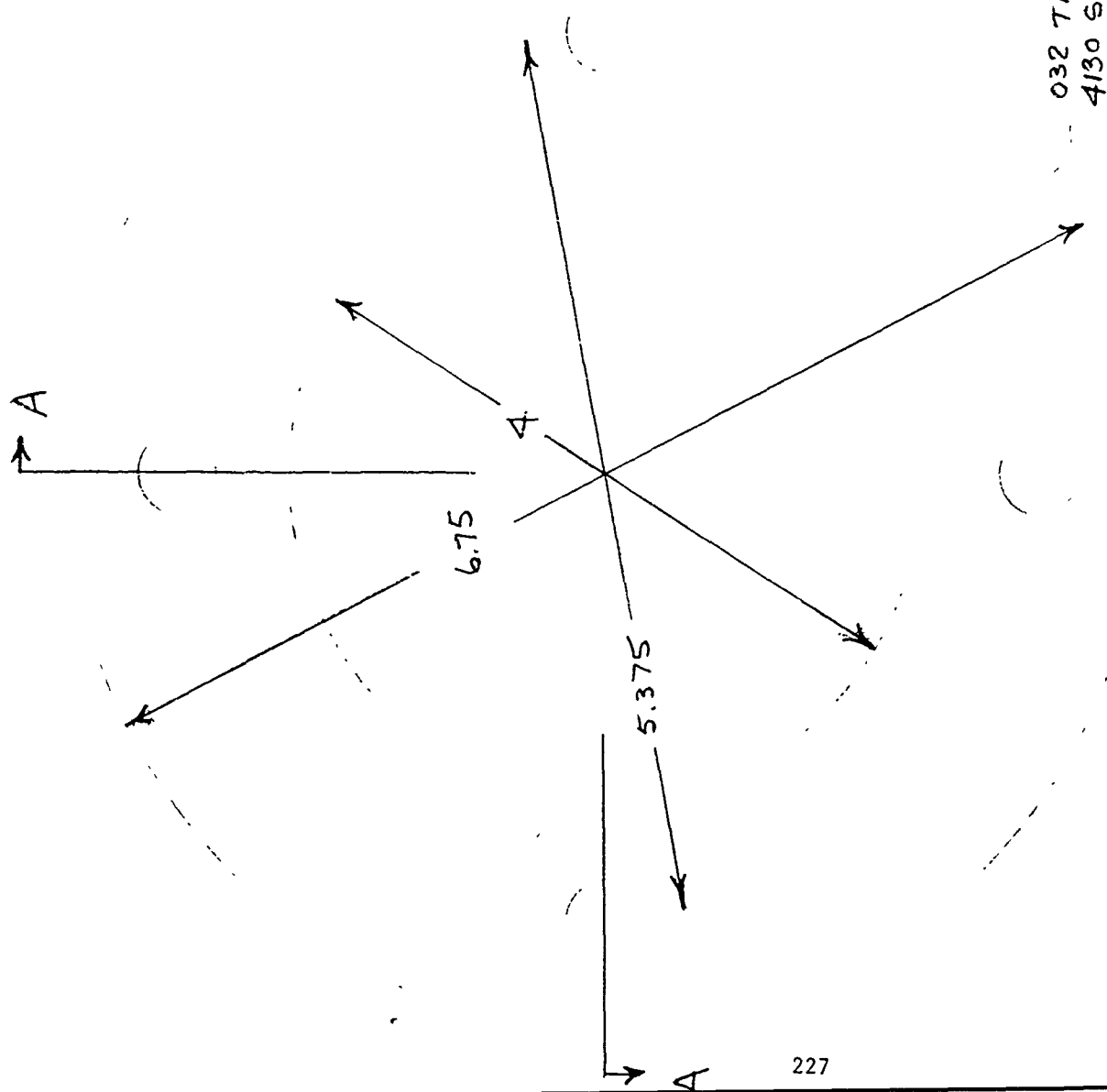
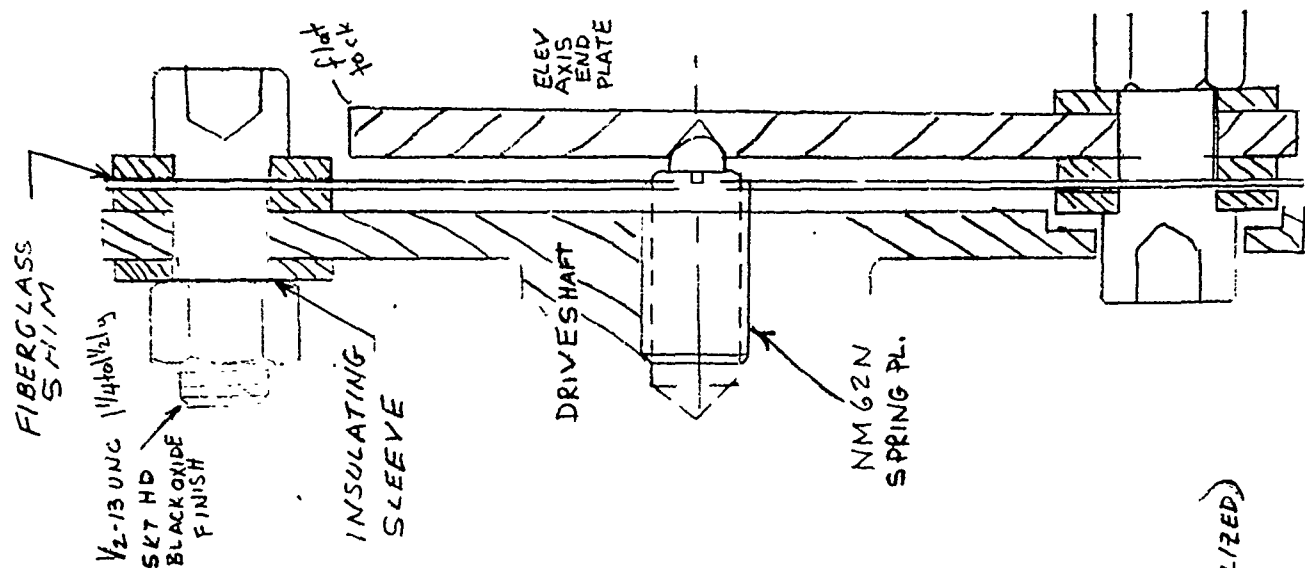


Figure 62. Self-Aligning Elevation Axis Mount.

additional system inertia and required counterweighting. An aluminum mirror weighing approximately four pounds appears to be a good compromise between heavier glass and more expensive beryllium materials.

The mirror mount must be designed for light weight, high rigidity and break-away capability. High rigidity is needed to prevent servo coupling, and servo response lag. Reasonable deflection is allowable in beam pointing, because both transmitting and receiving beams will be deflected equally with mirror mount structural deflection. Under normal circumstances, the mirror will be rotated away from its (protruding) operating angle prior to descent. If, for some reason it cannot be rotated, then a dependable method must be provided to prevent damage to the remainder of the system. Shear pins were initially considered, but discarded as too difficult to assure actuation during all possible landing conditions. Instead, the mirror support structure will be made of small diameter tubing, rigid enough to withstand normal operation and landing shocks, but slender enough to assure buckling if it strikes the ground. The mirror mount shown in Figure 63, is designed primarily to protect the main elevation package and secondarily to protect the mirror. A spare mirror would be available if needed.

XIII.2.3 Elevation Package Subsystems

The elevation structure is designed so that the basic BAPE experiment control package, (this is an environmentally controlled housing which contains the experiment control electronics, tracker electronics, phototubes and detection electronics), and auxiliary payloads can be easily removed and oriented to minimize the moments of inertia of the system.

If increased servo accuracy is required, the base plate and cover of the experiment control package will be enlarged to accommodate the larger tracker optics (see Section XIII.5), and a few additional circuit boards.

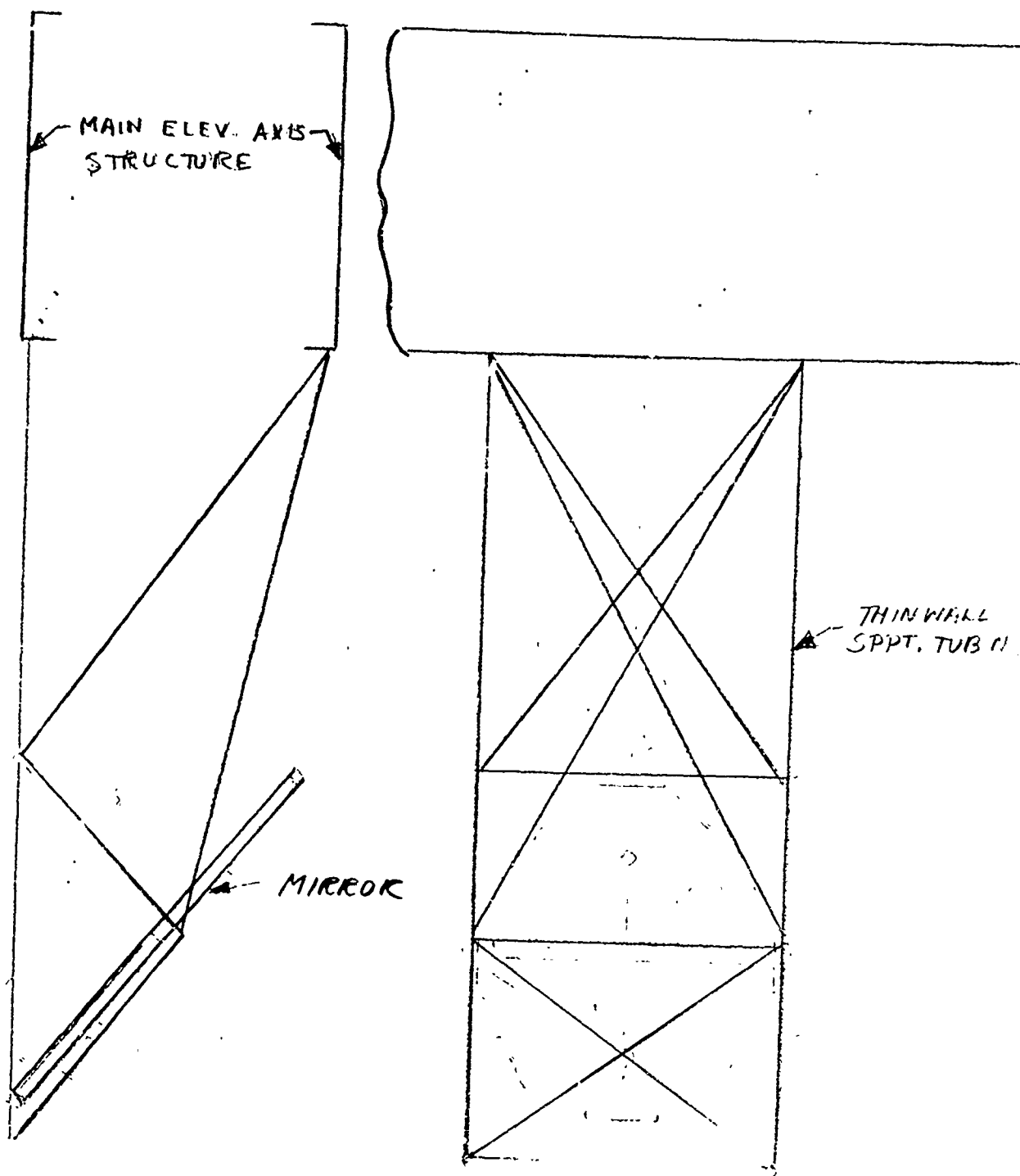


Figure 63. Mirror Support Structure.

The auxiliary laser package which is required for the reciprocity system is shown in Figure 64. It consists of a Hughes Model 3079H laser, collimation optics, and a Bulova L2C tuning fork chopper. The tuning fork enclosure is assembled in a clean room and sealed to prevent obstruction of the transmitted beam at the focus by dust particles. Required specification for the laser power supply were sent to Hughes (because their 28V units are special order). It was determined that a semi-standard design of their's would be suitable. The size of the unit is 5.25" x 2.63" x 1.75" and it weighs approximately 3 lbs.

XIII.3 Telemetry Range Extension

On several occasions during previous experiments with the BAPE gondola, the prevailing wind conditions caused the gondola to remain outside of the maximum slant range (50 KM) during part of the flight. In view of the uncertainties associated with balloon trajectory predictions, and the fact that flights must sometimes occur during non-optimum weather conditions, the maximum operating slant range will be increased to 100 KM for the OPTS experiments.

An increase in both the Up and Down Link RF Threshold sensitivity of at least 6 dB is required, if this performance is to be achieved. This 6 dB may come from a single improvement within each link's equipment or it may come from several improvements. For example: Any of the following modifications alone could be used to obtain the necessary 6 dB:

(A) The present 5 watt transmitters may be replaced with 20 watt units. (6 dB increase in output power).

(B) The present 4' parabolic ground antennas may be replaced with 8' units. (6 dB increase in gain)

(C) The present balloon-borne antennas might be replaced with larger arrays to obtain a gain increase of 6 dB.

(D) The receivers may be improved in performance so as to obtain a 6 dB increase in effective sensitivity.

These alternatives will be discussed below:

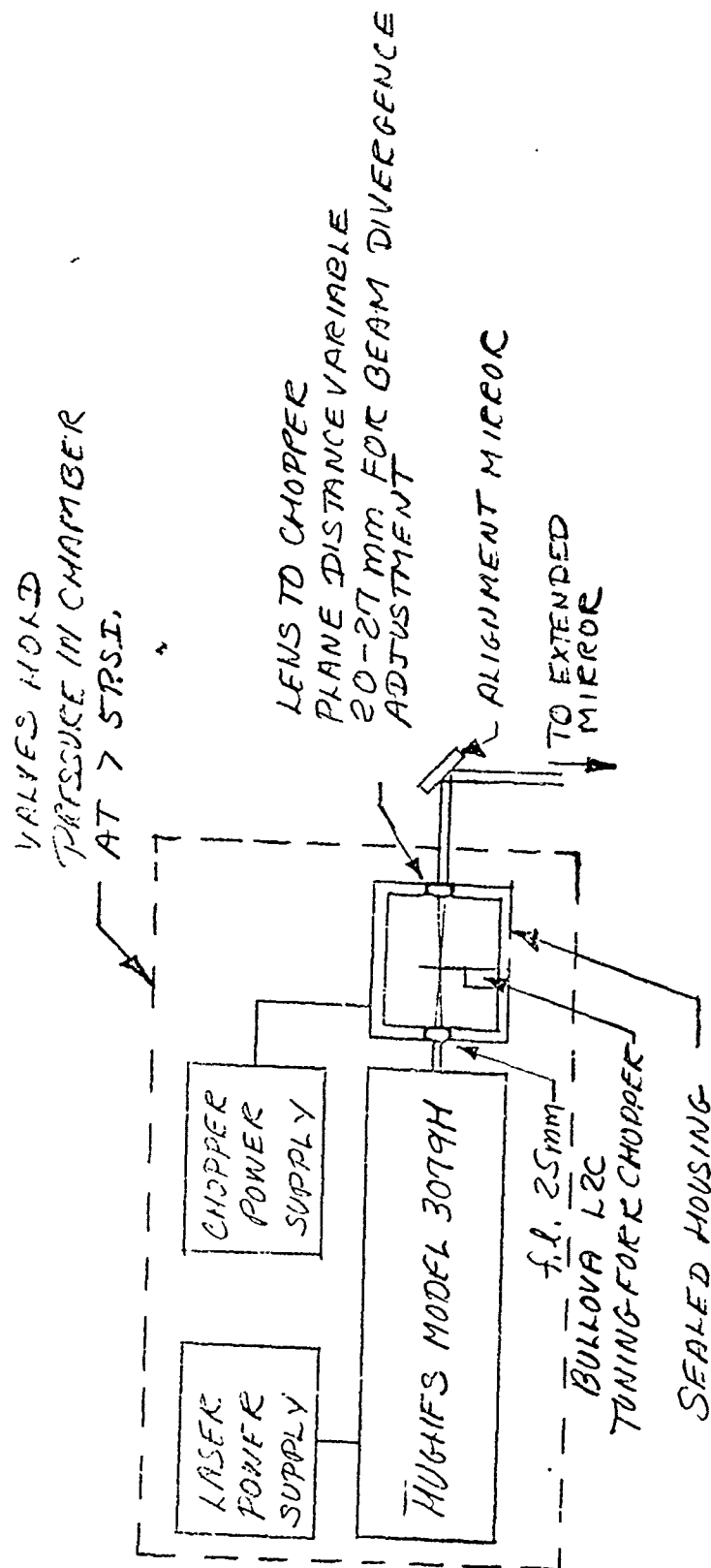


Figure 64. Balloon-Borne Laser Subsystem.

A. Transmitter Power Increase.

This is perhaps the simplest way to obtain 6 dB, but unfortunately the disadvantages are significant. The cost of 20 watt L and S band transmitters is high, about \$10,500 each. The additional power requirement means larger (heavier) batteries aboard the balloon gondola. Also, radiation of the additional heat loss from the gondola transmitter compartment would require additional study and modification.

B. The enlargement of the present 4 foot parabolic ground station antennas to 8 foot units is a possibility. Whereas the present 4 foot units were originally tripod supported and manually steered, they are now mounted upon a servo controlled pedestal assembly capable of handling two 8 foot dishes. As parabolic antennas are relatively inexpensive; about \$1,500 for the two units, this approach does have merit. One disadvantage to this approach is that the main lobe beam width of the 8' dish @ "S" band is only 4° (3 dB points) compared to 8° of the present 4 foot dish. This means that 8' dishes would have to be adjusted more frequently and pointed more accurately than the 4' antennas.

C. The present gondola antennas were specially designed and fabricated for this application by the Sylvania Antenna Group only after a thorough search for suitable commercially available designs. They are hemispherical in pattern without a vertical axis null, relatively small and very rugged. It is felt that the present units are so close to "state of the art" limits, considering both the performance and physical constraints involved, that further work on these items, especially to obtain a performance increase of 6 dB, is not economically practical.

D. The receivers were, at the time of the BAPE experiment, known to be the weak link of both the UP and DOWN Link T/M systems. They met the BAPE Program design specifications, but more sensitive receivers are now achievable.

There are two possible avenues to improved performance (sensitivity).

1) The present receivers may be replaced with new higher sensitivity units.

2) Low noise preamplifiers might be fitted "in front of" the present receivers so as to obtain an improvement in performance.

XIII.3.1 Proposed System Improvements

Of all the listed possibilities, improvement of overall system sensitivity (both up and down links) via the addition of current "state of the art" low noise "L" and "S" band preamplifiers ahead of the present receivers is both most cost effective and technically desirable. In addition, it is recommended that the downlink receiver antenna diameter be changed to 8'. The modifications are discussed below.

The effective sensitivity of a receiving system may be improved by preceeding the receiver with a preamplifier having a lower noise figure than that of the receiver. The effective system noise figure is given, in this case, by:

$$\text{Effective System NF} = \text{NF preamp} + \frac{\text{NF receiver} - 1}{\text{Preamp gain}}$$

In order to obtain accurate data sufficient to base effective sensitivity improvement calculations upon, both the "Up" Link "L" band and "Down" Link "S" band, receivers were returned to their manufacturer for testing. Below is a listing of the data taken by the Conic Corp. of San Diego on July 20, 1972.

"L" Band Receiver (Up Link)	
Noise Figure	16.5 dB
Threshold Sensitivity	-105 dB
"S" Band Receiver (Down Link)	
Noise Figure	10.5 dB
Threshold Sensitivity	-92 dB

The "Threshold Sensitivity" is that RF input level to the receiver with full channel deviation modulation (a normal situation) at which the subcarrier discriminators driven by the receiver would be expected to begin to output subcarrier data rather than raw noise. Although this measurement is both subjective and approximate, it is useful as a signal level from which a sufficient margin of sensitivity can be added which will certainly result in full quieting of the subcarrier discriminators. The measurement was made by observing the output of the receivers with an oscilloscope while increasing the RF input level to the receiver. When the receiver output modulation signal to noise ratio becomes sufficient to stably trigger the oscilloscope and make observation of the modulator possible, the RF input level to the receiver is the threshold sensitivity of the receiver. Normally, a system designer will set the minimum worst case limit input level to a telemetry receiver at not less than 20 dB over the threshold level.

A typical line of preamplifiers that might be used to improve the performance of the receivers is the AvanteK AM 1542N/2302N. These preamplifiers have noise figures of 4.5 dB and 5.5 dB and gains of 20 dB and 23 dB at "L" and "S" band respectively. Using those preamplifiers ahead of the receivers will result in the following improvement in receiving system sensitivity:

"L" Band (Up Link)

$$\text{Receiving System NF} = 4.5 \text{ dB} + \frac{16.5 \text{ dB} - 1}{20 \text{ dB}}$$

$$= 2.82 + \frac{44.6 - 1}{100} = 3.26$$

$$= 5.12 \text{ dB}$$

Since we had a threshold sensitivity before adding the pre-amplifier of -105 dB; with the preamp, the threshold sensitivity is improved to -105 -(16.5-5.1) or -116 dB.

"S" Band (Down Link)

$$\text{Receiving System NF} = 5.5 \text{ dB} + \frac{10.5 \text{ dB} - 1}{23 \text{ dB}}$$

$$= 3.54 + \frac{11.2 - 1}{200} = 3.59$$

$$= 5.55 \text{ dB}$$

Since we had a threshold sensitivity before adding the pre-amplifier of -92 dB; with the preamplifier the threshold sensitivity is improved to -92 - (11.5 - 5.55) or -98 dB.

The apparent difference in sensitivity between the two receivers with preamplifiers attached arise because the "S" band receiver has twice the RF bandwidth and better than ten times the video bandwidth than that of the "L" band receiver. This bandwidth is reduced somewhat by filtering (described later).

In summary, by adding up to-date preamplifiers, the Up Link may be improved by 10.5 dB and the Down Link by 6 dB. These preamplifiers are not the best available, but are representative; they cost \$575 each.

The Gain-Margin over Threshold is tabulated below:

Up Link

Propagation Loss (100 km)	-136 dB
Receiving Antenna	0 dB
Transmitting Antenna	23 dB
Bandpass Filter	-1 dB
Cables - Connecting	-2 dB

Transmitter	37 dB
Receiver with preamp (thresh)	<u>116 dB</u>
Gain Margin Over Threshold	+37 dB

Down Link

Propagation Loss (100 km)	-140 dB
Receiving Antenna	26 dB
Transmitting Antenna	0 dB
Bandpass	-1 dB
Cables - Connectors	-2 dB
Transmitter	37 dB
Receiver with preamp (thresh)	<u>98 dB</u>
Gain Margin Over Threshold	+18 dB

The +18 dB, margin over threshold, calculated for the "Down Link" is really worse than the real case by a few dB in that prior to the subcarrier discriminators, but after the tested receiver, the receiver output signal receives additional filtering. The effect of this is to reduce the effective signal bandwidth of the receiving system to somewhat less than the receiver itself is capable of, hence the threshold sensitivity of the complete receiving system is actually a few dB better than that figure obtained by measurement of the receiver alone. A conservative estimate of the improvement due to the additional filtering would be 3 dB. In spite of falling quite close to the "20 dB over threshold" rule of the thumb, this link with the added preamplifier will be 6 dB better than BAPE, which is to say that the BAPE level of performance may be expected out to a range of 120 km.

An additional Down Link improvement is recommended, however, to obtain a similar "margin over threshold" (range) to that of the Up Link. Usage of the best available preamplifiers known to date at "S" band could be used to obtain an improvement of 1.5 to 2.0 dB. Next, the present 4' receiving antenna should be replaced with an 8' unit. This will give an additional 6 dB for a margin over threshold of 29-30 dB.

The final system would then have a 30 dB gain margin over threshold for the down link and 37 dB for the up link. This represents a good safety margin and good balance because the "Up" or control Link must always out perform (range-wise) the data link.

XIII.4 Servo Modifications

The servo system in the BAPE equipment pointed the Argon and CO₂ detectors, each having a field of view of 34 mrad, to an accuracy of ≤ 7.5 mrad. The proposed OPTS experiments would require a better servo system. 0.1 mrad accuracies were considered initially because the added downlink laser would need to have a beam divergence (e^{-2} intensity points) of approximately 1 mrad for some of the experimental techniques.

However, for the diode array approach, the down link laser, and therefore, the increased servo accuracy, would be required for the NASA experiment, but not used directly in the A.F. experiment. For the reciprocity experiment, an improved servo would be required by both the A.F. and NASA, but the degree of improvement needed for the A.F. experiments remains to be determined.

The following section describes an analysis of the BAPE servo system. The feasibility of improving the present equipment is analyzed, and the recommended modifications are defined.

The azimuth and elevation servos of the BAPE were relatively simple, Figure 65, with resulting moderate performance matching the 7 milliradian accuracy requirements. First, let us examine employing these servos with the newly determined load characteristics. The pertinent parameters for the two axes are listed in the following table, and the corresponding open loop Bode plots of the position loops are presented in Figure 66.

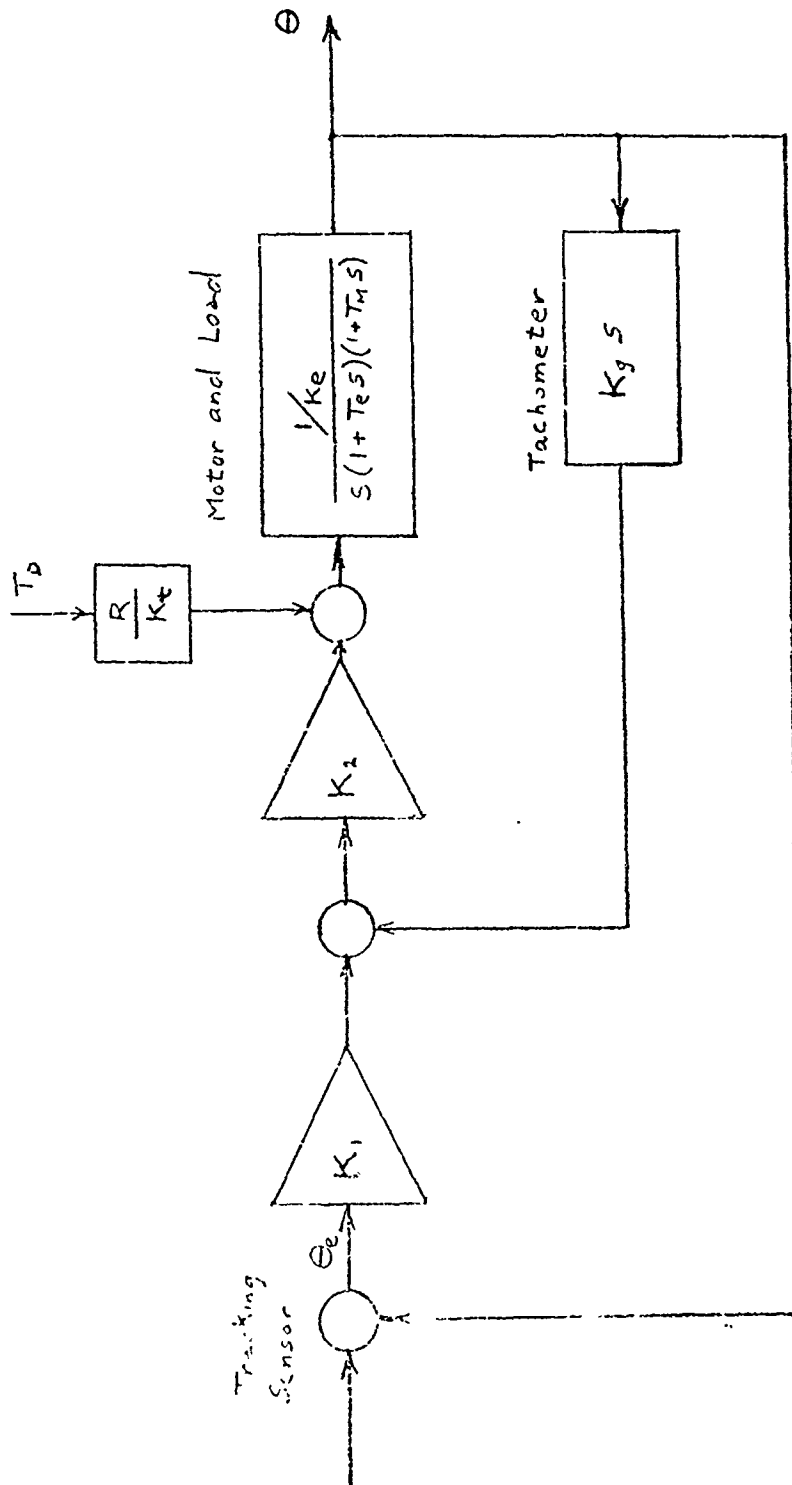


Figure 65. BAPE Servo.

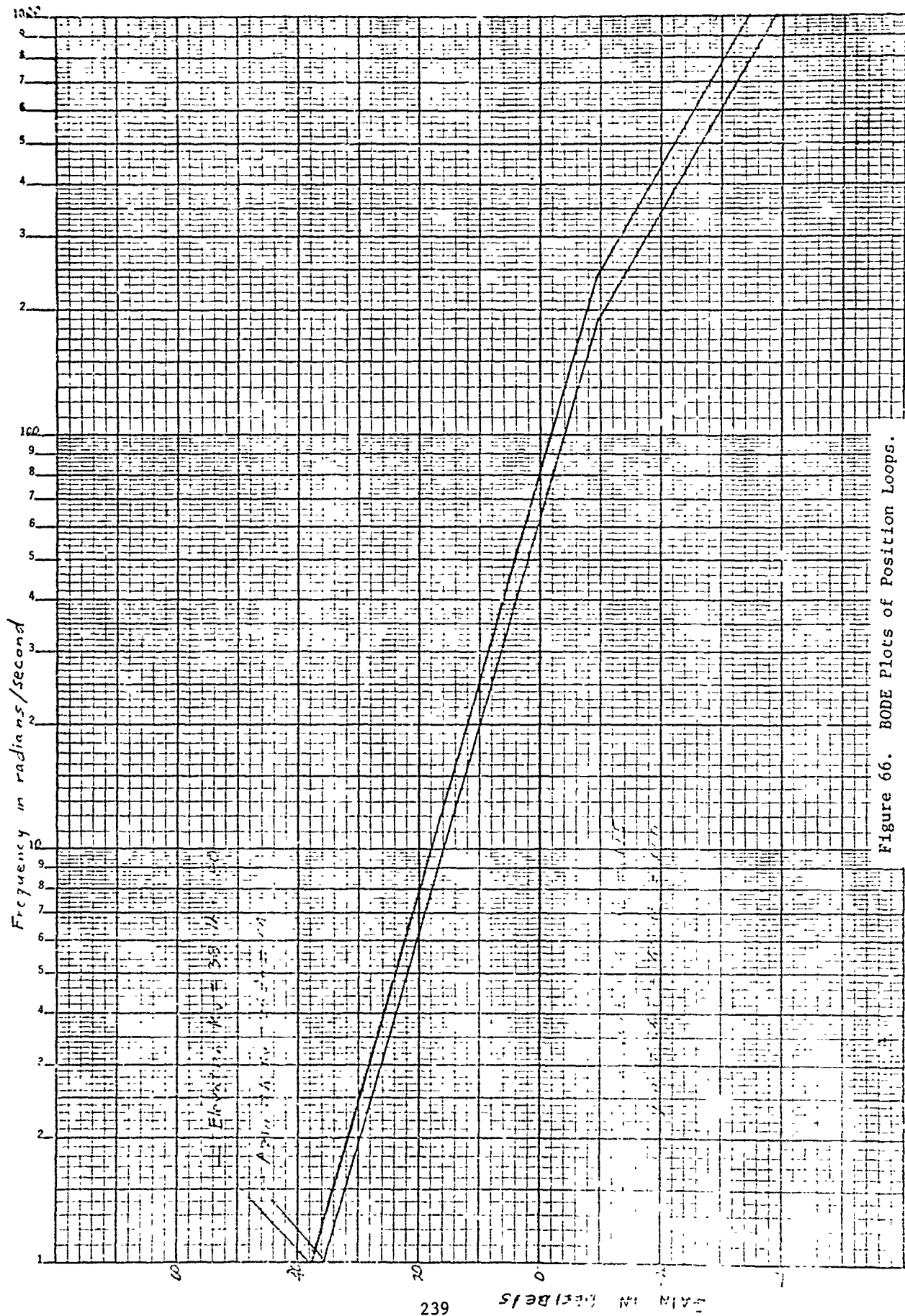


Figure 66. BODE Plots of Position Loops.

Frequency in Rad/Sec.

NAPE SERVO PARAMETERS

	<u>Azimuth</u>	<u>Elevation</u>
<u>Motor</u>		
Electrical Time Constant T_e	$2.7 \times 10^{-3} \text{ sec}$	$2.1 \times 10^{-3} \text{ sec}$
Electrical Corner Frequency ω_e	370 radians/sec	475 radians/sec
Moment of Inertia J_M	$5 \times 10^{-3} \text{ lb ft sec}^2$	$2.9 \times 10^{-4} \text{ lb ft sec}^2$
Inertial Time Constant		
Unloaded T_M	$20 \times 10^{-3} \text{ sec}$	$11.6 \times 10^{-3} \text{ sec}$
Torque Constant K_t	$.53 \frac{\text{ft lb}}{\text{amp}}$	$.37 \frac{\text{ft lb}}{\text{amp}}$
Back EMF Constant K_e	.72 volts/rad/sec	.5 volts/rad/sec
Inertial Time Constant		
Loaded $\left(\frac{J_L + J_M}{J_M} \right) T_M$	49.4 sec	30 sec
Inertial Corner Frequency ω_{ML}	.020 radians/sec	.033 radians/sec
D.C. Resistance R_M	1.5 Ω	7.5 Ω
Friction Torque	0.07 ft lb	0.017 ft lb
<u>Load</u>		
Moment of Inertia J_L	12.3 lb ft sec^2	$.75 \text{ lb ft sec}^2$
Friction Torque T_f	2.0 ft lb	.25 ft lb
Unbalance (Worst Case)	0	0.0083 ft lb
<u>Tachometer</u>		
Gradient K_g	1.2 volts/rad/sec	
Ripple		
Frequency	49 cycles/rev	
Magnitude	2%	
Friction Torque	1.2 in oz	

These design curves are based on the accepted good design practice associated with a servo employing a dc drive motor and tachometer feedback of closing the tachometer loop so as to have a cross over frequency of one half that of the motor electrical corner frequency and closing the position loop to cross zero db gain at one third the tachometer loop cross over frequency.

In these two cases, the locked rotor resonant frequency of the torsional spring-mass system comprised of the torque motor and load is assumed to be high enough to have no effect on the servo. The detector and signal amplifier are likewise assumed to be of high enough bandwidth to have no destabilizing effect on these servos. The tracking errors attributable to motion induced into the gondola by external disturbances are readily determined from the Bode plots. If one such motion was a constant angular drift of $2^\circ/\text{sec}$ (0.33 rpm), then the l.g in azimuth and elevation would be .55 milliradians and .44 milliradians respectively. In the presence of a pendulum motion of 1° magnitude with a 10 second period, the errors would be .175 mr in azimuth and .14 mr in elevation. The assumed pendulum would be torsional in azimuth and gravity type in elevation. These values are obtained directly from the Bode plots by utilizing the open loop gain at .1 Hz (.628 radians).

The error caused by friction loading of these servos must be examined particularly in azimuth where both the static and running friction of the slip ring assembly is considerable. Referring to Figure 65, it is seen that the relationship between position error and load torque is given by

$$\frac{\theta_e}{T_D} = \frac{R}{K_1 K_2 K_t}$$

where,

- θ_e = Angular error due to a load torque.
- T_D = Load Torque
- K_1 = Combined sensor and amplifier gain.
- K_2 = Rate loop amplifier gain.
- K_t = Motor torque constant.

K_2 is determined from the allowable rate open loop gain from stability considerations and the other proportionality factors in the rate loop. Based on the influence of the motor electrical time constant, the azimuth and elevation rate open loop gains were established at 185 and 237.5 respectively. Since this value is equal to $\frac{K_2 K_g}{K_e}$, K_2 is determined as follows:

Azimuth

$$K_2 = \frac{185 \times .72 \frac{\text{volts}}{\text{rad/sec}}}{1.2 \frac{\text{volts}}{\text{rad/sec}}} = 111 \frac{\text{volts}}{\text{volt}}$$

Elevation

$$K_2 = \frac{237.5 \times .5 \frac{\text{volts}}{\text{rad/sec}}}{1.2 \frac{\text{volts}}{\text{rad/sec}}} = 99 \frac{\text{volts}}{\text{volt}}$$

The closed loop gain of both rate loops is equal to $\frac{1}{K_g} =$

$$\frac{1}{1.2} = .833 \frac{\text{radian/sec}}{\text{volt}}$$

Since the position loop gains for stable operation have been determined as 64 and 80 for azimuth and elevation, the respective sensor/amplifier gains, K_1 will be

$$\frac{64 \frac{\text{rad/sec}}{\text{radian}}}{.833 \frac{\text{rad/sec}}{\text{volt}}} = 76.8 \frac{\text{volt}}{\text{radian}} \text{ and } \frac{80 \frac{\text{rad/sec}}{\text{radian}}}{.833 \frac{\text{rad/sec}}{\text{volt}}} =$$

$$96 \frac{\text{volt}}{\text{radian}} \text{ respectively.}$$

Employing the other known parameters, the angular error gradients due to friction loads are determined.

Azimuth

$$\frac{\theta_e}{T_D} = \frac{1.5 \frac{\text{volt}}{\text{amp}}}{76.8 \frac{\text{volt}}{\text{radian}} \cdot 111 \frac{\text{volt}}{\text{volt}} \cdot .53 \frac{\text{ft lb}}{\text{amp}}} = .332 \times 10^{-3} \frac{\text{radians}}{\text{ft lb}}$$

Elevation

$$\frac{\theta_e}{T_D} = \frac{7.5 \frac{\text{volt}}{\text{amp}}}{96 \frac{\text{volt}}{\text{radian}} \cdot 99 \frac{\text{volt}}{\text{volt}} \cdot .37 \frac{\text{ft lb}}{\text{amp}}} = 2.13 \times 10^{-3} \frac{\text{radian}}{\text{ft lb}}$$

Substituting the known static friction of the load and motor combinations, 2.0 ft lb in azimuth and .25 ft lb in elevation, the errors due these factors are obtained.

$$\text{Azimuth } \theta_e = .332 \frac{\text{mr}}{\text{ft lb}} \quad 2.0 \text{ ft lb} = .664 \text{ mr}$$

$$\text{Elevation } \theta_e = 2.13 \frac{\text{mr}}{\text{ft lb}} \quad .25 \text{ ft lb} = .53 \text{ mr}$$

It is apparent from these considerations that the servos as configured for BAPE would not yield a tracking error as low as .1 milliradian and therefore must be improved. A lag-lead filter in the decade between 3 and 30 radians would increase the low frequency gain by a factor of 10 and thus reduce the error due to the motions considered and friction torque by the same factor. The Bode plots of this configuration are shown in Figure 67, the block diagram is presented in Figure 68, and the resultant performance parameters are tabulated below.

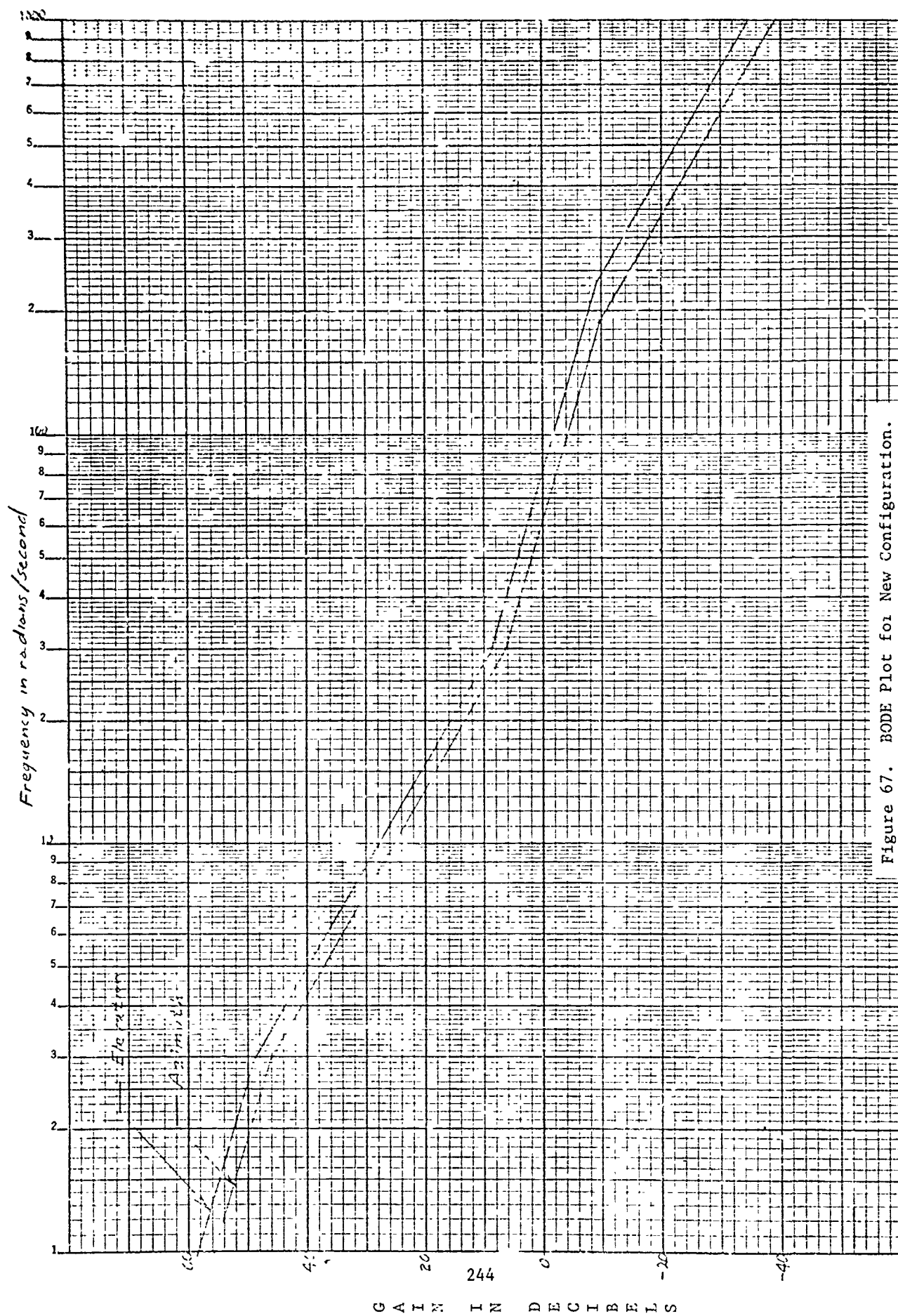


Figure 67. BODE Plot for New Configuration.

Frequency in Radians/sec.

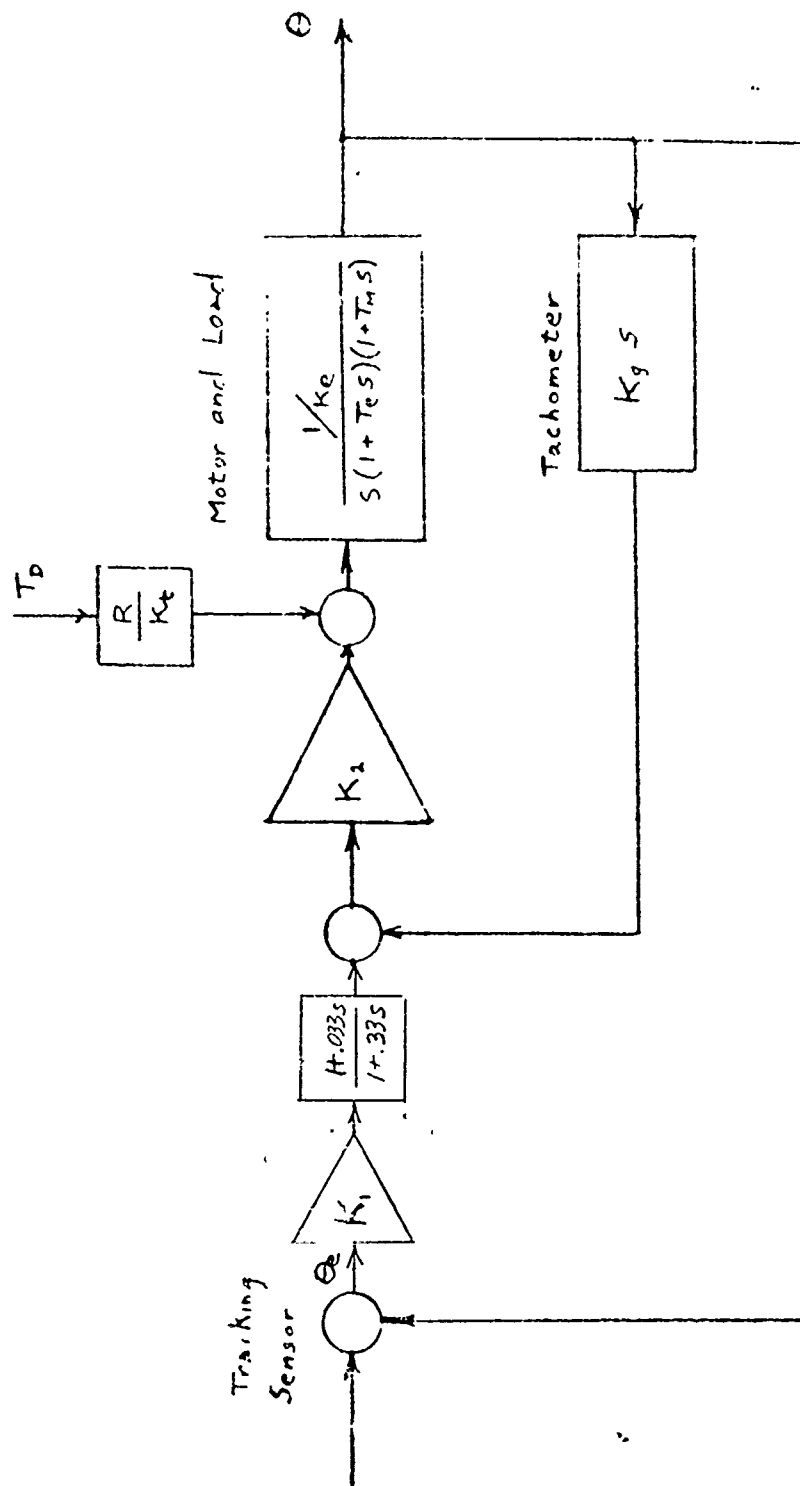


Figure 68. Block Diagram of New Servo Configuration.

<u>Error Source</u>	<u>Error</u>	
	<u>Azimuth</u>	<u>Elevation</u>
2°/sec steady drift	.055 mr	.044 mr
1°, 10 sec period oscillation	.018 mr	.014 mr
2 lb ft friction (Az)	.066 mr	--
.25 lb ft friction (El)	--	.053 mr

It is believed that the motions selected for determination of dynamic error are conservative in that the actual motions are likely to be less and are not likely to occur simultaneously. Nevertheless, the individual errors due to angular drift amount to a significant portion of the allowable. The errors due to friction are not conservative in that they are based on measurements made in the laboratory. If the azimuth friction went up by 50% under actual conditions, for example, the entire error allowance would be applied to this factor. With the errors due to the factors considered thus far reduced to the order indicated, the possible contribution of other sources such as bias, drifts, noise, and tachometer ripple must be examined.

XIII.4.1 Unbalance

From the analysis of the Photo Detector Angle Sensor, the error due to uncalibratable errors has been established as .039 milliradian. The Photo Detector Angle Sensor gradient is $152 \frac{\text{volts}}{\text{radian}}$.

XIII.4.2 Drift

The amplifier in the tachometer loop would typically have a drift referred to the input of 10 microvolts/degree centigrade. Without temperature control, a change of 65°C could be expected between ground level and float altitude, thus creating a signal change at the input to the tachometer loop (output of the position loop amplifier) of 650 microvolts. Transferring this through the sensor/amplifier combination yields an equivalent angular error of

$$\frac{650 \times 10^{-6} \text{ volts}}{10^3 \frac{\text{volts}}{\text{radian}}} = .00065 \text{ milliradians.}$$

Since the Photo Detector Angle Sensor gradient is $152 \frac{\text{volts}}{\text{radian}}$, an additional amplifier with a gain of approximately 7 must be included in the positional loop to produce the required loop gain. If the same drift of 10×10^{-6} volts/degree C were encountered at this point, the angular error would be 7 times as great as that calculated above or .00455 milliradians, a value that would still not influence the total error.

XIII.4.3 Noise

Noise creates an uncertainty band about the tracking signal null point which results in an angular error. The detector and amplifier noise cause an rms angular error of 300 μ rad in the present BAPE system. With the improved optics and cracker electronics, this error would be reduced to 60 μ rad.

XIII.4.4 Tachometer Ripple

The tachometer ripple voltage, which increases in magnitude and frequency as a function of speed, appears at the input to the tachometer loop. Its effect is determined by finding its equivalent value at the input to the angle sensor. Determining the equivalent input error must include the effect of the lag-lead filter. Once this has been determined, the closed loop forward characteristic yields the system response. Since several frequency dependent blocks are involved, this process is best done graphically as shown in Figure 69. From the tachometer characteristic it is known that the ripple frequency will be 49 times the rate of load rotation in radians/sec and the tachometer ripple voltage magnitude will be

$$1.2 \frac{\text{volts}}{\text{rad/sec}} \cdot .02 = .024 \frac{\text{volts}}{\text{rad/sec}} \text{ of load rotation or } \frac{.024}{49} = .00049 \frac{\text{volts}}{\text{rad/sec}}$$

of tach ripple or -66 dB at 1 rad/sec.

The position loop amplifier gains when the lag-lead filter has been added to the loop are 990 and 1110 $\frac{\text{volts}}{\text{radian}}$ respectively for azimuth and elevation, but for this calculation we shall consider them both the same and use 60 dB.

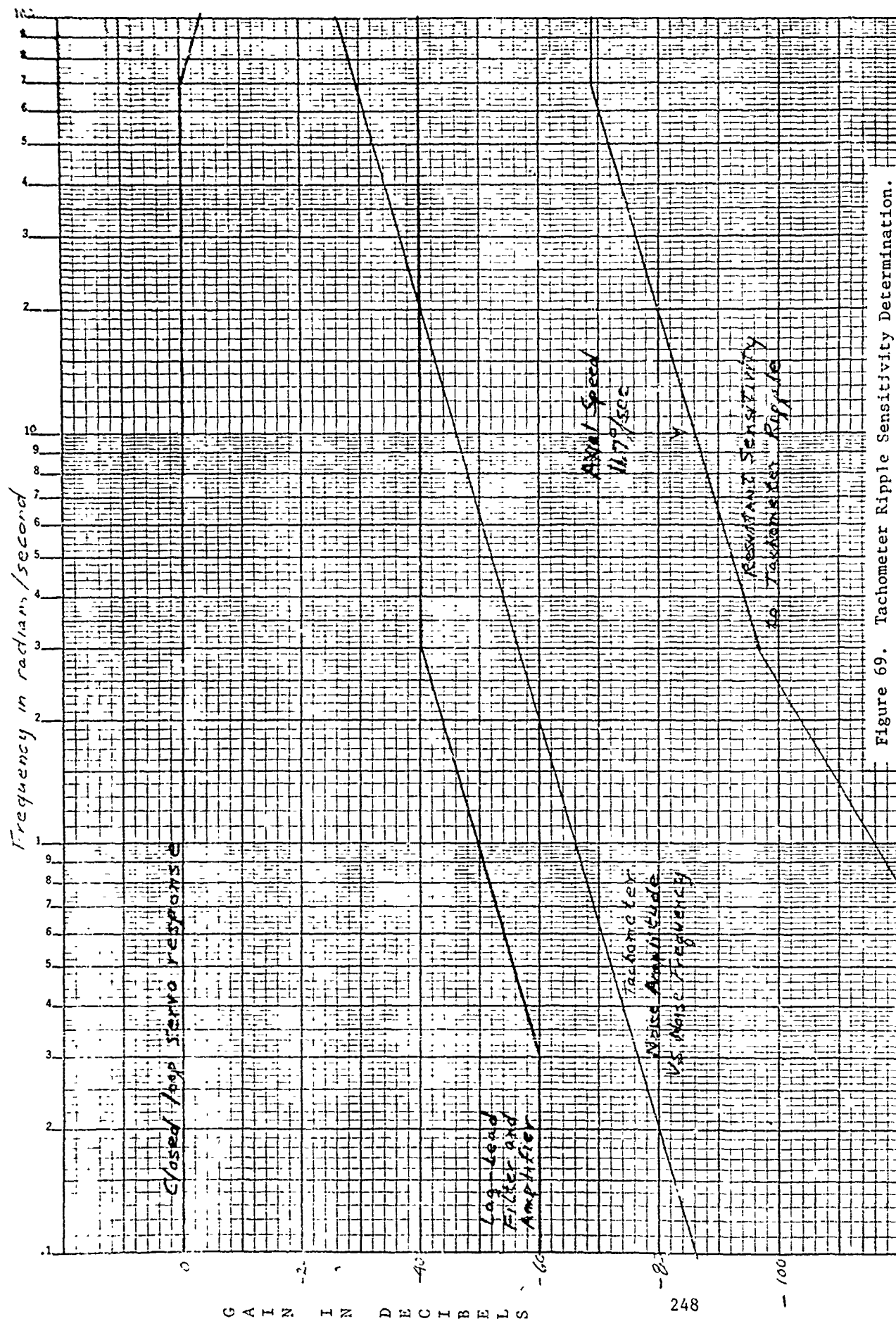


Figure 69. Tachometer Ripple Sensitivity Determination.

Frequency in radians/sec.

The resultant curve indicates that the system will be most sensitive to tachometer noise in the tachometer frequency range from 7 to 25 radians/seconds which corresponds to load rotational rates of .14 to .51 radians/second or 8 to 2° degrees/second which is higher than will be encountered. Even in this worse case, the response to tachometer ripple is -88 dB so that .51 radians/second velocity would have an associated error of $.4 \times 10^{-4} = .04$ milliradians. If a angular rate of 3°/sec were encountered, the corresponding tachometer ripple frequency would be $\frac{3}{57.3} \times 49 = 2.55$ radians/sec. From the curve, the corresponding error is -99 dB or .011 milliradians.

The errors that are over .1 of the total allowable error, i.e., over .01 mr are tabulated below. The method of combining the errors is approximate, but involves realistic assumptions which are described below. The sensor unbalance error is a maximum boresight deflection for a 20 dB excursion of received power at the tracking detector. In practice, the irradiance variations at the payload which are caused by slant range or beam divergence changes are compensated for by adjustments of transmitter power. From past experience with the payload, it is expected that the irradiance variations would not exceed 10 dB and that the sensor unbalance would therefore not exceed .004 mrad. The oscillation will induce an azimuth rotation under certain transmitter/payload geometries, but this azimuthal component will be negligible compared to the assumed 2°/sec rotation rate. The worst case boresight error would then be calculated by adding the 2°/sec steady drift plus friction plus sensor unbalance, yielding

$$.055 + .060 + .004 = 0.125 \text{ mrad.}$$

Superimposed upon this lag error will be a random dither caused by tracking electronics and tachometer noise. The RSS total of these is .061 mrad. The worst case error, with the assumed payload motions, would therefore be 186 μrad.

<u>Error Source</u>	<u>Error Magnitude in Milliradians</u>	
	<u>Azimuth</u>	<u>Elevation</u>
2°/sec steady drift	.055	
1°, 10 sec period oscillation	~0.0	.014
Friction	.066	.053
Sensor Unbalance	.039	.039
Tachometer Ripple	.011	.011
Detector and Amplifier Noise	.060	.060

Thus, it can be seen that it is feasible to realize an automatic tracker with an accuracy approaching .1 milliradian utilizing the BAPE equipment. However, several assumptions have been made which impose requirements on other portions of the design. These must not be neglected because a factor of 2 change in any one of them would cause an error larger than the acceptable value. Included in these assumptions are the following:

1. The locked rotor resonant frequency of the axial structures is approximately 5000 radians/sec.
2. The bandwidth of the error sensor/detector is 5000 radians/sec or greater.
3. The external disturbances are no greater than assumed.
4. The friction levels are the assumed values or less for all conditions.

This is not to say that the desired accuracy could not be obtained by other methods and/or with new equipment configured in the same way, but with improved detailed features. These alternatives would be more sophisticated and costly.

XIII.4.5 Modifications of the Present BAPE Equipment

As presently designed, the system does not satisfy these assumptions, particularly Assumption #1. We estimate there is a structural resonance in the elevation axis at 45 Hz (281 rad/sec). It, therefore, is more significant than the motor's electrical time constant. Assuming it could be characterized by a single pole and taking into account the effect of the pole due to motor armature resistance and inductance at 475 radians, the tachometer loop could be closed with a phase margin of 55

degrees at a zero dB crossing of 112 radians per second which is numerically equal to the gain. The positional loop gain (see Figure 70) containing a lag-lead filter would have a gain of 51 dB (360/1). The gain at the frequency of possible sinusoidal oscillation of the gondola, .628 radians/sec, is 55.5 dB (600).

Everything else being unaltered, the tach amplifier gain would then be 46.7, and the sensor/amplifier gain would be $431 \frac{\text{volt}}{\text{radian}}$. This yields a torque sensitivity of

$$\frac{\theta_e}{T_D} = \frac{R}{K_1 K_2 K_t} = \frac{7.5 \frac{\text{volt}}{\text{amp}}}{431 \frac{\text{volt}}{\text{radian}} 46.7 \frac{\text{volt}}{\text{volt}} .37 \frac{\text{ft lb}}{\text{amp}}} = 1.01 \times 10^{-3} \frac{\text{rad}}{\text{ft lb}}$$

The Photo Detector Angle Sensor gradient remains $152 \frac{\text{volts}}{\text{radian}}$, requires an amplifier of gain 2.84 following it in the position loop to yield the total sensor/amplifier gain of $431 \frac{\text{volts}}{\text{radian}}$.

From the foregoing, error figures can be determined as before.

Dynamic lag due to $2^\circ/\text{sec}$ drift

$$\frac{2 \frac{\text{deg}}{\text{sec}} \times .0175 \frac{\text{rad}}{\text{deg}}}{\frac{360}{\text{sec}}} = .097 \times 10^{-3} \text{ radian}$$

Dynamic error due to oscillation of 1° magnitude with .1 sec period.

$$\frac{.0175 \text{ radians}}{600} = .0292 \times 10^{-3} \text{ radian}$$

Error due to .25 ft lb friction.

$$.25 \text{ ft lb} \times 1.01 \times 10^{-3} \frac{\text{rad}}{\text{ft lb}} = .253 \times 10^{-3} \text{ radian}$$

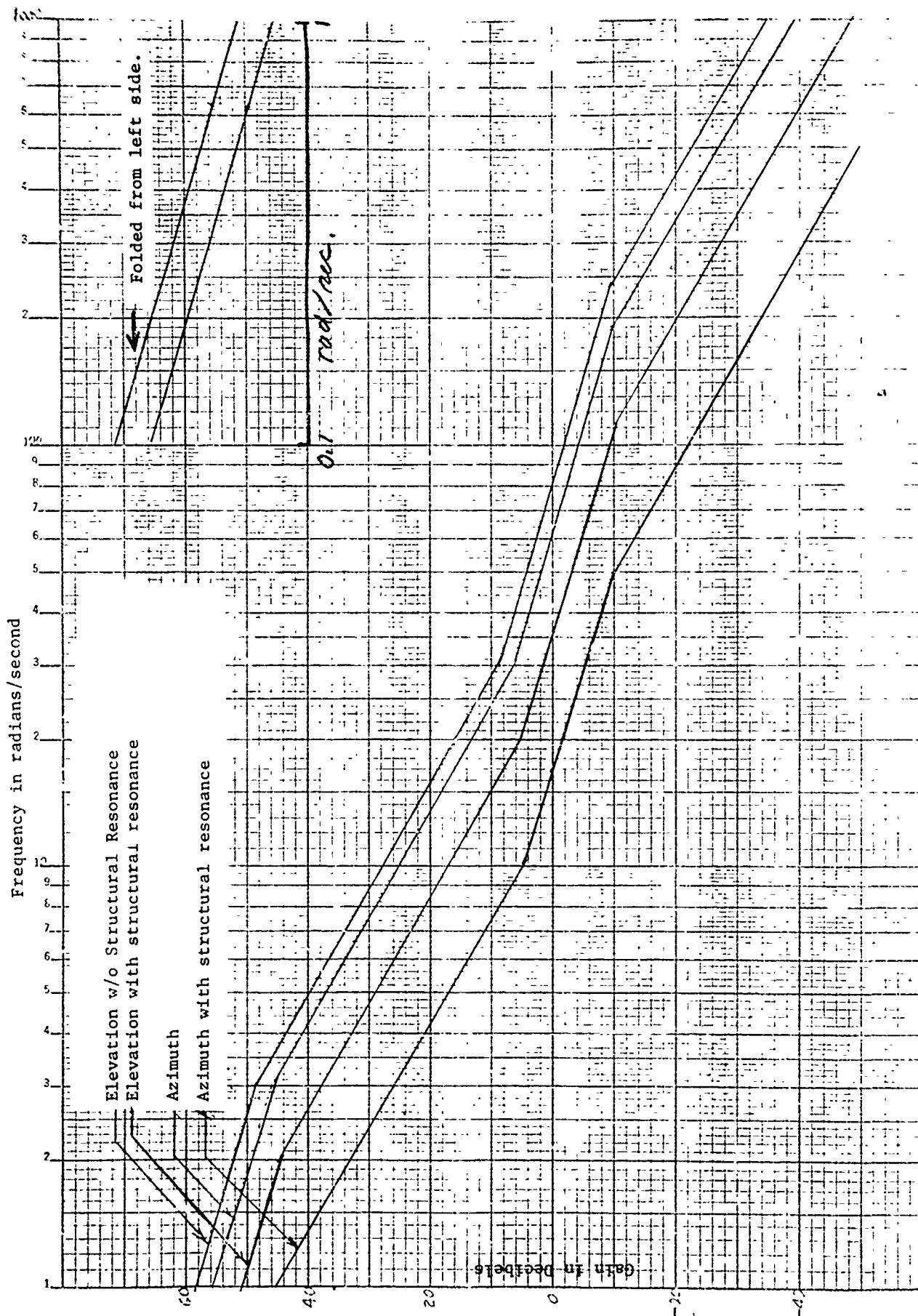


Figure 70. OPTS Servo's Open Loop Characteristics. Frequency in rad/sec.

From the plot of sensitivity to tachometer ripple, figure 71, it is seen that this servo has a sensitivity to tachometer ripple of -80 dB at a ripple frequency of 7 radians/second which corresponds to axial motion of 8.2 degrees per second. Since this is a higher rate than is expected to be encountered and since the sensitivity is lower for lower rates, the corresponding allotted error figure of $.10 \times 10^{-3}$ radians is considered conservative. The error due to sensor unbalance remains the same at .039 milliradians.

Since the positional loop and tachometer loop amplifiers have less gain than previously and it has been determined that their drift was not a significant factor in that case, it will not be a factor now.

<u>Error Source</u>	<u>Elevation Error Magnitude in Milliradians</u>
2°/sec steady drift	
1°, 10 sec period oscillation	.029
Friction	.253
Sensor Unbalance	.039
Tachometer Ripple	.100
Detector and amplifier noise	.060

Combining errors as described on page 250, the worst case error would be 0.403 mrad.

In azimuth, a structural resonant frequency of 20 Hz (125.6 radians/sec) is speculated, again considerably lower than the motor electrical corner at 370 radians per second. The tachometer open loop gain can cross zero at 50 radians/second to yield a phase margin of 60 degrees and, of course, a loop gain of 50. The position loop gain curve passes through 0 dB at 17 radians/sec and has a gain of 45 dB (180/1) when lag-lead series compensation is employed as in elevation. The gain at .628 radians is 49.5 dB (300).

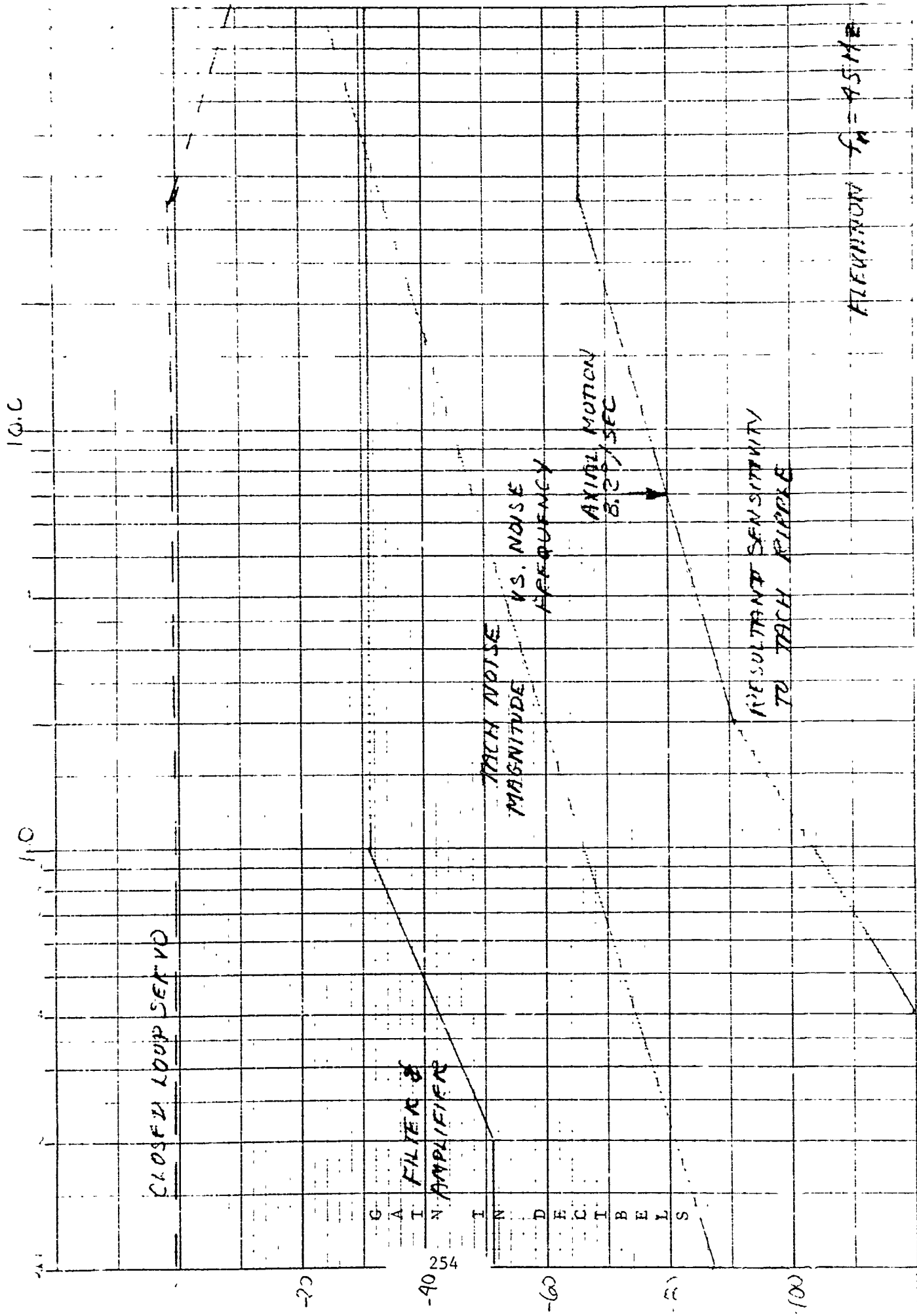


Figure 71. Tachometer Ripple Sensitivity Determination: Elevation.

The tachometer amplifier gain, K_2 , would be

$$111 \frac{\text{volts}}{\text{volt}} \frac{50}{185} = 30.0 \frac{\text{volts}}{\text{volt}}$$

and the sensor/amplifier gain, K_1 , would be

$$768 \frac{\text{volt}}{\text{radian}} \frac{18}{64} = 216 \frac{\text{volt}}{\text{radian}} .$$

The position loop amplifier gain would be $\frac{216}{152} = 1.42$.

$$\frac{\theta_e}{T_D} = \frac{R}{K_1 K_2 K_t} = \frac{1.5 \frac{\text{volt}}{\text{amp}}}{216 \frac{\text{volt}}{\text{radian}} 20 \frac{\text{volts}}{\text{volt}} .53 \frac{\text{ft lb}}{\text{amp}}} = .435 \times 10^{-3} \frac{\text{rad}}{\text{ft lb}}$$

The azimuth error figures are then as follows:

Lag due to $2^\circ/\text{sec}$ drift.

$$\frac{2 \frac{\text{deg}}{\text{sec}} \times .0175 \frac{\text{rad}}{\text{deg}}}{\frac{180}{\text{sec}}} = .1945 \times 10^{-3} \text{ radian}$$

Error due to oscillation of 1° magnitude with .1 sec period.

$$\frac{.0175 \text{ radians}}{300} = .0584 \times 10^{-3} \text{ radian}$$

Error due to 2.0 ft lb friction.

$$2 \text{ ft lb} \times .435 \times 10^{-3} \frac{\text{rad}}{\text{ft lb}} = .87 \times 10^{-3} \text{ radian.}$$

From the plot of sensitivity to tachometer ripple (Figure 72), the azimuth servo is seen to have an error of -80 dB or .0001 radians when the axial motion is $4.33^\circ/\text{sec}$ and less for lesser velocities. This conservative figures will be used in the error budget.

Sensor unbalance error will be the same as for elevation, .039 milliradians.

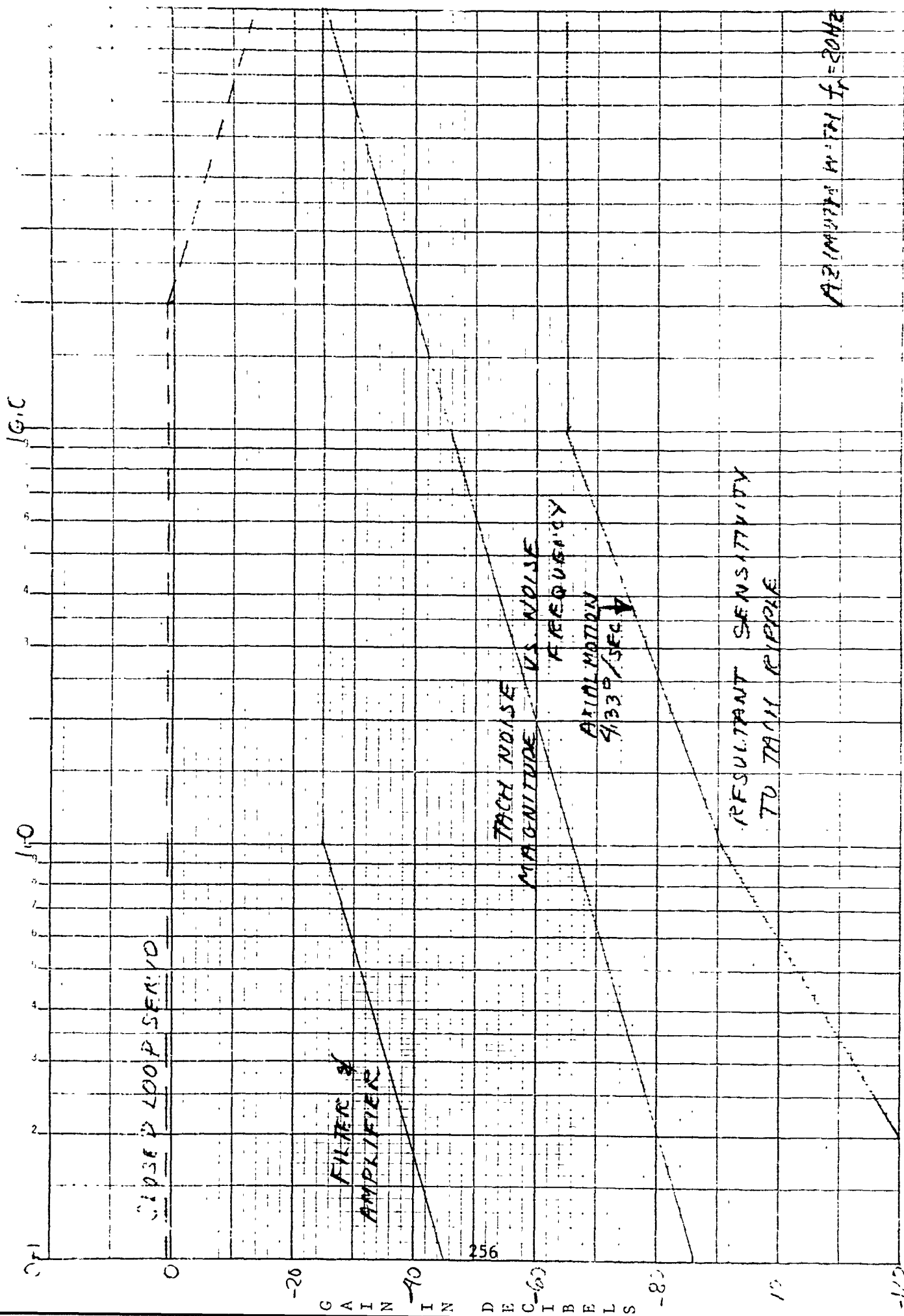


Figure 72. Tachometer Ripole Sensitivity Determination: Azimuth.

The errors excluding sensor noise are then as follows:

<u>Error Source</u>	<u>Azimuth Error Magnitude in Milliradians</u>
2°/sec steady drift	.1945
1°, 10 sec period oscillation	~0.0
Friction	.8706
Sensor Unbalance	.0390
Tachometer Ripple	.1000
Detector and Amplifier Noise	.060
Worst Case Error	1.18 mrad

XIII.5 Tracker Modification

XIII.5.1 Optics

Because of the doubled slant range capability which has been recommended for the OPTS experiments, the tracker sensitivity should be increased by 3 dB. In addition, if more accurate pointing of the balloon-borne servo is required, the focal lengths of the tracker lens should be increased. Figure 73 shows a design in which the focal length has been increased from 3" to 12" and the aperture from 2 1/8" to 4". The 12" focal length limits the pointing error caused by the unavoidable mismatch of the gain control elements of the tracker circuitry to 39 μ rad as described in the following section. The larger lens aperture will provide the required increase in sensitivity.

The field of view of the tracker system is given by

$$\theta = D/f$$

where D = diameter of active photodetector surface

f = focal length

For the existing equipment, $\theta \approx 2.5^\circ$. Since the magnetic-north sensor is only accurate to 1 or 2 degrees, the acquisition capability of the system would be marginal with the 2.5° tracker field of view. Therefore, to regain the 10° field of view, which has worked well for acquisition with the existing BAPE equipment, a segmented field lens and four PIN-10 diodes were added to the tracker. When the uplink beam is focussed on one of

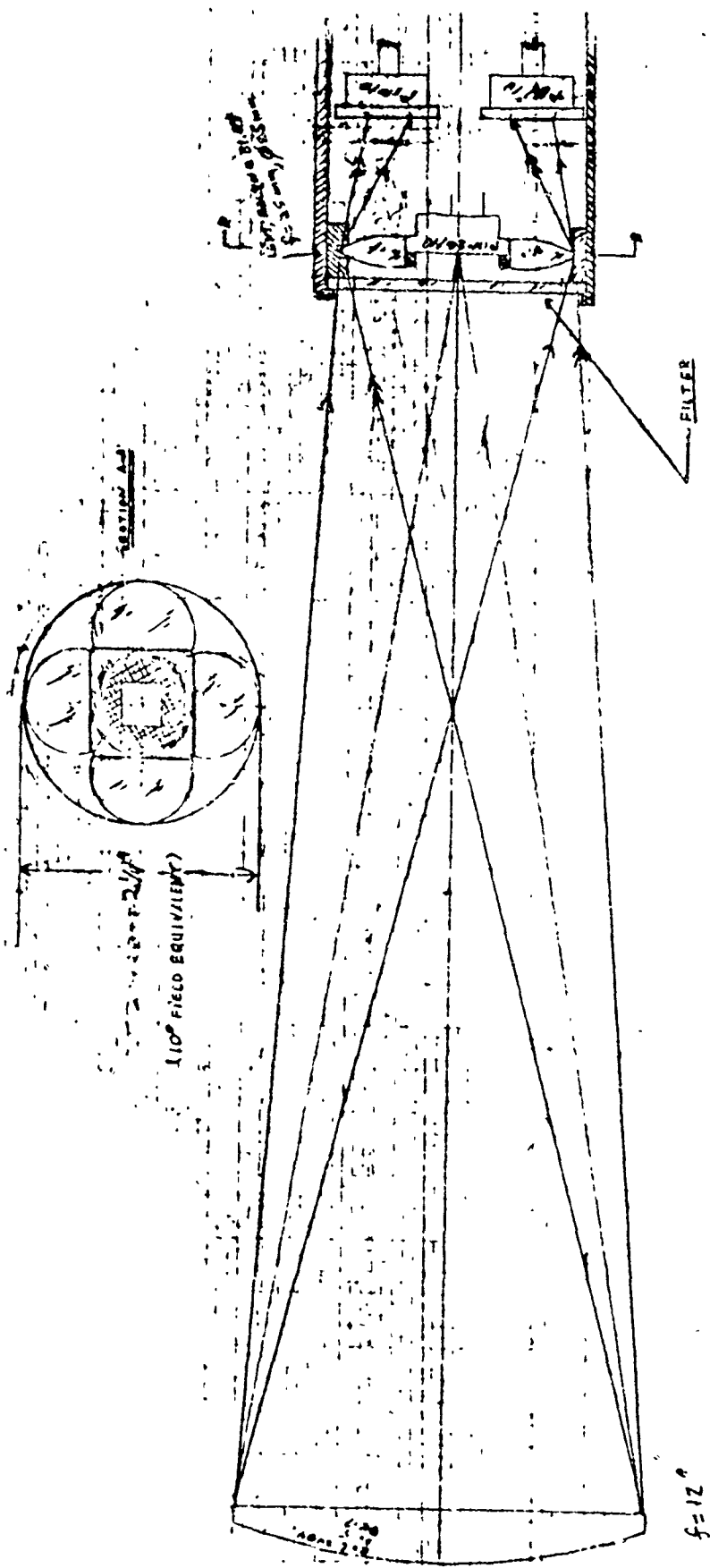


Figure 73. Balloon Package: Argon Receiver.

the field lens segments, it illuminates one of the diodes located behind the tracker photodiode. This actuates a circuit and generates a drive signal which effects a transient UP, DOWN, CW, or CCW motion of the servo system, depending upon which diode is illuminated. In effect, illumination of any of the diodes "kicks" the beam towards center where it is captured by the tracking diode.

XIII.5.2 Tracker Electronics

XIII.5.2.1 Sensitivity

Equivalent noise bandwidth and equivalent input noise density determine noise level at tracker electronics input. Equivalent noise bandwidth (B_e) is given by:

$$B_e = \sqrt{2 B_r B_v - B_v^2} \quad (\text{XIII-1})$$

where B_r = "RF" or pre-detection bandwidth
 B_v = "video" or post-detection bandwidth

for a square-law detector with Gaussian noise input.

A post-detection bandwidth (B_v) of 100 Hz is set for the "OPTS" tracker to minimize added phase shift in the servo loop. The pre-detection bandwidth is set for 400 Hz to facilitate gain matching over ± 50 Hz from center frequency of 5 kHz. Therefore,

$$B_e = 264 \text{ Hz.}$$

The photo detector noise contribution in this bandwidth is given by:

$$I_N = \sqrt{2 e i_D B_e}$$

where e = electronic charge, 1.6×10^{-19}
 i_D = dark current
 B_e = equivalent noise bandwidth
 I_N = 7.0 pA (equivalent noise current).

The equivalent noise (voltage) density for the optimum low noise amplifier design (Figure 74) is estimated to be uniformly distributed at $6 \text{ nV}/\sqrt{\text{Hz}}$. This is about one-half the level for the BB3500 op-amp and about 1/7 that of the LM308 which was previously applied.

The equivalent noise voltage input (e_n) of the tracker electronics is $6 \text{ nV}/\sqrt{\text{Hz}} \times \sqrt{264} \sqrt{\text{Hz}} = 97.4 \text{ nV}$. Converting the equivalent noise current of the photo detector to a voltage through its source resistance of 10K at null:

$$e_{No} \text{ (photo detector)} = I_N \times R_s = 70 \text{ nV.}$$

Consequently, the equivalent noise of the tracker is seen to be $97.4/70 = 1.39$ times the noise output of the photo detector.

The minimum signal current at the output of the photo detector is estimated to 10 nA which is 925 times higher than the combined estimated noise currents. An adequate signal-to-noise ratio could also be achieved using the BB3500 op-amp rather than the optimum (and more expensive) design shown in Figure 74. For this case.

$$\left(\frac{S}{N}\right)_r = 510$$

XIII.5.2.2 Photo Detector Angle Sensing Characteristics

The detector model is given on the data sheet for the U.D.T. SC/10, as shown in Figure 75. The function of the tracker circuitry is to provide an output which is a function only of the ratio of voltages V_A , V_E . For the photo detector model of Figure 75:

$$\frac{V_A}{V_B} = \frac{A}{B} = \frac{1 + \frac{R_F}{R_{2B}}}{1 + \frac{R_A}{R_{2A}}}$$

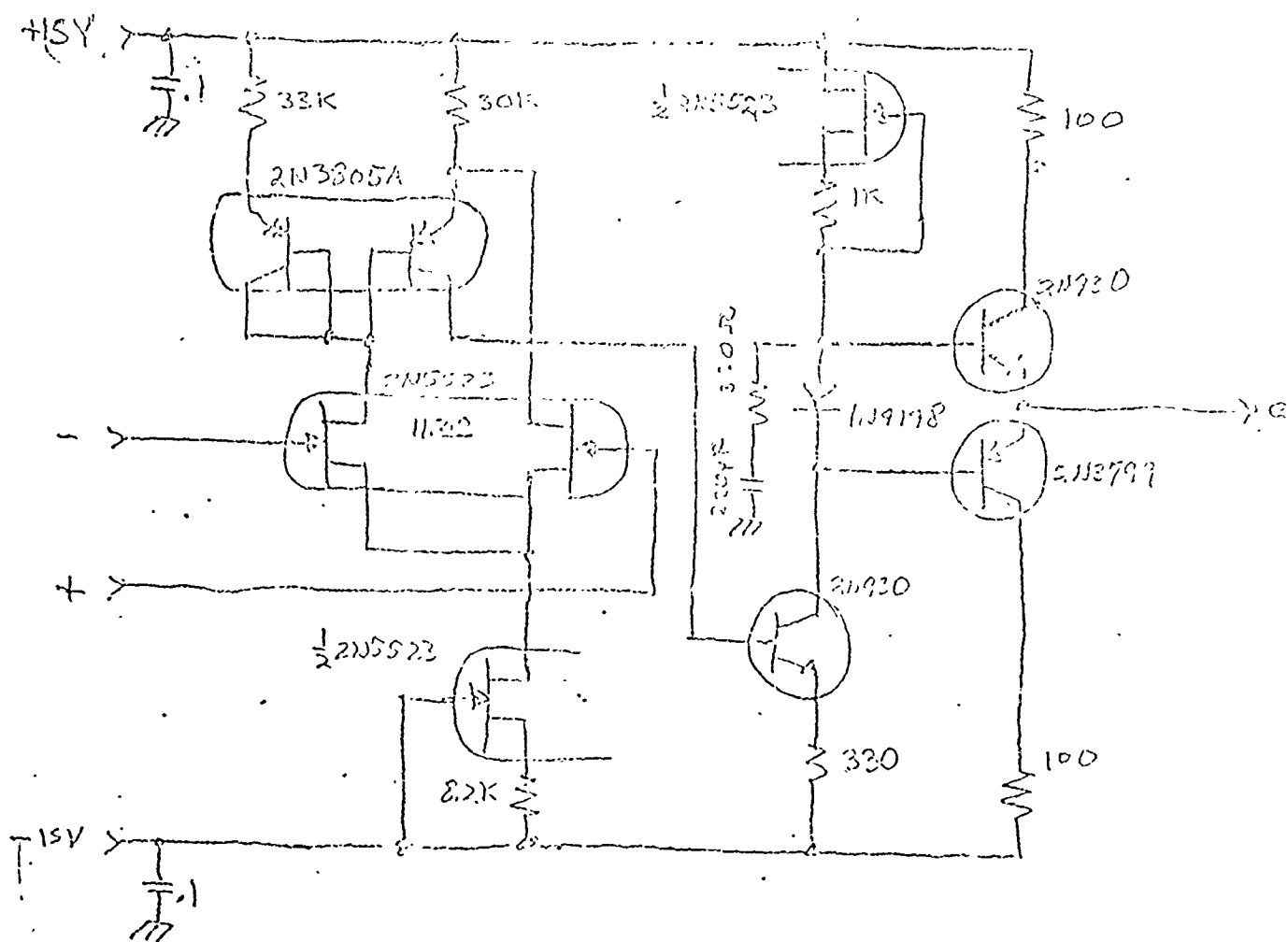
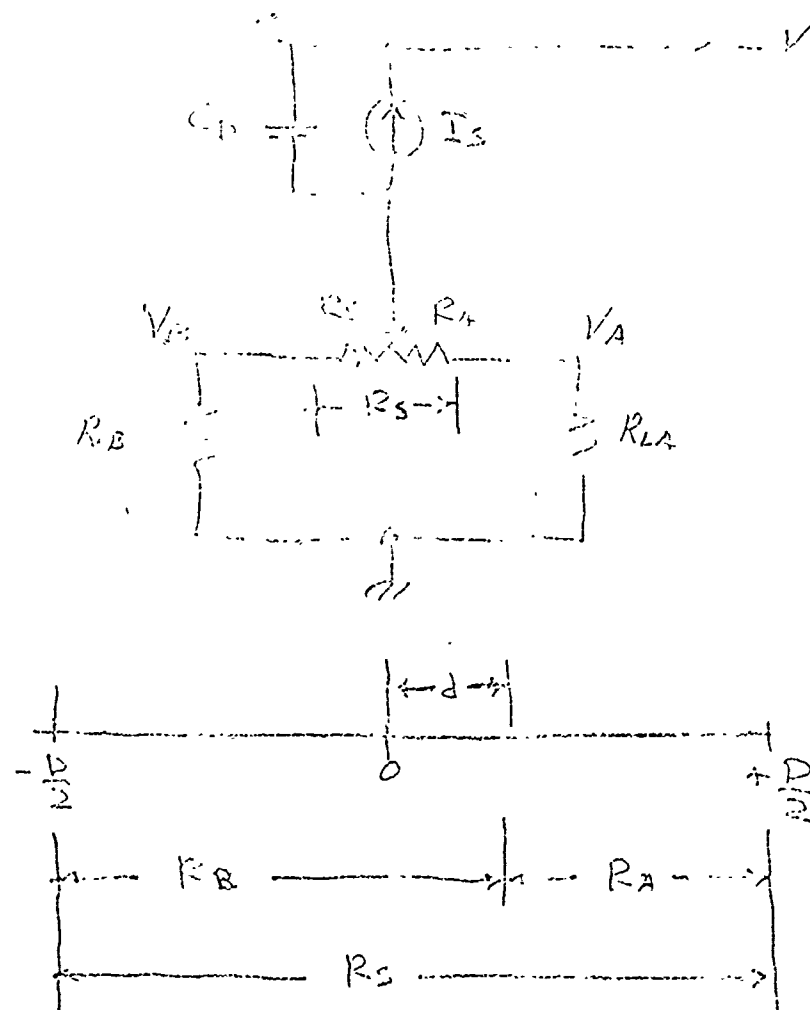


Figure 74. Low Noise Op-Amp.



$$R_B = \left(1 + \frac{d}{D/2}\right) \frac{R_s}{2}$$

$$R_A = \left(1 - \frac{d}{D/2}\right) \frac{R_s}{2}$$

Figure 75. Photo-Detector Equivalent Circuit.

Substituting for R_A , R_B from Figure 75:

$$\frac{A}{B} = \frac{1 + \frac{(1 + \frac{2d}{D}) R_S}{2}}{R_{LB}} \cdot \frac{1 - \frac{(1 - \frac{2d}{D}) R_S}{2}}{R_{LA}}$$

for maximum power transfer from photo detector to load, $R_{LA} = R_{LB} = \frac{R_S}{2}$:

$$\frac{A}{B} = \frac{1 + (1 + \frac{2d}{D})}{1 + (1 - \frac{2d}{D})} = \frac{1 + \frac{d}{D}}{1 - \frac{d}{D}}$$

However, if $R_{LA} = R_{LB} = 0$, then,

$$\frac{A}{B} = \frac{R_B}{R_A} = \frac{1 + \frac{2d}{D}}{1 - \frac{2d}{D}}$$

which shows that sensitivity of $\frac{A}{B}$ to displacement (d) is twice that for the conjugate matched load case. Consequently, since at these low frequencies (~ 5 Hz), impedance match is obtained inefficiently, the load giving the greatest angle gradient is selected, note

$$d = s\theta$$

where s = focal length
 θ = angle (radians).

XIII.5.2.3 Tracker Approaches

There are essentially two approaches to consider which produce an output which is a function of the ratio, $\frac{A}{B}$, (1) matched AGC, (2) log amplifiers. Examining the log amplifier approach first;

In the log amplifier approach, the A and B outputs of the photo detector are passed through switched log video amplifiers whose output difference forms the error signal

$$f_e = \ln A - \ln B = \ln \frac{A}{B}$$

$$f_e = \ln \frac{1 + \frac{2d}{D}}{1 - \frac{2d}{D}}$$

This error function is plotted in Figure 76 and Figure 77. Note that it is quite linear for small displacements. Also in practical log amplifiers, there will be a minimum output level corresponding to noise where the amplifier is no longer logarithmic so that the curve of Figure 76 will show saturation levels dependent upon input signal level. The slope and zero crossing remains independent of signal level.

In the AGC approach, the error function is

$$f_e = \frac{A - \frac{P}{B}}{A + B} = \frac{\frac{A}{B} - 1}{\frac{A}{B} + 1}$$

since,

$$\frac{A}{B} = \frac{1+x}{1-x}, \text{ where } x = \frac{2d}{D}$$

$$f_e = \frac{\frac{1+x}{1-x} - 1}{\frac{1+x}{1-x} + 1} = x$$

$$f_e = \frac{2d}{D} \quad \text{for } -\frac{1}{2} \leq \frac{d}{D} \leq \frac{1}{2}$$

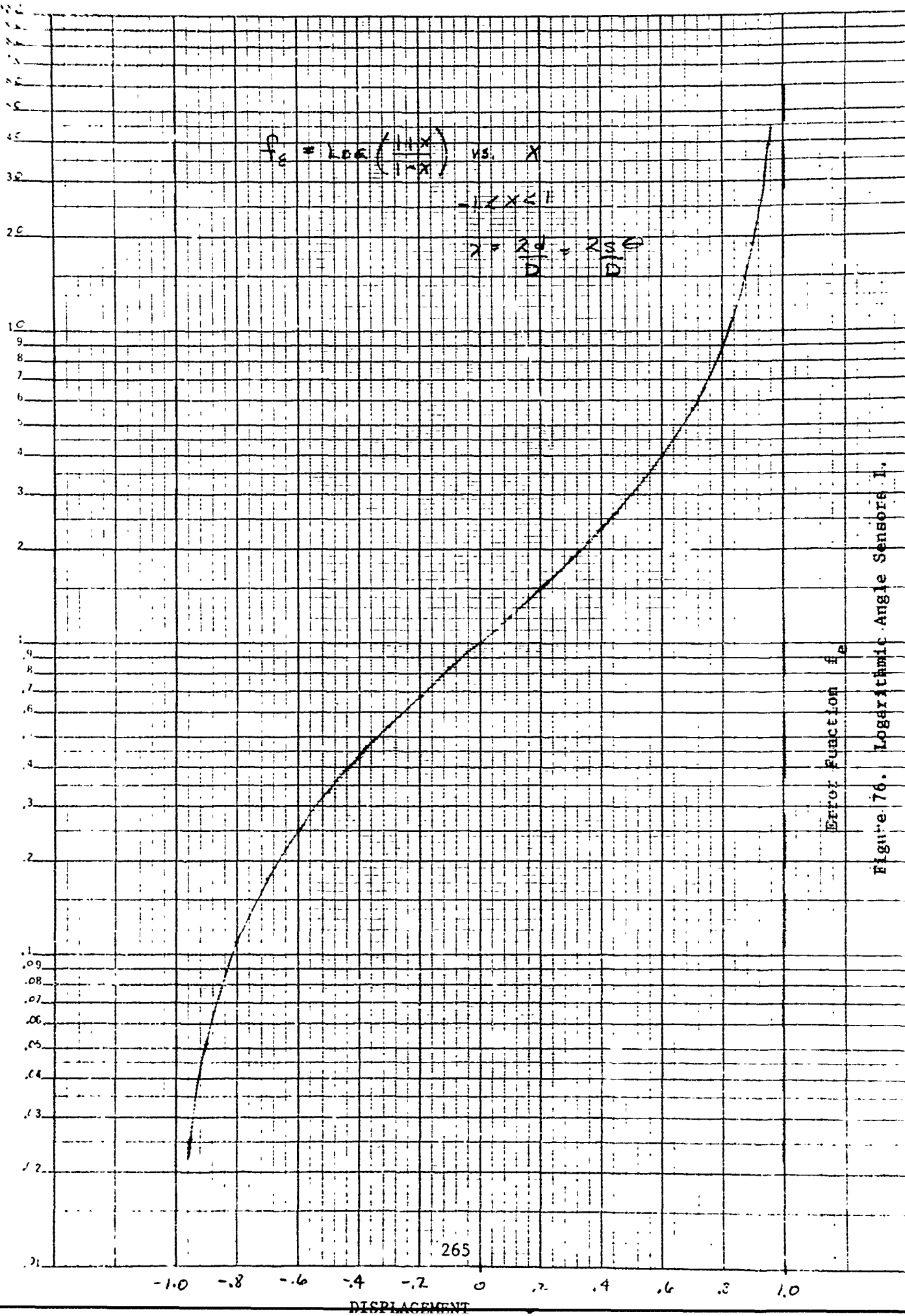


Figure 76. Logarithmic Angle Sensors I.

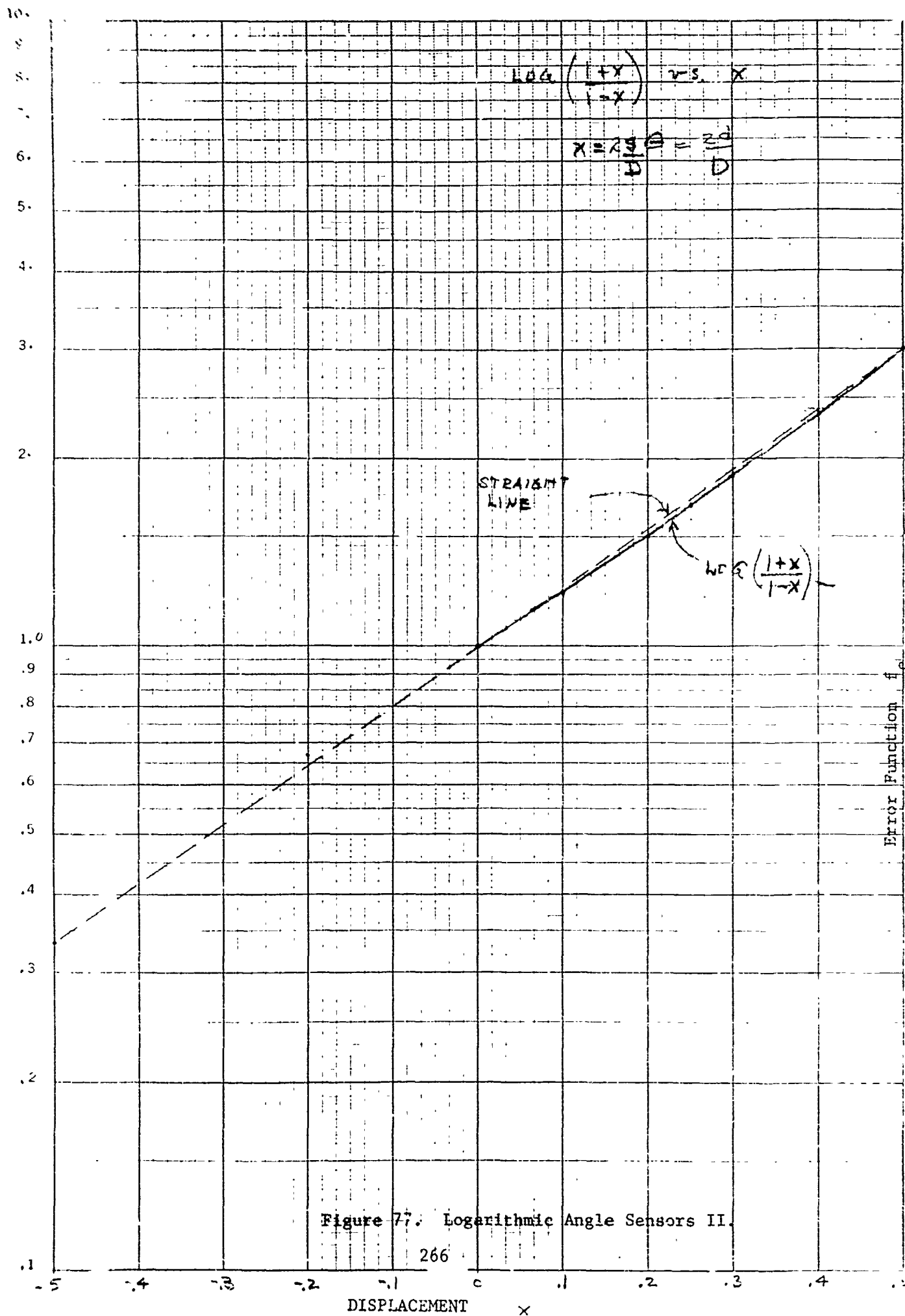


Figure 77. Logarithmic Angle Sensors II.

as shown in Figure 78.

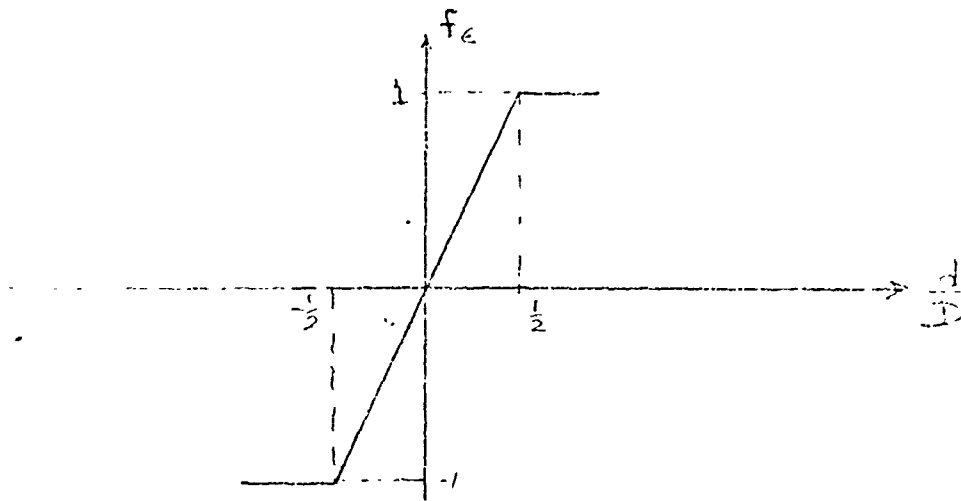


Figure 78: AGC Error Functions.

Both approaches produce desirable error function characteristics. The choice between the two approaches rests on which best fits the accuracy and dynamic range requirements for the "OPTS" project.

XIII.5.2.4 Accuracy Analysis

In making accuracy analysis, there is a distinction made between calibratable and uncalibratable errors. An example of calibratable error would be gain imbalance in linear amplifiers between channels - this can be adjusted out or "calibrated". An uncalibratable error is one which results in a gain imbalance or level shift which is dependent upon signal level (or temperature if no compensation made).

From the block diagram of Figure 79 for the AGC approach

$$c_s = 2I_s R_T^V G^V L \left(\frac{S}{D} \right) c$$

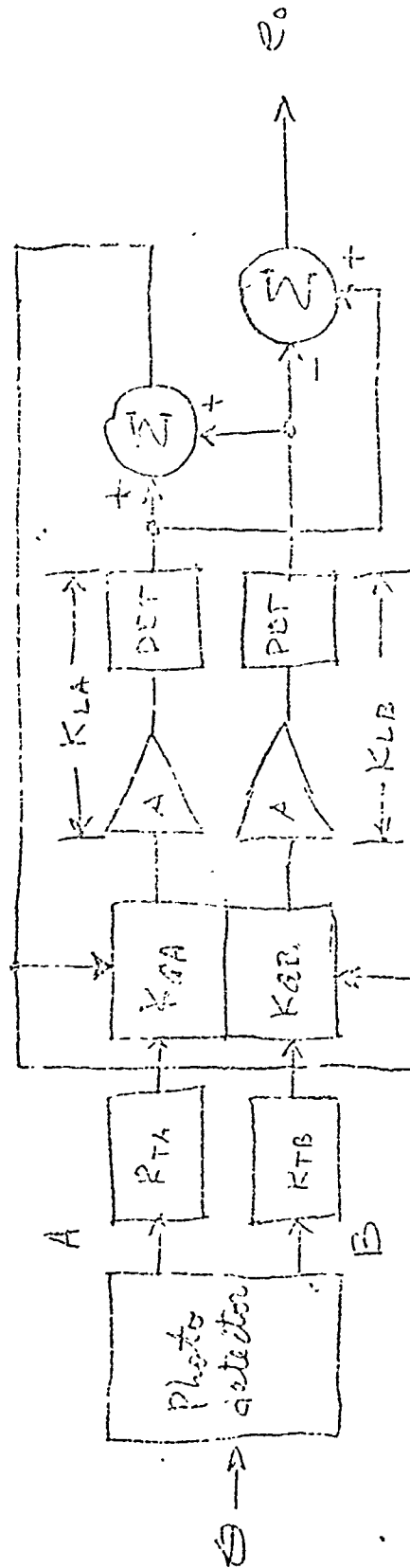


Figure 79. Block Diagram for AGC Approach.

Within the dynamic range of the AGC, the detector levels are held constant so that the only uncalibratable error is the mismatch in gain characteristics of the gain control elements $K_{GA} - K_{GB} = \Delta K_G$.

The error $\Delta\theta$ is given by:

$$\Delta\theta = \frac{1}{4} \frac{D}{S} \frac{\Delta K_a}{K_a}$$

where D = distance across active region of detector
 S = focal length

$\frac{\Delta K_a}{K_a}$ = fractional mismatch in gain of the gain control element.

For the NSC-FM1105A dual matched FET as gain control element,
 $\Delta\theta = 3.91 \times 10^{-5}$ radian for temperature (0 - 85°C) and signal level variation.

$$\Delta\theta = \frac{1}{4} \frac{D}{S} \frac{\Delta K_L}{K_L} \ln \left(R_T \frac{I_s}{2} \right)$$

where D = distance across active region of photo detector
 S = focal length

$\frac{\Delta K_L}{K_L}$ = fractional gain imbalance referred to input of the
 log amplifiers

R_T = transimpedance of input amplifier

I_s = photo detector current due to signal.

The first factor of the error equation is analogous to that of the AGC case which for a 1 dB match between log amplifiers gives

$$\Delta\theta = 1.03 \times 10^{-3} \ln \left(R_T \frac{I_s}{2} \right) \text{ radians,}$$

but the second factor above can be made less than unity in magnitude for less than a 10 dB range in I_s . Whereas, the previous result for the AGC case is valid for a dynamic range of 40 dB. Consequently, for this application, the AGC approach is appropriate.

XIII.5.2.5 AGC Dynamics

To determine AGC dynamic characteristics, the gain control element is first modeled with results shown in Figure 80. After making a linear approximation to the gain control characteristic, the block diagram of the loop follows directly as in Figure 81. The previous AGC system parameters were inserted and open and closed loop response calculated with results shown in Figure 82.

The "OPTS" AGC would have a wider response bandwidth consistent with the desired 100 Hz detector bandwidths and no peaking.

XIII.5.2.6 Sensitivity to Chop Frequency

The laser transmitter beam is CW chopped at a 5 kHz \pm 50 Hz rate. Amplitude matching of input bandpass filters is important to minimize boresight shifts due to changes in chopping frequency. The input bandpass transimpedance amplifiers are to be realized through the use of a low-noise discrete component op-amp with a notch filter in feedback. The notch filter response near center frequency is to be adjustable so that amplitude differences can be balanced out.

XIII.5.3 Summary

A design which will yield a mismatch error contribution of only 39 μ rad has been discussed. The final design specifications, however, will depend upon the required servo performance.

FET AS VOLTAGE CONTROLLED RESISTOR

NORMALIZED CONDUCTANCE (DRAIN TO SOURCE)
VS.

NORMALIZED CONTROL VOLTAGE (GATE TO SOURCE)

WOM 5-25-72

$$V_{es} = 0$$

$$r_{ds} = \frac{1}{g_{ds}}, \quad V_{GS} = V$$

$$V_p = V_{GS} \quad I_D = 1 \text{ nA}$$

REF. STATCOMIX APPLICATION TIP
"UNIFETS AS VOLTAGE CONTROLLED
RESISTORS", JULY 15, 1963.

LINEAR: APPROXIMATION:

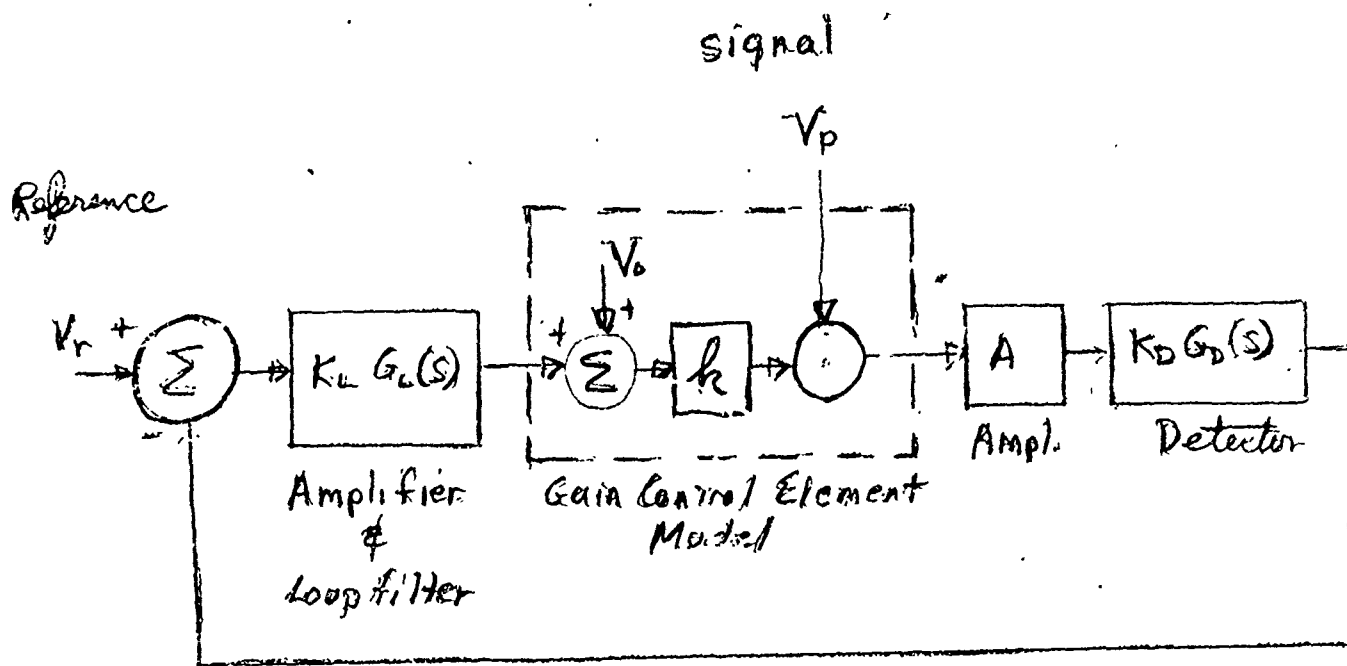
$$g_4 = 5V_4 + k$$

$$\phi = \psi|_{\mathcal{U}_A = \emptyset} = 1.145$$

$$S = \frac{\Delta A_2}{\Delta \psi_n} = \frac{-1.145}{.86} = -1.32$$

Figure 80. FET Voltage Controlled Resistor
Normalized Conductance vs.
Normalized Control Voltage.

$$v_r = (V_{GS}/V_p) \rightarrow$$



Units:

V_o	volts
h	unitless
A	dim. less
K_D	" "
$G_D(s)$	" "
K_L	" "
$G_L(s)$	" "

Open Loop Gain

$$A_{OL} = [A K_D K_L R V_p] G_D(s) G_L(s)$$

$$A_{OL} = -K_D G_D(s) G_L(s)$$

K_D proportional to input signal level

Figure 81. AGC Loop Dynamics Block Diagram.

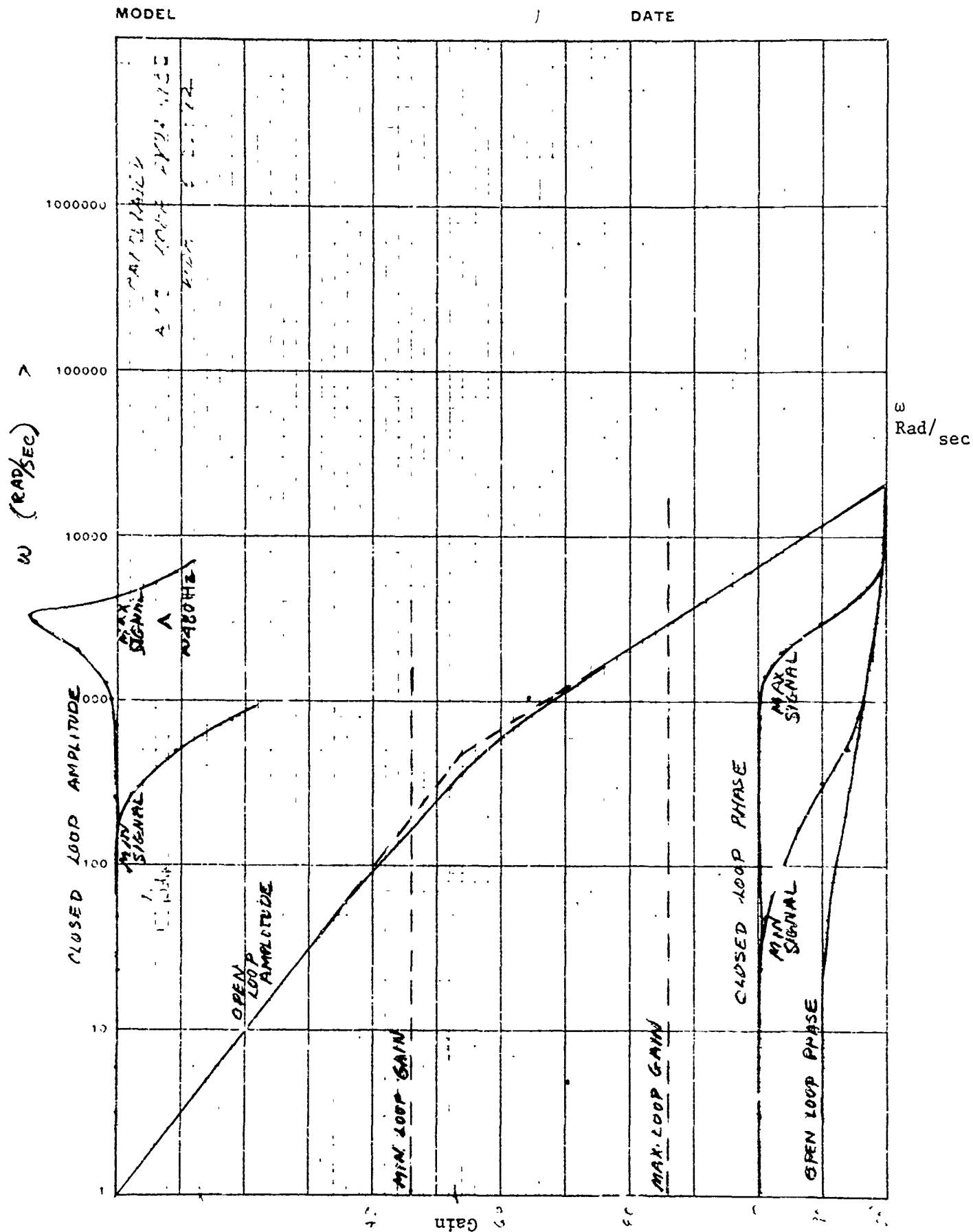


Figure 82. Open and Closed Loop Response.

APPENDIX XIV

BORESIGHT MONITOR AND FOCUSING EQUIPMENT

XIV.1 Introduction

The focus requirements of the reciprocity package are such that a stable, accurate reference is required for beam divergence/bore-sight maintenance

XIV.2 Discussion of Technique

The heart of this system is a specially modified temperature stabilized Questar telescope. This instrument is designed for thermal image compensation - maintaining an axially stable primary focal plane over the temperature range 10 to 50°C. By equipping the Questar with a calibrated vernier micrometer eyepiece with appropriate reticle in its focal plane, the Questar may be "preset" to focus the output beam of the reciprocity transmitter at the fila of the reticle.

Such a system, of course, would be sensitive to any accommodation by the observing eye. In order to remove the eye as a significant error source, the questar monitor is followed by a 43x alignment telescope (Hilgar-Watts or equivalent), resulting in a very restricted depth of field in the prime catadioptric focus region of the Questar. The autocollimator sees the fila of the Questar eyepiece at all times, and a sharp image of the reciprocity transmitter only when its output falls sharply coplanar with the Questar focus. Thermal shifts in the auto collimator have a negligible effect on the focus determination because of the 43 x magnification and observer "depth of field" at the auto collimator eyepiece.

XIV.3 Error Analysis

The normal observer will begin to have difficulty distinguishing a difference in focus between two objects viewed through a monocular telescope eyepiece when that Δf is on the order of 0.1 Diopter (depth perception is not involved, but rather parallax motion of the two images). Translated to object space for the Questar, with a nominal

100 x magnification, .1 Diopter becomes $.1/(100)^2$ Diopter, or 1×10^{-5} Diopter. Thus the reticle with an apparent focus at infinity would be locationally indistinguishable from an object at 100 kilometers. With the aid of the auto collimator, this Δf is further reduced (here to $.1/(43 \times 100)^2 = 5.45 \times 10^{-9}$ Diopter, or an apparent object distance of 1.84×10^5 Km). This corresponds to a beam convergence or divergence error of .005 microradians.

Appendix XV

TURBULENCE MEASUREMENTS

XV.1 Introduction

The turbulence effects on optical propagation are characterized by a parameter $C_N^2(h)$, the index of refraction structure parameter. In this section, we derive its relationship with other atmospheric parameters, reiterate the dependence of the optical parameters on it, and discuss and select an experimental technique to measure it during the OPTS experiments.

XV.2 Relation of $C_N^2(h)$ to Other Atmospheric Parameters

The index of refraction of a turbulent atmosphere randomly fluctuates due to pressure and temperature fluctuations. The governing equation is⁽¹⁰⁾

$$n - 1 \equiv \left\{ 77.6 \frac{P}{T} + \frac{0.584 P}{T \lambda^2} \right\} 10^{-6} \quad (\text{XV-1})$$

for λ = optical wavelength (microns)

P = atmospheric pressure (millibars)

T = atmospheric temperature ($^{\circ}\text{K}$)

n = index of refraction

Using the general gas law⁽¹¹⁾

$$\rho = \alpha P / RT \quad (\text{XV-2})$$

for ρ = density in gm/cm^3

P = pressure in millibars

R = gas constant = $2.876 \times 10^6 \text{ sec}^{-2} \text{ deg}^{-1}$

α = constant relating millibars to dynes/cm^2

and substituting in Equation (XV-1),

$$\begin{aligned}
 n-1 &= \rho \frac{R}{\alpha} \left\{ 77.6 + \frac{0.584}{\lambda^2} \right\} 10^{-6} \\
 &= \frac{\rho}{\rho_0} \left\{ 288 + \frac{1.34}{\lambda^2} \right\} 10^{-6}
 \end{aligned}
 \tag{XV-3}$$

for ρ_0 the density at sea level.

Therefore, Δn is proportional to $\Delta \rho$ and changes in density are directly reflected in changes in refractive index.

By partial differentiation,

$$\Delta \rho = \frac{\alpha}{R} \left\{ \frac{\Delta P}{T} - \frac{P \Delta T}{T^2} \right\}
 \tag{XV-4}$$

Experimentally^(1.), the first term in the brackets has been found to be negligible relative to the second, so that

$$\Delta \rho = -\rho \frac{\Delta T}{T}
 \tag{XV-5}$$

Using $C_N^2 \propto (\Delta n)^2$ and $C_T^2 \propto (\Delta T)^2$ we find

$$C_N^2(h) = \left[\frac{\rho(h)}{\rho_0} \left(288 + \frac{1.34}{\lambda^2} \right) \frac{10^{-6}}{T} \right]^2 C_T^2(h)
 \tag{XV-6}$$

Therefore, measuring the temperature structure parameter $C_T^2(h)$ will yield the index of refraction structure parameter, $C_N^2(h)$.

XV.3 Relation of $C_N^2(h)$ to the Optical Propagation Results

As seen in detail in the Appendices, the power fluctuations of a beam transmitted through the atmosphere depend crucially on this $C_N^2(h)$, the index of refraction structure parameter.

We showed in Appendix II that the power fluctuations due to scintillation alone have a normalized variance

$$\overline{\sigma_p^2} \equiv e^4 C_\ell - 1
 \tag{XV-7}$$

$$C_{\lambda}^2 \propto \int_a^H C_N^2(h) \left(\frac{1-h}{H} \right)^{5/6} g(h) dh \quad (XV-8)$$

for H = altitude of the receiver.

a = altitude of the transmitter.

$g(h)$ = function of altitude and the source parameters.

For a point source, $g(h) = h^{5/6}$, and the power fluctuations are dominated by the strength of $C_N^2(h)$ at high altitudes, i.e., the tropopause.

For a large beam source, $g(h)$ has a far more complicated dependence on h , but the overall result is the same, i.e., the high altitude turbulence dominates for most cases. If, in fact, focusing on or above the tropopause reduces the effects of that turbulence proportionately, then the low lying turbulence might become equally important.

We showed in Appendix III and V that the power fluctuations due to beam wander alone have a normalized variance

$$\frac{\overline{C_p^2}}{C_p^2} = \frac{4\alpha^2}{4\alpha+1} \quad (XV-9)$$

where

$$\alpha = \frac{\overline{\rho^2}}{w^2} \quad (XV-10)$$

$\overline{\rho^2}$ = mean square displacement of beam center

w = e^{-2} irradiance radius of the (gaussian) beam.

and

$$\overline{\rho^2} = \left(\lambda Z / \pi \rho_0 \right)^2 \quad (XV-11)$$

$$\text{From Appendix VI, } \rho_0^2 \propto \left[\int_a^H C_N^2(h) dh \right]^{-6/5} \quad (XV-12)$$

for a plane wave, and

$$\rho_0^2 \propto \left[\int_a^H C_N^2(h) \left(\frac{1-h}{H} \right)^{5/3} dh \right]^{-6/5} \quad (XV-13)$$

for a spherical wave originating at altitude H .

Therefore, for a satellite source ($H \gg$ all h at which $C_N^2(h) > 0$), the turbulence has an integrated effect, i.e., there are no weighting factors.

For most conditions, the turbulence near the ground will contribute heavily to the beam wander effects.

These points are made explicit by considering a typical profile,

$$C_N^2(h) = 10^{-13} \left\{ h^{-4/3} + 0.00243 \exp - \left(\frac{h - 1.5 \times 10^4}{10^3} \right)^2 \right\} \quad (\text{XV-14})$$

For no weighting function,

$$\int_a^\infty C_N^2(h) dh = 10^{-13} \left\{ \frac{3}{a^{1/3}} + 4.3 \right\} \quad (\text{XV-15})$$

Therefore, for this special profile, the strengths of near-ground and tropopause effects are equivalent. However, the tropopause changes strength slowly, while the near-ground profile and strength can change within a few minutes, especially near midday. ⁽¹³⁾

XV.4 Application to OPTS

Based on the facts discussed above, to fully relate optical results to turbulence results will require frequent measurements of the near earth turbulence and some sampling of the high altitude turbulence strength and distribution.

Appendix XVI

ADAPTIVE THRESHOLD EFFECTS

XVI.1 Introduction

After the submission of the draft of this report in September, 1972, we were informed by Michael Fitzmaurice of NASA-Goddard and G. F. Lee and N. F. Ruggieri of McDonnell-Douglas Astronautics that an "adaptive threshold" would change the results of the analysis of Appendix IV. The key idea of an adaptive threshold is that when the atmospheric effects are slow compared to the rate at which information is being transmitted, the receiver can act to adjust its detection threshold to the optimum for the short term average signal level.

The purpose of this Appendix is to indicate how such a threshold modifies our previous results.

XVI.2 Average P_E for Beam Wander Effects

Tycz, Fitzmaurice and Premo⁽⁵⁴⁾ have calculated the average P_E for a PGBM system (which they call OOK). The beta distribution of Appendix IV describes the average signal level, and the threshold is adaptive. Then result for an extinction ratio (ϵ^{-1}) of 20 and number of background photo-electrons (N) = 1 is shown in Figure 83.

Their parameter $\xi/\sigma = [2\alpha]^{-1/2}$ where α is defined in Appendix IV. Therefore, $\alpha = .1 \leftrightarrow \xi/\sigma = 2.236$, and we see that the adaptive threshold does not change our previous criterion for the effects of wander, i.e., $\alpha \leq 0.1$ is still necessary. (The reason is that they have used realistic extinction and background values.)

XVI.3 Average P_E for Scintillation Effects

Tycz et al⁽⁵⁵⁾ have also performed calculations for an adaptive threshold PGBM system with log-normal signal fading. Their results are shown in Figure 84 for an extinction ratio (ϵ^{-1}) = 20, $N = 1$ again.

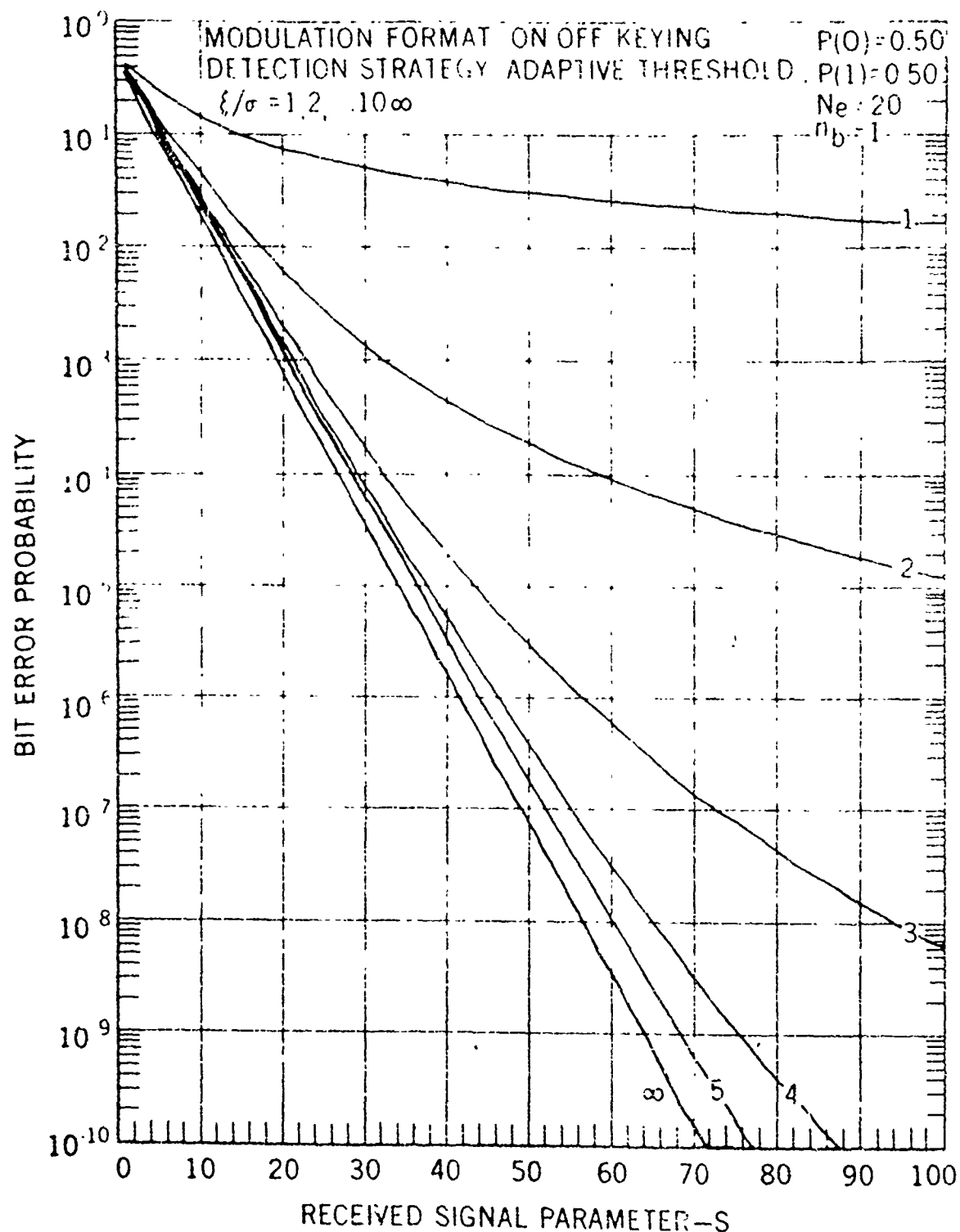
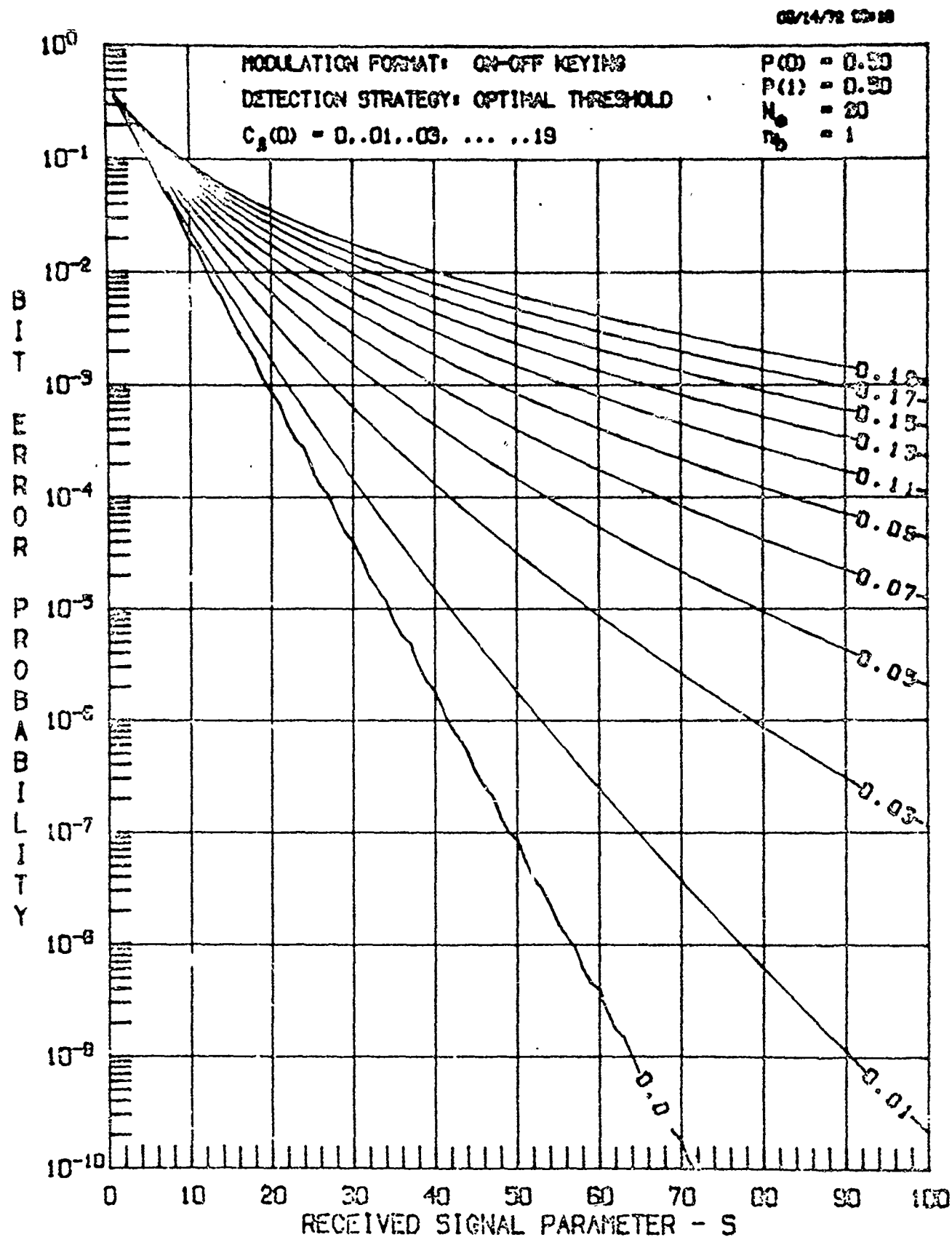


Figure 83. Binary Optical Communication System Performance with Tracking Induced Signal Fading.



BINARY OPTICAL COMMUNICATION SYSTEM PERFORMANCE
WITH ATMOSPHERIC INDUCED SIGNAL FADING

Figure 84.

Lee, Ruggieri and Fluchel⁽⁵⁶⁾ have performed like calculations, but with $s = (30)^{-1}$, $N = 0$. Their results are shown in Figure 85.

Comparing these two figures to our previous result (Figure 44), we see that there is a significant change in the required level of C_ℓ allowable for a low number of photoelectrons, i.e., perhaps $C_\ell \leq 0.03$ is a realistic criterion for the necessary scintillation level.

XVI.3.1 Scintillation on the High Data Rate Uplink

Adaptive threshold techniques are most directly applicable to the high-data-rate link, and the fixed threshold criterion of $C_\ell \leq 0.01$ can be restated as $C_\ell \leq 0.03$ or even $C_\ell \leq 0.05$, depending on the extinction ratio actually achieved. However, before definitely accepting this new estimate, a number of points mentioned earlier should be repeated, such as:

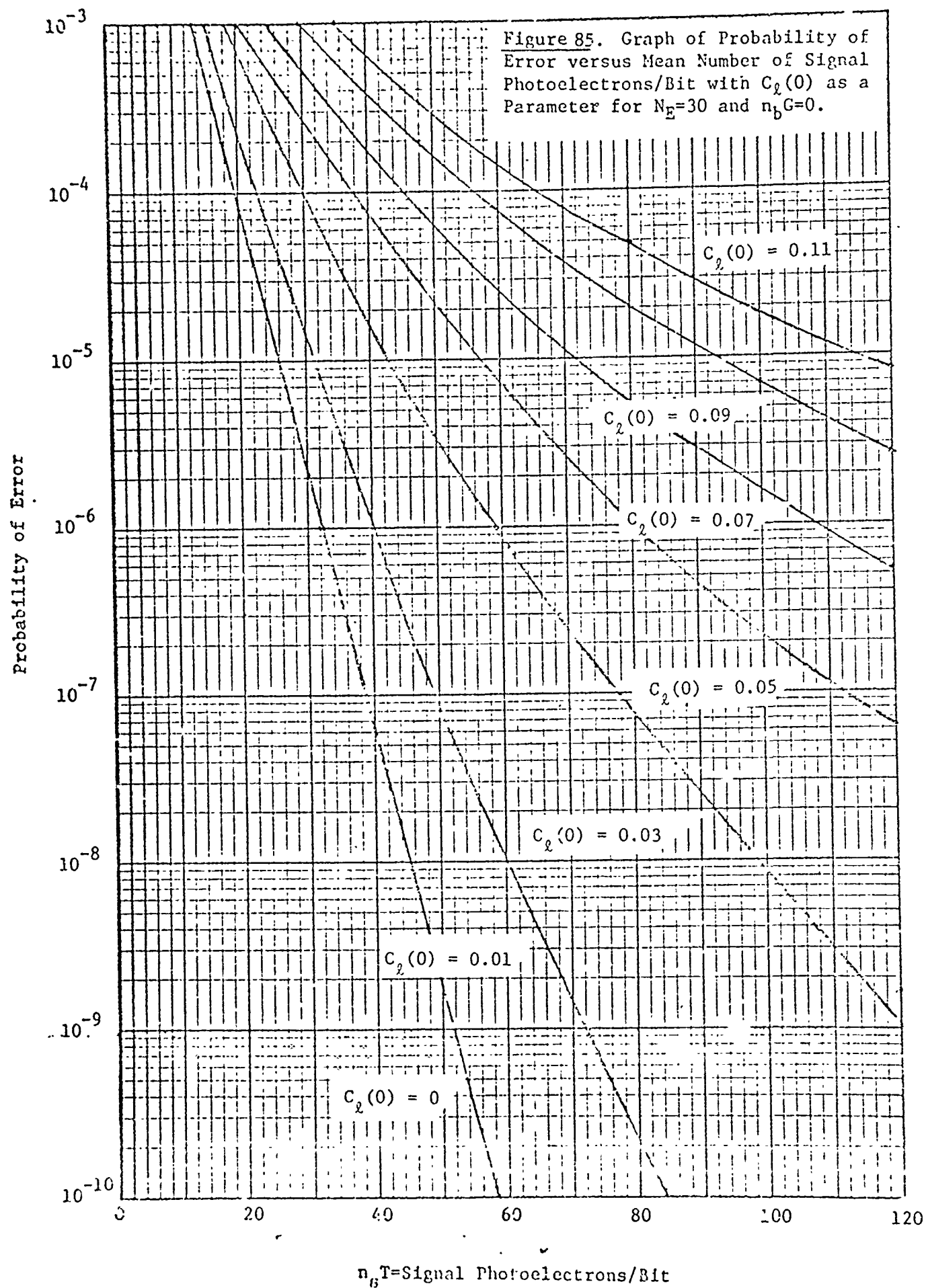
(1) For atmospheric effects to be negligible, $C_\ell \leq 0.01$ is still a best choice, i.e., it requires only ≈ 1 dB of margin as seen in Figure 85 (i.e., $10 \log_{10} (40/32) \approx 1$ dB).

(2) As pointed out in Appendix IV (and recently by Kerr)⁽⁵⁷⁾, the value of C_ℓ that characterizes a beam is minimum at beam center and increases as the distance from beam center increases. Therefore, even a small amount of wander will result in a value of C_ℓ larger than the value previously computed at beam center. Therefore, for the real situation where both wander and scintillation occur simultaneously, a minimum value of C_ℓ at beam center will be required. Therefore, $C_\ell \leq 0.01$ at beam center might still be a reasonable criterion. A definitive statement in this area requires further analysis and experiments.

XVI.3.2 Scintillation and the Beacon Uplink

Clearly Figures 84 and 85 do not apply to the previously discussed beacon uplink (Sections 4.3 and 9.3) for a number of reasons:

- (1) The beacon link is a PIM system, not PGBM.
- (2) The number of signal photoelectrons (and background photoelectrons) far exceeds those in the two figures, and extinction ratio loses its meaning in this signal format since the beacon laser does not pass through a modulator.



(3) Most importantly, pulses are being transmitted at a 1600 pp sec rate. An adaptive threshold averages over a number of received pulses to set the optimum level. At this low pulse rate, the atmosphere has randomly changed between every few pulses so that the adaptive threshold techniques would not significantly affect the detection probability on a short term basis.

Therefore, we think that preserving an average $P_{E1} < 10^{-6}$ requires the additional 20 dB margin (over the present design¹) as discussed in Section 4.3.

REFERENCES

1. Space Data Relay Sybsystem; Laser Communications; Preliminary Subsystem Design, Nov. 1971, SAMSO TR-71-251.
2. Reference 1, Volume III Appendicies, P. J. Titterton, D. P. Woodman and E. Paddon, Atomopheric Prediction Analysis.
3. Reference 1, Volume III Appendicies, P. J. Titterton, Atmospheric Experiment Analyses.
4. P. O. Minott et al, Results of RAPE I, March 1972. X-524-72-125.
5. P. J. Titterton, L. E. Mallery and T. A. Arken, Lightweight Thermosonde System, December, 1971, Contract NAS5-11493
6. J. H. Shapiro, "Reciprocity of the Turbulent Atmosphere," submitted to J. Opt. Soc. Am.
J. H. Shapiro "Diffraction-Limited Communication Through Atmospheric Turbulence," to be published.
H. T. Yura and D. L. Fried, "Telescope Performance Reciprocity for Propagation in a Turbulent Medium," 15 Jan., 1972, SAMSO TR-72-5
D. M. Chase, "Power Loss in Propagation Through a Turbulent Medium for an Optical-Heterodyne System with Angle Tracking".
7. D. L. Fried and R. A. Schmeltzer, "The Effect of Atmospheric Scintillation on an Optical Data Channel - Laser Radar and Binary Communications," App. Opt., Vol. 6 (10) P 1729-1737, 1967.
8. Chester Wheeler, Boller and Chivens, phone conversation and visit with P. J. Titterton and D. P. Woodman.
9. Catherine Rice, AFCLRL completed the relevant balloon motion data, and it was forwarded to P. J. Titterton in a letter from Mr. Tom Danaher, AFCLRL, on 10 May, 1972.
10. Handbook of Geophysics, pp. 13-1, 13-2, MacMillan Co., (New York 1960).
11. The law in this form is given in F. W. Sears Thermodynamics, The Kinetic Theory of Gases and Statistical Mechanics, Addison-Wesley (Reading, Mass., 1959), p. 16. Utilization of more complex laws such as van der Wal's equation, p. 17, or the Beattie-Bridgman equation, only, adds a small correction.

REFERENCES

1. Space Data Relay Sybsystem; Laser Communications; Preliminary Subsystem Design, Nov. 1971, SAMSO TR-71-251.
2. Reference 1, Volume III Appendicies, P. J. Titterton, D. P. Woodman and E. Paddon, Atomopheric Prediction Analysis.
3. Reference 1, Volume III Appendicies, P. J. Titterton, Atmospheric Experiment Analyses.
4. P. O. Minott et al, Results of BAPE I, March 1972. X-524-72-125.
5. P. J. Titterton, L. E. Mallery and T. A. Arken, Lightweight Thermosonde System, December, 1971, Contract NAS5-11493
6. J. H. Shapiro, "Reciprocity of the Turbulent Atmosphere," submitted to J. Opt. Soc. Am.
J. H. Shapiro "Diffraction-Limited Communication Through Atmospheric Turbulence," to be published.
H. T. Yura and D. L. Fried, "Telescope Performance Reciprocity for Propagation in a Turbulent Medium," 15 Jan., 1972, SAMSO TR-72-5
D. M. Chase, "Power Loss in Propagation Through a Turbulent Medium for an Optical-Heterodyne System with Angle Tracking".
7. D. L. Fried and R. A. Schmeltzer, "The Effect of Atmospheric Scintillation on an Optical Data Channel - Laser Radar and Binary Communications," App. Opt., Vol. 6 (10) P 1729-1737, 1967.
8. Chester Wheeler, Boller and Chivens, phone conversation and visit with P. J. Titterton and D. P. Woodman.
9. Catherine Rice, AFCLRL completed the relevant balloon motion data, and it was forwarded to P. J. Titterton in a letter from Mr. Tom Danaher, AFCLRL, on 10 May, 1972.
10. Handbook of Geophysics, pp. 13-1, 13-2, MacMillan Co., (New York 1960).
11. The law in this form is given in F. W. Sears Thermodynamics, The Kinetic Theory of Gases and Statistical Mechanics, Addison-Wesley (Reading, Mass., 1959), p. 16. Utilization of more complex laws such as van der Wal's equation, p. 17, or the Beattie-Bridgman equation, only, adds a small correction.

12. R. E. Hufnagel and N. R. Stanley, "Modulation Transfer Function Associated with Image Transmission through Turbulent Media," J. Opt. Soc. Am., v. 54, pp. 52-61, January 1964.
13. J. L. Bufton, P. O. Minott, M. W. Fitzmaurice and P. J. Titterton, "Measurements of Turbulence Profiles in the Troposphere," J. Opt. Soc. Am., Sept., 1972.
14. Freeman Hall, N.O.A.A., Personal Communication to P. J. Titterton on 3 May, 1972.
15. Height limits at Cloudcroft would be 500 feet, and at the NASA ground site, 2800 feet. Moreover, it takes 30 minutes to raise or lower the device to the 2800 feet level. This information was obtained from Mr. Tom Danaher, AFCRL.
16. Developed by Aerojet General under contract to NASA.
17. This is a typical value needed to provide the required beam expansion.
18. Mr. D. C. Robinson, Goodyear Aerospace, Letter and personal communication to P. J. Titterton and D. P. Woodman, July 27, 1972.
19. J. L. Bufton, "An Investigation of Atmospheric Turbulence by Stellar Observations," NASA TR R-369, August, 1971.
20. For unequal beam sized at the transmitter, equation V-27 of Appendix V becomes:

$$\frac{\eta}{\alpha} = \frac{4a_1^2 R^2 Z^2 + R^2 k^2 a_1^2 a^4}{4R^2 a^2 Z^2 + k^2 a^2 a_1^2 (R-Z)^2}$$

for a_1 = new beam e^{-2} radius = 7.5 cm

R = wavefront curvatures = 5.06×10^4 , as desirable from equations I-2 and I-3 of Appendix I.

Z = range from transmitter to receiver

a = collimated beam e^{-2} radius = 6.27 cm

k = wave # $2\pi/\lambda$

Inserting these values for $\lambda = 5320\text{\AA}$ and $Z = 35,000$ hm,

$\eta/\alpha \approx .0165$. Therefore η (the reduced α) = $(.137)(.016) = .002$.

21. H. Kogelnik and T. Li "Laser Beams and Resonators," Proc. IEEE, Vol 54 (10), p. 1312-1329, 1966.

22. D. L. Fried and J. D. Cloud, "Propagation of an Infinite Plane Wave in a Randomly Inhomogeneous Medium," J. Opt. Soc. Am., Vol. 56 (12), p. 1667-1677, December 1966.
23. R. A. Schmeltzer "Means, Variances, and Covariances for Laser Beam Propagation Through a Random Medium", Quart. App. Math. Vol. 24, p 339-354, 1967.
24. A. Ishimaru, "Fluctuations of a Focused Beam Wave for Atmospheric Turbulence Probing," Proc. IEEE, Vol. 57, (4), p. 407-414, 1969 Figure 11.
25. R. W. Lee and J. C. Harp, "Weak Scattering in Random Media, with Applications to Remote Probing," Proc. IEEE, Vol 57 (4), p. 375-406, 1969.
26. D. L. Fried and J. B. Seidman, "Laser Beam Scintillation in the Atmosphere," J. Opt. Soc. Am., Vol. 57 (2), p. 181-185, 1967.
27. D. L. Fried "Scintillation of a Ground-to-Space Laser Illuminator," J. Opt. Soc. Am., Vol. 57, (8), p 980-983, Aug. 1967.
28. J.R. Kerr and J. P. Dunphy, "Transmitter-Aperture Effects on Laser Scintillation," Paper WE17, O.S.A., 1972 Spring Meeting, New York.
29. R. E. Hufnagel, "An Improved Model Turbulent Atmosphere," in Restoration of Atmospherically Degraded Images, Woods Hole Summer Study (1966), Vol. 2, Appendix 3, pp. 15-18.
30. E. Brookner, "Improved Model for the Structure Constant Variations with Altitude," Appl. Opt., Vol. 10 (8), p. 1533-1534, August 1967.
31. R. Esposito, "Power Scintillations Due to the Wandering of the Laser Beam," Proc. IEEE (Letters), Vol. 55 (8), p. 1533-1534, August 1967.
32. J. I. Marcum, "Table of Q Functions," AD 116551, January 1, 1950.
33. F. Bowman, "Introduction to Bessel Functions," (Dover, New York) 1958.
34. J. P. Speck, "Effects of Atmospheric Turbulence on Poisson Detection Processes," Paper WB20, O.S.A., Spring Meeting, 1971, Tucson.
35. V. I. Tatarski, Wave Propagation in a Turbulent Medium (Dover, New York) 1967.
36. T. L. Ho, "Log-Amplitude Fluctuations of Laser Beam in a Turbulent Atmosphere," J. Opt. Soc. Am., Vol 59 (4), p. 385-390, April, 1969.

37. R. F. Lutomirski and H. T. Yura, "Wave Structure Function and Mutual Coherence Function of an Optical Wave in a Turbulent Atmosphere," J. Opt. Soc. Am., Vol. 61 (4), p. 482-487, April, 1971.
R. F. Lutomirski and H. T. Yura, "Propagation of Finite Optical Beam in an Inhomogeneous Medium," App. Opt., Vol. 10 (7), p. 1652-1658, July, 1971.
38. D. L. Fried, "Limiting Resolution Looking Down Through the Atmosphere," J. Opt. Soc. Am., Vol. 56 (10), p. 1380-1389, 1966.
39. D. L. Fried, "Atmospheric Modulation Noise in an Optical Heterodyne Receiver," IEEE JQE, Vol. QE-3 (6), p. 213-221, 1967.
40. Non-identical beam sizes result in a like expression, as discussed in Reference 20.
41. Z. I. Feizulin and Yu A. Kravtsov, "Broadening of a Laser Beam in a Turbulent Medium," Radiophysics and Quantum Electronics, Vol. 10 (1), p. 33-35, 1967.
42. R. S. Lawrence and J. W. Strohbehn, "A Survey of Clear-Air Propagation Effects Relevant to Optical Communications," Proc. IEEE, Vol. 58 (10), p. 1523-1545, October, 1970.
43. D. L. Fried, "Statistics of a Geometric Representation of Wavefront Distortion," J. Opt. Soc. Am., Vol. 55 (11), p. 1427-1435, Nov., 1965.
44. M. V. Klein, Optics, John Wiley and Sons, New York 1970, Section 9.6.
45. M. A. Kallistiatova, "Fluctuations in the Direction of Propagation of Light Waves in an Inhomogeneous Turbulent Medium," Izv. Vuz Radiofizika, Vol. 9 (1), p. 50-56, 1966.
46. D. L. Fried, "Propagation of a Spherical Wave in a Turbulent Medium," J. Opt. Soc. Am., Vol. 57 (2), p. 175-180, Feb., 1967.
47. D. L. Fried, "Aperture Averaging of Scintillation," J. Opt. Soc. Am., Vol. 57 (2), p. 169-175, Feb., 1967.
48. J. P. Campbell and L. G. DeShazer, "Near Fields of Truncated-Gaussian Apertures," J. Opt. Soc. Am., Vol. 59 (11), p. 1427-1429, Nov., 1969.
49. G. Oluremi Olaofe, "Diffraction by Gaussian Apertures," J. Opt. Soc. Am., Vol. 60 (12), p. 1654-1657, Dec., 1970.
50. R. G. Schell and G. Tyras, "Irradiance from an Aperture with a Truncated-Gaussian Field Distribution," J. Opt. Soc. Am., Vol. 61 (1), p. 31-35, Jan., 1971.

51. D. A. Holmes, J. E. Korka, and P. V. Avizonis, "Parametric Study of Apertured Focused Gaussian Beams," App. Opt., Vol. 11 (3), p. 565-574, March 1972.
52. W. E. Webb, "Near Field Antenna Patterns of Obstructed Cassegrainian Telescopes," BER Report #143-70, Jan., 1972, NASA-25562.
53. H. Skenker, J. A. Dowling and J. A. Curcio, "Propagation of Focused Laser Beams," Paper presented at Electro-Optical Systems Design Conference '71 West, May 18, 1971.
54. M. Tycz, M. W. Fitzmaurice and D. O. Premo, "Optical Communications System Performance with Tracking Error Induced Signal Fading", submitted to PROC. IEEE.
55. M. W. Fitzmaurice, Private Communication, 11/3/72.
56. G. M. Lee, N. F. Ruggieri and R. B. Fluchel, Private communication, 10/24/72.
57. J. R. Kerr, J. R. Dunphy, "Experimental Effects of Finite Transmitter - Apertures on Scintillations", to be published in J. Opt. Soc. Am.

UNCLASSIFIED

Security Classification

DOCUMENT CONTROL DATA - R & D

(Security classification of title, body of abstract and indexing annotation must be entered when the overall report is classified)

1. ORIGINATING ACTIVITY (Corporate author) GTE Sylvania Inc., Electronic Systems Group Western Division, P.O. Box 188 Mountain View, California 94040		2a. REPORT SECURITY CLASSIFICATION UNCLASSIFIED	
3. REPORT TITLE OPTICAL PROPAGATION TESTS STUDY		2b. GROUP	
4. DESCRIPTIVE NOTES (Type of report and inclusive dates) Final Report, April 1972 - September 1972			
5. AUTHOR(S) (First name, middle initial, last name) Paul J. Titterton Douglas P. Woodman, Martin L. Boehme, W. Don Huber, Robert W. Jones Frank Lord, Scott Overstreet, William Schick, Norman Spaulding.			
6. REPORT DATE September, 1972		7a. TOTAL NO OF PAGES 305	7b. NO OF REFS 57
8a. CONTRACT OR GRANT NO F33615-72-C-2051 b. PROJECT NO 405B c. -01 d. -56		9a. ORIGINATOR'S REPORT NUMBER(S) 9b. OTHER REPORT NO'S. (Any other numbers that may be assigned this report) AFAL-TR-72-307	
10. DISTRIBUTION STATEMENT Distribution limited to U.S. Government agencies only, test and evaluation, applied March, 1972. Other requests for this document must be referred to AFAL/TEL, Wright Patterson AFB, Ohio 45433.			
11. SUPPLEMENTARY NOTES		12. SPONSORING MILITARY ACTIVITY Air Force Avionics Laboratory Air Force Systems Command Wright-Patterson Air Force Base, Ohio	
13. ABSTRACT <p>The Optical Propagation Tests Study has analyzed the effects of atmospheric turbulence on atmospheric laser links. Our analyses have found that scintillation (beam breakup), beam spread and beam wander will preclude operation of a high data rate uplink at 1 Gbps with an average P_E of 10^{-6}, unless special techniques are utilized in the ground transmitter design. We have predicted that focusing the beam at or above the tropopause will reduce the scintillation effects sufficiently, and pointing the uplink beam along the instantaneous normal to a downlink wavefront of a beam which originates at the satellite transmitter (reciprocity tracking) will remove most of the wander effects.</p> <p>We have explored a number of possible experimental techniques, suitable for testing these predictions. Our recommendation is to perform an experiment in May/June 1974 using a variable focus reciprocity tracking ground transceiver and a balloon-borne (altitude 100,000 feet) system that is a modification of that developed in the Balloon Atmospheric Propagation Experiment. This recommendation allows for full utilization of the techniques (and equipment) developed under the 405B Acquisition/Tracking Brassboard programs and will specify the design constraints for the ground station by June 30, 1974.</p>			

KEY WORDS	LINK A		LINK B		LINK C	
	ROLE	WT	ROLE	WT	ROLE	WT
Optical Propagation						
Atmospheric Turbulence Effects						
Scintillation						
Beam Wander						
Beam Spread						
Experimental Tests over Vertical Paths						
Reciprocity Tracking						
High Data Rate Uplinks						
Probability of Error for PGBM.						